Messung der W-Boson-Helizitätsanteile in Top-Quark-Zerfällen mit dem CDF II Experiment und Studien zu einer frühen Messung des $t\bar{t}$-Wirkungsquerschnitts mit dem CMS Experiment

Zur Erlangung des akademischen Grades eines
DOKTORS DER NATURWISSENSCHAFTEN
von der Fakultät für Physik des
Karlsruher Institut für Technologie (KIT)

genehmigte

Dissertation

von

Dipl. Phys. Thorsten Chwalek
aus Rastatt

Tag der mündlichen Prüfung: 12.02.2010

Referent: Prof. Dr. W. Wagner, Fachbereich C - Experimentelle Teilchenphysik,
Bergische Universität Wuppertal

Korreferent: Prof. Dr. Th. Müller, Institut für Experimentelle Kernphysik,
Karlsruher Institut für Technologie (KIT)

Zusammenfassung

Aus was besteht die Welt? Die Frage nach den fundamentalen Bausteinen der Materie beschäftigte Wissenschaftler und Gelehrte zu allen Zeiten. Ausgehend von abstrakten philosophischen Überlegungen wurde das Konzept von kleinsten, nicht weiter zerteilbaren Grundbausteinen der Materie bereits einige Jahrhunderte vor Christus von indischen und griechischen Philosophieschulen entwickelt. Etwa 450 v. Chr. prägte Demokrit den Begriff *átomos*, das "Unzerschneidbare", für die diskreten Grundbausteine der Materie. Doch erst in der jüngeren Vergangenheit konnte dieses philosophische Konzept auch experimentell überprüft werden.
Auf ihrer Suche nach den elementaren Bausteinen der Materie drangen Wissenschaftler zu immer kleineren Skalen vor. Ende des 19. Jahrhunderts galt es als experimentell erwiesen, dass alle Materie tatsächlich aus kleinsten Bautsteinen besteht. In Anlehnung an Demokrit nannte man diese Bestandteile Atome. Maßgeblich beeinflusst von den Ergebnissen der Rutherford'schen Experimente [1] verfestigte sich zu Beginn des 20. Jahrhunderts das moderne Bild des Atoms. Nach dem bis heute gültigen Verständnis besteht ein Atom aus einem dichten, positiv geladenen Kern, der von einer negativ geladenen Elektronenwolke umgeben ist. Doch während Elektronen elementare, punktförmige Teilchen sind, zeigte sich bald, dass der Atomkern ein zusammengesetztes Objekt ist, bestehend aus positiv geladenen Protonen und elektrisch neutralen Neutronen. Wie sich bald herausstellte waren mit Proton und Neutron jedoch erneut nicht die elementaren Bestandteile der Materie entdeckt worden.
Dank neuer experimenteller Möglichkeiten wurden in den 50er und 60er Jahren des 20. Jahrhunderts zunächst in der Höhenstrahlung, später auch in Beschleunigerexperimenten, immer neue Mesonen und Baryonen entdeckt. Um Ordnung in die immer größer werdende Schar von neu entdeckter Teilchen zu bringen, postulierten Murray Gell-Mann und George Zweig 1964, dass Proton und Neutron sowie alle anderen bekannten Hadronen aus punktförmigen Elementarteilchen bestehen [2]. Gell-Mann prägte den Begriff "Quarks" für diese Grundbausteine der Materie. Obwohl ursprünglich nur als mathematisches Konzept gedacht, mithilfe dessen sich die Vielzahl der beobachteten Teilchen in ein Ordnungsschema einordnen ließ, wurden bald experimentelle Hinweise auf diese Quarks gefunden. Da Quarks nicht einzeln vorkommen, sondern immer nur in gebunden Zuständen auftreten, können sie allerdings nur indirekt nachgewiesen werden. 1968 fand man in tiefinelastischen Streuexperimenten am Stanford Linear Accelerator Laboratory Hinweise darauf, dass das Proton eine Substruktur aus punktförmigen Teilchen besitzt. Später identifizierte

man diese punktförmigen Teilchen mit den Up- und Down-Quarks. Mittlerweile sind sechs verschiedene Arten oder "Flavors" von Quarks bekannt. Neben dem Up- und dem Down-Quark, aus denen alle gewöhnliche Materie aufgebaut ist, gibt es vier weitere Quark-Sorten, die allerdings in der uns umgebenden stabilen Materie nicht vorkommen. Sie können jedoch in Kollisionen gewöhnlicher Teilchen aus der dabei frei werdenden Energie erzeugt werden. Diese Kollisionen können sich sowohl in der Atmospähre ereignen, wenn Teilchen der kosmischen Strahlung auf Luftmoleküle treffen, oder in Beschleunigerexperimenten künstlich erzeugt werden. In diesen Experimenten werden Strahlen von Protonen, Antiprotonen, Elektronen oder Positronen zur Kollision gebracht und dabei neue Teilchen produziert. Einmal erzeugt, zerfallen die schwereren Quarks allerdings sukzessive in leichtere Quarks und können durch eine Analyse ihrer Zerfallsprodukte in speziell hierfür entwickelten Detektoren, die um den Kollisionspunkt installiert sind, nachgewiesen werden.
Seit ihrer Postulierung wurden alle sechs Quark-Sorten experimentell nachwiesen. Als letztes wurde 1995 das Top-Quark mit den CDF- und DØ -Experimenten am Tevatron-Beschleuniger am Fermi National Accelerator Laboratory in der Nähe von Chicago entdeckt [3, 4]. Es ist mit Abstand das schwerste der sechs Quarks, seine Masse wird derzeit mit $173.1 \pm 1.3\,\mathrm{GeV}/c^2$ [5] angegeben. Aufgrund seiner großen Masse nimmt das Top-Quark eine Sonderrolle unter den Quarks ein. Anders als seine leichteren Geschwister geht das Top-Quark keine gebundenen Zustände mit anderen Quarks ein, sondern zerfällt nahezu instantan, nachdem es produziert wurde. Seine Eigenschaften gehen daher direkt auf seine Zerfallsprodukte über, ohne durch Wechselwirkung mit anderen Quarks innerhalb eines gebundenen Systems beeinflusst zu werden. Damit bietet das Top-Quark die einmalige Gelegenheit, ein nacktes, ungebundenes, frei zerfallendes Quark zu untersuchen. Abgesehen von seiner Masse, die mit sehr großer Präzision bestimmt wurde, sind viele andere Eigenschaften des Top-Quarks, wie etwa seine Ladung oder sein Spin, nach wie vor nur wenig oder gar nicht bestimmt und machen das noch relativ junge Gebiet der Top-Quark-Physik zu einem spannenden Teilbereich der Teilchenphysik.
Elementare Teilchen und ihre gegenseitigen Wechselwirkungen werden theoretisch im Rahmen des Standardmodell der Elementarteilchenphysik beschrieben. In diesem Modell finden die Wechselwirkungen zwischen Elementarteilchen durch den Austausch sogenannter Eichbosonen statt. Jeder Kraft werden im Standardmodell eigene Bosonen zugeschrieben. Top-Quarks werden vorwiegend über die starke Kraft in Paaren von Top- und Antitop-Quarks erzeugt und zerfallen ausschließlich über die schwache Wechselwirkung. Die geladene schwache Wechselwirkung, die für den Top-Quark-Zerfall verantwortlich ist, findet durch Austausch von $W^{\pm}$-Bosonen statt und wird im Standardmodell theoretisch durch einen Vertexfaktor mit einer reinen Vektor-Minus-Axialvektor-Struktur beschrieben. Aufgrund dieser Struktur koppeln die W-Bosonen im Standardmodell nur an linkshändige Teilchen und rechtshändige Antiteilchen. Die Händigkeit ist eine intrinsische Teilcheneigenschaft, die in den beiden genannten Zuständen vorkommt. Sie ist eng verknüpft mit der Helizität von Teilchen, die die Orientierung des Spins in Bezug auf die Bewegungsrichtung eines Teilchens angibt. Für masselose Teilchen sind Händigkeit und Helizität identisch, für leichte Teilchen gilt dies in erster Näherung. Eine interessante Eigenschaft von Top-

Quarks ist die Helizität der W-Bosonen, die im Top-Quark-Zerfall entstehen. Aufgrund der beschriebenen Struktur der schwachen Wechselwirkung und aus Gründen der Drehimpulserhaltung können die W-Bosonen aus dem Top-Quark-Zerfall nur bestimmte Helizitätszustände annehmen. Das Standardmodell sagt voraus, dass 70% der W-Bosonen aus Top-Quark-Zerfällen longitudinal polarisiert sind und dass 30% linkshändig sind, während der Anteil an rechtshändigen W-Bosonen stark unterdrückt ist. Experimentell lässt sich die Helizität der W-Bosonen durch die Analyse der Winkelverteilung der Zerfallsprodukte des W-Bosons bestimmen. Für ein leptonisch zerfallendes W-Boson ist der Zerfallswinkel θ^* definiert als der Winkel des Impulsvektors des geladenen Leptons aus dem W-Boson-Zerfall relativ zu der Bewegungsrichtung des W-Bosons im Ruhesystem des zerfallenden Top-Quarks.

Im ersten Teil dieser Arbeit wird eine Messung der Anteile der verschiedenen W-Boson-Helizitätszustände vorgestellt. Für diese Analyse wurde ein Datensatz verwendet, der einer integrierten Luminosität von $1.9\,\mathrm{fb}^{-1}$ entspricht und mit dem CDF-II-Experiment am Tevatron-Beschleuniger aufgezeichnet wurde. Der betrachtete Zerfallskanal ist hierbei der sogenannte Lepton+Jets Kanal, in dem ein Top-Quark semileptonisch in ein b-Quark und ein geladenes Lepton und das entsprechende Neutrino und das andere Top-Quark hadronisch in ein b-Quark und zwei leichtere Quarks zerfällt. Die experimentelle Signatur solcher Ereignisse besteht aus einem Elektron oder Myon, fehlender Transversalenergie aufgrund des entstehenden Neutrinos und mindestens vier Jets. Nach einer entsprechenden Ereignisselektion bleiben 484 Kandidaten für Top-Quark-Ereignisse übrig. Die verwendete Untergrundabschätzung bestimmt eine Kontamination des Datensatzes durch Untergrundereignisse von etwa 18%.
Zur Messung der Helizitätsanteile wurde die Verteilung des Cosinus des Zerfallswinkels θ^* verwendet. Um für jedes Ereignis einen Wert für $\cos\theta^*$ zu erhalten, müssen zunächst die Vierervektoren der Top-Quarks und W-Bosonen aus den im Detektor aufgezeichneten Signalen rekonstruiert werden. Da die Rekonstruktion des beim W-Boson-Zerfall entstehenden Neutrinos, das nicht mit dem Detektor wechselwirkt, nicht eindeutig ist und es mehrere Möglichkeiten gibt, die Jets zu den Quarks aus dem Top-Quark-Zerfall zuzuordnen, gibt es für jedes Ereignis mehrere Rekonstruktionshypothesen. Unter Ausnutzung von geeigneten Größen wurde ein Selektionskriterium entwickelt, das in jedem Ereignis eine der vielen möglichen Rekonstruktionshypothesen auswählt. Mithilfe von simulierten Top-Quark-Ereignissen wurde diese Hypothesenauswahl optimiert um im Mittel ein möglich gutes Ergebnis zu erzielen. In einer Maximum-Likelihood-Methode können aus der beobachteten $\cos\theta^*$ Verteilung die Anteile longitudinal polarisierter W-Bosonen, F_0, und rechtshändiger W-Bosonen, F_+, extrahiert werden. Zur korrekten Interpretation der rekonstruierten Verteilung müssen mehrere Effekte und deren Einflüsse berücksichtigt werden. Die $\cos\theta^*$-abhängige Effizienz der Ereignisselektion einerseits und die endliche Auflösung der Rekonstruktion der Kinematik des $t\bar{t}$-Systems andererseits verändern die theoretisch vorhergesagte Verteilung. Mithilfe von simulierten Ereignissen können diese Effekte studiert und ihr Einfluss auf die $\cos\theta^*$-Verteilung bestimmt und berücksichtigt werden. In der vorgestellten Analyse wurden die Helizitätsanteile in drei verschiedenen Szenarien gemessen. Zunächst wurden F_0 und F_+ in zwei unabhängigen Mes-

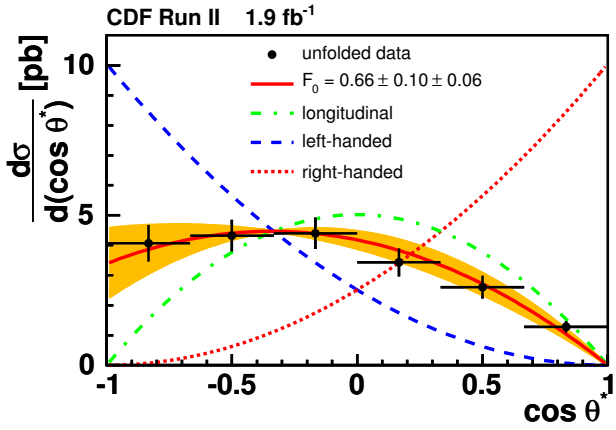

Abbildung 1: Korrigierte $\cos\theta^*$-Verteilung im Vergleich zu den theoretisch vorhergesagten Kurven für rein linkshändige, rein rechtshändige und rein longitudinal polarisierte W-Bosonen. Die durchgezogene rote Kurve entspricht dem gemessenen F_0-Wert. Die Unsicherheit auf dieses Ergebnis wird durch das gelbe Band angezeigt.

sungen einzeln bestimmt, wobei der jeweils andere Parameter auf seinen vom Standardmodell vorhergesagten Wert gesetzt wurde. Die ermittelten Resultate und ihre statistischen (stat.) und systematischen (syst.) Unsicherheiten sind:

$$\begin{aligned} F_0(F_+ = 0.0) &= 0.66 \pm 0.10\ (\text{stat.}) \pm 0.06\ (\text{syst.}) \\ F_+(F_0 = 0.7) &= 0.01 \pm 0.05\ (\text{stat.}) \pm 0.03\ (\text{syst.}) \end{aligned}$$

Die korrigierte $\cos\theta^*$-Verteilung für die Bestimmung von F_0 ist in Abbildung 1 dargestellt. Da die Messung von F_+ innerhalb der ermittelten Unsicherheiten keinen von Null verschiedenen Wert ergab, wurde zusätzlich mittels einer Bayes'schen Methode eine obere Grenze auf den Anteil rechtshändiger W-Bosonen bestimmt:

$$F_+ < 0.12\ @\ 95\%\ \text{C.L.}$$

In einer dritten Messung wurden dann beide Parameter simultan ermittelt:

$$\begin{aligned} F_0 &= 0.38 \pm 0.21\ (\text{stat.}) \pm 0.07\ (\text{syst.}) \\ F_+ &= 0.15 \pm 0.10\ (\text{stat.}) \pm 0.05\ (\text{syst.}) \end{aligned}$$

Die Ergebnisse aller drei Messungen befinden sich innerhalb ihrer Unsicherheiten im Einklang mit den vom Standardmodell vorhergesagten Werten und sind kompatibel mit den Ergebnissen einer weiteren Analyse innerhalb der CDF-Kollaboration [6] und der aktuellsten Messung der DØ -Kollaboration [7].
Obwohl das Top-Quark aufgrund seiner großen Masse eine Sonderrolle unter den Quarks einnimmt, ließ sich mit dieser Messung kein vom Standardmodell abweichendes Verhalten des Top-Quarks feststellen. Es bleibt aber abzuwarten, ob zukünftige Messungen dieser und anderer Größen das Bild, welches das Standardmodell von seinem schwersten Quark zeichnet, bestätigen, oder ob neue, bisher unbekannte Effekte in den Wechselwirkungen des Top-Quarks zutage treten.

Die präzise Vermessung der Eigenschaften von Top-Quarks ist neben der Suche nach dem Higgs-Boson und neuer Physik jenseits des Standardmodells eines der Hauptziele, die mit dem Large Hadron Collider (LHC) am CERN in Genf verfolgt werden. Im LHC kollidieren Protonen mit Protonen bei einer Schwerpunktsenergie von 10 TeV, die später auf 14 TeV erhöht werden soll. Bei einer Schwerpunktsenergie von 10 TeV ist der von der Theorie vorhergesagt Wirkungsquerschnitt für die paarweise Produktion von Top-Quarks mit $\sigma_{t\bar{t}} = 414^{+41}_{-33}$ pb etwa 50 mal größer als am Tevatron. Daher erwartet man, dass schon recht früh große Mengen an $t\bar{t}$-Ereignissen produziert werden, und somit Messungen von Top-Quark-Eigenschaften mit bisher unerreichter statistischer Präzision durchgeführt werden können. Ein erster Schritt in diese Richtung sind die Wiederentdeckung der $t\bar{t}$-Produktion am LHC und die Messung des Produktionswirkungsquerschnitts. Darüber hinaus ist $t\bar{t}$-Produktion eine typische "Standardkerze", deren Untersuchung zum besseren Detektorverständnis beitragen wird.

Im zweiten Teil der Arbeit wird eine Studie zur Messung des $t\bar{t}$-Wirkungsquerschnitts in frühen LHC-Kollisionsdaten mit dem CMS-Experiment vorgestellt. Für diese Studie wird ein Datensatz angenommen, der einer integrierten Luminosität von $20\,\mathrm{pb}^{-1}$ bei einer Schwerpunktsenergie von 10 TeV entspricht. Basierend auf simulierten Datensätzen wurde eine Analyse entwickelt, mit der der $t\bar{t}$-Wirkungsquerschnitt gemessen werden kann.
In der Ereignisselektion werden zunächst Ereignisse mit typischer $t\bar{t}$-Signatur selektiert. Der Fokus liegt hierbei auf dem Elektron+Jets Kanal. Mit der in dieser Arbeit entwickelten Ereignisselektion erwartet man für die angenommene integrierte Luminosität, etwa 300 Ereignisse zu selektieren, von denen 184 $t\bar{t}$-Ereignisse sein werden, was einem erwarteten Untergrundanteil von etwa 39% entspricht.
Im Gegensatz zur $t\bar{t}$-Produktion und zu allen anderen Untergründen, die zuverlässig in ausreichender Anzahl simuliert werden können, ist die Simulation von QCD-Multijet-Ereignissen sehr schwierig. Bei diesem sogenannten instrumentellen Untergrund wird entweder einer der produzierten Jets als Elektron fehlidentifiziert oder ein aus einem Jet stammendes sekundäres Elektron fälschlicherweise als primäres Elektron aus dem harten Prozess rekonstruiert. Trotz der sehr geringen Fehlidentifikationsrate stellen Ereignisse dieser Untergrundkategorie aufgrund ihrer riesigen Wirkungsquerschnitte einen beträchtlichen Anteil des Gesamtuntergrunds dar. Als Folge der im Vergleich zu anderen Prozessen winzigen Selektionseffizienz für QCD-Multijet-Ereignisse, müssen riesige Mengen an Ereignissen simuliert werden, was auf vernünftigen Zeitskalen unmöglich ist. Desweiteren ist nicht klar, inwieweit der Monte Carlo Simulation dieser Prozesse getraut werden kann. Es ist daher unabdingbar, diesen Untergrundbeitrag direkt aus Daten zu bestimmen. Zu diesem Zweck wurde eine Methode entwickelt, die unter Ausnutzung einer diskriminierenden Variable den QCD-Multijet-Anteil in einem Seitenband bestimmt und daraus den Anteil dieses Untergrundes im final selektierten Datensatz extrapoliert. In Studien mit simulierten Ereignissen wurde die Unsicherheit dieser Methode zu 57% bestimmt, was vergleichbar zu alternativen Methoden in anderen CMS-Studien ist [8, 9].
Im dritten Schritt der Analyse wird der Anteil an $t\bar{t}$-Ereignissen anhand einer geeigneten Verteilung bestimmt. Die verwendete M3-Variable ist sensitiv auf die

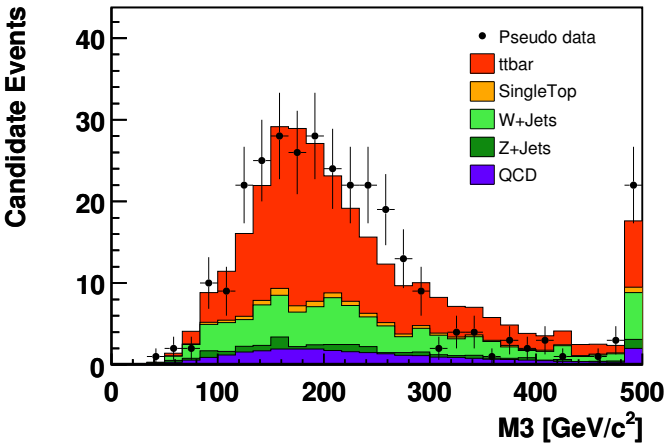

Abbildung 2: M3-Verteilung für die unterschiedlichen Prozesse im selektierten Datensatz. Die Punkte sind Pseudo-Daten, die zufällig aus dem simulierten Datensatz gezogen wurden, um die statistischen Fluktuationen, die für eine integrierte Luminosität von $20\,\mathrm{pb}^{-1}$ erwartet werden, zu illustrieren.

Masse des Top-Quarks und eignet sich dadurch sehr gut, um $t\bar{t}$-Ereignisse von Untergrundereignissen zu trennen. Sie ist definiert als die invariante Masse der Kombination aus den drei Jets mit dem größten vektoriell summierten Transversalimpuls. Abbildung 2 zeigt die M3-Verteilung für einen simulierten Datensatz mit der erwarteten Zusammensetzung aus den unterschiedlichen Prozessen. In einer Maximum-Likelihood-Methode kann dann unter Einbeziehung des zuvor bestimmten QCD-Multijet-Anteils die Anzahl der $t\bar{t}$-Ereignisse und daraus der Wirkungsquerschnitt für $t\bar{t}$-Produktion bestimmt werden. Mit dieser Methode wird man den $t\bar{t}$-Wirkungsquerschnitt mit der folgenden Präzision messen können:

$$\sigma_{t\bar{t}} = \sigma_{t\bar{t}}^{\mathrm{fit}} \ \pm 22\%(\mathrm{stat.}) \ \pm 24\%(\mathrm{syst.}) \ \pm 10\%(\mathrm{lumi.})$$

Neben statistischer (stat.) und systematischer (syst.) Unsicherheit ergibt sich ein relativer Fehler von 10% aufgrund der Unsicherheit in der Bestimmung der integrierten Luminosität (lumi.). Die ermittelten Unsicherheiten sind vergleichbar mit den Unsicherheiten anderer Studien, die innerhalb der CMS-Kollaboration im Elektron+Jets und Myon+Jets Kanal durchgeführt wurden [8, 9].

Es kann erwartet werden, dass mit zunehmendem Detektorverständnis die angegebenen systematischen Unsicherheiten deutlich reduziert werden können. Desweiteren wird mit verfeinerten Selektionsalgorithmen die $t\bar{t}$-Reinheit der selektierten Datensätze auf das Tevatron-Niveau angehoben werden können. Aufgrund der deutlich höheren Anzahl an $t\bar{t}$-Ereignissen wird es dann möglich sein, das Top-Quark und seine Eigenschaften mit deutlich verbesserter Präzision zu untersuchen.
Das Gebiet der Top-Quark-Physik bleibt also weiterhin interessant und spannend, gerade jetzt, da man sich auf der Schwelle zur Massenproduktion von Top-Quarks am LHC befindet.

Measurement of W-Boson Helicity-Fractions in Top-Quark Decays with the CDF II Experiment and Prospects for an Early $t\bar{t}$ Cross-Section Measurement with the CMS Experiment

Zur Erlangung des akademischen Grades eines
DOKTORS DER NATURWISSENSCHAFTEN
von der Fakultät für Physik des
Karlsruher Institut für Technologie (KIT)

genehmigte

Dissertation

von

Dipl. Phys. Thorsten Chwalek
aus Rastatt

Tag der mündlichen Prüfung: 12.02.2010

Referent: Prof. Dr. W. Wagner, Fachbereich C - Experimentelle Teilchenphysik, Bergische Universität Wuppertal

Korreferent: Prof. Dr. Th. Müller, Institut für Experimentelle Kernphysik, Karlsruher Institut für Technologie (KIT)

Introduction

What is the world made of? This is one of the fundamental questions that scientists have been devoted to at all ages. Early Indian and Greek philosophers were the first to propose the idea of smallest, indivisible components of matter. Their ideas were founded on abstract and purely philosophical reasons only rather than on experimental findings. More than 2,000 years later the philosophical motivated concept of fundamental constituents of matter became subject to experimental research. On their quest for the building blocks of matter, physicists discovered ever smaller constituents. At the end of the 19th century it was known that all matter is indeed made of smallest components which were named atoms. The naming has been adopted from the Greek philosopher Democritus who minted the term *átomos* for the smallest, indivisible pieces of matter around 450 BC. In the beginning of the 20th century the modern picture of the atom was drawn, mainly based on the results of Rutherford's experiments [1]. Atoms consist of a dense, positively charged nucleus and negatively charged electrons orbiting around this nucleus. Further investigations revealed that the nucleus of an atom is comprised of positively charged protons and electrical neutral neutrons. But even protons and neutrons are not elementary. In 1964 Murray Gell-Mann and George Zweig postulated that protons and neutrons are made of elementary particles, which they named quarks [2]. Originally introduced as mathematical concept as part of an ordering scheme for the huge number of discovered particles, the experimental confirmation of quarks as fundamental building blocks of matter has not been long in coming. In 1968, deep inelastic scattering experiments at the Stanford Linear Accelerator Center discovered that the proton contains point-like objects, which were later identified with the up quark and the down quark. Today, six flavors of quarks are known. While all ordinary matter is made of the two lightest quarks, the up and down quarks, the remaining four quark flavors can only be produced in collisions of high-energy particles. This can occur in collisions of cosmic ray particles with molecules of the atmosphere or in the laboratory environment of modern particle accelerators.

Since their postulation all six quarks have been experimentally observed. The last quark to be discovered was the top quark, which has been observed in 1995 [3, 4] by the CDF and DØ collaborations at the Tevatron collider at the Fermi National Acceleration Laboratory near Chicago, USA. The top quark is the heaviest fundamental particle known so far and its large mass grants the top quark a special role among all other quarks. Once produced, the top quark decays nearly instantly due to its large mass. This is in contrast to its lighter siblings, which form bound states

with each other. Consequently, all properties of the top quark are directly handed over to its decay products. Thus, studying the top quark offers the unique opportunity to study as close as possible the properties of a bare quark. Apart from its mass which has been determined to high accuracy the other properties of the top quark are not precisely measured up to now and the top quark remains the least well studied of the six quarks.
The elementary particles and the interactions between them are described by the standard model of elementary particle physics. In this theoretical framework all interactions between particles are mediated via the exchange of so-called gauge bosons. While top quarks are mainly produced pairwise through the strong interaction, the decay of the top quark proceeds via the weak interaction. In the standard model charged current weak interactions proceed via the exchange of a W boson and are theoretically described by a vertex factor that has a pure vector minus axialvector structure. While weak interactions have been studied precisely at low momentum transfer, the vertex structure could be altered at high momentum transfers due to contributions of new physics. The large mass of the top quark gives thereby access to high momentum transfers and allows to test the structure of the weak interaction at these high scales. One property of top quarks which is directly related to the nature of the weak interaction is the helicity of the W bosons from top-quark decays. This quantity becomes apparent in the angular distributions of the W-boson decay products. In the standard model the W bosons couple only to left-handed particles and to right-handed antiparticles. As a result of this property the standard model predicts that the W bosons from top-quark decays are either longitudinally polarized or left-handed. The standard model also yields precise quantitative predictions for the fractions of the different W-boson helicity-states. Exploiting the distribution of an appropriate angle, the fractions of different helicities can be measured. In the first part of this thesis this measurement on a dataset corresponding to an integrated luminosity of $1.9\,\mathrm{fb}^{-1}$ collected with the CDF II detector at the Tevatron collider at a center-of-mass energy of 1.96 TeV is described.
With the start of the operation of the Large Hadron Collider (LHC) of the European Organization for Nuclear Research (CERN) in Geneva, Switzerland, the monopoly of the Tevatron on producing top quarks, comes to an end. Due to the higher center-of-mass energies the cross section for $t\bar{t}$ production in LHC collisions is about 50 to 100 times larger compared to the cross section at the Tevatron. Thus, the LHC will serve as a top-quark factory and will guide top-quark physics into a new era of precision measurements. A first step towards this era is the rediscovery of top-quark production and the measurement of its cross section at the LHC. The $t\bar{t}$ production is one of several standard candles which have to be understood prior to focussing on new and exotic physics processes. Moreover, $t\bar{t}$ production will be one of the main backgrounds for searches for new physics like supersymmetric particles. In the second part of this thesis the prospects for an early measurement of the $t\bar{t}$ production cross-section are evaluated based on samples of simulated events. The study assumes a dataset of LHC collisions at a center-of-mass energy of 10 TeV corresponding to an integrated luminosity of $20\,\mathrm{pb}^{-1}$ collected by the CMS detector.

Contents

Chapter 1

Top-Quark Production and Decay within the Standard Model

1.1 The Standard Model of Elementary Particle Physics

The standard model (SM) of elementary particle physics [2, 10–18] is a quantum field theory that combines quantum mechanics and the concepts of special relativity. It provides a very elegant theoretical framework to describe the fundamental particles and their interactions. Since its formulation in the 1960s and 1970s it has undergone a large number of experimental tests and passed all of them successfully. Although there remain some open questions that cannot be answered by the SM, it is nevertheless the theory most successfully tested with highest precision up to now.

1.1.1 Building Blocks of Matter - The Fermions of the Standard Model

Elementary particles of spin $s = \frac{1}{2}$, called fermions, are the building blocks of matter in the SM. They obey Fermi-Dirac-statistics and the Pauli exclusion principle, which implies that two fermions cannot share the same quantum state.
The SM contains twelve of these elementary fermions, six leptons and six quarks, which can be arranged in three generations, as shown in table 1.1. Each generation consists of an up-type quark (up (u), charm (c), top (t)) and a down-type quark (down (d), strange (s), bottom (b)), a charged lepton (electron (e), muon (μ), tau (τ)) and the corresponding neutrino (electron-neutrino (ν_e), muon-neutrino (ν_μ), tau-neutrino (ν_τ)). To each elementary fermion exists in addition a corresponding antipartner, which has the same properties as the fermion but opposite charges.
All ordinary matter of our universe is composed of particles of the first generation. The higher-generation fermions appear solely in high-energy interactions as for example in collisions of cosmic rays with molecules of the atmosphere or in

Flavor	Fermion	Symbol	El. charge [e]	Mass [MeV/c^2]
up	quark	u	$\frac{2}{3}$	$(1.5 - 3.3)$
down	quark	d	$-\frac{1}{3}$	$(3.5 - 6.0)$
electron	lepton	e	-1	0.511
e-neutrino	lepton	ν_e	0	$< 2 \cdot 10^{-6}$
charm	quark	c	$\frac{2}{3}$	$(1.27^{+0.07}_{-0.11}) \cdot 10^3$
strange	quark	s	$-\frac{1}{3}$	104^{+26}_{-34}
muon	lepton	μ	-1	105.658
μ-neutrino	lepton	ν_μ	0	< 0.190
top	quark	t	$\frac{2}{3}$	$(173.1 \pm 1.3) \cdot 10^3$
bottom	quark	b	$-\frac{1}{3}$	$(4.20^{+0.17}_{-0.07}) \cdot 10^3$
tau	lepton	τ	-1	1776.84 ± 0.17
τ-neutrino	lepton	ν_τ	0	< 18.2

Table 1.1: The three generations of fermions and their electric charges and masses [28] (the top-quark mass is taken from [5]). The electric charge is given in units of the elementary charge $e = 1.602176487(40) \times 10^{-19}\,\mathrm{C}$. The mass of the electron and the muon are measured with high precision, the uncertainties are in the order of $10^{-8}\,\mathrm{MeV}/c^2$ and $10^{-6}\,\mathrm{MeV}/c^2$. The values for the neutrino masses are limits obtained from direct measurements. Cosmological constraints on the sum of all neutrino masses lead to stricter limits on the masses of ν_μ and ν_τ [28].

the laboratory environment of collider experiments. Once produced, these massive fermions decay subsequently into the lighter fermions of the first generation.

Charged leptons (e, μ, τ) carry an electric charge of one elementary charge, while the corresponding neutrinos are electrical neutral. Neutrinos are assumed to be strictly massless in the SM. Various observations [19–22] however indicate that neutrinos have non-vanishing masses. This requires an extension [23, 24] of the SM accommodating these results.

The members of the second group of fermions, the quarks, carry fractional electric charges of either $+\frac{2}{3}$ (up-type quarks) or $-\frac{1}{3}$ (down-type quarks) of the elementary charge. Quarks cannot exist as free particles, they are forced to form bound states, called hadrons, of either three quarks (baryons) or quark-antiquark pairs (mesons). This feature of the interaction between quarks is named quark confinement. The top-quark due to its large mass decays before it can form bound states. The special role of the heaviest quark will be discussed in more detail in section 1.2. In order to satisfy the Pauli exclusion principle in the formation of bound states of quarks it becomes necessary to introduce an additional quantum number for quarks. This quantum number is called color [25–27] and can be of three types (red, blue, and green). Color is a non-observable quantum number, thus only colorless quark combinations are realized in nature. This implies that quarks do not occur as free particles and is the theoretical explanation for quark confinement. Colorless mesons consist of a quark of a certain color and of an antiquark carrying the corresponding anticolor. Combinations of three differently colored quarks result in colorless baryons.

1.1.2 Fundamental Interactions and their Mediators

In our present understanding of the world, all known interactions between particles can be ascribed to four fundamental forces: the electromagnetic force, the strong and the weak nuclear forces, and gravitation, see table 1.2. Three of them can be formulated as quantum field theories and have therefore been successfully incorporated in the SM, while gravity is described by the theory of general relativity [29,30]. The fact that gravity and the quantum-field framework of the SM seem to be mathematically incompatible is an indication that the SM in its contemporary form cannot be the ultimate theory of everything. Nevertheless, due to the extreme separation of scales on which gravity[1] and the three forces of the SM[2] are relevant, we can make use of both theories to explain the physics in our experimental reach.
The dynamics of a physical system are formulated in functions called Lagrangians. In gauge theories the Lagrangians are invariant under a certain group of local transformations, i.e. local change of variables. To ensure this local invariance, additional vector fields have to be introduced to compensate for the effects raised by the transformations. In quantized field theories the quanta of the gauge fields represent particles transmitting the forces. These gauge bosons are particles with integer spin that obey Bose-Einstein-statistics. This allows several bosons to occupy the same quantum state as opposed to the half-integer spin fermions which follow Fermi-Dirac statistics. The gauge bosons of the three SM forces have all spin $s = 1$. A compilation of these force mediators and some of their properties can be found in table 1.3.

Force	Couples to	Effect	Rel. strength	Range
strong	color charge	binds quarks and gluons	10^{0}	10^{-15} m
electro-magnetic	electric charge	interaction between el. charged particles	10^{-2}	infinite
weak	weak charge	radioactive β-decay	10^{-5}	10^{-18} m
gravitation	mass	attraction of masses	10^{-38}	infinite

Table 1.2: The four fundamental forces in nature and some of their characteristics.

Force	Bosons	Symbol	El. charge [e]	Mass [GeV/c^2]
strong	8 gluons	g	0	0
electromagnetic	photon	γ	0	0
weak	W	$W^{\pm}$	± 1	80.398 ± 0.025
weak	Z	Z^{0}	0	91.188 ± 0.002

Table 1.3: The gauge bosons of the three SM forces and their electric charges and masses [28].

[1] Gravity plays an important role on large scales, e.g. for the foundation of galaxies and solar systems, but can be neglected on subnuclear scales.

[2] The electromagnetic, weak, and strong force are the dominating forces in elementary particle reactions but can be neglected on large scales.

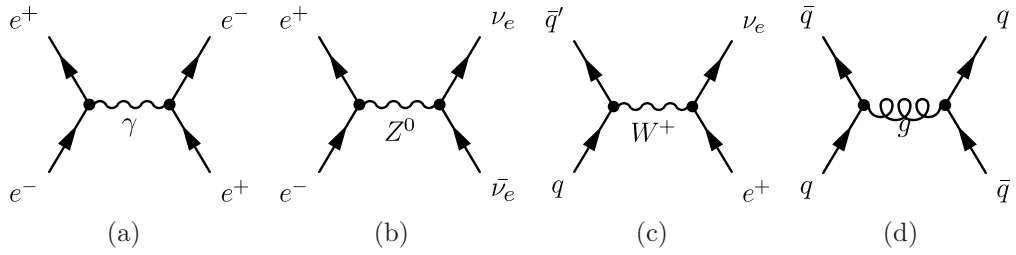

Figure 1.1: Example Feynman diagrams for typical fundamental interactions. In each diagram two incoming particles annihilate and produce a virtual gauge boson that decays into the two outgoing particles: Electron-positron annihilation via (a) the electromagnetic force into a photon or via (b) the weak force into a Z boson, (c) quark-antiquark annihilation into a W boson, and (d) quark-antiquark annihilation via the strong interaction into a gluon. In this description time evolves from left to right, while the spatial dimensions expand in the vertical direction.

Figure 1.1 shows how one can imagine such interactions between elementary particles via gauge boson exchange graphically. So called Feynman diagrams are visualizations of the mathematical expressions describing fundamental interactions. The propagation of particles in space-time is here represented by lines, whereas the couplings are represented by vertices. Applying the Feynman rules one can translate each diagram into a formula and calculate the transition amplitude of a given process by summing over all possible Feynman graphs contributing to this process. From this, the cross section of the process, a measure for the probability for an interaction to occur, can be computed. In section 1.2.1 this will be discussed in more detail by the example of the top-quark production in hadron collisions.

Interactions between electrically charged particles are described by the theory of Quantum Electrodynamics (QED) [31–37]. The gauge boson mediating the electromagnetic force is the photon, which is the excitation of the massless photon field. The infinite range of the electromagnetic force is a direct consequence of the zero-mass of the photon.

The strong force between color charged particles is described by a similar theory, the theory of Quantum Chromodynamics (QCD) [16–18, 27]. Massless gluons coupling to the color charge are the gauge bosons of the strong interaction. Unlike the electrically neutral photons, gluons themselves carry the charge they couple to, and gluons therefore do not only mediate the strong interaction but also participate in it. The theory requires gluons to carry one unit of color and one unit of anticolor, or more precisely superpositions of these, like for example $(r\bar{b} + b\bar{r})/\sqrt{2}$, where r and b indicate red and blue color charge and $\bar{r}$ and $\bar{b}$ the corresponding anticolors. Due to the eight possible independent combinations of color and anticolor, which lead to a non-zero net color charge, there exist eight different gluons. The decrease in the strength of the strong interaction at short distances, named asymptotic freedom, and its increase at large distances that forces quarks to create colorless bound states are direct consequences of the color charge of gluons.

The weak force differs in several aspects from the two other forces in the SM. In contrast to the massless photon and gluons, the mediators of the weak force are

massive gauge bosons, the electrically neutral Z^0 boson and the charged $W^{\pm}$ bosons. The large mass of the weak gauge bosons limits the range of the weak force to subnuclear scales. Weak gauge bosons couple to the weak charge, which is called weak isospin. Thus the weak force is the only force in the SM that affects neutrinos, which possess isospin, but carry neither electric nor color charge.
Another uniqueness of the weak interaction is the capability of flavor change through the exchange of charged W bosons. The eigenstates of the weak interaction are not identical with the mass eigenstates. With the Cabibbo-Kobayashi-Maskawa (CKM) matrix [38, 39] one can transform the different eigenstates into each other. By convention the CKM matrix is a 3×3 unitary matrix that operates on the mass eigenstates of the downtype quarks (d, s, b) resulting in the corresponding weak eigenstates (d', s', b'):

$$\begin{pmatrix} d' \\ s' \\ b' \end{pmatrix} = \begin{pmatrix} V_{ud} & V_{us} & V_{ub} \\ V_{cd} & V_{cs} & V_{cb} \\ V_{td} & V_{ts} & V_{tb} \end{pmatrix} \begin{pmatrix} d \\ s \\ b \end{pmatrix} . \tag{1.1}$$

For example the weak partner of the top quark is b', a linear combination of the mass eigenstates of the three downtype quarks d, s, and b. In general, the coupling of two quarks q_1 and q_2 to a W boson is proportional to the corresponding matrix element $V_{q_1 q_2}$. The current values of the matrix elements, under the assumption of a unitary CKM matrix, are [28]:

$$V_{\mathrm{CKM}} = \begin{pmatrix} 0.97419 \pm 0.00022 & 0.2257 \pm 0.0010 & 0.00359 \pm 0.00016 \\ 0.2256 \pm 0.0010 & 0.97334 \pm 0.00023 & 0.0415^{+0.0010}_{-0.0011} \\ 0.00874^{+0.00026}_{-0.00037} & 0.0407 \pm 0.0010 & 0.999133^{+0.000044}_{-0.000043} \end{pmatrix} . \tag{1.2}$$

It is obvious that the diagonal elements have by far the largest values, so that transitions of quarks within a family are favoured over transitions into quarks of other families. For the given example this implies that the top quark can in principle decay in any of the three downtype quarks, but the decay into the b quark is the most probable one.
The law of parity conservation says that the physics remain the same under the reversal of all spatial axes. While the electromagnetic and the strong force respect this principle, it is violated in weak interactions mediated by charged W bosons. The parity violation of the weak force is closely linked to the concept of chirality of particles. Something is chiral, if it cannot be mapped to its mirror image by simple rotations and translations alone. An example of chiral objects are human hands: the left hand is a non-superposable mirror image of the right hand and vice versa. The two possible chiral states are named left-handed and right-handed after this every day's life example. Wave functions of particles can be linear combinations of left-handed and right-handed components. In the SM the W boson couples only to the left-handed part of the wave function of particles and to the right-handed part of the wave function of antiparticles. Since the parity transformed object of a left-handed particle is a right-handed particle this behavior of the W bosons means

a maximal violation of the law of parity conservation. This feature of the weak interaction and its implications will be discussed in more detail in section 1.2.3.
In contrast, the neutral mediator of the weak interaction, the Z boson, couples to both chiral components, but with different strengths depending on the particular quark or lepton involved.

Although at first sight electromagnetic effects and phenomena of the weak interaction seem very different, above a certain energy scale both can be explained within the electroweak theory [10–12, 14] as two aspects of one single interaction.
A consequence of local gauge invariance is that all particles described by the theory have to be massless. Introducing mass terms for particles into the Lagrangian would spoil the local gauge invariance. The gauge theory of electroweak interactions contains four massless gauge bosons. But at low energies the electromagnetic force with its massless photon and the weak force with its massive gauge bosons appear very different. Therefore the symmetry of the electroweak theory has to be broken such, that three of the four massless gauge bosons acquire mass and one remains massless.
The most promising candidate mechanism providing such a breakdown of the electroweak symmetry is the Higgs mechanism [40–42] in which the symmetry is spontaneously broken. Spontaneous symmetry breaking occurs, if the Lagrangian possesses symmetries which do not hold for the vacuum state of the system. In the Higgs mechanism a complex isodoublet scalar field, the Higgs field, with a non-vanishing vacuum expectation value ($v \approx 246\,\mathrm{GeV}$) is introduced into the Lagrangian, leading to symmetry breaking terms. According to Goldstone's theorem [43–46] for each broken generator of a symmetry group one would expect the existence of a massless Goldstone boson. But if a gauge boson is coupled to one of the broken generators, the Goldstone boson vanishes and replaces the missing longitudinal degree of freedom of the former massless gauge boson. In other words the Goldstone boson gets "eaten up" by the gauge boson, giving it its mass. In the Higgs mechanism the symmetry of the electroweak theory is broken in a way that the symmetry of the electromagnetic force remains as a symmetry of the vacuum. As a consequence the gauge bosons of the weak interaction become massive, while the photon remains massless. As a remnant of this mechanism, the theory predicts a massive scalar spin-zero particle, which is the excitation of the Higgs field and therefore named Higgs particle. This particle is the last particle predicted by the SM yet to be observed and its discovery would be a major success for the SM itself.
But not only the weak gauge bosons acquire their masses through the interaction with the Higgs field. The coupling of the lepton fields to the Higgs field, the so-called Yukawa coupling, leads to mass terms for the charged leptons in the Lagrangian. In a similar way mass terms for the quarks can be found by Yukawa coupling of the quark fields to the Higgs field. The Higgs mechanism can provide an explanation for the masses of the fermions, but since the Yukawa couplings are free parameters of the theory, the SM cannot predict the mass values of any of its fermions.

1.2 The Top Quark

The top quark was discovered in 1995 by the CDF and DØ collaborations at Fermilab's Tevatron [3, 4]. Over the intervening years, the mass of the top quark has been measured with ever increasing precision. The most recent combination of top-quark mass-measurements by the Tevatron Electroweak Working Group, including preliminary CDF and DØ results from Run II, yields a value of $173.1 \pm 1.3\,\mathrm{GeV}$ [5][3]. Nearly as massive as a gold nucleus and about 40 times heavier than the next heaviest quark, the top quark stands out as the heaviest among the observed fundamental particles.
Its large mass gives rise to speculations that the discovered particle might not be the weak isospin partner of the b quark as predicted by the SM, but an exotic quark, for example with an electric charge of $-\frac{4}{3}e$ instead of $+\frac{2}{3}e$. Since the top-quark mass is in the range of the electroweak symmetry breaking scale ($v \approx 246\,\mathrm{GeV}$) and its Yukawa coupling to the Higgs field ($g_Y = \frac{m_t}{v/\sqrt{2}}$) is close to one, it has also been speculated that the top quark might play a role in the process of electroweak symmetry breaking [47, 48].
But even if the top quark turns out to be the third generation up-type quark as predicted by the SM, its huge mass still grants the top quark a special role among the other quarks. Although it decays only via the weak interaction the large mass leads to a very short lifetime of $\tau_t \approx 5 \times 10^{-25}\,\mathrm{s}$, an order of magnitude smaller than the typical time scale for hadronization processes, ${\Lambda_{\mathrm{QCD}}}^{-1} \approx 10^{-23}\,\mathrm{s}$. As a result, top quarks on average decay before they can form bound states with other quarks. And since the typical time scale on which spin depolarization by the strong interaction takes place is even larger [49], the polarization of the top-quark spin remains undisturbed and is directly handed over to the top-quark decay-products. The extreme short lifetime of the top quark and all its implications provide the unique opportunity to study a bare quark and thus make the top quark an extremely interesting object. For a detailed review of the recent status of top-quark physics see [50] and references therein.

1.2.1 Production of Top Quarks

The dominant source of top quarks at hadron colliders is the production of top-antitop quark pairs via the strong interaction. Even though $t\bar{t}$ production is also possible through Z^0 or photon exchange, these production modes are negligible in hadron collisions. The production of single top-quarks via the weak interaction has recently been observed by the CDF and DØ collaborations [51, 52], but has only subleading character compared to the pairwise production of top quarks.

[3] For simplicity from now on in this chapter the so called natural units with $\hbar = c = 1$ will be used.

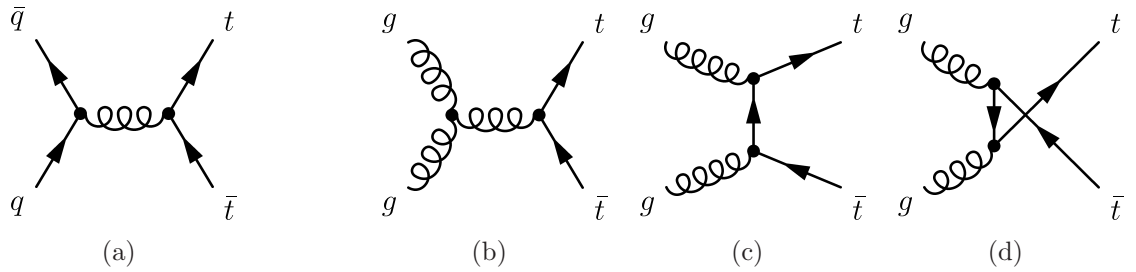

Figure 1.2: Leading order Feynman diagrams for $t\bar{t}$ production (a) via quark-antiquark annihilation and (b)–(d) via gluon-gluon fusion.

Partonic Cross Section

The cross sections of hard parton-parton processes $ij \to t\bar{t}$ can be calculated in perturbative QCD for all possible initial partons i and j. The leading order (LO) subprocesses quark-antiquark annihilation ($q\bar{q} \to t\bar{t}$) and gluon-gluon fusion ($gg \to t\bar{t}$) contribute with α_s^2 to the perturbation series, where α_s^2 is the coupling constant of the strong interaction. The Feynman diagrams for these LO subprocesses are depicted in figure 1.2. Applying the Feynman rules which provide a prescription of how to translate diagrams into formulas, one can calculate the transition amplitudes of the corresponding processes and consequently the differential hard cross sections $\frac{d\hat{\sigma}}{d\hat{t}}$. The LO differential cross sections for $t\bar{t}$ production via quark-antiquark annihilation and via gluon-gluon fusion are for example given by [53]:

$$\frac{d\hat{\sigma}}{d\hat{t}}(q\bar{q} \to t\bar{t}) = \frac{4\pi\alpha_s^2}{9\hat{s}^4} \cdot [(m_t^2 - \hat{t})^2 + (m_t^2 - \hat{u})^2 + 2m_t^2\hat{s}] \,, \tag{1.3}$$

$$\begin{aligned}\frac{d\hat{\sigma}}{d\hat{t}}(gg \to t\bar{t}) = \frac{\pi\alpha_s^2}{8\hat{s}^2} \cdot \Bigg[& \frac{6(m_t^2 - \hat{t})(m_t^2 - \hat{u})}{\hat{s}^2} - \frac{m_t^2(\hat{s} - 4m_t^2)}{3(m_t^2 - \hat{t})(m_t^2 - \hat{u})} \\ & + \frac{4}{3} \cdot \frac{(m_t^2 - \hat{t})(m_t^2 - \hat{u}) - 2m_t^2(m_t^2 + \hat{t})}{(m_t^2 - \hat{t})^2} \\ & + \frac{4}{3} \cdot \frac{(m_t^2 - \hat{t})(m_t^2 - \hat{u}) - 2m_t^2(m_t^2 + \hat{u})}{(m_t^2 - \hat{u})^2} \\ & - 3 \cdot \frac{(m_t^2 - \hat{t})(m_t^2 - \hat{u}) + m_t^2(\hat{u} - \hat{t})}{\hat{s}(m_t^2 - \hat{t})} \\ & - 3 \cdot \frac{(m_t^2 - \hat{t})(m_t^2 - \hat{u}) + m_t^2(\hat{t} - \hat{u})}{\hat{s}(m_t^2 - \hat{u})} \Bigg] \,. \end{aligned} \tag{1.4}$$

In equations 1.3 and 1.4 $\hat{s}$, $\hat{t}$, and $\hat{u}$ are the Mandelstam variables of the partonic process, defined as $\hat{s} = (p_i + p_j)^2$, $\hat{t} = (p_i - p_t)^2$, and $\hat{u} = (p_i - p_{\bar{t}})^2$. They can be identified with the square of the partonic center-of-mass energy ($\hat{s}$) and the squares of the momentum transfer from the incoming parton to the top ($\hat{t}$) or antitop ($\hat{u}$) quark. In case of $q\bar{q}$ annihilation, i represents the incoming quark and j the incoming antiquark, in case of gluon-gluon fusion, i and j denote the initial gluons.

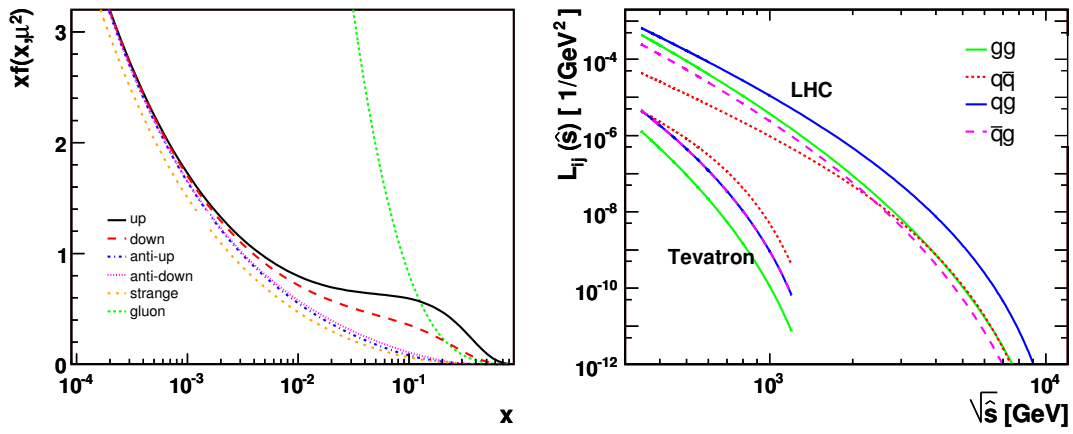

(a) (b)

Figure 1.3: (a) The CTEQ6.5 [54] parton distribution functions of u,$\bar{u}$,d,$\bar{d}$,s quarks and gluons inside the proton at a scale of $\mu^2 = (171\,\text{GeV})^2$. (b) Parton luminosities [55] for gluon-gluon, quark-antiquark, quark-gluon, and antiquark-gluon interactions at the Tevatron ($\sqrt{s} = 1.96\,\text{TeV}$) and the LHC ($\sqrt{s} = 14\,\text{TeV}$). The scale and parametrization are the same as used for the calculation of the cross sections in table 1.4.

Parton Distribution Functions

However, at hadron colliders compound particles (hadrons A and B) are collided with each other. The momentum of a hadron is therefore shared between its constituents. A proton for example consists of two u quarks and one d quark. The three valence quarks are bound together by virtual gluons that can split in quark-antiquark pairs, so-called sea quarks. The probability density for finding a parton i inside the hadron A carrying a momentum fraction $x_i = \frac{p_i}{p_A}$ of the momentum of A is given by the parton distribution function (PDF) $f_{i/A}(x_i, \mu^2)$. The PDFs depend on a scale μ, which describes the typical energy scale of the considered interaction. In the calculation of top-quark production cross-sections μ is usually set to the top-quark mass m_t. Figure 1.3(a) shows exemplarily the PDFs in the CTEQ6.5 [54] parametrization at a scale of $\mu = m_t = 171\,\text{GeV}$ for the valence quarks (u and d), the sea-quarks (here: $\bar{u}$,$\bar{d}$,s), and gluons inside the proton. For an antiproton, quarks and antiquarks have to be reversed.
The square of the total energy of the partonic subprocess, $\hat{s} = (p_i + p_j)^2$, can be expressed in terms of momentum fractions, x_i and x_j, and the square of the total hadronic center-of-mass energy, $s = (p_A + p_B)^2$,

$$\hat{s} = (p_i + p_j)^2 = (x_i p_A + x_j p_B)^2 \approx 2 x_i x_j p_A p_B \approx x_i x_j s \;, \tag{1.5}$$

neglecting the rest masses p_A^2 and p_B^2 of the incoming hadrons.
The energy in the partonic interaction has to be at least large enough to produce a $t\bar{t}$ pair at rest, $\hat{s} \geq 4m_t^2$, which leads together with equation 1.5 and the approximation $x_i \approx x_j$ to the typical x value for $t\bar{t}$ production at the kinematic threshold: $x \approx \frac{2m_t}{\sqrt{s}}$.
At the Tevatron, the top-quark mass m_t is relatively large compared to the Tevatron center-of-mass energy $\sqrt{s} = 1.96\,\text{TeV}$, thus $t\bar{t}$ production is driven by the region of

relatively large x around the typical value of $x \approx 0.18$. In this region the PDF of the u quark is larger than those of the gluon and the d quark, which are comparable to each other, as can be seen in figure 1.3(a). For this reason the dominant subprocess for $t\bar{t}$ production at the Tevatron is $q\bar{q}$ annihilation with a 85% contribution.
At higher energies $t\bar{t}$ production occurs already in the region of lower x, where the PDF of the gluon is much larger compared to those of the quarks. Thus the dominant subprocess at the LHC with a center-of-mass energy of 14 TeV(10 TeV) at a typical value of $x \approx 0.025$ (0.035) is gluon-gluon fusion with about 90% contribution. In order to compare different collider setups it is instructive to compute parton luminosities which are defined as:

$$L_{ij}(\hat{s}, s, \mu) = \frac{1}{s} \int_{\hat{s}}^{s} f_{i/A}(\frac{\tilde{s}}{s}, \mu^2) f_{j/B}(\frac{\tilde{s}}{s}, \mu^2) \frac{1}{\tilde{s}} d\tilde{s} \ . \tag{1.6}$$

The corresponding functions for different initial partons for the Tevatron and the LHC can be found in figure 1.3(b). In $p\bar{p}$ collisions at the Tevatron the dominating contribution to the total hadronic cross section comes from quark-antiquark annihilation, since the incoming quarks and antiquarks are valence quarks. For the LHC the highest flux is provided by quark-gluon initial states, but since the cross section of this process is of the order α_s^3 it gives only a contribution on the percent level to the total hadronic cross section. The dominating process is gluon-gluon fusion. Therefore at the LHC it makes no difference[4] if one collides protons with protons or protons with antiprotons and one can therefore avoid the technical challenge of producing antiprotons in a sufficient number.

The Total Hadronic Cross Section (The Factorization Ansatz)

The total hadronic cross section for $t\bar{t}$ production in hadron collisions $\sigma(AB \to t\bar{t})$ is then calculated by folding the partonic subprocess cross sections $\hat{\sigma}_{ij}$ with the PDFs of the colliding hadrons:

$$\sigma(AB \to t\bar{t}) \ = \ \sum_{i,j} \int dx_i dx_j f_{i/A}(x_i, \mu^2) f_{j/B}(x_j, \mu^2) \cdot \hat{\sigma}_{ij}(ij \to t\bar{t}; \hat{s}, \mu^2) \ . \tag{1.7}$$

The sum in equation 1.7 runs over all pairs of initial partons contributing to the process.
Table 1.4 shows the most recent results [56] for the calculation of the hadronic cross section[5] for $t\bar{t}$ production at the Tevatron and the LHC. For the latter, cross sections for two different center-of-mass energies have been evaluated, one for a startup-scenario with 10 TeV and one for the design energy of 14 TeV. The quoted results have been calculated at next-to-leading order in α_s and soft-gluon next-to-leading threshold logarithms (NLO+NLL) using the CTEQ6.5 [54] parametrization. The scale μ has been set to a top-quark mass of $m_t = 171$ GeV.
The central cross-section values in table 1.4 are quoted in the form $\sigma \pm \Delta\sigma_\mu \pm \Delta\sigma_{\mathrm{PDF}}$.

[4] The $t\bar{t}$ production cross-section in pp collisions at $\sqrt{s} = 10$ TeV (14 TeV) is 95% (97%) of the value for $\sigma_{t\bar{t}}$ in $p\bar{p}$ collisions.

[5] Cross sections are usually given in the unit of barns [b], where $1\,\mathrm{b} = 10^{-28}\,\mathrm{m}^2$.

Collider (initial hadrons)	$\sqrt{s}$ [TeV]	$\sigma(171\,\text{GeV})$ [pb]	B [pb/GeV]	C [pb/GeV^2]	D [pb/GeV^3]
Tevatron ($p\bar{p}$)	1.96	$7.61^{+0.29\ +0.53}_{-0.53\ -0.37}$	-0.237	4.38×10^{-3}	-6.28×10^{-5}
LHC (pp)	10	$414^{+36\ +20}_{-28\ -18}$	-11.7	0.205	-2.79×10^{-3}
LHC (pp)	14	$908^{+82\ +30}_{-85\ -29}$	-24.5	0.411	-5.46×10^{-3}

Table 1.4: NLO+NLL $t\bar{t}$ production cross-sections for the Tevatron and the LHC. The cross sections are calculated using the CTEQ6.5 PDF parametrization and a scale of $\mu = m_t = 171\,\text{GeV}$. The quoted errors of $\sigma(171\,\text{GeV})$ are the uncertainties due to variations in the scale and due to the uncertainties from the PDF. In addition the coefficients of the parametrization $\sigma(m_t) = \sigma(171\,\text{GeV}) + B \cdot \Delta M_t + C \cdot (\Delta M_t)^2 + D \cdot (\Delta M_t)^3$ are given [56].

The uncertainty $\Delta\sigma_\mu$ due to the scale uncertainty has been evaluated by varying μ in the range $0.5m_t \leq \mu \leq 2m_t$, while $\mu = m_t$ was used for the calculation of the central value. The uncertainty $\Delta\sigma_{\text{PDF}}$ due to the uncertainty in the used PDF has been explored using not only the central PDF but also a number of other PDFs, i.e. a set of uncorrelated positive and negative variations that cover all sources of uncertainty in the CTEQ6.5 PDF set.
In order to be able to easily derive cross-section values corresponding to different top-quark masses, the results are given in the form of the coefficients of the parametrization depending on the difference in the top quark mass $\Delta M_t = m_t - 171\,\text{GeV}$:

$$\sigma(m_t) = \sigma(171\,\text{GeV}) + B \cdot \Delta M_t + C \cdot (\Delta M_t)^2 + D \cdot (\Delta M_t)^3 \,, \tag{1.8}$$

which yields exact results in the range $150\,\text{GeV} \leq m_t \leq 190\,\text{GeV}$.

1.2.2 Decay of Top Quarks

Top quarks decay via the weak interaction almost exclusively into a b quark and a W boson. The decay rates into other down-type quarks, $t \to W^+ d$ and $t \to W^+ s$, are suppressed due to the small CKM-Matrix elements of these decays, see equation 1.2. Since the top-quark mass exceeds the sum of the masses of the W boson and the b quark, it decays into a real W boson, while lighter quarks decay only into virtual W bosons. This is the reason for the extreme short lifetime of top quarks.
Figure 1.4 illustrates the decay of the top quark and the different decay modes of the W boson. The W boson can decay leptonically into a charged lepton and the corresponding neutrino or hadronically into a quark-antiquark pair.
Depending on the decay modes of the W bosons one distinguishes between several $t\bar{t}$ event topologies: dilepton events in which both W bosons decay leptonically, all-hadronic events in which both W bosons decay hadronically, and lepton+jets events in which one W boson decays leptonically and the other one hadronically.
The universality of the weak interaction implies equal probabilities (disregarding

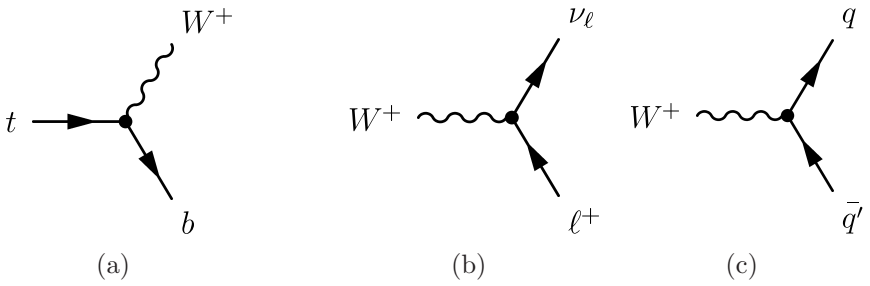

Figure 1.4: (a) Top quarks decay predominantly into a b quark and a W^+ boson. The topology of the $t\bar{t}$ event depends on the decay modes of the W bosons. They can either decay into (b) a charged lepton and the corresponding neutrino or into (c) a quark-antiquark pair.

phase space) for the different fermionic decays. Due to the three different quark color charges, the decay into quark-antiquark pairs is enhanced by a factor of three, leading to a branching ratio of 1/9 for each of the three leptonic decay modes and branching ratios of 3/9 for decays into a $u\bar{d}$ or $c\bar{s}$ pair. Figure 1.4 illustrates the branching ratios of the different decay channels.

The analyses described in this thesis were carried out in the lepton+jets channel, where "lepton" in this case refers only to electrons and muons, not to taus. This channel is often called "golden channel", since it is a compromise between the low background contribution but small branching ratio of the dilepton channel and the high branching ratio but also large background contribution of the all-hadronic channel.

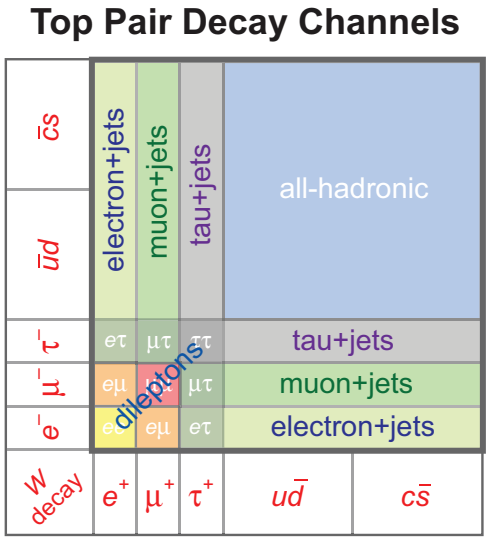

Figure 1.5: The different topologies of $t\bar{t}$ events. The sizes of the different areas reflect the branching ratios of the different decay channels.

1.2.3 The Helicity of W Bosons from Top-Quark Decays

Charged current weak interactions proceed via the exchange of $W^{\pm}$ bosons and are theoretically described by a vertex factor that has a pure vector minus axial-vector ($V-A$) structure. By applying the Feynman rules the vertex of the charged weak interaction can be written as

$$\frac{g}{\sqrt{2}}\gamma^{\mu}\frac{1}{2}(1-\gamma^{5}) \ , \tag{1.9}$$

where γ^{μ} denotes the Dirac matrices, γ^{5} the chirality operator, and g the coupling constant of the weak interaction. By multiplying Dirac spinors ψ_1 and ψ_2 of involved particles to this vertex one can identify the vector-current $V^{\mu}=\bar{\psi}_1\gamma^{\mu}\psi_2$ which transforms like a four-vector and the axial-vector current $A^{\mu}=\bar{\psi}_1\gamma^{\mu}\gamma^{5}\psi_2$ transforming like an axial-vector. Since the vector and the axial-vector component contribute with the same weight to the vertex factor of charged weak processes, the conservation of parity is violated in these processes in a maximal way and the W boson couples only to left-handed fermions and right-handed antifermions.

To understand this feature of the weak interaction it is crucial to discuss first the concepts of chirality and helicity. As already mentioned in section 1.1.2, there are two different chirality states, called left-handed and right-handed, which are the eigenstates of the chiral projection operators $P_{-}=\frac{1}{2}(1-\gamma^{5})$ and $P_{+}=\frac{1}{2}(1+\gamma^{5})$. Using these chiral projection operators every fermion field can be decomposed into its chiral components: $\psi=P_{-}\psi+P_{+}\psi=\psi_L+\psi_R$. Exploiting the two properties of the left-handed projection operator,

$$P_{-}=P_{-}^{2} \quad \text{and} \quad \gamma^{\mu}P_{-}=P_{+}\gamma^{\mu} \ , \tag{1.10}$$

one can see that the charged weak force projects out the left-handed chiral component of fermions and the right-handed components of antifermions:

$$\begin{aligned}\bar{\psi}_1\gamma^{\mu}\frac{1}{2}(1-\gamma^{5})\psi_2 &= \bar{\psi}_1\gamma^{\mu}P_{-}\psi_2=\bar{\psi}_1\gamma^{\mu}P_{-}^{2}\psi_2 \\ &= \bar{\psi}_1P_{+}\gamma^{\mu}P_{-}\psi_2=(\bar{\psi}_1)_R\gamma^{\mu}(\psi_2)_L \ . \end{aligned} \tag{1.11}$$

Thus particles produced in weak interactions are always chiral left-handed while antiparticles are always chiral right-handed.
Helicity is defined by the projection of a particle's spin on the axis given by its direction of motion:

$$h=\vec{\sigma}\cdot\hat{p}, \quad \text{with} \quad \hat{p}=\frac{\vec{p}}{|\vec{p}|} \ . \tag{1.12}$$

The helicity operator applied to transversely polarized particles has two eigenstates with the spin either along or opposite to the direction of motion. A particle is of positive helicity, if the spin is projected parallel to its momentum, and of negative helicity, if the projection is antiparallel to the direction of motion. Since in the extreme relativistic limit, the chirality operator is equal to the helicity operator these two modes are also called right-handed and left-handed, respectively. Longitudinally

polarized particles, with the spin oriented perpendicular to the direction of motion are no eigenstates of the helicity operator.
The difference between chirality and helicity for massive particles is that chirality is Lorentz invariant while helicity is not. It is always possible for an observer to overtake a massive particle which implies that its direction of motion is reversed in the observer's rest-frame, while the spin orientation is not affected. As a result the opposite helicity state is observed. Consequently, for example the chiral left-handed state ψ_L of a massive particle possesses contributions from both positive and negative helicity components $\psi_L = \psi_- + \psi_+$, where the degree of polarization scales with $\beta = \frac{v}{c}$. In this example, the wave function is dominated by the contribution from the negative helicity component ψ_-, which becomes 100% in the ultra relativistic limit, where helicity equals chirality.
The experimental advantage of helicity is that it shows up in the angular distributions of decay products from weak decays, while chirality is an intrinsic quantum number that is not directly observable. Thus, analyzing the helicity of particles from weak interactions can provide a test on the structure of the underlying weak interaction.

While weak interactions have been tested with high precision at low momentum transfer, e.g. in radioactive β decay, the vertex structure may be altered in interactions at high momentum transfer due to new physics contributions. The large mass of the top quark thereby gives access to high momentum scales. It has for example been suggested that the top quark may have non-universal gauge couplings as a result of dynamical breaking of the electroweak symmetry [47, 48, 57].

The *Wtb* Vertex in the SM

Assuming the $V - A$ structure of the standard electroweak theory, the part of the SM Lagrangian relevant for the top-quark decay is:

$$\mathcal{L} = \frac{g}{\sqrt{2}} W_\mu^- \bar{b} \gamma^\mu V_{tb} \frac{1}{2}(1 - \gamma^5) t + h.c \; . \tag{1.13}$$

W_μ, t, and b denote the vector field of the W boson and the fermion fields of top and bottom quarks. The W boson solely couples to b quarks of left-handed chirality, which translates into left-handed helicity, assuming the b quark to be massless. This assumption is justified by the small b-quark mass compared to the masses of the top quark and the W boson. In the rest frame of the top quark the W boson and the b quark are emitted back to back and due to angular momentum conservation the W^+ boson can then only either be longitudinally polarized or left-handed, depending on the orientation of the top-quark spin. In the charge conjugated case of a decaying antitop quark, the massless anti-b quark is always right-handed and therefore the W^- is then forced to be either also right-handed or longitudinally polarized.
For simplicity only the decay of top quarks will be discussed further and therefore only W^+ bosons will be considered. Unless explicitly stated otherwise, W will always refer to positively charged W bosons in the following.
In LO perturbation theory and under the assumption of a massless b quark four

non-vanishing helicity amplitudes can be calculated. For each amplitude the helicity states of the top quark, the W boson, and the b quark are given in the notation (h_t, h_W, h_b), where "0" refers to longitudinal polarization and "+" and "−" refer to positive and negative helicity, respectively. The four helicity amplitudes in the SM are [58]:

$$(-\ 0\ -)^{\mathrm{SM}} = \frac{m_t}{m_W} V_{tb} \sin\frac{\theta}{2} \cdot C\ , \tag{1.14}$$

$$(+\ 0\ -)^{\mathrm{SM}} = \frac{m_t}{m_W} V_{tb} \cos\frac{\theta}{2} e^{i\phi} \cdot C\ , \tag{1.15}$$

$$(-\ -\ -)^{\mathrm{SM}} = \sqrt{2} V_{tb} \cos\frac{\theta}{2} e^{i\phi} \cdot C\ , \tag{1.16}$$

$$(+\ -\ -)^{\mathrm{SM}} = -\sqrt{2} V_{tb} \sin\frac{\theta}{2} e^{2i\phi} \cdot C\ , \tag{1.17}$$

$$\text{with}\ \ C = \frac{-g}{\sqrt{2}} \sqrt{m_t^2 - m_W^2}\ , \tag{1.18}$$

where θ and ϕ denote angles referring to the direction of motion of the W boson in the top-quark rest-frame. In principle, θ and ϕ can be randomly chosen, since for unpolarized top quarks the dependency on these angles vanishes when obtaining the averaged squared amplitudes.
From these helicity amplitudes the partial decay widths for top quarks decaying into longitudinally polarized W bosons (Γ_0), into left-handed W bosons (Γ_-), and into right-handed W bosons (Γ_+) can be calculated by calculating the squared amplitudes and summing over the helicities of the top quark and the b quark for a given helicity h_W of the W boson. In addition a spin factor of $\frac{1}{2}$ and a phase-space factor of $\left(1 - \frac{m_W^2}{m_t^2}\right) / (16\pi m_t)$ have to be included:

$$\Gamma_{h_W} = \frac{1}{2} \cdot \frac{1 - \frac{m_W^2}{m_t^2}}{16\pi m_t} \cdot \sum_{h_t, h_b} (h_t, h_W, h_b) \cdot (h_t, h_W, h_b)^*\ . \tag{1.19}$$

The partial top-quark decay-widths in the SM calculated using the SM helicity amplitudes and equation 1.19 are:

$$\Gamma_0^{\mathrm{SM}} = \frac{1}{2} \left(\frac{m_t}{m_W} V_{tb}\right)^2 \cdot C'\ , \tag{1.20}$$

$$\Gamma_-^{\mathrm{SM}} = V_{tb}^2 \cdot C'\ , \tag{1.21}$$

$$\Gamma_+^{\mathrm{SM}} = 0\ , \tag{1.22}$$

$$\text{with}\ \ C' = \frac{g^2}{32\pi} \cdot \left(1 - \frac{m_W^2}{m_t^2}\right)^2 \cdot m_t\ . \tag{1.23}$$

Due to the $V - A$ structure of the Lagrangian in equation 1.13, the helicity of the b quark is fixed to be left-handed and due to angular momentum conservation the partial decay width for top quarks decaying into right-handed W bosons is zero.

The W-boson helicity-fractions F_{h_W} are defined as the ratio of the partial decay width Γ_{h_W} and the total decay width Γ_{total},

$$F_{h_W} = \frac{\Gamma_{h_W}}{\Gamma_{\text{total}}} \ , \ \text{with} \ \ \Gamma_{\text{total}} = \sum_i \Gamma_i \ , \tag{1.24}$$

and can be calculated using the partial decay widths given in equations 1.20–1.22:

$$F_0 = \frac{m_t^2}{2m_W^2 + m_t^2} \ , \tag{1.25}$$

$$F_- = \frac{2m_W^2}{2m_W^2 + m_t^2} \ , \tag{1.26}$$

$$F_+ = 0 \ . \tag{1.27}$$

Using $m_t = 173.1\,\text{GeV}$ [5] and $m_W = 80.398\,\text{GeV}$ [28] the values for the three W-boson helicity-fractions in the SM are:

$$\begin{aligned} F_0 &= 0.699 \ , \\ F_- &= 0.301 \ , \\ F_+ &= 0 \ . \end{aligned}$$

The production of longitudinally polarized W bosons is enhanced due to the fact that the coupling of the longitudinal mode of the W boson as generated through the spontaneous symmetry breaking increases with the fermion mass [58]. The decay rate into longitudinally polarized W bosons scales therefore with the third power of the top-quark mass, while the decay to transversely polarized W bosons is governed by the gauge coupling and increases only linearly with m_t. This can be seen in equations 1.20 and 1.21 taking the common factor C' given in equation 1.23 into account.

Next-to-leading-order (NLO) QCD and electroweak corrections as well as corrections due to the finite width of the W boson and corrections due to the non-zero mass of the b quark reduce the total decay width of the top quark by 8.8% [59–63]. The partial decay width into longitudinally polarized W bosons and the decay width into left-handed W bosons are also reduced by 10% and 6.7% [64, 65], respectively. This translates into corrections on the helicity fractions of $\Delta F_0 = -0.0075$ and $\Delta F_- = +0.006$. The fraction of top-quark decays into right-handed W bosons is only hardly altered, and is predicted to be 0.0015, where the largest contribution comes from the consideration of the non-zero b-quark mass.
Thus it is safe to say that, if the top quark reveals a violation of the $V-A$ structure of the weak interaction exceeding the few percent level, the violations must have a non-SM origin.

An Effective Wtb Vertex with Additional Non-SM Couplings

In new physics models, departures from the SM expectation $V_{tb} \approx 1$ are possible [66] as well as new radiative contributions to the Wtb vertex [67]. These corrections can be parameterized with the effective operator formalism [58]:

$$\mathcal{L} = \frac{g}{\sqrt{2}} \left[W_\mu^- \bar{b} \gamma^\mu (f_1^L P_- + f_1^R P_+) t - \frac{1}{m_W} \partial_\nu W_\mu^- \bar{b} \sigma^{\mu\nu} (f_2^L P_- + f_2^R P_+) t \right] + h.c. \quad (1.28)$$

$$\text{with} \quad P_\pm = \frac{1}{2}(1 \pm \gamma_5) \quad \text{and} \quad i\sigma_{\mu\nu} = -\frac{1}{2}[\gamma^\mu, \gamma^\nu] \ . \quad (1.29)$$

In addition to the given terms proportional to γ^μ and $\sigma_{\mu\nu} p_W^\nu$, the most general Wtb vertex also contains terms proportional to p_W^ν and p_t^μ, where p_W^ν and p_t^μ are the four-momenta of the W boson and the top quark, respectively. Each additional term is of the form $(f_i^L P_- + f_i^R P_+)$ and therefore comes along with two additional form factors $f_i^{L,R}$. The total number of eight form factors can be reduced to six by using the Gordon identity

$$(m_t + m_b) \bar{b} \gamma^\mu t = \bar{b} (p_t^\mu + p_b^\mu - i\sigma_{\mu\nu} p_W^\nu) t \quad \text{with} \quad p_b^\mu = p_t^\mu - p_W^\mu \ , \quad (1.30)$$

which allows to rewrite the terms proportional to the top-quark four-vector in terms of the remaining three degrees of freedom. Assuming the W boson to be on its mass shell, the terms proportional to p_W^μ vanish and the number of form factors is further reduced to the four given in equation 1.28.
Although these four form factors can in general be complex, assuming that the interaction in equation 1.28 preserves CP symmetry they are taken to be real. For $f_1^L = V_{tb}$ and vanishing values for f_1^R and $f_2^{L,R}$ the effective Lagrangian in equation 1.28 is reduced to the SM Lagrangian in equation 1.13 with its pure $V - A$ structure of the charged weak interaction.

Though non-zero values for f_1^R and $f_2^{R,L}$ are possible in SM extensions without spoiling the agreement with low-energy measurements, several constraints on these anomalous couplings exist. The coupling to right-handed b quarks through f_1^R and f_2^L is constraint to be less than 0.004 [68] by the $b \to s\gamma$ branching ratio, which would be increased considerably, if such couplings existed. On the other hand, the decay $b \to s l^+ l^-$ can be sensitive to anomalous left-handed couplings through $f_2^R \neq 0$, and it imposes a constraint of the order of 0.03 [68] to this form factor. However, all these constraints are model dependent, obtained from indirect measurements assuming that there are no other sources of new physics that could cancel the effects of theses couplings on the data. For example the amplitude involving f_1^R contains the product $V_{ts} \cdot f_1^R$ and thus the constraint on f_1^R is based on the value of $V_{ts} = 0.04$ assuming 3×3 CKM unitarity and does not hold if heavier quarks exist.

Neglecting the mass of the b quark the eight non-vanishing helicity amplitudes for the different possible helicity combinations (h_t, h_W, h_b) of the three involved particles

are given by [58]:

$$(-\ 0\ -) = \left[\frac{m_t}{m_W} f_1^L + f_2^R\right] \sin\frac{\theta}{2} \cdot C\ , \tag{1.31}$$

$$(+\ 0\ -) = \left[\frac{m_t}{m_W} f_1^L + f_2^R\right] \cos\frac{\theta}{2} e^{i\phi} \cdot C\ , \tag{1.32}$$

$$(-\ 0\ +) = -\left[\frac{m_t}{m_W} f_1^R + f_2^L\right] \cos\frac{\theta}{2} e^{-i\phi} \cdot C\ , \tag{1.33}$$

$$(+\ 0\ +) = \left[\frac{m_t}{m_W} f_1^R + f_2^L\right] \sin\frac{\theta}{2} \cdot C\ , \tag{1.34}$$

$$(-\ -\ -) = \sqrt{2}\left[f_1^L + \frac{m_t}{m_W} f_2^R\right] \cos\frac{\theta}{2} e^{i\phi} \cdot C\ , \tag{1.35}$$

$$(+\ -\ -) = -\sqrt{2}\left[f_1^L + \frac{m_t}{m_W} f_2^R\right] \sin\frac{\theta}{2} e^{2i\phi} \cdot C\ , \tag{1.36}$$

$$(-\ +\ +) = -\sqrt{2}\left[f_1^R + \frac{m_t}{m_W} f_2^L\right] \sin\frac{\theta}{2} e^{-2i\phi} \cdot C\ , \tag{1.37}$$

$$(+\ +\ +) = -\sqrt{2}\left[f_1^R + \frac{m_t}{m_W} f_2^L\right] \cos\frac{\theta}{2} e^{-i\phi} \cdot C\ , \tag{1.38}$$

$$\text{with}\ \ C = \frac{-g}{\sqrt{2}}\sqrt{m_t^2 - m_W^2}\ . \tag{1.39}$$

For reasons of angular momentum conservation it is not possible to find a left-handed W boson together with a right-handed b quark or a right-handed W boson together with a left-handed b quark. Consequently, amplitudes corresponding to these combinations do not exist.
Using equation 1.19 the partial decay widths Γ_{h_W} for the effective Wtb vertex can be calculated from the helicity amplitudes given in equations 1.31–1.38:

$$\Gamma_0 = \frac{1}{2}\left|\frac{m_t}{m_W} f_1^L + f_2^R\right|^2 \cdot C' + \frac{1}{2}\left|\frac{m_t}{m_W} f_1^R + f_2^L\right|^2 \cdot C'\ , \tag{1.40}$$

$$\Gamma_- = \left|f_1^L + \frac{m_t}{m_W} f_2^R\right|^2 \cdot C'\ , \tag{1.41}$$

$$\Gamma_+ = \left|f_1^R + \frac{m_t}{m_W} f_2^L\right|^2 \cdot C'\ , \tag{1.42}$$

$$\text{with}\ \ C' = \frac{g^2}{32\pi} \cdot \left(1 - \frac{m_W^2}{m_t^2}\right)^2 \cdot m_t\ . \tag{1.43}$$

For $f_1^R = f_2^{R,L} = 0$, these partial decay widths are equal to the Γ_i^{SM} in equations 1.20–1.22. The resulting fractions of W-boson helicities can then be calculated as in the SM case using equation 1.24.

As long as all other couplings are zero the fraction of longitudinally polarized W bosons F_0 does not depend on deviations $\delta f_1^L = f_1^L - 1$ from the SM value. Significant deviations from the SM predicted values for the three helicity fractions can

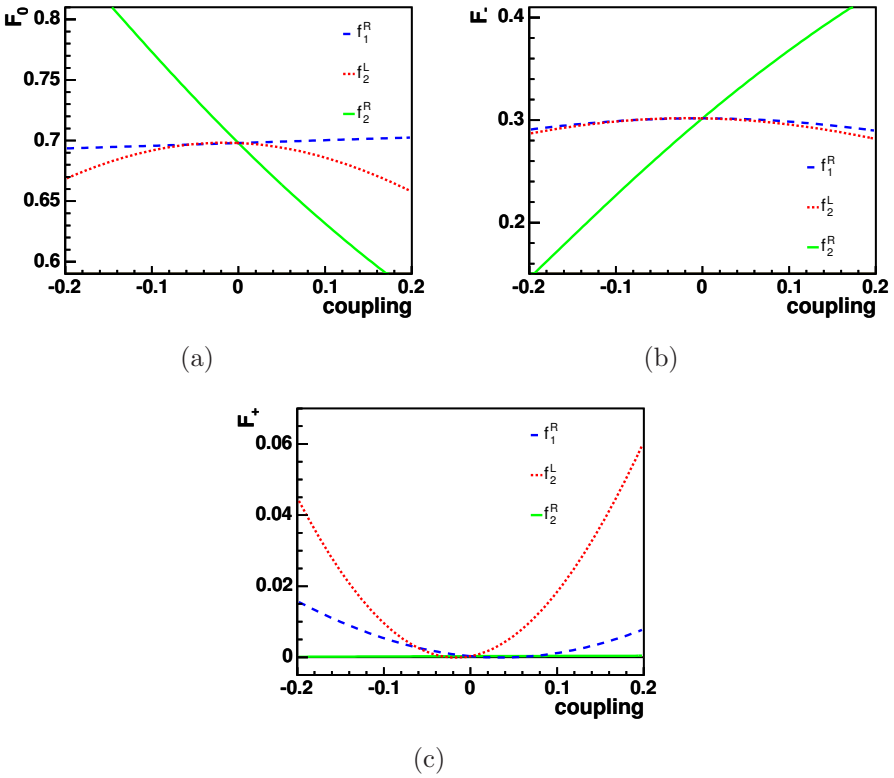

Figure 1.6: Dependence of the helicity fractions (a) F_0, (b) F_-, and (c) F_+ on the anomalous couplings f_1^R,f_2^L, and f_2^R, while f_1^L is set to its SM value of $V_{tb} = 1$. The anomalous couplings are assumed as not CP violating and the form factors are taken to be real. The partial decay widths for the calculation of the helicity fractions are taken from [69].

only arise in the presence of anomalous couplings which would be a clear signal for new physics.
Corrections to the helicity fractions for possible theories beyond the SM such as supersymmetry (SUSY) or topcolor-assisted technicolor models (TC2) have been calculated. In most of the SUSY parameter space the one loop SUSY-QCD corrections and supersymmetric electroweak corrections to the helicity fractions are less than 1% in magnitude and tend to cancel each other [67]. In technicolor models the corrections to the decay widths can reach under certain conditions the order of the SM NLO corrections [70].

Figure 1.6 shows the influence of the anomalous couplings f_1^R, f_2^L, and f_2^R on the three helicity fractions independent from any theoretical model for physics beyond the SM. For these studies f_1^L is fixed to its SM value of $V_{tb} = 1$ and only one of the other couplings is different from zero at a time. From figures 1.6 (a) and 1.6 (b) one can see that F_0 and F_+ are very sensitive to a non-vanishing f_2^R. Non-zero values of F_+ can arise only due to non-vanishing f_1^R or f_2^L, while the additional coupling via f_2^R does not change the fraction of right-handed W boson.

1.2.4 Sensitive Observable $\cos\theta^*$

The different W-boson helicity-states are distinguished from each other by the angular distribution of the W-boson decay products in its rest-frame. In the leptonic decay $W \to \ell\nu_\ell$ the angle θ^* is defined as the angle between the momentum of the charged lepton in the rest frame of the W boson and the direction of motion of the W boson in the rest frame of the decaying top quark. For hadronically decaying W bosons which are not subject to this analysis the charged lepton in the definition of θ^* has to be replaced with the down-type quark from the decay $W \to q\bar{q}'$. The definition of the decay angle θ^* is illustrated in figure 1.7.
The anomalous couplings introduced into the effective top-quark decay-vertex are restricted to the top-quark decay, the decay of the W has been well studied and understood and has been shown to proceed via the standard weak interaction. Due to the $V-A$ structure of the W-boson decay the neutrino can only be chiral left-handed and since neutrinos are nearly massless they are always of left-handed helicity.
As a consequence of momentum and spin conservation the charged lepton in the W-boson decay has then always to be right-handed. Due to the singly allowed spin configuration of the decay leptons, different distributions of the angle θ^* are obtained for the three helicity modes of the W boson.
Figure 1.7 shows the decay of differently polarized W bosons in the W-boson rest-frame. Charged leptons from left-handed W bosons are likely to fly in the direction of the b quark, leading to large values for θ^*, while charged leptons from right-handed W bosons fly mostly in the opposite direction, leading to small values of θ^*. The charged leptons from decaying longitudinally polarized W bosons have a high probability to be emitted perpendicular to the direction of the b-quark momentum. The quantitative description of this behavior can be obtained from the well known helicity amplitudes for the process $W^+ \to \ell^+\nu_\ell$ [58]:

$$(h_W = 0) = -gM_W \frac{\sin\theta^*}{\sqrt{2}} \,, \tag{1.44}$$

$$(h_W = -) = -gM_W e^{-i\phi^*} \frac{1-\cos\theta^*}{2} \,, \tag{1.45}$$

$$(h_W = +) = -gM_W e^{i\phi^*} \frac{1+\cos\theta^*}{s} \,, \tag{1.46}$$

where θ^* and ϕ^* are the polar and the azimuthal angle of the momentum of the charged lepton defined in the rest frame of the W boson. This frame is oriented such that its z axis represents the direction of motion of the W boson in the rest frame of the decaying top quark. Thus θ^* is the angle between the momentum of the charged lepton in the rest frame of the W boson and the direction of motion of the W boson in the top-quark rest-frame, as introduced in the beginning of this section. By squaring and normalizing these helicity amplitudes the relative phase difference due to the azimuthal angle ϕ^* vanishes and one obtains the $\cos\theta^*$ distributions for

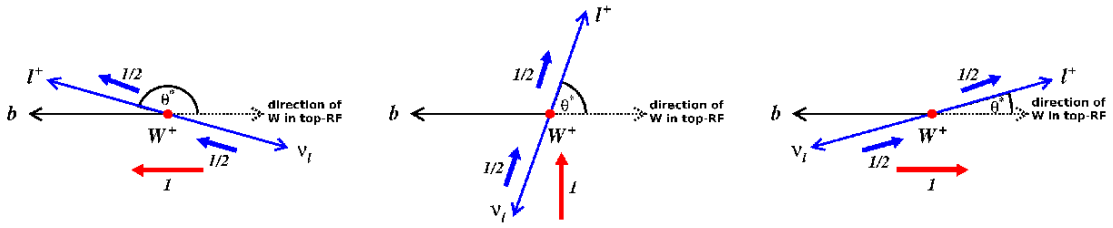

Figure 1.7: Illustration of the decay of (a) a left-handed, (c) a right-handed, and (b) a longitudinally polarized W boson into a charged lepton and a neutrino in the W boson rest frame. The dotted black arrow represents the direction of motion of the W boson top-quark rest-frame.

the three different helicity states shown in figure 1.8:

$$f_0 = \frac{3}{4}(1 - \cos^2\theta^*) \ , \tag{1.47}$$

$$f_- = \frac{3}{8}(1 - \cos\theta^*)^2 \ , \tag{1.48}$$

$$f_+ = \frac{3}{8}(1 + \cos\theta^*)^2 \ . \tag{1.49}$$

With this the normalized differential decay rate for unpolarized top quarks is given by [69]:

$$\frac{1}{\Gamma}\frac{d\Gamma}{d\cos\theta^*} = F_0 \cdot \frac{3}{4}(1 - \cos^2\theta^*) + F_- \cdot \frac{3}{8}(1 - \cos\theta^*)^2 + F_+ \cdot \frac{3}{8}(1 + \cos\theta^*)^2 \ . \tag{1.50}$$

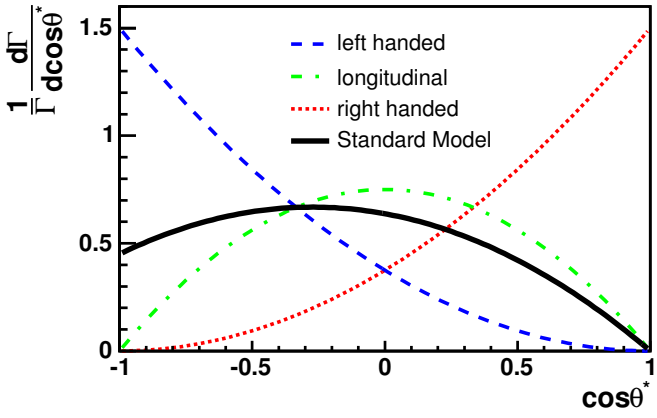

Figure 1.8: Differential $\cos\theta^*$ distributions for the three different W boson helicities. In addition the distribution obtained from the SM predicted values for the helicity fractions is shown (black curve).

As mentioned earlier, for simplicity only the decay of top quarks has been discussed and therefore only W^+ bosons have been considered. The fraction of longitudinally

polarized W bosons does not depend on the charge of the W boson while the fractions of left-handed and right-handed W bosons are reversed. In the charge conjugated case an antitop quark decays into a W^- boson and an anti-b quark. Neglecting its mass the anti-b quark has to be right-handed, forcing the W^- to be either longitudinally polarized or right-handed. However, right-handed W^- bosons and left-handed W^+ bosons exhibit the same $\cos\theta^*$ distribution and thus in all considerations the charge-conjugated case is always implied.

Chapter 2

Colliders and Detectors

Like the other fermions of the second and third generation, top quarks do not occur in our natural environment but rather have to be produced artificially. For this purpose particle physicists use large machines to accelerate and collide ordinary particles like electrons or protons with each other. According to Einstein's famous relation between energy and mass, $E = mc^2$, in collisions of sufficient energy, new particles can be produced. The collisions and the emerging particles are studied using large detectors which are installed hermetically around the interaction point. Today's most powerful colliders are located at the Fermi National Acceleration Laboratory, abbreviated Fermilab, near Chicago, USA, and at CERN[1] in Geneva, Switzerland. The Tevatron at Fermilab is operating since 1985 and the Large Hadron Collider (LHC) at CERN recently started operation and will reveal its total discovery potential within the next decade. In this chapter, these two particle accelerators will be briefly described. The main focus in the description of particle detectors is hereby on the Collider Detector at Fermilab (CDF) and the Compact Muon Solenoid (CMS) at CERN.

2.1 Colliders

The mass range for new particles being produced in collisions of high-energetic ordinary particles is limited by the total available energy, the so-called center-of-mass energy. On their search for ever heavier particles, physicists have developed a variety of powerful accelerators and colliders.
In modern accelerators charged particles are accelerated using resonant microwave cavities, where electric fields oscillate with the adequate frequency, that leads to an acceleration effect. A consequence of this method is that particles cannot be accelerated in a continuous particle beam but are rather grouped into so-called bunches. The bunch size and the distance between two bunches depend on the frequency of the oscillating electric fields. The required length of an accelerator strongly depends

[1] CERN is the European Organization for Nuclear Research. The acronym stands for its former name Conseil Europeén pour la Reserche Nucléaire.

on the center-of-mass energy aimed for. One way to reach high energies with a limited machine length is to use circular accelerators, in which the particles pass the accelerating sections in each turn and are thus consecutively accelerated. In order to force charged particles on circular orbits, magnetic fields have to be used and must be turned up with increasing particle momenta to maintain a constant curvature of the orbit. Accelerators based on this technique of synchronously adjusting the magnetic field to the energy of the accelerated particles are called synchrotrons.
In practice, a whole preaccelerator chain, consisting of different accelerators is used with a large circular collider typically being the final stage, where two beams of accelerated particles are collided. Per beam crossing only a few particles actually collide with each other, the majority leaves the collision point without having interacted. Therefore in circular colliders bunches can be reused for a huge number of collisions until the particle density per bunch is significantly reduced. This feature is another advantage of the concept of circular colliders.
Besides the need of sufficient center-of-mass energy, another aspect has to be considered. Since most of the processes to be studied are rare, the interaction rate must be large enough to provide a sufficient number of these interactions. The interaction rate $\dot{N}$ for a certain process is proportional to its cross section σ and to the luminosity L of the collider, $\dot{N} = L\sigma$. The luminosity for head-on collisions of two bunches a and b containing N_a and N_b particles with a collision frequency f is given by

$$L = f \cdot \frac{N_a N_b}{4\pi\sigma_x\sigma_y} \ , \tag{2.1}$$

where σ_x and σ_y characterize the transverse size of the bunches, assumed to have a Gaussian profile, at the collision point. Taking more realistic assumptions into account, the luminosity for a collider can be formulated as [71]

$$L = f \cdot N_{\text{bunch}} \cdot \frac{\gamma N_a N_b}{4\pi\epsilon_{\text{n}}\beta^*} F \ , \tag{2.2}$$

where f is again the collision frequency, N_{bunch} is the number of bunches per beam, and N_a and N_b are the numbers of particles in a bunch of beam A and beam B, respectively. ϵ_{n} stands for the normalized transverse beam emittance, a measure of the phase space area associated with either of the two transverse degrees of freedom of the beams. β^* and γ denote the amplitude function at the interaction point and the Lorentz factor, respectively. The geometric reduction factor F accounts for a possible crossing angle of the beams at the interaction point. In the design of a particle collider all these parameters have to be considered in order to achieve luminosities that are sufficient to produce the desired interactions at reasonable rates.
One of the main limitations on the achievable maximal center-of-mass energy is the energy loss due to synchrotron radiation. The energy an accelerated charged particle looses through synchrotron radiation increases significantly with the particle's energy. The energy loss ΔE per particle and per turn can be expressed as

$$\Delta E = -\frac{4\pi\alpha}{3R}\beta^3\gamma^4 \ , \tag{2.3}$$

where R is the radius of the accelerator and γ is given by $\gamma = \frac{E}{mc^2}$. In the ultra relativistic scenario $\beta = \frac{v}{c}$ equals one. Thus the energy loss is proportional to the inverse of the radius and to the fourth power of the ratio energy over mass of the accelerated particles. For example, an electron with an energy of 100 GeV accelerated at the former Large Electron Positron collider (LEP) at CERN radiated about 2.3 GeV of its energy per turn, which had to be compensated for by the accelerator facility. In order to reduce the energy loss due to synchrotron radiation one can either enlarge the radius of the accelerator or accelerate heavier particles. The second approach is followed by hadron colliders like the Tevatron, where protons are collided with antiprotons, and the LHC, where two beams of protons are accelerated and collided. As protons are about 2,000 times heavier than electrons and due to the fourth power dependence on the inverse mass of the accelerated particles, the energy loss for protons or antiprotons is about ten orders of magnitude smaller than for electrons and can be neglected.
However, electrons are point-like objects, while protons and antiprotons are composite particles made of quarks and gluons. In collisions of composite particles the actual interaction takes place between the constituents, quarks and gluons, carrying only a fraction of the proton's momentum. Therefore, the design of the collider has to foresee to be well above the energy threshold of the desired processes. On the other hand, the wide spectrum of effective collision energies arising from this makes hadron colliders ideal discovery machines, while electron colliders are used for precise measurements at certain energy scales.

2.1.1 The Tevatron at Fermilab

Figure 2.1: Aerial view of the Tevatron collider at the Fermilab site. The circular ring is the Tevatron maintenance road, the collider itself is located in a tunnel eight meters below the surface. At the eight o'clock position the CDF site is located, while DØ sits at the twelve o'clock position.

The Tevatron collider is located at the Fermilab in Batavia, Illinois (USA), in the vicinity of Chicago. For a picture of the Fermilab site and the Tevatron main ring see figure 2.1. The proton-antiproton collider with a circumference of about 6.3 km

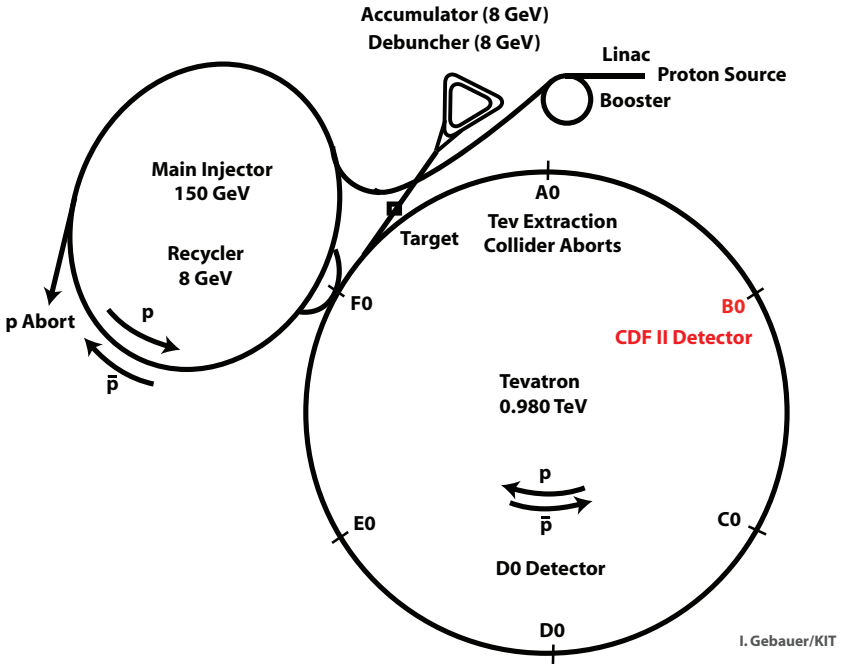

Figure 2.2: Schematic view of Fermilab's accelerator facilities.

started operation in 1985 with a center-of-mass energy of $\sqrt{s} = 1.8\,\text{TeV}$. Run I, which lasted until 1996, brought among other interesting results the discovery of the top quark in 1995. After a five year shutdown in which the accelerator complex was upgraded, Run II started in 2001 with a slightly increased center-of-mass energy of $\sqrt{s} = 1.96\,\text{TeV}$. In order to reach beam energies of nearly one TeV, the protons and antiprotons have to pass several acceleration stages. Figure 2.2 gives a schematic overview of Fermilab's accelerator facilities.

Proton Source and Preaccelerators

The first stage of acceleration is the Cockcroft-Walton preaccelerator. Inside this device, a Magnetron ion source [72] produces negative hydrogen ions by surface ionization effects. The Magnetron consists of a central cylindrical cathode surrounded by an anode, with hydrogen gas injected into the volume between. The conditions inside the cavity caused by applied electric and magnetic fields create a dense plasma. Protons obtained from this plasma are accelerated towards the cathode and collide with its surface, which is coated with caesium to decrease the work function of the metal. The protons striking the low work function surface capture two electrons and reflect from the surface as H^- ions. These ions are extracted and accelerated to an energy of 750 keV by a positive voltage in the Cockcroft-Walton preaccelerator and then sent to the Linear Accelerator (LINAC) [73].
In the LINAC the H^- ions are accelerated by oscillating electric fields produced by radio frequency (RF) resonators. Over a distance of 130 m the ions pass two acceleration stages featuring two different technical designs. The low energy end of

the LINAC is instrumented with drift tube cavities, where the ions are accelerated up to an energy of 116 MeV. In the high energy part of the LINAC the negative charged hydrogen ions are further accelerated to an energy of 400 MeV by several side coupled cavities. In both sections the drift tubes and side coupled cavities as well as the gaps between them are dimensioned such that the bunches of H^- ions feel only the accelerating part of the oscillating electric fields and are shielded from the decelerating part. After the LINAC the H^- ions enter in a multiturn injection process the third stage of acceleration, the Booster.
In this circular accelerator with a circumference of about 940 m the H^- ions pass trough a carbon foil, where the two electrons are stripped. The resulting proton bunches are accelerated to an energy of 8 GeV by several RF cavities located along the Booster. With this energy the protons leave the Booster and are transferred to the Main Injector.

Main Injector and Antiproton Source

The Main Injector [74], a synchrotron with a circumference of about 3.3 km, was commissioned in 1999. As one of the major upgrades for Run II it significantly increased the performance of the Tevatron. It supports several operation modes as for example providing proton beams for fixed target experiments. The role of the Main Injector in Tevatron's accelerator chain is to provide protons with an energy of 120 GeV needed for the production of antiprotons and to accelerate protons and antiprotons up to an energy of 150 GeV.
The protons accelerated to 120 GeV are sent to the antiproton source where they hit a nickel target. The interaction of the protons with the nickel target produces a wide range of secondary particles including numerous antiprotons. A lithium lens behind the target focuses the spray of produced particles. Using magnetic fields, antiprotons with energies around 8 GeV are separated, collected and finally transferred to the Debuncher. Here the momentum spread of the antiprotons is reduced by RF manipulation, called bunch rotation, in which the antiprotons loose their bunch structure. From the Debuncher a continuous beam of 8 GeV antiprotons is then sent to the Accumulator which resides in the same tunnel as the Debuncher. As the name implies, the antiprotons are collected in this storage ring with a mean radius of 75 m for hours at an energy of 8 GeV and are continuously cooled down using stochastic cooling [75]. Stochastic cooling reduces the transverse momentum spread in the antiproton beam by detecting and correcting momentum fluctuations within each bunch via a negative feedback loop.
As soon as a sufficient number of antiprotons has been accumulated, they are sent to the Recycler. The Recycler [76] is a ring of permanent magnets and resides in the same tunnel as the Main Injector. It was originally designed to recycle antiprotons left over from the previous Tevatron store (the time interval between two fillings of the Tevatron) and merging them together with those from the Antiproton Source. In the early Run II phase, those plans were abandoned and the Recycler now acts as a storage ring in which the antiprotons from the Accumulator are further cooled by the electron cooling-system [77, 78]. This system mainly reduces the longitudinal

Accelerator	Final beam energy [GeV]
Cockroft Walton	0.75×10^{-3}
LINAC	0.4
Booster	8
Main Injector	150
Tevatron	980

Table 2.1: Summary of the acceleration stages from the proton source to the Tevatron (for simplicity only the proton acceleration is considered).

emittance of the beam by mixing the antiprotons with a continuous 4.3 MeV beam of electrons which are provided by a Pelletron accelerator, a type of electrostatic particle accelerator. The electron beam travels for approximately 20 m along the same path as the antiprotons and is then sent back to the Pelletron for recirculation. The electrons interact via Coulomb scattering with the antiprotons, thus cooling the beam and reducing the spread in longitudinal momentum. The Recycler stores the antiprotons at an energy of 8 GeV until the Tevatron is ready for injection. Then the antiprotons are fed into the Main Injector and are accelerated together with the protons in opposite directions up to the Tevatron injection energy of 150 GeV within 2 seconds before they finally enter the Tevatron.

The Tevatron Collider

Table 2.1 summarizes the different stages of the accelerator chain and their final beam energies from the proton source to the final stage, the Tevatron. In the Tevatron the protons and antiprotons are accelerated from the injection energy of 150 GeV to the final beam energy of 980 GeV by eight accelerating RF cavities. At the final energy the protons travel the circumference of 6.3 km in about 21 µs. The frequency of the oscillating electric field is 53.1 MHz, which leads to the total number of 1,113 RF buckets. Buckets are regions in phase space in which the protons and antiprotons feel only the accelerating effect of the oscillating fields, and therefore the number of buckets sets the maximal limit for the number of bunch positions along the ring. The proton beam and the antiproton beam consist each of 36 bunches, ordered in three so-called trains. Each train consists of twelve bunches, each separated by 20 buckets or 396 ns. Each proton bunch consists of 2.7×10^{11} protons, while the number of antiprotons per bunch is about ten times smaller. The trains are separated from each other by gaps of 139 buckets or 2.6 µs, which allows fast kicker magnets to ramp up and to dump the beam in a controlled way in case of a Tevatron malfunction.
Both beams share the same beam pipe circulating in opposite directions. Since protons and antiprotons are oppositely charged, the same magnetic field can be used to bend both beams on circular orbits. For this purpose 774 dipole magnets, providing the necessary magnetic field of 4.2 T, are located around the ring. In order to reach such high magnetic fields, superconducting electromagnets made of

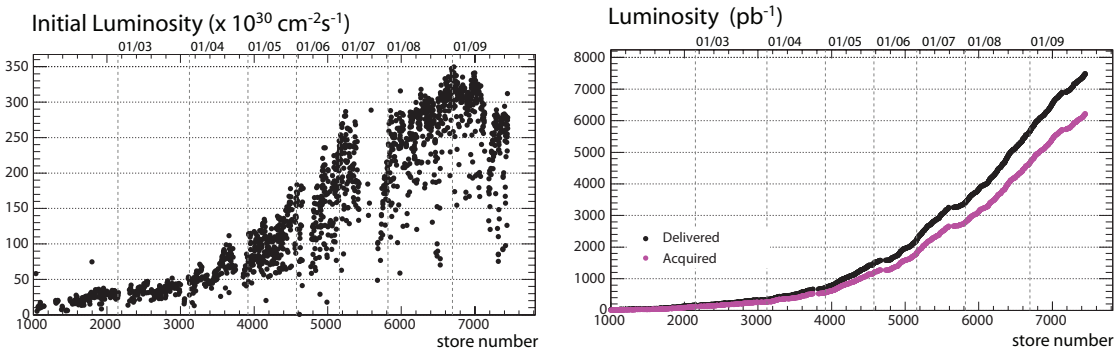

(a) (b)

Figure 2.3: Performance of the Tevatron in Run II: (a) The initial luminosity per store and (b) the total integrated luminosity. In (b) the upper curve represents the luminosity delivered by the Tevatron and the lower curve the luminosity recorded by the CDF II experiment. The dotted vertical lines indicate the beginning of a new calendar year.

niob-titanium are used. To ensure superconductivity, the dipole magnets are kept at an operation temperature of 4 K using liquid helium.
In addition, 240 quadrupole magnets and several correction magnets are installed around the Tevatron to focus and stabilize the two beams.
For 36 bunches per beam there are 72 possible interaction points along the Tevatron. At two of them the beams are forced to collide with each other, leading to head-on collisions at a center-of-mass energy of $\sqrt{s} = 1.96\,\text{TeV}$. The two collision points B0 and D0 host one experiment each, the Collider Detector at Fermilab (CDF) at the interaction point B0 and the DØ experiment at the D0 interaction point. To avoid beam-beam interactions outside these dedicated collision points, which would lead to proton and antiproton loss, electrostatic separators force the bunches to spiral around each other on helical orbits.

Due to several upgrades before and during Run II, the Tevatron achieves initial luminosities up to the current record luminosity of $355 \times 10^{30}\text{cm}^{-2}\text{s}^{-1}$, exceeding the design goal of $270 \times 10^{30}\text{cm}^{-2}\text{s}^{-1}$ [79] for Run II. Figure 2.3(a) shows the peak luminosity per store, which is reached at the beginning of each store and is therefore often also named initial luminosity. Due to collisions and beam gas interactions the number of protons and antiprotons stored in the Tevatron decreases leading to an exponential luminosity decrease. A typical store lasts 14 hours which is approximately one luminosity lifetime. Till the end of 2009 the Tevatron delivered an integrated luminosity of about $7.47\,\text{fb}^{-1}$, whereof $6.21\,\text{fb}^{-1}$ have been collected by the CDF II detector, which is illustrated in figure 2.3(b). It is planned to continue Tevatron operations at least until the end of the fiscal year 2010, when its successor as the world's most powerful accelerator, the Large Hadron Collider at CERN, will be fully operational.

2.1.2 The Large Hadron Collider at CERN

The Large Hadron Collider (LHC) has been constructed in the already existing 26.7 km tunnel of the former Large Electron Positron collider (LEP) at CERN in Geneva near the franco-swiss border. Figure 2.4 shows a view over the CERN site near Geneva. The locations of the LHC and its preaccelerators are indicated by white lines.
The aim of the LHC is to discover the Higgs boson and to reveal physics beyond the standard model at the TeV scale. Therefore, it is designed to provide center-of-mass collision energies up to $\sqrt{s} = 14\,\text{TeV}$. Since the pursued events are very rare, the LHC has to provide large instantaneous luminosities. The LHC aims a peak luminosity of $2 \times 10^{33}\text{cm}^{-2}\text{s}^{-1}$ in the low luminosity runs of the first years of operation and $10^{34}\text{cm}^{-2}\text{s}^{-1}$ in the high luminosity runs. Especially for this high instantaneous luminosity a high beam intensity is required, which excludes the use of antiprotons, since their production in sufficient numbers would take too much time. Fortunately, at these large energies interactions with high momentum transfer are mostly gluon initiated and the choice of proton-proton collisions does therefore not decrease the cross sections of these processes significantly.

Figure 2.4: Aerial view of the CERN site near Geneva located at the five o'clock position of the main ring. The white lines indicate the location of the several preaccelerators and the LHC below the surface.

Proton Production and Preaccelerator Chain

Figure 2.5 provides a schematic view of CERN's accelerator complex with the final stage being CERN's flagship, the LHC. As at the Tevatron, the starting point is the production of protons. In contrast to the proton production at Fermilab, at CERN the protons are produced directly instead of first producing H^- ions and stripping off the electrons after the first stage of acceleration. The protons are produced in a Duoplasmatron source, where hydrogen atoms are ionized through interaction with high-energy electrons. Through an applied high voltage the generated protons are extracted from the Plasmatron and are sent to a radio frequency quadrupole

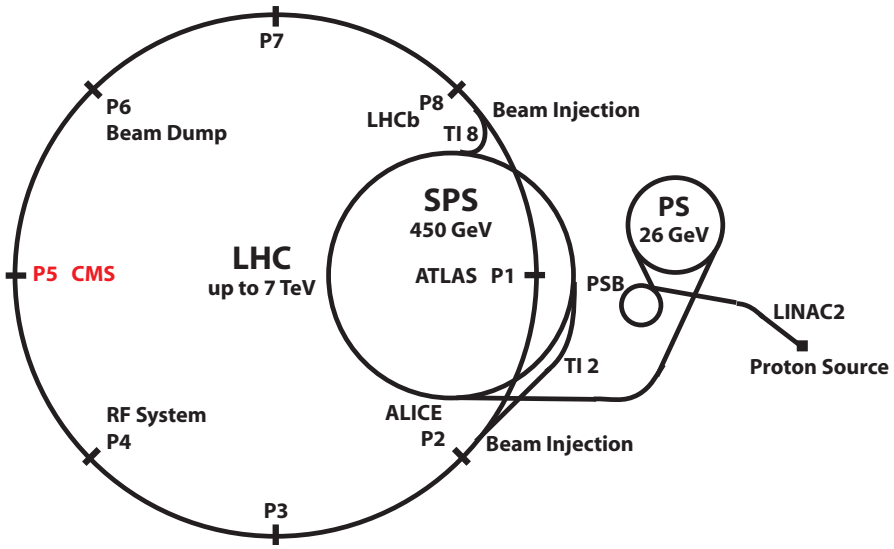

Figure 2.5: Schematic view of CERN's accelerator complex (not to scale).

(RFQ), a small linear accelerator with a length of 1.5 m. Here the protons are not only accelerated to an energy of 750 keV but also focussed and grouped into bunches. Afterwards the proton bunches are transferred to CERN's LINAC2. This linear collider with a length of 30 m is based on an RF concept and accelerates the protons up to an energy of 50 MeV.
Update plans for the near future foresee a different design for the proton source, similar to the one used at Fermilab. A Magnetron is planned to produce negative charged hydrogen ions which will be accelerated by the new linear collider LINAC4 [80], which is currently under construction. At the end of LINAC4 the H^- ions will pass through a carbon foil, where all orbiting electrons will be stripped off. The protons provided by LINAC2 are further accelerated by two circular accelerators. The Proton Synchrotron Booster (PSB) [81] increases the beam energy to 1.4 GeV, while in the Proton Synchrotron (PS) [82], an accelerator with a circumference of 630 m, the protons are accelerated to an energy of 26 GeV. With this energy the protons arrive at the last step of the LHC pre-injector chain, the Super Proton Synchrotron (SPS) [83], which is located 20 to 50 meters below the surface. With a circumference of 6.9 km the SPS is larger than Fermilab's Tevatron, but is based on conventional magnets with a maximum magnetic field of 2 T, which limits the maximum achievable beam energy to 450 GeV. Since its commissioning in 1976 it has served as accelerator for protons, antiprotons, electrons, positrons, and heavy ions. Between 1981 and 1984, it was used as a proton-antiproton collider (during this period is was named S$p\bar{p}$S), providing collisions for the two experiments UA1 and UA2, where in this time the W and Z bosons were discovered [84–87]. Its current role in the LHC preaccelerator chain is to accelerate the proton bunches to the LHC injection energy of 450 GeV. As soon as the protons have reached this energy, the beam is split and extracted via two transfer lines, TI 2 and TI 8 in figure 2.5, with a length of about 2.8 km per line into the LHC in opposite directions.

Accelerator	Final beam energy [GeV]
RFQ	0.75×10^{-3}
LINAC2	0.05
PSB	1.4
PS	26
SPS	450
LHC	up to 7,000

Table 2.2: Summary of the acceleration stages from the proton source to the LHC.

The whole CERN preacceleration complex, summarized in table 2.2, has already been used for several experimental purposes in the past. Since the end of LEP operation in 2000 it has been extensively upgraded to fulfil the requirements of delivering protons of sufficient energy to the LHC.

The LHC

The LHC main ring [71] has been installed in the existing 26.7 km tunnel that was constructed between 1984 and 1989 for the LEP machine. This tunnel consists of eight arcs and eight straight sections located between 45 m and 170 m below the surface on a plane sloping towards the Lake Geneva. This special tunnel geometry was needed for the installation of long acceleration sections instrumented with RF cavities in the straight sections around the ring, which had to compensate the high synchrotron radiation losses of LEP. Although hadron accelerators do only negligibly suffer from energy loss due to synchrotron radiation and are therefore ideally constructed with longer arcs and shorter straight sections for the same circumference, the cost effective solution was to reuse the LEP tunnel for the installation of the LHC. Eight RF cavities installed around point 4 accelerate the proton beams in the LHC from the injection energy to the operation energy. Although the choice for colliding protons with protons does not restrict the physics potential of the accelerator, it had a large impact on the design of the LHC. It cannot exploit the opposite charge of the accelerated particles by using a single beampipe as at the Tevatron. Rather, the two proton beams have to be accelerated in separate beam pipes. On the other hand, the chosen layout results in a reduction of beam-beam interaction and therefore increasing beam quality.
The space limitations in the tunnel made it hard to install two separated beam pipes embedded in separate magnet systems. Due to this and in order to keep costs low, a two-in-one design for almost all superconducting magnets has been adopted, in which the two beampipes are embedded in a common cryostat. The disadvantage of this layout is that the two rings are magnetically coupled resulting in a complicated magnetic structure.
1,232 superconducting dipole magnets, each 15 m long, are the core of the LHC and keep the proton beams on circular orbits. Since the LHC is not a perfect circle, but consists of arcs and straight lines, the bending radius of the dipole magnets has

to be smaller (2.8 km) than the LHC radius (4.8 km). In order to keep particles with an energy of 7 TeV in the beam pipe, the dipole magnets have to provide a magnetic field of 8.33 T, which is about two times the magnetic field used at the Tevatron. In order to achieve a magnetic field strength of 8.33 T with dipole coils made of niob-titanium, the magnets have to be operated at a temperature below 2 K. In contrast to the Tevatron, where liquid helium is used in oder to keep the magnets at a temperature of 4 K, the LHC dipole magnets are cooled with superfluid helium, flowing through all excavations of the dipole coldmass. In addition about 7,000 magnets have been installed to clean and focus the beams and correct their trajectories.
Special fast ramping magnets, called injection kickers, inject the beams into the different accelerators. At each stage of the accelerator chain, the rise time for these injection kickers leaves gaps of missing bunches in the beam. In nominal operation the 40 MHz RF of the PS generates bunches of protons with a spacing of 25 ns. This leads to 3,564 RF buckets[2] over the whole LHC ring. At nominal operation the LHC will be filled in twelve cycles of the SPS, with a spacing of 38 buckets due to the LHC injection-kicker rise-time of 0.94 µs. During each cycle the SPS transfers three or four batches to the LHC, whereby a batch consists of 72 bunches and eight empty buckets due to the SPS injection-kicker rise-time of 220 ns. In addition, an abort gap of 3 µs according to the LHC beam-dump kicker rise-time has to be included in order to be able to dump the LHC beam controlled within one revolution. This leads in total to 2,808 bunches per beam, each one consisting of 1.15×10^{11} protons in nominal operation.
The LHC is not only designed to accelerate and collide protons. During few weeks of each year it is planned to operate in the heavy ion mode, where lead ions will be accelerated and collided. Since this operation mode is not relevant for the study described in this thesis, it will not be further discussed.
Each of the eight straight sections of the LHC provides a possible interaction point (called point 1 to point 8), where experimental insertions could be installed. At four of these possible interaction regions the two beam pipes intersect each other and the proton beams are forced to collide. In underground caverns at these certain interaction regions the four main LHC experiments have been installed. Two of these experiments are multipurpose detectors. ATLAS (A Toroidal LHC Apparatus) is located at point 1 and CMS is located at point 5. In addition, the LHC hosts two special purpose detectors, the ALICE (A Large Ion Collider Experiment) experiment for heavy ion physics at point 2 and LHCb (Large Hadron Collider beauty), dedicated to b quark physics, at point 8.

Table 2.3 summarizes some of the machine parameters of the LHC in comparison with the Tevatron. While the numbers for the Tevatron are current values from the ongoing Run II operation, the quoted numbers for most of the LHC parameters are design values for proton-proton collisions. From experience with the Tevatron one can expect that it will take some years until these design values will be reached.

[2] Although the frequency of the LHC RF system is 400 Hz which would lead to 35,640 RF buckets over the whole ring, the maximum number of possible bunch locations is limited by the PS bunch spacing of 25 ns, resulting in 3,564 buckets.

Machine parameter	Tevatron ($p\bar{p}$)	LHC (pp)
Circumference [km]	6.3	26.7
Energy per (anti)proton [GeV]	980	7,000
Rotation frequency [kHz]	47.6	11.2
Number of bunches per beam	36	2,808
Number of (anti)protons per bunch	$2.7(0.3) \times 10^{11}$	1.15×10^{11}
Bunch spacing [ns]	396	25
Initial luminosity [$\mathrm{cm}^{-2}\mathrm{s}^{-1}$]	3.7×10^{32}	100×10^{32}
Number of dipoles	774	1,232
Magnetic field of dipoles [T]	4.2	8.33
Temperature of dipoles [K]	4	1.9
Crossing angle at IP [µrad]	-	300
Stored energy per (anti)proton beam [MJ]	1.6 (0.2)	362
Collisions per bunch crossing	≈ 6	≈ 20

Table 2.3: Collider parameters of the Tevatron (values of today) and the LHC (design parameters for the high luminosity run and with 7 TeV energy per beam). For early LHC operation periods with $\sqrt{s}$ between 7 TeV and 10 TeV and lower initial luminosities some parameters will change.

The LHC was successfully commissioned in 2008 with the first beam circulating at injection energy on September 10th but had to be shut down only nine days later. A failure in an electrical connection between two dipole magnets led to serious damage. It took over a year to repair and consolidate the LHC to ensure that such an incident cannot happen again. In November 2009 the LHC operation has been restarted and within a few days first collisions at injection energy have been observed by all four experiments. During December the LHC set a new world record and delivered collisions at a center-of-mass energy of 2.36 TeV. Following a short technical stop to prepare the machine for higher beam energies and for the start of the main research program, the LHC will resume operation in February 2010.

2.2 Detectors

In order to record and reconstruct interactions taking place in the collisions of high-energetic particles, physicists install detectors hermetically around the interaction regions. In the following the typical layout of multipurpose detectors, which pursue a broad physics program, is discussed. These detectors are designed azimuthally and forward-backward symmetric and aim to cover as large an area around the interaction point as possible in order to observe all possible products of an interaction. Different subdetectors, each specialized in the detection of different types of particles, are wrapped around each other in an onion-like structure. This structure is exemplarily shown in figure 2.6 for the CMS detector.
The heart of each particle detector is the tracking system in which the trajectories of

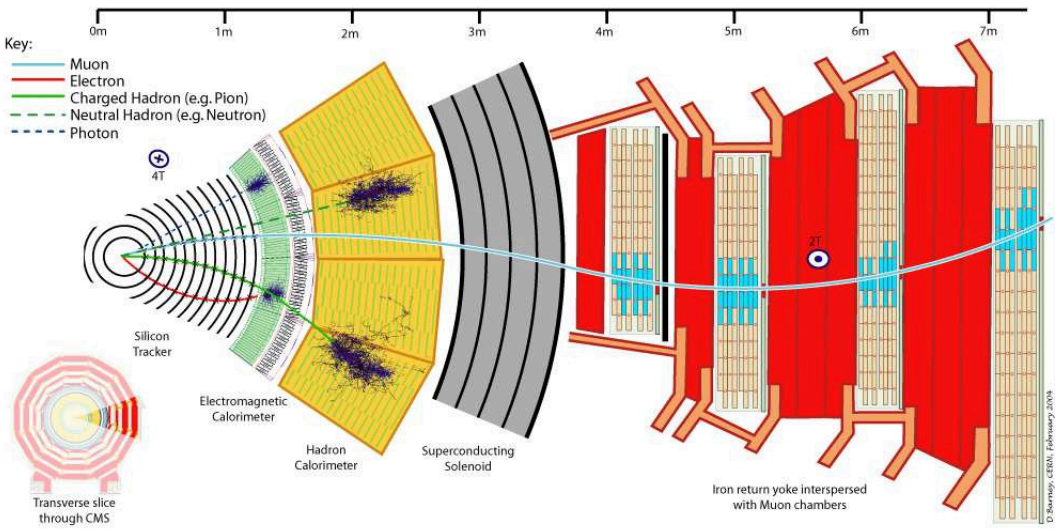

Figure 2.6: Transverse slice through the CMS detector as an example for the typical onion-like design of multipurpose particle detectors. In addition, the typical signatures (tracks and energy deposits) of electrons, muons, charged and neutral hadrons, and photons are depicted. One can clearly see the curved trajectories of charged particles within the magnetic field. Electrons and photons are stopped within the electromagnetic calorimeter, while hadrons loose their energy mainly in the hadronic calorimeter. Muons pass the calorimeters as minimal ionizing particles and are therefore the only observable particles reaching the muon chambers.

charged particles are recorded. This subdetector is usually based on silicon technology or on drift chambers. Both technologies exploit the ionization of material along the trajectory of a charged particle, either in form of electron-hole pairs in charge depleted silicon or as ionized gas molecules and free electrons in drift chambers. By applying a high voltage the generated charge carriers are separated and travel to their corresponding electrodes, which results in a measurable current. The tracking devices are embedded in an homogeneous magnetic field with the field lines parallel to the beam axis. This field bends the trajectories of charged particles traversing the detector and the curvature of a particle's track can be used to determine its momentum and the sign of its charge.

The tracking volume is surrounded by calorimeters, whose function is to stop particles and to absorb and measure their energy. Particles penetrating a calorimeter interact with the material, generate particle showers, and deposit their energy in the calorimeter. One distinguishes between electromagnetic calorimeters and hadronic calorimeters. Electromagnetic calorimeters are designed to measure the energy of particles that interact primarily via the electromagnetic force like photons or electrons and positrons. These particles create electromagnetic showers as cascades of secondary photons and e^+e^- pairs through bremsstrahlung and pair production. The characteristic length scale to describe the longitudinal thickness of calorimeter material of a given density is the radiation length X_0. It is defined as the distance over which a high-energetic electron looses all but $1/e$ of its energy by bremsstrahlung. For high-energetic photons, X_0 corresponds to 7/9 of the mean free path for pair

production.
Hadronic calorimeters measure the energy of particles that interact via the strong force. The hadronic showers resulting from the strong interactions of hadrons with nuclei of the typical heavy material of the calorimeter are called calorimeter jets. The typical scale for the description of the thickness of hadronic calorimeters is the hadronic interaction length λ_{I}, which is a measure for the mean free path of an high-energetic particle for inelastic interactions with the traversed material. Depending on the energy of the hadron, a thickness of about $8\lambda_{\mathrm{I}}$ is needed to collect 95% of the shower energy.
Calorimeters are often designed in the so-called sandwich concept, where the absorbing material that produces the particle showers is distinct from the material that measures the deposited energy. The two different materials are arranged in an alternating order. Electromagnetic calorimeters can also feature a homogeneous design, in which the entire volume is sensitive and contributes to the signal. The advantage of the latter is that one can measure the total energy deposited in the calorimeter, while in the sandwich concept only the part deposited in the sensitive material can be measured.
On the outside of a typical hermetic multipurpose detector resides the muon system consisting of additional scintillators and several wire chambers. Muons are heavier than electrons and therefore emit less bremsstrahlung. They also do not interact strongly with the detector material and can traverse the calorimeters loosing only a small fraction of their energy. Apart from neutrinos, that do not interact at all with the detector material, muons are the only particles that are not stopped within the detector volume. Thus, muons can be identified by signals in the muon system.

The Collider Detector at Fermilab (CDF) at the Tevatron and the Compact Muon Solenoid (CMS) at CERN's LHC both feature the described design. They combine precision charged particle tracking with fast projective calorimetry and fine grained muon detection needed for the detection and identification of all decay products emerging from the interaction point. In the following two sections these two detectors will be briefly described.

In order to compare the angular coverage of different subdetectors and the layout of CDF and CMS, it is useful to define a coordinate system, describing the detector geometry. Figure 2.7 shows the CDF coordinate system with the origin in the nominal collision point inside the detector. In that system the z axis is defined along the proton beam, and the x axis points radially away from the center of the Tevatron, the y axis is pointing vertically upwards. The azimuthal angle ϕ and the polar angle θ are defined with respect to the x and z axis, respectively. For the description of the CMS detector a similar coordinate system is used, with the difference, that x points radially inwards towards the center of the LHC. Consequently also the z axis points in opposite direction compared to the CDF coordinate system. But since both detectors are constructed azimuthally and forward-backward symmetric, this makes no difference for the description of the detectors.
In particle physics it is common to use a dimensionless quantity related to the polar

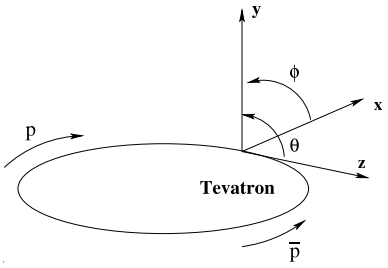

Figure 2.7: Coordinate system for the description of the geometry of the CDF II detector.

angle to describe the kinematics of particles. The rapidity y is defined as

$$y = \frac{1}{2} \ln \left(\frac{E + p_z}{E - p_z} \right) \ , \tag{2.4}$$

where E is the energy of the particle and p_z the z component of its momentum. Differences Δy of rapidities are invariant under longitudinal Lorentz boosts in z direction. However, for the description of detector geometries, the purely geometrical defined pseudorapidity[3]

$$\eta = -\ln \left(\tan \frac{\theta}{2} \right) \tag{2.5}$$

is more suitable. For massless particles both quantities are equal, for massive particles they are equal in the ultra relativistic limit. Using the azimuthal angle ϕ and the pseudorapidity η, the angular distance between two point-like objects inside the detector volume can be expressed as $\Delta R = \sqrt{(\Delta\eta)^2 + (\Delta\phi)^2}$. The transverse energy and transverse momentum of a particle are defined as $E_\mathrm{T} = E \cdot \sin\theta$ and $p_\mathrm{T} = p \cdot \sin\theta$, respectively.

2.2.1 The CDF II Experiment at the Tevatron

The Collider Detector at Fermilab (CDF) [88] has been installed around Tevatron's interaction point B0, eight meters below the surface. It is a cubical general purpose solenoidal detector with an edge length of 12 m and a total weight of about 5,000 tons. In 1985, the CDF experiment observed first Tevatron collisions and entered the era of real physics data taking two years later in 1987. After a first period of data taking, called Run I, which lasted until 1996, CDF was upgraded to deal with the higher collision frequencies of Tevatron's Run II. During a five year shutdown the tracking system and parts of the calorimetry were replaced and new muon chambers added. Consequently, the upgraded detector for Run II has been renamed as CDF II. For a picture of the installation of the new tracking system into the CDF II detector, see figure 2.8. Run II started in 2001 and after one year of commissioning the

[3]The pseudorapidity used for the description of the detector geometry is calculated with respect to the center of the detector and therefore also often named detector-η. The pseudorapidity of particles is calculated with respect to the interaction vertex of the event.

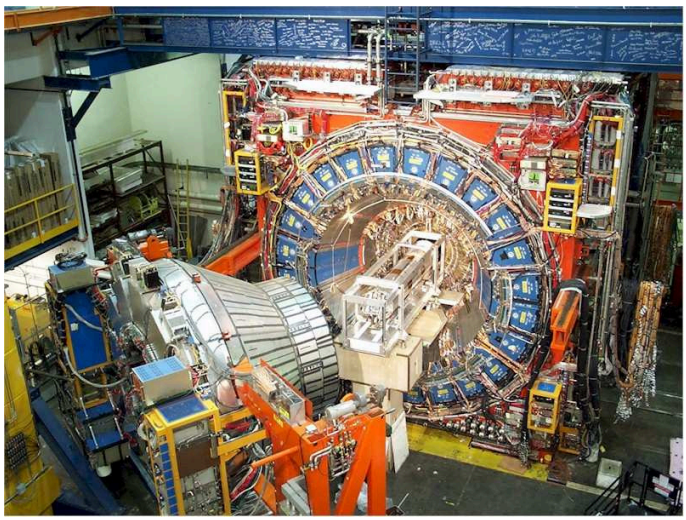

Figure 2.8: Photograph of the installation of the Run II tracking system into the CDF II detector.

upgraded detector started to take physics quality data. Till the end of 2009, the CDF II experiment has collected data corresponding to an integrated luminosity of $6.21\,\mathrm{fb}^{-1}$.
Figure 2.9 provides a solid cut-away view of the CDF II detector, showing the typical design of a multipurpose particle detector with a tracking system surrounded by a solenoid magnet, calorimeters, and muon chambers. The different subdetectors will be described briefly in the following, starting with the tracking system.

Tracking System

The CDF II tracking system features two different technologies to measure the momenta of charged particles. The inner tracker is based on silicon technology and consists of three subsystems. The innermost part, called Layer 00 [89] is a one layer radiation-hard single-sided silicon microstrip detector, glued directly onto the beam pipe. The next five layers of double-sided silicon microstrip detectors comprise the Silicon Vertex detector (SVX II) [90]. The layers with a total length of 96 cm are arranged in three cylindrical barrels at radii from 2.4 cm to 10.7 cm. Three of these five layers combine $r-\phi$ measurement on one side with 90° stereo measurement on the other side. The remaining two layers combine $r-\phi$ measurement with small angle stereo measurement. In the central region ($|\eta| < 1.0$) an additional layer is placed at a radius of 22 cm, while the regions $1.0 < |\eta| < 2.0$ are each instrumented with two layers at radii of 20 cm and 28 cm. These additional layers provide linking between track segments in the SVX II and the Central Outer Tracker and are therefore called Intermediate Silicon Layers (ISL) [91]. The five double sided layers feature each $r-\phi$ measurement on one side and a small stereo measurement with a 1.2° stereo angle on the other side. SVX II and ISL together provide a total angular coverage of $|\eta| \leq 2$ and allow track reconstruction in three dimensions with an impact parameter resolution of 40 µm. The total active area of the CDF II silicon

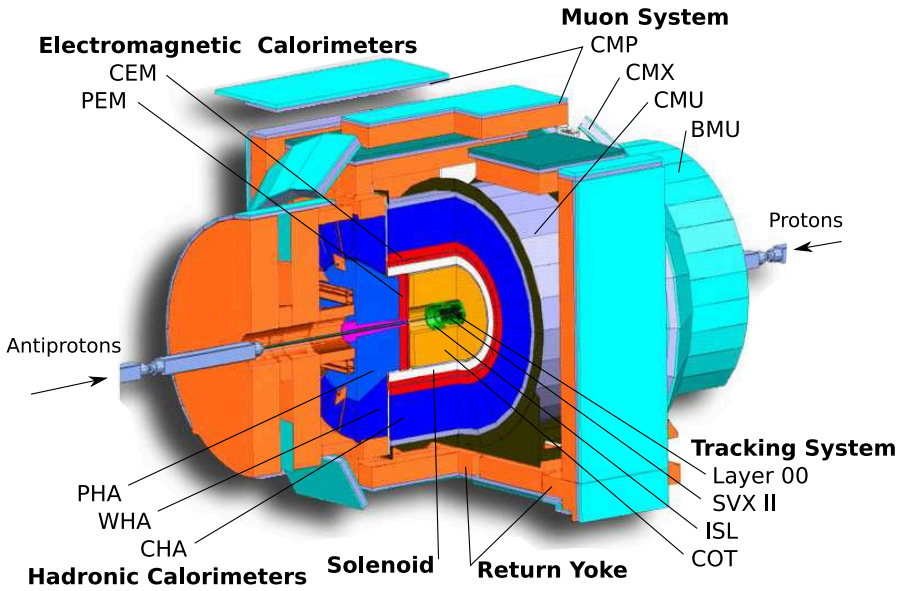

Figure 2.9: Solid cut-away view of the CDF II detector. The main components are indicated with the abbreviations explained in the text.

tracker amounts to $6\,\mathrm{m}^2$.
The outer part of the tracker volume is occupied by CDF's main tracking chamber, a 3.1 m long cylindrical open-cell drift chamber with a radial range between 44 cm and 132 cm, whose active volume covers the central region $|\eta| < 1$, and therefore is called Central Outer Tracker (COT) [92]. The COT is filled with equal amounts of argon and ethane with an admixture of 1.7% isopropanol and some oxygen to reverse aging effects. In order to handle the high luminosities of Run II, the COT has been designed to operate with a maximum drift time of 100 ns. It is segmented into eight alternating axial and stereo superlayers. Each superlayer consists of twelve sense wires, arranged parallel to the z axis in the axial superlayers and with a 2° stereo angle in the stereo superlayers. In the COT the momenta of charged particles are measured precisely with a momentum resolution of $\sigma(p_\mathrm{T})/{p_\mathrm{T}}^2 = 0.0015\,(\mathrm{GeV}/c)^{-1}$. In addition, the COT provides also dE/dx information for the measured tracks. Table 2.4 lists the different tracker subsystems with their geometrical coverage and the single hit resolution in $r-\phi$. The location of the individual subsystems of the CDF II tracker is illustrated in figure 2.10.

Solenoid

The tracking system is embedded into a superconducting solenoid [93], 3 m in diameter and 4.8 m long, made of an aluminium stabilized niob-titanium conductor. The solenoid is cooled with liquid helium and provides a magnetic field of 1.4 T over a useful volume of radius 1.4 m and length 3.5 m.

Subsystem	Geometrical coverage [cm]		SHR [µm]
Layer 00	$1.35 < r < 1.62$	$\|z\| < 47$	7
SVX II	$2.4 < r < 10.7$	$\|z\| < 48$	17
ISL	$20 < r < 28$	$\|z\| < 90$	32
COT	$40 < r < 132$	$\|z\| < 155$	140

Table 2.4: Summary of the geometrical coverage and the single hit resolution (SHR) in $r - \phi$ of the different subsystems of the CDF II tracker. The geometrical coverage is given in cylindrical coordinates, where r refers to the radial expansion from the beam axis and z refers to the length of the device along the beam axis.

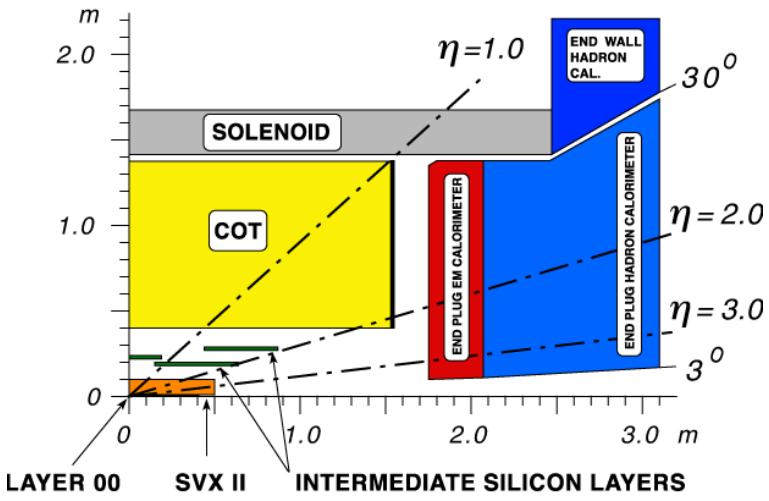

Figure 2.10: Longitudinal view of one quarter of the CDF II tracking system and the forward calorimeters [88].

Calorimetry

The CDF II calorimeters surrounding the solenoid are all sampling calorimeters either with lead-scintillator sampling in case of the electromagnetic calorimeters or with steel-scintillator sampling in case of the hadronic calorimeters. The read out is performed using plastic fibers and phototubes. The calorimeter system provides an angular coverage of $|\eta| \leq 3.6$ and consists in total of five subsystems.
The electromagnetic section of the calorimetry is divided into the Central Electromagnetic (CEM) calorimeter [94] covering the central region up to $|\eta| = 1.1$ and the Plug Electromagnetic (PEM) calorimeter [95,96] which instruments the forward (or plug) region $1.1 \leq |\eta| \leq 3.6$. The hadronic calorimeter is composed of the Central Hadronic (CHA) and the Wall Hadronic (WHA) calorimeters [97], covering the $|\eta|$ range up to 1.3, and the Plug Hadronic (PHA) calorimeter [95] completing the coverage up to $|\eta| = 3.6$.
All five subsystems are segmented in a projective tower geometry with the towers pointing back towards the nominal interaction point. Each tower covers a small range in η and ϕ. Hadronic and electromagnetic calorimeter possess the same tower

Calorimeter	η range	Thickness	Energy resolution
CEM	$\lvert\eta\rvert \leq 1.10$	$18X_0$, $1\lambda_\mathrm{I}$	$13.5\%/\sqrt{E_\mathrm{T}} \oplus 1.5\%$
PEM	$1.10 \leq \lvert\eta\rvert \leq 3.64$	$23.2X_0$, $1\lambda_\mathrm{I}$	$16\%/\sqrt{E} \oplus 1\%$
CHA	$\lvert\eta\rvert \leq 0.90$	$4.7\lambda_\mathrm{I}$	$50\%/\sqrt{E_\mathrm{T}} \oplus 3\%$
WHA	$0.90 \leq \lvert\eta\rvert \leq 1.30$	$4.7\lambda_\mathrm{I}$	$75\%/\sqrt{E_\mathrm{T}} \oplus 4\%$
PHA	$1.30 \leq \lvert\eta\rvert \leq 3.64$	$6.8\lambda_\mathrm{I}$	$80\%/\sqrt{E} \oplus 5\%$

Table 2.5: Summary of the η range, the thickness, and the energy resolution of the electromagnetic and hadronic calorimeters of CDF II [98]. The energy resolution for the electromagnetic calorimeters are for high energy electrons and photons, while the energy resolutions quoted for the hadronic calorimeters are for charged pions that do not interact in the electromagnetic part of the calorimeter system. The values are given in the form $\frac{\sigma(E_{(\mathrm{T})})}{E_{(\mathrm{T})}} = \frac{X\%}{\sqrt{E_{(\mathrm{T})}}} \oplus Y\%$, where X is the stochastic term and Y the constant term and $E_{(\mathrm{T})}$ is measured in GeV. The total resolution is obtained by adding the two terms in quadrature. The thickness is given in units of radiation lengths X_0 and hadronic interaction lengths λ_I. The values refer to an incident angle of 90°.

segmentation, which facilitates clustering and measuring of deposited energy. The CEM and CHA are segmented in towers of 15 ° in ϕ and 0.1 in η with a depth of 18 radiation lengths and 4.7 hadronic interaction lengths, respectively. The forward calorimeters are segmented in $\Delta\phi = 7.5\,^\circ$ towers for $|\eta| < 2.11$ and $\Delta\phi = 15\,^\circ$ for $|\eta| > 2.11$. Depending on the η region the granularity of the towers in $\Delta\eta$ varies between 0.009 and 0.18. The depth of the PEM is 23.2 radiation lengths, while the material of the PHA corresponds to a depth of 6.8 hadronic interaction lengths. In terms of hadronic interaction lengths the electromagnetic calorimeters feature a depth of one interaction length. The coverage in η, the thickness, and the energy resolution of the five calorimeter subsystems are summarized in table 2.5.

Muon System

The muon system resides beyond the calorimetry and consists of four subsystems [99]. The Central Muon detector (CMU) [100] consists of four layers of planar drift chambers and detects muons with p_T larger than $1.4\,\mathrm{GeV}/c$, which penetrate the five absorption lengths of calorimeter steel. The Central Muon Upgrade (CMP) [101] is composed of a second set of muon chambers behind an additional 60 cm of steel in the region $|\eta| \leq 0.6$. The chambers are of fixed length in z and form a box around the central detector. The Central Muon Extension (CMX) [101] consists of conical sections of drift tubes and scintillation counters located at each end of the central detector and extends the $|\eta|$ coverage of the muon system from 0.6 to 1.0.
For Run II several new chambers have been added to close gaps in the azimuthal coverage of the CMU, CMP, and CMX. In addition the forward muon system has been replaced by the Barrel Muon system (BMU) covering a pseudorapidity range of $1.0 \leq |\eta| \leq 1.5$.

2.2.2 The CMS Experiment at the LHC

The Compact Muon Solenoid experiment [102,103] resides at LHC's point 5 in Cessy in France in an underground cavern about 100 m below the surface. The construction of this cavern began with the end of LEP operation in 2000 and was completed in 2004. In order to be able to start building up the CMS detector already during the excavation of the cavern and to allow for simultaneous work on different detector parts it has been decided to construct CMS in a modular concept. A further advantage of this concept is the better accessibility and maintenance during LHC shutdowns. Consequently, the CMS detector has been built on the surface in 15 separate sections, which were then lowered down into the experimental cavern for assembly and installation. The last of these heavy elements was lowered in January 2008. Figure 2.11 shows a picture of CMS during installation in the underground cavern. The modular concept with separate disks can clearly be seen.
The complete detector has an overall length of 21.5 m, a diameter of 15 m, and a total weight of 12,500 tons. The large weight is mainly due to the enormous return yoke made of steel guiding the magnetic field outside the coil and housing CMS's muon system. Despite its huge weight the CMS experiment is relatively compact, at least compared to the other multipurpose detector at LHC, ATLAS, which has twice the volume of CMS but only about half the weight.
In September 2008 first beam events were observed with the CMS detector, but unfortunately the LHC had to be shut down only few days later due to a severe damage. Nevertheless, from October 2008 to November 2008 the experiment has been intensively tested under real operation conditions using about 270 million cosmic muon triggered events [104]. The lessons learned from this exercise, known as Cosmic Run at Four Tesla (CRAFT), were addressed in the one year LHC shutdown to finalize the work on the detector and to better prepare CMS for resumed beam operation. Only few days after the restart of LHC operation in November 2009, first collisions have been observed with the CMS experiment.

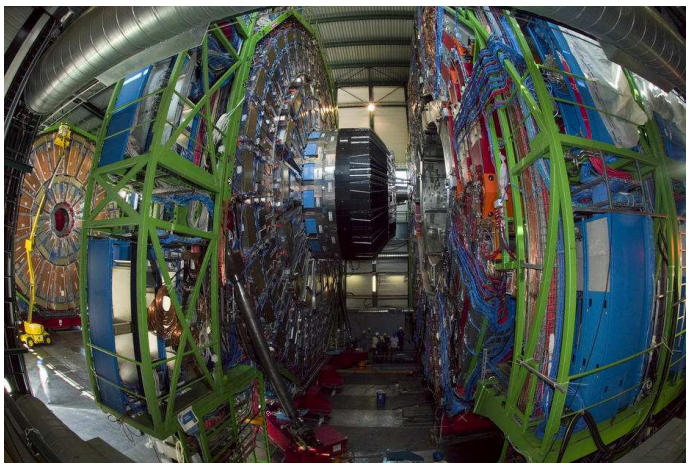

Figure 2.11: A picture of CMS during installation in the underground cavern at LHC's point 5.

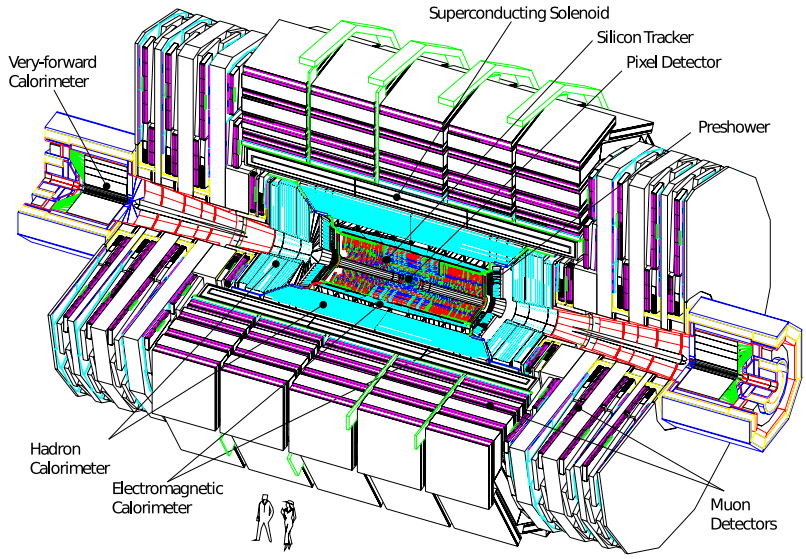

Figure 2.12: A perspective view of the CMS detector with all its major subsystems [103].

The layout of CMS, worked out in the early 1990s, was driven by the main physics goals of the LHC, the discovery of the Higgs boson and the search for supersymmetric particles. Due to the large background to Higgs boson production from QCD multijet events and due to the poor mass resolution that can be obtained with jets, the focus in the Higgs boson search lies on final states including leptons (like $H \rightarrow ZZ^* \rightarrow \mu\mu\mu\mu$) or photons ($H \rightarrow \gamma\gamma$). Therefore, the main focus in the CMS design lies in the detection and precise measurements of isolated leptons and photons. The clearest signatures of supersymmetric processes on the other hand are significant amounts of missing transverse energy. In order to be also sensitive to these processes, the detector must be constructed as hermetic as possible. The main detector requirements to meet the goals of the LHC physics program can be summarized as good muon identification over a large range of momenta and angles, good reconstruction efficiency and momentum resolution for charged particles in the inner tracker and good electromagnetic energy resolution. In addition a good missing transverse energy resolution and dijet mass resolution was aimed for, requiring an as hermetic as possible hadronic calorimeter.
The different subdetectors, needed to fulfil these requirements, are arranged in the typical onion-like structure, similar to the layout of the CDF II experiment. The main difference is that in contrast to the CDF II detector, where the calorimeters are placed outside the solenoid magnet, the CMS tracking system as well as the calorimeters are embedded inside the bore of the solenoid magnet. This is a consequence of the pursued compact design and as simple as possible architecture of the CMS detector. Figure 2.12 shows a perspective view of CMS with all its subsystems, which will be briefly described in the following, starting with the innermost part, the tracking system.

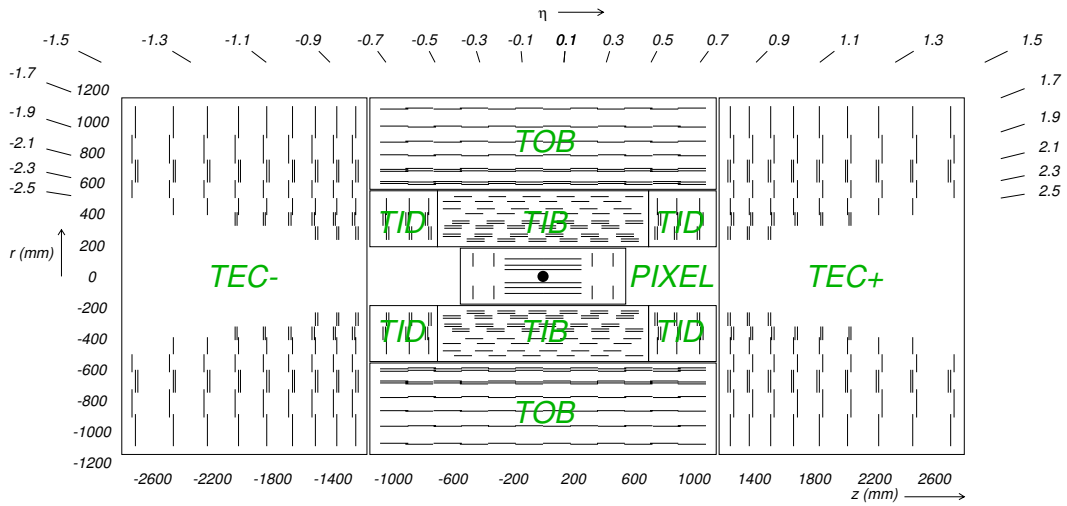

Figure 2.13: The CMS tracking system in $r - z$ view. Each line represents a detector module, stereo modules are indicated by double lines [103].

Tracking System

As a result of the high LHC design luminosity about 1,000 particles from up to 20 collisions per bunch crossing will be present in the innermost part of the detector at nominal operation. Therefore, the design of the tracking system must not only guarantee precise and fast track reconstruction but has also to deal with the intense particle flux and the resulting radiation damage. In 1999, at the time of the approval of the CMS tracker layout, problems with the microstrip gas counters, that were originally planned for the outer part of the tracking volume, led to the decision to build an all-silicon tracker [105, 106]. This became possible due to the evolution of silicon strip sensor technology from a customized technology into an industrialized one. The active silicon area of the tracking system amounts to about 200 m^2, more than 30 times larger than that of the CDF II silicon tracker. With an overall length of 5.8 m, a diameter of 2.3 m, and with an angular acceptance of $|\eta| < 2.4$ the CMS tracker is the largest silicon tracking system ever built. It can be divided into two subsystems employing different silicon designs, for a schematical illustration see figure 2.13.

Closest to the interaction point a pixel based detector is placed, which is capable of operating in this harsh environment for an expected lifetime of ten years. The pixel detector consists of three barrel layers with a total length of 53 cm at radii between 4.4 cm and 10.2 cm and two endcap disks at each end at $|z| = 34.5$ cm and $|z| = 46.5$ cm with a radial expansion from 6 cm to 15 cm. In total, 66 million pixels with a typical size of $100 \times 150\,\mu\mathrm{m}$ cover an area of about 1 m^2. The single point resolution of this subsystem is about 10 µm in $r - \phi$ and about 15 µm in the z coordinate.

The pixel detector is enclosed by the second component of the tracking system, the silicon strip detector composed of 9.6 million silicon strips, which are grouped in 15,400 modules and mounted on carbon fibre structures. The barrel part of the

strip detector consist of ten detection layers, of which the inner four layers comprise the Tracker Inner Barrel (TIB) covering a region up to $|z| = 0.65\,\mathrm{m}$. The six outer layers comprise the Tracker Outer Barrel (TOB) and extend up to $|z| = 1.1$ m. The system is completed by two Tracker End Caps (TEC) with nine discs each, reaching from $|z| = 1.2\,\mathrm{m}$ to $|z| = 2.8\,\mathrm{m}$ and three small discs at each end, the Tracker Inner Discs (TID), closing the gap between TIB and TEC. In each of the strip subsystems several layers provide additional stereo measurement in $r-\phi$ and $r-z$ coordinates, with a stereo angle of 5.7°. The single hit resolution of the fully aligned strip detector in $r-\phi$ is typically $23-35\,\mu\mathrm{m}$ in the TIB and $35-53\,\mu\mathrm{m}$ in the TOB. The resolution in z is about ten times more coarse and depending on the actual layer typical values lie between $230\,\mu\mathrm{m}$ and $530\,\mu\mathrm{m}$. The resolution of momentum measurements of charged particles is $\sigma(p_\mathrm{T})/{p_\mathrm{T}}^2 = 0.15\,(\mathrm{TeV}/c)^{-1}$ in the region $|\eta| \leq 1.6$, and thus about ten times better than the resolution of the CDF II tracking system. With increasing $|\eta|$ the performance decreases down to a resolution of $\sigma(p_\mathrm{T})/{p_\mathrm{T}}^2 = 0.60\,(\mathrm{TeV}/c)^{-1}$ for $|\eta| = 2.5$.
The whole tracking system is embedded in a chilled outer support tube and is operated at a temperature of about −20°C. Table 2.6 summarizes the geometrical coverage and the single hit resolutions of the different subsystems of the CMS tracking system.

Subsystem	Geometrical coverage [cm]		SHR [µm]
Pixel	$4.4 < r < 15$	$\lvert z\rvert < 46.5$	10
TIB/TID	$20 < r < 50$	$\lvert z\rvert < 65$	23–35/29–41
TOB	$50 < r < 108$	$\lvert z\rvert < 110$	35–53
TEC	$20(50) < r < 108$	$120 < \lvert z\rvert < 280$	28–53

Table 2.6: Summary of the geometrical coverage and the single hit resolution (SHR) in $r-\phi$ of the different subsystems of the CMS tracker. The geometrical coverage is given in cylindrical coordinates, where r refers to the radial expansion from the beam axis and z refers to the length of the device along the beam axis.

Calorimetry

The tracking system is followed by the electromagnetic calorimeter (ECAL) [107]. It exhibits the characteristic barrel and endcap structure that can be found all over CMS with 61,200 lead tungstate ($PbWO_4$) crystals in the barrel part ($|\eta| < 1.479$), called Electromagnetic Barrel (EB), closed by 7,324 crystals in each of the two Electromagnetic Endcaps (EE), leading to a total angular coverage of $|\eta| < 3.0$. In contrast to CDF's electromagnetic calorimeter, the CMS ECAL is a homogeneous calorimeter, where absorbing and sensitive material are the same. This is possible due to the properties of the chosen material, lead tungstate, which features not only a high density of $8.28\,\mathrm{g/cm^3}$ but also a short radiation length of $X_0 = 0.89\,\mathrm{cm}$. In addition, the scintillation decay time of this material is in the same order as the bunch crossing time, and within 25 ns about 80% of the light is emitted, which enables fast energy measurement.

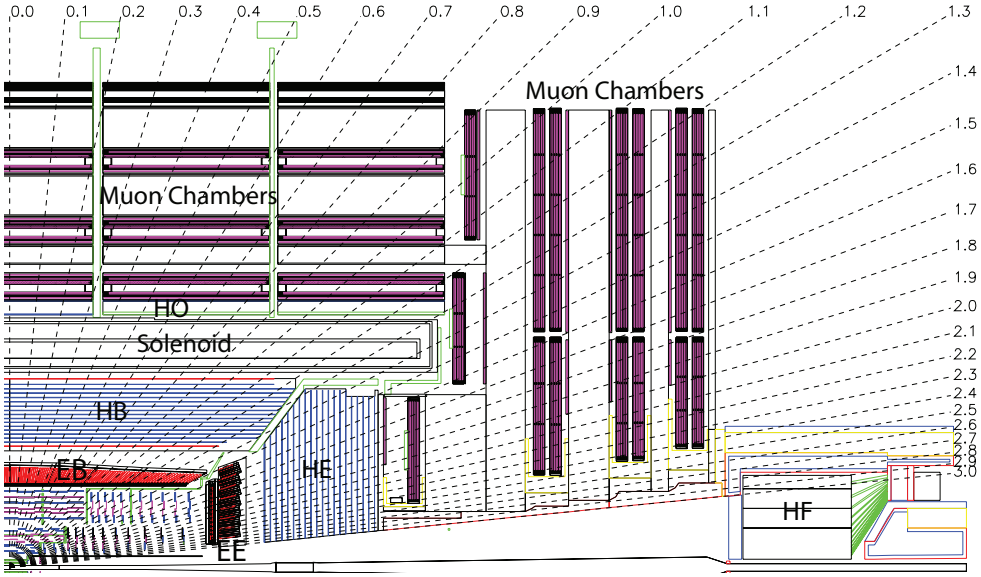

Figure 2.14: Longitudinal view of one quarter of the CMS detector showing the location of the electromagnetic and hadronic calorimeters, the magnetic coil, and the muon chambers [103]. The preshower is placed in front of the ECAL endcap (EE).

The crystals in the barrel region are arranged in a quasi projective geometry and cover each 0.0174 in $\Delta\phi$ and $\Delta\eta$ at a length of 23 cm, corresponding to 25.8 radiation lengths. The endcap part is composed of crystals of the same type grouped in mechanical units (called supercrystals) of 5×5 crystals with a length of 22 cm or $24.7X_0$. The energy resolution of the ECAL has been estimated with test-beam electrons to be $2.8\%/\sqrt{E} \oplus 0.3\%$ [108].
In 2009, an additional preshower detector has been mounted in front of the endcaps, covering the η range from 1.65 to 2.6. This self-contained subsystem is comprised of two layers of silicon strip detectors each preceded by a layer of lead radiators with a total depth of three radiation lengths. The purpose of the preshower is to differentiate energy deposits from single photons from energy deposits from two closely spaced photons. The latter originate from neutral pion decays and are a major background for the Higgs boson search in the $H \rightarrow \gamma\gamma$ channel.

Due to the compact construction of the CMS detector, the calorimeter system has to be installed within the bore of the solenoid magnet and therefore within the magnetic field. Thus, the design of the calorimeters is mainly driven by the magnetic properties of the used material and the requirement to provide a good overall coverage. The hadronic calorimeter (HCAL) [109] has been designed as a sampling calorimeter with non magnetic brass as absorber material, featuring a reasonable short interaction length of 16.42 cm, interspersed with plastic scintillator tiles as active material.
The Hadronic Barrel (HB) part is segmented into towers of 0.087 in $\Delta\phi$ and $\Delta\eta$ and covers the angular region of up to $|\eta| < 1.3$ with a thickness of 5.8 hadronic interaction lengths. It is completed by the Hadronic Outer calorimeter (HO), scintil-

Calorimeter	η range	Thickness	Energy resolution
EB	$\lvert\eta\rvert \leq 1.479$	$25.8X_0$, $1\lambda_\mathrm{I}$	$2.8\%/\sqrt{E} \oplus 0.3\%$
EE+Preshower	$1.479 \leq \lvert\eta\rvert \leq 3.0$	$(24.7+3.0)X_0$, $1\lambda_\mathrm{I}$	$5.7\%/\sqrt{E} \oplus 0.3\%$
HB+HO	$\lvert\eta\rvert \leq 1.3$	$(5.8+1.4)\lambda_\mathrm{I}$	$100\%/\sqrt{E} \oplus 5\%$
HE	$1.3 \leq \lvert\eta\rvert \leq 3.0$	$9\lambda_\mathrm{I}$	$100\%/\sqrt{E} \oplus 5\%$
HF	$3.0 \leq \lvert\eta\rvert \leq 5.0$	$10\lambda_\mathrm{I}$	$198\%/\sqrt{E} \oplus 9\%$
			$280\%/\sqrt{E} \oplus 11\%$

Table 2.7: Summary of the η range, the thickness, and the energy resolution of the electromagnetic and hadronic calorimeters of CMS. The value for EB is obtained with test-beam electrons [108] and the higher value of the stochastic term of EE is due to the additional contribution of 5% from the preshower [107].The values for HB+HO and HE are the design resolutions [109], test beam results for a combined ECAL and HCAL segment yield a resolution of $85\%/\sqrt{E} \oplus 7\%$ [110]. The values for HF are the electromagnetic and hadronic energy resolution as obtained with test beams [111]. The thickness is given in units of radiation lengths X_0 and hadronic interaction lengths λ_I. The values refer to an incident angle of 90°.

lators mounted outside the vacuum tank of the coil using the solenoid as additional absorbing material, corresponding to $1.4\lambda_\mathrm{I}$. The HO follows the HB tower geometry and covers an η range of up to 1.26. It is used to identify late starting showers and to collect the energy of hadron showers leaking through the calorimeters.
The Hadronic Endcaps (HE) cover the $|\eta|$ region from 1.3 to 3.0 with a granularity of 0.087 in $\Delta\phi$ and $\Delta\eta$ for $|\eta| < 1.6$, which changes to a value of 0.17 for increasing pseudorapidity. The thickness of the absorber material corresponds to nine hadronic interaction lengths. Additional coverage in the forward region up to $|\eta|$ values of 5.0 is provided by the Hadronic Forward (HF) calorimeter, a cylindrical structure with an outer radius of 1.3 m consisting of steel absorber plates and quartz fibers as Cherenkov light radiators.
Due to the sandwich concept of the HCAL, most of the shower energy is deposited in the absorber material, leading to a worse energy resolution compared to the ECAL. The energy resolutions of the CMS calorimeter system are listed in table 2.7. Figure 2.14 provides an overview of the location of the different calorimeter subsystems within the CMS detector together with the location of the muon chambers.

Solenoid

Tracking system and calorimetry are embedded in the solenoid with an inner diameter of 5.9 m and a length of 12.9 m. The design is similar to the one of the CDF II solenoid. Again, a high-purity aluminium stabilized and mechanically reinforced niob-titanium conductor is used in a four layer winding. The CMS solenoid provides a homogeneous 3.8 T magnetic field parallel to the beam axis, which is 2.7 times larger than the magnetic field generated by the CDF II solenoid. The magnetic field is returned via the enormous iron yoke with a weight of $10,000$ t, where the magnetic field strength is still nearly 2 T.

Muon System

The magnetic return yoke returns not only the magnetic flux of the CMS solenoid but also accommodates the CMS muon system [112]. As the name of the experiment already indicates, the muon system plays an important role in order to meet the physics goals of the CMS research program. The CMS design with the muon system inside the magnetic field allows to measure the muon momentum both inside the magnetic coil by the tracking devices and outside of the coil by the muon system. For the three muon subsystems three types of gaseous detection technologies have been chosen according to the different background rates and magnetic fields the individual detector parts have to withstand. One important source of background arises from thermal neutrons getting captured by a nucleus, which leads to the emission of a photon. Electrons or positrons emerging from electromagnetic reactions of the emitted photon can cause hits in the muon system. Most of these neutrons stem from hadronic interactions in the beampipe, the forward calorimeters, or in the lower endcaps. In the barrel region up to $|\eta| < 1.2$, where the neutron background is small, 250 Drift Tubes chambers (DT) are arranged in four layers at radii of about 4.0 m, 4.9 m, 5.9 m, and 7.0 m from the beam axis. In the endcaps, covering the $|\eta|$ range between 0.9 and 2.4, where the background rate is higher and the magnetic field is more intensive than in the barrel, 468 Cathode Strip Chambers (CSC) are installed, organized in four layers. In addition, several Resistive Plate Chambers (RPC) are installed in both regions. While the DT and CSC sensors yield a precise measurement of positions and thus momenta of muons, the very fast RPCs provide worse spatial resolution but are well designed to offer information for the first level trigger.

2.2.3 Data Acquisition and Trigger System

The bunch spacings of 396 ns at the Tevatron and 25 ns at the LHC result in bunch crossing rates of 2.5 MHz and 40 MHz, respectively. Taking empty buckets in the beams into account, these numbers are reduced to effective bunch crossing rates of 1.7 MHz at the Tevatron and 31.5 MHz at the LHC. For the latter one expects about 20 inelastic interactions per bunch crossing at high luminosity and design center-of-mass energy. This means roughly 10^9 events per second. It is impossible to store and process the large amount of data associated with the high event rates at either the Tevatron or the LHC. A drastic reduction of the event rates has therefore to be achieved using special trigger systems.
For this purpose, events are considered sequently in a tiered deadtimeless trigger architecture at different levels of approximation. Each level thereby provides a sufficient rate reduction for the next level to guarantee minimal deadtimes. Figure 2.15 provides schematic block diagrams of the dataflow in the CDF II and CMS trigger systems.
In a first step, based on customized hardware, the systems decide whether an event is sufficiently interesting to be further processed by using a subset of the data. During the time of decision the complete read-out data of an event is buffered in a pipeline

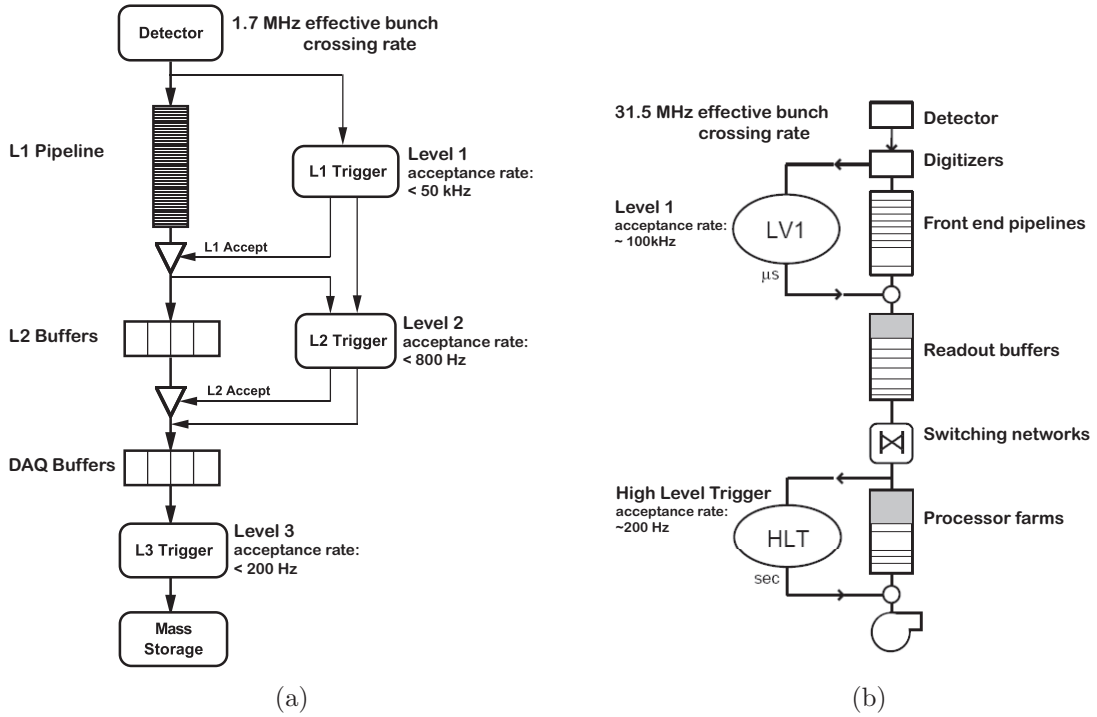

Figure 2.15: Functional block diagram of (a) the CDF II and (b) the CMS trigger system.

and only further processed if the event is accepted.
At CDF II this first step is realized in a two level design. The Level-1 trigger consists of a synchronous system of three parallel subsystems, where calorimeter-based objects are found by the calorimeter boards, muons are identified by the muon-trigger and COT tracks are reconstructed and matched to energy depositions in the calorimeters or muon signals in the muon chambers by the Extreme Fast Trigger (XFT). The Level-2 trigger is also based on customized hardware but features an asynchronous architecture. It performs a minimal event reconstruction and reduces the event rate together with Level-1 to about 800 events per second.
The CMS trigger system has only one single hardware based level, the Level-1 trigger, which reduces the initial event rate to 100 kHz using coarse information from the calorimeters and the muon system.
All events accepted by the first tier of the trigger system, either Level-1 and Level-2 at CDF II or Level-1 at CMS, are forwarded to the next stage of triggering, called Level-3 at CDF II and High Level Trigger (HLT) at CMS. This second tier uses filtering software running on a farm of parallel processors and has access to the complete read-out data at full granularity and can therefore perform complex calculations. CDF's Level-3 and the CMS HLT reduce the event rate to up to 200 events per second, which are then written to permanent storage for the offline-analyses.

The data recorded by the CDF II detector are centrally stored at Fermilab. The size of these data is still manageable and physicists can copy samples of recorded or simulated events to their home institutes and analyze the data locally.

Due to the higher center-of-mass energy and due to the larger number of detector read-out channels the event size for data recorded by the CMS detector is significantly larger compared to CDF II data. In order to deal with this huge amount of data from the four LHC experiments a globally distributed model for data storage and analysis has been installed. This computing and data Grid is provided by a global collaboration of more than 1,700 computing centers in 34 countries. The computing centers are organized in three layers, called tiers, each dedicated to special tasks like data storage, data processing, or data analysis.
Rather than analyzing data locally, physicists in the CMS collaboration submit analysis jobs to the Grid, which then are executed at one of the computing centers, that store the data to be analyzed.

Chapter 3

Generation, Simulation, and Reconstruction of Events

The elementary hard interactions between partons of colliding hadrons resulting in the production of new elementary particles can be described within the SM using perturbation theory. However, annihilation or fusion of partons and production of other elementary particles like top-antitop quark pairs is not the whole story. A typical $t\bar{t}$ event for example results in the production of about 1,000 outgoing particles due to additional radiation and the process of hadronization and decay. In the end, most of these particles are observed as electronic signals in chambers, calorimeters, or the tracking devices of particle detectors.
The aim of each physics analysis is to reconstruct and identify as good as possible the elementary hard interaction and the particles produced therein. Therefore the electronic detector signals have to be translated into a deduced setup of charged tracks or neutral energy depositions and then further assigned to physics objects like electrons and muons, or jets originating from quarks and gluons.
In order to estimate efficiencies and acceptances of analysis algorithms and to compare kinematic distributions of reconstructed objects with theory predictions, physicists make use of simulated events. The hard process and the evolution of the generated particles in simulated events is provided by event generators. The response of the detector and the interaction of particles with the material and the magnetic field inside the detector are simulated using dedicated detector simulations. Finally, this procedure leads to the same signatures as real data - electronic signals in the detector. Simulated and observed events share therefore exactly the same data format with the one crucial difference, that in each generated and simulated event the true information of the elementary hard interaction is accessible.
In the following sections the generation of events, the simulation of the detector response, and the reconstruction of physics objects from detector signals is described.

3.1 Event Generation

The purpose of event generators is to provide simulated events in the same form, with the same average behavior, and with the same fluctuations as real data. The fluctuations in observed data arise from the quantum mechanical character of nature. Due to this property of nature it is not possible to predict exactly what will happen in each single event. Only when averaging over a large sample of events the expected probability distributions are observed. In order to emulate this effect, Monte Carlo (MC) techniques are used, which make choices based on random numbers according to the desired probability distributions at various stages of the generation process. The structure of events in high energy collisions is complex and not predictable from first principle. Event generators exploit the fact that a generic hard process can be factorized into several components, roughly corresponding to increasing scales of distance and time. Therefore, the generation of events is subdivided into several steps which are carried out subsequently.

Elementary Hard Process

The generation of an event starts with the calculation of the cross section of the elementary hard process to be simulated. The compoundness of the colliding particles (protons or antiprotons in the case of hadron colliders) is taken into account by folding the partonic cross section with the PDFs of the incoming particles, for an example see equation 1.7.

Inital- and Final-State Radiation

In every elementary process containing colored or electrically charged objects in the initial or final state, additional radiation of gluons or photons can occur, leading to possibly large corrections to the event topology of the hard process. Among the different MC event generators exist two approaches to either compute or estimate the effects of these higher-order corrections in perturbation theory.

In the matrix-element method the matrix elements of hard processes with a given number of additional emissions are calculated at leading order, taking into account the exact kinematics and the full interference and helicity structure of the process. Since a perturbative treatment of these calculations is only possible for large momentum transfers, where α_s is small, only diagrams corresponding to real emissions, i.e. radiation of hard gluons, are taken into account.

In the second approach, known as the parton-shower method, the higher order effects, leading to additional jets in the event, are simulated by combining an arbitrary number of branchings of single partons into two or more other partons. In this method not the full matrix element expression but only approximations derived by simplifying the kinematics, interference, and helicity structure, are used. Thus, it is possible to model multiple jets final-states without an explicit upper limit on the number of partons involved. Initial-state showers in the parton-shower approach are modeled within the backward-evolution scheme. For this purpose, evolved PDFs are

used, which already include the inclusive effects of initial-state radiation. Starting from the incoming parton the showers are then traced backwards in time to the shower initiators.

Both approaches are complementary in many respects. While the parton-shower method yields good descriptions of relatively soft gluon emission and therefore substructures of jets, it has limited predictive power for the rate of well-separated jets resulting from hard gluon radiation. At higher energy scales the perturbative expansion is better behaved due to the running of α_s. For this reason matrix-element methods yield more reliable results for inclusive measurements such as the rate of well-separated jets. Since in analyses with multijet final-states often both aspects are of interest, it has become essential to properly combine the two approaches in order to describe the whole phase space as good as possible. To avoid double counting of the same final-state configurations, either arising from the matrix-element method or the parton-shower approach, a proper matching between the two becomes necessary.

At this stage of the generation of an event its final state consists of partons, more precisely of leptons and bare quarks and gluons. The evolution of the colored partons into colorless hadrons is carried out in the next step of event generation, called either hadronization or fragmentation[1].

Hadronization and Fragmentation

QCD describes the world of quarks and gluons, but experimentally accessible are only colorless hadrons. Due to the asymptotic freedom, the short distance strong interactions at high momentum transfer can be well described within QCD perturbation theory. But at long distances and low momentum transfer, where α_s becomes large, perturbation theory breaks down. Thus, there exists no firm theoretical understanding of the mechanism of confinement, that transfers colored partons into colorless hadrons. Different phenomenological models exist for the description of this process, the two most prominent ones are the models of string fragmentation and cluster fragmentation.

In the string fragmentation model, also referred to as Lund string model [113, 114], color flux tubes are stretched between final-state quarks and antiquarks moving apart from their common production vertex. The potential energy stored in these strings increases as quark and antiquark move apart and can be converted into new quark-antiquark pairs. By this the system splits into two color-singlet systems, i.e. colorless hadrons. Further breaking of strings can occur as long as the invariant mass of resulting string pieces is large enough.

The second approach, the cluster fragmentation-model [115], exploits a special property of perturbative QCD, the so-called preconfinement [116]. Although perturbative QCD cannot provide information on the confinement mechanism itself, it neverthe-

[1] Hadronization and fragmentation are often used as synonyms in the literature to describe the formation of hadrons. Sometimes hadronization is being defined as the combination of fragmentation and the subsequent decay of unstable particles.

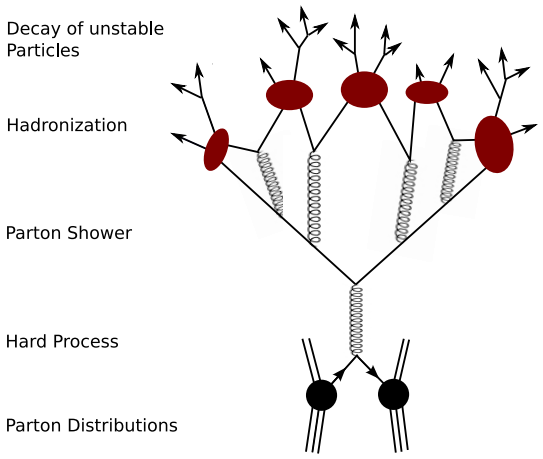

Figure 3.1: Illustration of the different steps of the event generation, exemplarily depicted for an event generated with a parton shower event generator using a cluster hadronization-model.

less predicts that the process of hadron formation depends only on the local structure of the parton system and is independent of the hard elementary process and its energy scale. The perturbative phase of parton cascade development leads at its end in a natural way to the clustering of partons generated in the branching process. This tendency of partons which are close in color to be also close in phase space and to become therefore arranged in color-singlet clusters is called preconfinement. Long range correlations are strongly suppressed and the fragmentation acts only on these color-singlet clusters, which subsequently decay into hadrons.
Exploiting this property, in the cluster fragmentation model all secondary gluons from the perturbative parton branching are split non-perturbatively into quark-antiquark pairs resulting in color-singlet clusters. These clusters are then considered as the basic units out of which hadrons arise in this model. Depending on their invariant mass, clusters are fragmented into one, two, or more hadrons.

Decay of Unstable Particles

Many of the particles produced in the fragmentation process are unstable and subsequently decay into observable particles. In MC generators the decay of unstable particles follows the rules of branching ratios and decay modes, which are implemented into the programs. The decay products are hadrons, leptons, and photons. Depending on the actual decay package used in the event generator, spin information of the decay is preserved or not.

In addition to these four steps, schematically summarized in figure 3.1, event generation programs account also for effects due to additional hadron collisions in the same bunch crossing and due to the underlying event structure. The latter is generated by including beam remnants and the interactions of the other partons from the initial particle not partaking in the elementary hard process.

3.1.1 Monte-Carlo Event-Generators

One distinguishes between two kinds of MC event generators. Matrix-element event-generators like Alpgen [117] or MadGraph/MadEvent [118] generally do not include the modelling of hadronization, thus their final states consist of leptons, quarks, and gluons. In order to generate realistic events, these generators have to be interfaced with one of the MC generators from the second group, the parton showering and hadronization event generators like Pythia [119] or Herwig [120]. As already mentioned, parton showering by one of the parton shower and hadronization generators gives a good description of soft parton emissions, while for the description of hard, well-separated emissions, matrix-element event-generators perform better. In order to combine these two descriptions, it is essential to perform a proper matching between the two that avoids double counting of emissions in overlapping regions of phase space. The most common matching schemes available are the CKKW algorithm [121] and the MLM scheme [122]. In the following the generators relevant for this thesis are briefly introduced.

Alpgen

Alpgen is dedicated to the study of multiparton hard processes in hadronic collisions with emphasis on final states with large numbers of jets. The code performs an exact calculation of the partonic matrix elements at leading order in perturbation theory for a large set of QCD and electroweak processes. Together with the generated events the full color and flavor structure of each event is provided, enabling the evolution of partons into fully hadronized states by passing the events to a shower and hadronization generator.

MadGraph/MadEvent

The second widely used matrix-element event-generator is MadEvent, which comes together with the matrix-element generator MadGraph. MadGraph produces Feynman diagrams for the desired process and subroutines that compute the squared amplitudes of the diagrams. MadGraph can manage processes with up to eight final state partons. The calculated matrix elements and phase-space mappings for the integration over the phase space are then passed to the actual event generator, MadEvent. For a realistic description of the desired process the obtained events have to be passed to a shower and hadronization generator.

Pythia

Pythia is a general purpose event generator for the description of collisions at high energies between elementary particles such as e^+, e^-, p, and $\bar{p}$ in various combinations. It contains theory and models for a number of physics aspects, including hard and soft interactions, parton distributions, initial- and final-state parton-showers, multiple interactions, fragmentation and decay. For the treatment of the hadronization process the Lund string model is implemented. The program is largely based

on original research, but also borrows many formulae and other knowledge from the literature. Due to the used string fragmentation model, PYTHIA features a large number of parameters and as a result of this, several tunes of the program exist, each optimized to model a certain aspect of collision data.

Herwig

HERWIG is a general-purpose event-generator for high-energy hadronic processes which includes the simulation of hard lepton-lepton, lepton-hadron and hadron-hadron scattering and soft hadron-hadron collisions in one package. Particular emphasis is thereby put on the detailed simulation of QCD parton showers. Therefore, HERWIG uses the parton-shower approach for initial state and final state QCD radiation, including color coherence effects and azimuthal correlations both within and between jets. In contrast to PYTHIA, HERWIG uses a cluster model for jet hadronization via non-perturbative gluon splitting, and a similar cluster model for soft and underlying hadronic events.

3.2 Detector Simulation

So far, the generated events describe the desired processes on the particle level, only defined by the initial conditions like the kind of the colliding particles and the center-of-mass energy. In particular, they are independent from the detector, with which they are to be observed.
In order to be able to compare generated events with observed events, the interaction of the different outgoing particles with the detector material and its magnetic field have to be simulated as well as the response of the different detector subsystems. A commonly used tool for this purpose is the GEANT (Geometry And Tracking) package [123], which provides a rich set of physics processes to model the electromagnetic and hadronic interactions of particles with matter within a magnetic field. Interactions of particles with material like energy loss through ionization, multiple scattering, bremsstrahlung, and electromagnetic and hadronic showering are simulated based on MC methods. As input for the detector simulation not only precise knowledge of the used material is essential, but also a detailed description of the detector geometry is needed. The latter provides the simulation program with information on the sensitive parts of the detector as well as on support structures and cabling material.

For the simulation of particles traversing the CDF II detector, GEANT3 together with several special packages is used. The drift chamber simulation package GARFIELD [124] for the simulation of the COT and the shower development program GFLASH [125] for the simulation of the calorimeter response complete the simulation software.

In the CMS collaboration two approaches are pursued in order to satisfy the need for a detailed detector description on the one hand and fast detector simulation on

the other hand. In the full simulation, the GEANT4 package is used to generate simulated hits in the subdetectors being traversed by the generated particles. The interaction of the initial outgoing particles with the detector material can result in a large number of secondary particles. Depending on the actual number the detector simulation can be very time consuming. Therefore, an alternative approach called fast simulation (FastSim) has been developed, in which large numbers of events can be simulated on reasonable time scales. The reason for the lower computing time lies in several simplifying assumptions, parametrizations, and optimized algorithms on the cost of a lower accuracy compared to the full GEANT4 simulation.

3.3 Event Reconstruction

While the generation and simulation of events tries to model the evolution of outgoing partons from the initial hard process into particles and finally into electronic signals in the detector, the reconstruction of an event aims the opposite direction. Starting from the electronic signals from all subdetectors, physics objects are reconstructed in several steps aiming at a full reconstruction and understanding of the elementary hard process. In a first step electronic signals are converted into detector objects like charged particle tracks in the tracking system and clusters of deposited energy in the calorimeters. In a second step these objects are further associated with physics objects candidates. As described in section 1.2.2, the basic components of $t\bar{t}$ events, that need to be reconstructed, are electrons, muons, jets, and neutrinos. Consequently, the following description of the event reconstruction at CDF II and CMS is focussed on these objects.

3.3.1 Charged Particle Tracking

Charged particles traversing the tracking volume of a particle detector leave distinct signals in the tracking devices along their trajectories. To reconstruct the trajectory of a charged particle, these measure points have to be combined in the correct way. Inside homogeneous magnetic fields, charged particles move on helicoidal trajectories, with the curvature of the trajectory depending on the electric charge and the momentum of the particle. Therefore, the precise reconstruction of the trajectory is essential for the determination of the particle's charge and momentum.

Track Reconstruction at CDF II

The CDF II tracking system, described in section 2.2.1, consists of two main subsystems featuring different technologies. While the COT is a gaseous detector, the inner tracker is based on silicon technology. As a result, individual tracking methods have to be used for each of the two subsystems.
Compared to the inner tracker, the radial distance from the beamline and the volume of the COT are larger and the COT therefore exhibits a lower occupancy.

Furthermore, tracks in the COT are more isolated, which results in less ambiguities and clearer allocations. For these reasons, the default track reconstruction [126] at CDF II starts in the COT. One of the two algorithms employed for COT tracking finds trajectories by reconstructing and linking track segments in the COT superlayers. Another approach starts with one segment in the outer superlayer and the expected position of the beamline as a constraint. The trajectory in this approach is found iteratively based on single hits. Track reconstruction in the COT is only possible for particles that have traversed at least half of the COT in radial direction and therefore restricted to the region $|\eta| \leq 1.6$.
After a COT track has been reconstructed, in a second step information from the inner tracker is added. In this so-called outside-in tracking, COT tracks are used as seeds and are extrapolated into the silicon detectors, adding subsequently axial and stereo silicon hits to the trajectory. This approach however is limited by the COT geometry and can provide tracking with a high efficiency only in the central region up to $|\eta| = 1.0$.
The tracking efficiency of the outside-in approach decreases dramatically in the region $1.0 \leq |\eta| \leq 1.6$. Two additional tracking strategies have therefore been developed to increase the angular range in which tracking is possible with reasonable efficiencies.
Silicon-standalone tracking provides track reconstruction outside the acceptance of the COT up to the angular coverage of the silicon tracker of $|\eta| \leq 2$. In contrast to the outside-in method, COT tracks cannot be used as seeds for the hit search. Therefore, silicon-only seeds have to serve as starting points for the trajectory reconstruction. These seed tracks are formed from two 3D hits in the silicon and the position of the beam axis. The 3D hits are constructed combining axial and stereo hits on the same detector.
In order to address cases in which the charged particle traversed the COT only partially and which are not covered by the default outside-in algorithm, another method, the so-called inside-out tracking [127] is used. In this algorithm, tracks reconstructed with the silicon-standalone algorithm are used as seeds to define search roads for hits within the COT. From hits found on that road a COT track is fitted by using silicon-track information as constraints. In the end, the silicon hits are refitted using the new COT track. The parameters from this fit define then the inside-out track.

Track Reconstruction at CMS

In contrast to CDF's outside-in approach (with additional strategies to enlarge the trackable region with silicon-standalone and inside-out tracking), an inside-out approach is realized for the CMS track reconstruction [128]. Furthermore, since the CMS tracking system is constructed in an all-silicon design, pixel and strip detector can be treated as one single tracking system. Consequently, only one method is used for the reconstruction of tracks in the whole tracking volume.
In this method, tracks are grown from the first pixel layers to the outer layers of the silicon-strip detector. In the first step, starting points for possible track candi-

dates, called seeds, are searched using information from both the pixel and the strip detector. In a second step, trajectories are constructed from a given seed, layer to layer using a combinatorial Kalman filter [129]. On each new layer, new trajectories are constructed with updated parameters for each compatible hit in the layer. In addition, at each layer also one further trajectory is created explicitly not using a measured hit, to account for the possibility that the particle did not leave any hit on that layer. The procedure is repeated until the outermost layer is reached. In this treatment each seed usually results in a large number of trajectory candidates. These hit assignment ambiguities are resolved by selecting a subset of compatible candidates, based on the number of hits shared by the trajectories and the track quality. Tracks are removed if there is another track, sharing at least half of the hits, with more hits in total or if the number of hits is equal, yielding a smaller χ^2 in the fit. In the end, after construction and cleaning of the trajectories, a final global fit is performed, using all measurement points associated to the track. The whole procedure of combinatorial track finding and global fitting is repeated in an iterative approach for multiple times. At each iteration the hits used by the previous iteration are removed from consideration and the algorithm runs again with progressively looser settings.

Reconstruction of the Primary Vertex

In any physics analysis, knowledge of the exact position of the primary interaction point of the hard elementary process is essential in order to determine the kinematics of the event. Because of the finite dimensions of the hadron bunches and the interaction region of two bunches, the location of the point of the elementary hard interaction varies event by event and thus has to be determined for each event individually. The primary vertex of an event is found by associating tracks satisfying certain quality criteria to a common point of origin and finding the best estimate for the vertex parameters for the given tracks.

3.3.2 Reconstruction of Electrons

The reconstruction of electron candidates uses information of the tracking system and of the electromagnetic calorimeter. In principle one has to match a reconstructed track in the tracking system to a localized energy deposit in the electromagnetic calorimeter. While at CDF II, electrons are reconstructed in this way, the reconstruction of electron candidates at CMS is a bit more complicated [130].
The CMS tracker is completely based on semiconductor technology and therefore contains larger amounts of material than gaseous tracking detectors as for example CDF's COT. The bulk of tracker material in the CMS detector ranges from 0.4 to 1.6 radiation lengths, depending on η. In the presence of a strong magnetic field and such large amounts of material, electrons loose a considerable fraction of their energy through bremsstrahlung. Since the direction of the bremsstrahlung photons does in general not coincide with the electron's ϕ direction, the energy of the electron reaches the ECAL with a significant spread in ϕ. To account for this in

the reconstruction of electron candidates, first special clusters of clusters, so-called superclusters, have to be formed. Starting from these superclusters, two hits in the tracker have to be found acting as seeds for possible electron trajectory candidates. This procedure is called supercluster-driven pixel-seed finding. The energy loss through bremsstrahlung leads to non-Gaussian contributions to event-by-event fluctuations of calorimetry and tracking measurements. Therefore, not only the clustering of energy is different for the electron reconstruction but also the seeding and building of tracks has to be done by dedicated algorithms which can deal in a better way with the non-Gaussian fluctuations. Also the final fit of the trajectories is different compared to the default CMS track reconstruction and relies on a dedicated Gaussian sum filter (GSF) [131, 132] and a specific energy loss modeling. The GSF is a non-linear generalization of the Kalman filter with weighted sums of Gaussians instead of a single Gaussian.

3.3.3 Reconstruction of Muons

Offline reconstruction of muons in its basic form requires a track in the tracking system that matches to a signal in the muon system. Since muons traverse the detector as minimum ionizing particles and therefore loose only little of their energy in the calorimeters, information from this detector component is not used.
In the CDF II muon reconstruction at least three collinear hits in the four layer muon chambers are fitted to a so-called stub, which is then in a second step matched with the nearest track reconstructed in the tracker volume. The momentum of the muon candidate is exclusively derived from the trajectory.
At CMS, two different approaches to identify and reconstruct muon candidates exist. Since muons are typically the only particles reaching the muon chambers, a standalone muon reconstruction can be obtained by using only information from the muon system. Starting with the track segments detected in the innermost muon chamber, a Kalman filter method subsequently uses additional measurements from neighbouring layers. Finally, the muon tracks are propagated back towards the interaction point.
Another procedure uses these standalone muons as starting point and combines them in the global tracking approach with tracker information. The muon trajectory extrapolated towards the interaction point is compared with observed hits in the tracker system. The final track fit yields then global muons. While in general, information on the muon momentum is mainly taken from the measurement in the tracker, at CMS additional information from the global track is taken into account. This leads to an improved momentum resolution, especially for high energy muon candidates with $p_{\mathrm{T}} > 200\,\mathrm{GeV}/c$. The decreasing curvature of high-energy muons leads to a decreasing tracker performance in the momentum resolution. This can be partially compensated by exploiting the large lever arms of the CMS muon system and the magnetic field between tracker and muon system.

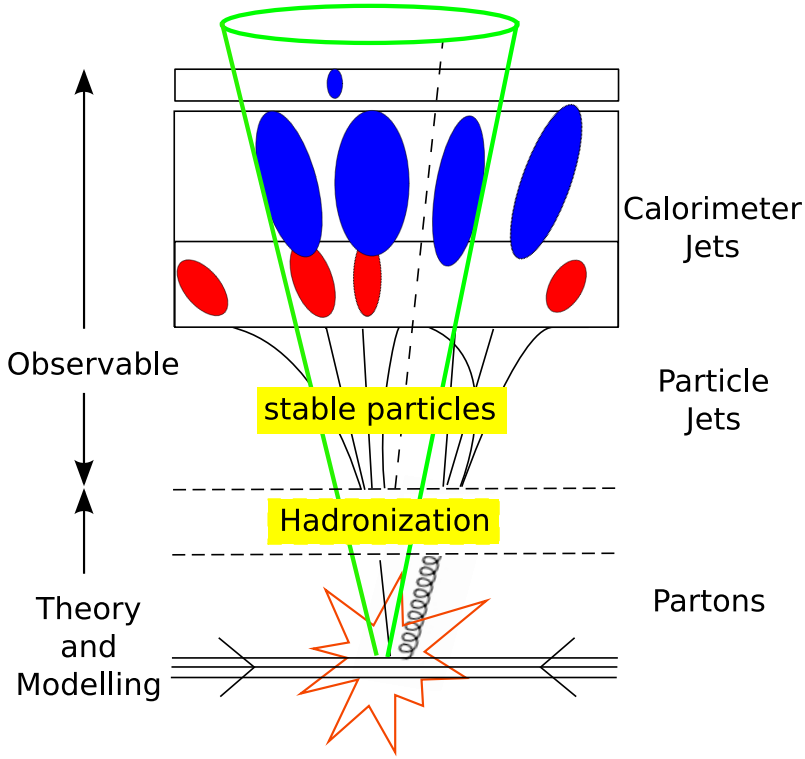

Figure 3.2: Schematic picture of the process of hadronization and the formation of jets. The red and blue ellipses indicate energy deposits in the electromagnetic and hadronic calorimeter, respectively. The aim of cone clustering algorithms is to define jets as dominant directions of energy flow.

3.3.4 Reconstruction of Jets

Colored partons underly the confinement principle of QCD and therefore hadronize and fragment into collimated streams of color-neutral particles, called particle jets. A particle jet thus is the cluster of all particles originating from the same initial elementary outgoing parton. These jets appear in the detector in the form of energy deposits in the electromagnetic and hadronic calorimeter as footprints of the non-observable partons. This evolution from the hard parton interaction to the energy deposits in the calorimeters is schematically depicted in figure 3.2.
The energy of a calorimeter jet is calculated as the unweighted sum of the energy deposits in the electromagnetic and hadronic calorimeter towers using jet cluster algorithms. The electromagnetic and hadronic calorimeter of the CDF II detector share the same tower geometry and thus calorimeter towers simply consist of one combined electromagnetic and hadronic tower. In contrast to this, in the CMS detector each HCAL cell corresponds to 5×5 crystals of the ECAL.
From the experimental point of view a jet is defined by the used clustering algorithm and its parameters and by the applied recombination scheme, the way how the constituents are added to form the four-vector of the jet.

Jet Clustering Algorithms

Each commonly used jet cluster algorithm falls in one of the two categories: successive recombination algorithms and cone algorithms.

Algorithms based on successive recombination work by defining a distance between any pair of objects and a beam distance for each object. If the smallest distance in the event is a beam distance, the corresponding object is defined as a jet and is removed from the event. Otherwise the two objects with the minimal distance are recombined into a single one. The procedure is repeated until no objects are left in the event. Well-known examples of this family of jet cluster algorithms are the k_{T} [133], the anti-k_{T} [134], and the Cambridge/Aachen [135, 136] algorithm. The only difference between the three is the actual definition of the distances.

Cone algorithms define jets as dominant directions of energy flow and therefore construct jets as the sum of all particles within a stable cone of given radius $R = \sqrt{(\Delta\eta)^2 + (\Delta\phi)^2}$ in the $\eta - \phi$ plane. The radius used varies between different analyses and experiments. In the CDF II top-quark physics-group it is common to use a radius of 0.4, while the CMS top-quark physics-group agreed upon 0.5 as default cone size. Since in the analyses presented in this thesis, jets are clustered using cone algorithms, this method is described in more detail.
A simple cone-based algorithm is the so-called iterative cone algorithm. In this algorithm first all calorimeter towers or particles with $E_{\mathrm{T}} > 1\,\mathrm{GeV}$ are considered as seeds for the iterative search for stable cones. Starting with the highest-E_{T} seed tower, adjacent seed towers within a cone of radius R are grouped together to form preclusters, such that each seed tower is assigned to exactly one precluster and each precluster consists at least of one seed tower. The search for stable cones starts with the calculation of the E_{T} weighted centroid of each precluster. In the next step clusters are formed which contain all towers above a certain threshold in E_{T} within a cone of radius R around the centroid. For these clusters the centroid is recalculated and new clusters are formed. This procedure is repeated iteratively until the tower list of each cluster is stable, meaning that the geometric center of the cluster corresponds to the cluster centroid within a certain tolerance. Since stable cones might overlap, they cannot be directly defined as jets. Two different techniques for the solution of this overlapping problem exist.
JetClu [137], the iterative cone algorithm used in CDF II analyses, performs a so called split-merge procedure on all overlapping stable cones. If all towers of a cone are completely contained within a second one, the smaller of the two clusters is dropped. In case of partially overlapping cones, an overlap fraction is computed as the E_{T} sum of the shared towers divided by the total E_{T} of the smaller cluster. If the overlap fraction surpasses a certain threshold, the two clusters are merged. Otherwise the towers in the overlap region are assigned to the cluster with the nearest centroid in the $\eta - \phi$ space.
The CMS iterative cone algorithm [138] uses a method called progressive removal to overcome the problem of overlapping stable cones. In this approach the stable cone search is started from the hardest seed in the event. Once this cone is found to be stable, it is defined as jet and all its constituents are removed from the event. Based

on the remaining objects, and using the remaining hardest seed as starting point, the next stable cone in the event is searched. This procedure is repeated until all objects have been clustered.
Two important and desired features of jet cluster algorithms are collinear safety and infrared safety. Collinear safety is achieved when the outcome of a clustering procedure remains unchanged if the energy carried by a single particle is instead distributed among two collinear particles. The result of jet finding is infrared safe, if it is stable against the addition of soft partons. However, since in both described cone algorithms the search for stable cones is based on seeds with some thresholds on the energy of the seed candidates, they are by construction not collinear safe. Furthermore, they are also not infrared safe.
A solution to this problem is to search for all stable cones in the event without using seeds and afterwards run a split-merge procedure on all stable cones found. Since the input sets for a seedless stable cone search can be very large, advanced approaches had to be developed in order to avoid exponential rising computing times. The Seedles Infrared-Safe Cone (SisCone) algorithm [139] has implemented such an advanced procedure to reduce the actual number of cones that have to be checked for stability. This is achieved by exploiting the fact that each circle enclosing a set of at least two given input objects can be moved around without changing the enclosure content until two points lie on its boundary. Conversely, considering every cone whose boundary is defined by a pair of points in the input set and in addition considering all four possible permutations of the edge points being contained or not in the enclosure, leads to the identification of all distinct circular enclosures. Then only these cones have to be tested for stability. Using this approach, one has a practical infrared and collinear safe cone algorithm at hand.

Recombination Scheme

When the jet clustering algorithm is terminated, one of the several different recombination schemes is applied to the N calorimeter towers which are clustered to the jet, in order to define the final jet kinematics. Rather than using the stable cone variables directly, which are usually calculated as the E_{T} weighted sum over all jet constituents, at CDF II and CMS the so-called scheme E is applied to calculate the four-vector of the jet. This method is also called four-vector recombination. The N calorimeter towers comprising the jet are treated as massless pseudo particles defined by their energy and geometrical position. These four-vectors are then combined to yield the final four vector of the reconstructed jet:

$$p_{\mathrm{jet}} = (E_{\mathrm{jet}}, \vec{p}_{\mathrm{jet}}) = \sum_{i=1}^{N} (E^i, p_x^i, p_y^i, p_z^i), \quad \text{with} \quad |\vec{p}_{\mathrm{jet}}| = E_{\mathrm{jet}} \ . \tag{3.1}$$

For the CDF II analysis described in chapter 4, jets clustered with the JetClu iterative cone algorithm with a radius of 0.4 and an energy threshold for calorimeter towers of 100 MeV have been used. The CMS study presented in chapter 5 has been carried out using jets defined by the SisCone algorithm with a cone size of 0.5 and

an energy threshold for calorimeter towers of 300 MeV. In both analyses the jet four-vectors are obtained using the recombination scheme E.

Jet Energy Corrections

In many physics analyses, the determination of the four-momenta of quarks produced in the hard interaction is essential. Therefore, one is often more interested in the energy and momentum of partons than in that of jets. With the adequate corrections one can link the measured properties of calorimeter jets like momentum and energy to the underlying parton. In principle the procedure of jet energy corrections tries to reverse the process of hadronization and formation of jets, as it is visualized in figure 3.2. Starting from jet energies measured as energy deposits in the calorimeters and clustered to calorimeter jets they are corrected for instrumental effects as well as for radiation and fragmentation effects.
The corrections can be factorized into sequentially applied steps, often referred to as Levels, each considering a certain effect. Jet energy correction at CDF II [98] and CMS [140] are very similar and differences arise mainly in the additional corrections described in the end of this paragraph.
The first three corrections aim to cover all instrumental effects and correct for any nonlinearity and inefficiency in the calorimeter response.

Relative Correction / η Dependence: Due to different responses of the different calorimeter subsystems and due to inefficiencies arising at the edges of the subsystems and in uninstrumented regions, the response of the calorimeters is not uniform in η. The purpose of this correction is to remove these variations and to ensure a homogeneous response over the entire angular region.

Correction for Multiple Interactions: At high luminosities more than one interaction between incoming hadrons occurs in the same bunch crossing. The average number of collisions per bunch crossing is currently about six at the Tevatron and up to 20 at the LHC in the high luminosity run. These extra interactions increase the measured jet energies if their final state hadrons overlap with the ones from the primary interaction. Their average contribution therefore needs to be subtracted from the jet energy.

Absolute Correction / p_{T} Dependence: The absolute jet energy correction aims to transform the measured jet energy, corrected with the first two corrections, into the energy corresponding to the underlying particle jet. The calorimeter response to a particle jet is smaller than unity and varies as a function of the particle jet p_{T}. Therefore the absolute correction is p_{T} dependent and is designed to remove these variations and make the response equal to unity on average at all p_{T}.

The energy scale of jets after these three correction steps (referred to as Level 1, Level 4, and Level 5 at CDF; and as Level 1 – Level 3 at CMS) is that of particle

jets corrected for all instrumental effects and therefore independent from the experimental setup.
In a second set of additional jet energy corrections, the energy of the particle jet is corrected further in order to determine the energy of the initial parent parton. This is relevant in analyses where one is interested in the four-vectors of the partons from the hard scattering. For this purpose in CDF II analyses two optional corrections, referred to as Level 6 and Level 7, can be applied:

Correction for Underlying Event: Particles from initial-state gluon-radiation or particles from spectator partons with color connection to the other partons of the proton can contribute to the particle jet of the parton from the hard interaction. The contributions of these underlying events are thought to be uncorrelated with the direction of the outgoing parton and almost independent of the jet energy. The additional energy is subtracted from the particle jet energy in this correction step.

Correction for Out-of-Cone Effects: On the other hand, a substantial fraction of the parton energy can also be lost from the jet cone due to final-state gluon-radiation at large angles with respect to the parent parton. Another reason for this energy loss are particles escaping in the process of fragmentation or due to the small curvature radius of low p_{T} particles in the magnetic field. These effects are correlated with the direction and energy of the primary jet and are expected to decrease with increasing distance from the jet core. In this correction step the energy, which is lost on average due to the described effects, is added to the jet energy.

For CMS analyses also additional optional corrections exist, which correct for the response dependence on the electromagnetic fraction of jets, the flavor dependence of the response, and effects due to the underlying event. Finally, a MC based correction can be applied to take the jet back to the corresponding parent parton. However, in the CMS study described in this thesis those additional corrections have not been applied, since it is assumed that they will not be available for early analyses.

3.3.5 Identification of *b* Jets

In the challenge of classifying event topologies and to select certain processes, it is often useful to separate reconstructed jets into two categories: jets originating from light quarks and gluons and jets originating from b quarks. This categorization can for example be exploited in the selection of $t\bar{t}$ events. Due to the large value of V_{tb} these events typically feature two jets originating from b quarks.
Outgoing b quarks hadronize into B hadrons, which usually carry most of the large transverse momentum of the b quarks in $t\bar{t}$ events. Since hadrons containing b quarks decay only via the electroweak interaction, they have a considerable long lifetime of about 1.6 ps. Therefore they travel typically an observable distance L_{xy} in the transverse plane of several millimetres before they decay.

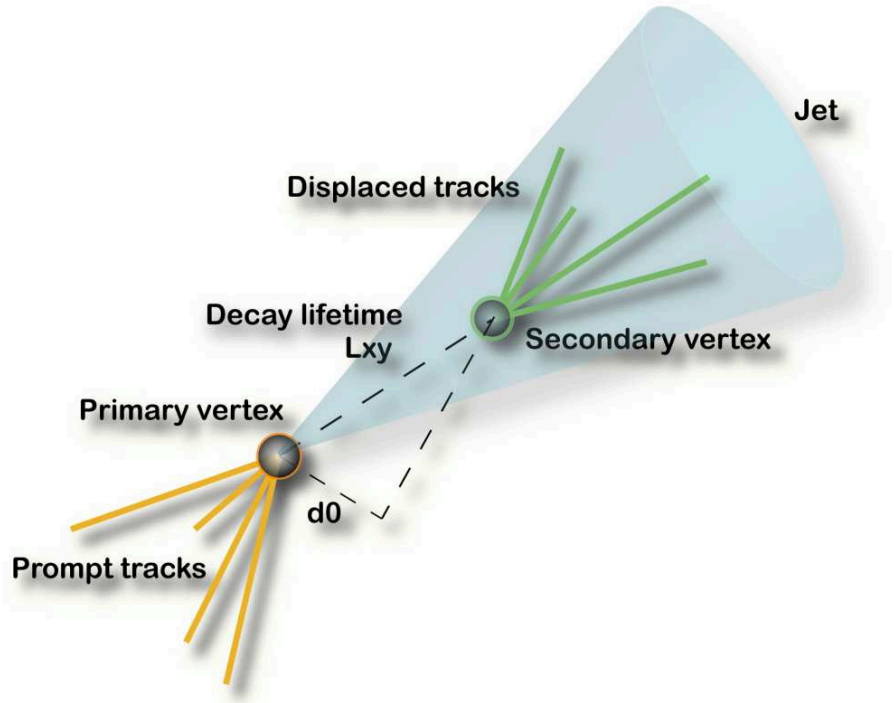

Figure 3.3: Schematic view of a secondary vertex with displacement L_{xy} and an impact parameter d_0 of one of the tracks drawn in.

This property of B hadrons is exploited at CDF by the Secondary Vertex (SecVtx) algorithm [141], which relies on the displacement of secondary vertices relative to the primary interaction vertex of the event to identify B hadron decays. The SecVtx algorithm looks for tracks within each jet cone of an event, that do not match to the primary vertex of the event but intersect in a secondary, displaced vertex. Only tracks fulfilling several quality criteria are used as input for SecVtx to reduce the contribution from poorly reconstructed tracks. Since at least two tracks are needed for the reconstruction of a vertex, only jets with at least two good tracks are defined taggable. Once a secondary vertex is found, the two dimensional distance between primary and secondary vertex in the $r-\phi$ plane projected on the momentum vector of the secondary vertex, L_{xy}, is calculated. To be identified as b jet (often also referred to as b tagged jet) the significance $\frac{L_{xy}}{\sigma(L_{xy})}$ of the displacement has to equal or exceed the threshold of 7.5. Figure 3.3 gives a schematic view of a secondary vertex.

In addition to algorithms searching for secondary vertices, several other b jet identification algorithms exist at CDF and CMS exploiting different properties of B hadrons and their decay, like the presence of soft charged leptons in b jets or the large invariant mass of b jets compared to light quark jets. More sophisticated approaches combine several discriminating quantities to classify the flavor of the parent partons of jets, see for example [142].

3.3.6 Reconstruction of Neutrinos

Neutrinos interact only weakly with matter and can therefore not be observed directly in particle detectors. At hadron colliders a suitable quantity from which their presence can instead be inferred is the total transverse momentum of an event. Since the hard interaction occurs between partons carrying only a fraction of the hadron's momentum, only the transverse part of the momentum of the initial state is known to be zero, while the third component is unknown. Due to momentum conservation any imbalance in the vector sum of all measured transverse momenta of an event can be attributed to the presence of neutrinos that carry away momentum undetected. In practice one uses information from the calorimeters and vectorially sums all transverse energy deposits in the calorimeters rather than determine the transverse momenta of all particles in the event. Thus the energy imbalance in the transverse plane, called missing transverse energy ($\vec{\not{E}}_{\mathrm{T}}$), is defined as

$$\vec{\not{E}}_{\mathrm{T}} = -\sum_i E_{\mathrm{T}}^i \hat{n}_i \ , \tag{3.2}$$

where $\hat{n}_i$ is a unit vector perpendicular to the beam axis and pointing at the i^{th} calorimeter tower. It is useful to also define the magnitude of this vector $\not{E}_{\mathrm{T}} = |\vec{\not{E}}_{\mathrm{T}}|$. Once $\vec{\not{E}}_{\mathrm{T}}$ is calculated, several corrections have to be applied for towers associated with objects for which energy corrections are known. For example the jet energy corrections that are applied to jets are subtracted vectorially from $\vec{\not{E}}_{\mathrm{T}}$.
Muons traverse the detector as minimum ionizing particles and therefore deposit only a small fraction of their energy in the calorimeters. Thus they carry away $\vec{p}_{\mathrm{T}}$ undetected by the calorimeter system, which would lead to a substantial contribution to missing transverse energy. In order to account for this, the p_{T} of identified muons has to be added to the sum of all transverse energies in the event. To avoid double counting, the small transverse energy contribution resulting from the little but non-zero energy loss of muons in the calorimeters has to be subtracted from the sum in equation 3.2.

The reconstructed electron, muon, and jet candidates have to pass several additional quality criteria in order to be associated with a prompt electron or muon or with a jet from the hard process. Depending on the experiment and the individual analysis, the definition of what is considered a good electron, good muon, or good jet and therefore the criteria the candidates have to pass can vary. The individual requirements applied in each of the two analyses presented in this thesis are described in the chapters 4.1.2 and 5.1.3.

Chapter 4

Measurement of the W-Boson Helicity-Fractions in $t\bar{t}$ Events

Since the discovery of $t\bar{t}$ production at the Tevatron, dedicated procedures have been developed and established to select highly $t\bar{t}$ enriched datasets out of the huge number of interactions. Together with the steadily increasing integrated luminosity and the therefore increasing number of $t\bar{t}$ candidate events this enables physicists not only to confirm the existence of top quarks but also to measure their properties. The subject of the analysis described in this chapter is the measurement of one top-quark property, namely the helicity fractions of W bosons in top-quark decays. This measurement is performed utilizing the distribution of the cosine of the decay angle θ^*. It is defined as the angle between the momentum of the charged lepton in the rest frame of the W boson and the direction of motion of the W boson in the top-quark rest-frame. Its distribution is highly sensitive to the couplings at the Wtb vertex and therefore to the helicity of the produced W boson.
The analysis is based on data collected by the CDF II detector between 2002 and 2007 corresponding to an integrated luminosity of $1.9\,\mathrm{fb}^{-1}$. This translates roughly to 10^{14} inelastic interactions, out of which a highly $t\bar{t}$ enriched dataset of 484 events is selected. For each selected event the angle θ^* is reconstructed and the $\cos\theta^*$ distribution for the whole dataset is obtained. The event-selection efficiency and the resolution of the event reconstruction have to be taken into account for the correct interpretation of the obtained distribution.
In this chapter the selection of $t\bar{t}$ candidate events, the full kinematic reconstruction of these events, and the extraction of the W-boson helicity-fractions from the observed $\cos\theta^*$ distribution are described.

4.1 Event Selection and Background Estimation

The analysis is carried out in the lepton+jets channel, where lepton in this case refers to an electron or muon or the corresponding antiparticles. This channel provides not only a clear experimental signature, which leads to a good signal to background ratio,

but also allows for a full reconstruction of the kinematics of the involved partons. In this step the angle θ^* which is essential for the whole analysis can be calculated. In the following the selection criteria that are applied on the recorded events in order to select $t\bar{t}$ events in the lepton+jets channel are described. It is impossible to extract a 100% pure signal sample and there will always remain background contributions of processes that exhibit the same experimental signature as the signal. In order to account for this, a proper estimation of the individual background contributions and a proper modelling of their kinematics is crucial.

4.1.1 Analyzed Data Samples

The selection of lepton+jets events starts already during data taking in the CDF II trigger system. One prominent feature of lepton+jets events is the appearance of a high-energy charged lepton. Therefore only events passing one of the Level 3 high-p_{T} lepton-triggers are considered.
Central electrons have to pass the `ELECTRON_CENTRAL18` trigger, which requires a reconstructed COT track with $p_{\mathrm{T}} > 9\,\mathrm{GeV}/c$ that matches an energy deposit with $E_{\mathrm{T}} > 18\,\mathrm{GeV}$ in the CEM. Muons have to pass either the `MUON_CMUP18` trigger or the `MUON_CMX18` trigger. The main muon trigger requirements are a reconstructed COT track with $p_{\mathrm{T}} > 18\,\mathrm{GeV}/c$ and a matching signal in the corresponding detector component, i.e. a signal in both the CMU and CMP for the `MUON_CMUP18` trigger and a signal in the CMX for the `MUON_CMX18` trigger. Depending on the fired trigger, the events are stored in different trigger streams. All events passing one of the high-p_{T} lepton-triggers end up in the same trigger stream.
Collected data are reprocessed offline before being analyzed by the different physics groups. During the reprocessing the calibrations which were used online are checked and corrected, the silicon alignment is corrected, tracks are refit, cluster energies are checked, and the lepton candidates are identified. Also special algorithms identifying jets and searching for secondary vertices are run. According to the passed trigger, the reprocessed events are further stripped into different datasets. The *bhel* samples contain central electron trigger data and the *bhmu* samples contain events triggered by one of the muon triggers.
Each Tevatron store is usually divided into several cycles of CDF II data taking, which are called runs. A run typically ends when a detector subsystem fails, making full read-out temporarily impossible. Each run is examined both online and offline to verify the quality of the recorded data. Depending on the physics topic of the analysis, the impeccable operation of different detector components during the run is essential. Therefore several so-called goodrun lists exist containing all runs determined to be usable for the given requirements. For the analysis described in this chapter, a fully functional tracking system, calorimetry, and muon system are required.
Data taken from February 2002 to May 2007 are used in this analysis. The recorded events are divided into several subsamples corresponding to different data taking periods and trigger-lepton types. These subsamples are summarized in table 4.1 together with their run range and the corresponding integrated luminosity. The

Period	Run range	Name	$\int Ldt$ [pb^{-1}]	
			CEM/CMUP	CMX
0	138,425 – 186,598	bhel0d, bhmu0d	331	318
1-4	190,697 – 203,799	bhel0h, bhmu0h	363	360
5-7	203,819 – 212,133	bhel0i, bhmu0i	258	258
8	217,990 – 222,426	bhel0i, bhmu0i	166	166
9	222,529 – 228,596	bhel0i, bhmu0i	157	153
10	228,644 – 233,111	bhel0j, bhmu0j	243	243
11	233,133 – 237,795	bhel0j, bhmu0j	235	230
12	237,845 – 241,664	bhel0j, bhmu0j	162	155
Total	138,425 – 241,664		1,915	1,883

Table 4.1: Summary of the analyzed CDF II datasets with period, run range, sample name, and integrated luminosity in the different subsystems for each sample.

latter has been calculated using the goodrun list v18 [143], which includes all runs in the run range corresponding to the analyzed data satisfying the requirements mentioned above. The luminosities are quoted separately for the CEM/CMUP and the CMX, where in some periods due to a temporarily not fully functional CMX, the luminosity is slightly lower. In total the analyzed dataset corresponds on average to an integrated luminosity of $1.9 \pm 0.1\,\text{fb}^{-1}$.

4.1.2 Event Selection

The final state of a $t\bar{t}$ event in the lepton+jets channel is composed of two b quarks from the decaying top quarks, one charged lepton and one neutrino from the leptonically decaying W boson, and two light quarks due to the hadronically decaying W boson[1]. The experimental signature of such an event thus consists of one isolated high-p_T lepton, substantial missing transverse energy, and four jets. These kinematic features are exploited by the common CDF II lepton+jets event selection, which is briefly described in the following.

Lepton Requirements

The electron or muon candidates from the offline reconstruction described in section 3.3 have to pass several additional identification criteria before they can be classified as a physics object considered in the analysis.
Central electrons with a track-p_T greater than $10\,\text{GeV}/c$ and a matching energy deposit of $E_\text{T} > 20\,\text{GeV}$ in the CEM are called CEM electrons. The ratio of energy

[1] Actually, the final state is composed of a b quark and a $\bar{b}$ quark and, depending on whether the top quark or the antitop quark decays semileptonically, a charged lepton of positive or negative charge and a corresponding neutrino or antineutrino. For the sake of simplicity the terms b quark, top quark, electron, muon, and neutrino are used as umbrella terms for particles and antiparticles.

deposited in the hadronic calorimeter to the energy deposited in the electromagnetic calorimeter has to be smaller than $E_{\mathrm{had}}/E_{\mathrm{lep}} < 0.055 + 0.00045 \cdot E/\mathrm{GeV}$. In addition, the lateral shower profile in the calorimeter must be compatible with those obtained from electron test-beam data. Electrons detected in the forward calorimeter PEM are called Phoenix (PHX) electrons. They are required to have $E_{\mathrm{T}} > 20\,\mathrm{GeV}$ and $E_{\mathrm{had}}/E_{\mathrm{lep}} < 0.05$. In addition a track reconstructed from at least three silicon hits pointing to the primary vertex is required.
Since muons are not stopped in the calorimeters, their energy cannot be measured directly. Instead a transverse momentum of $p_{\mathrm{T}} > 20\,\mathrm{GeV}/c$ is required. Central muon candidates have to be detected either in the CMX or simultaneously in the CMU and in the CMP. The latter are named CMUP muons. Muons leaving a stub in the forward muon chamber BMU are called BMU muons.
Finally, the lepton candidates have to be isolated. A lepton candidate is considered isolated if the E_{T} not assigned to the lepton in a cone of $R = 0.4$ centered around the lepton track is less than 10% of the electron's (muon's) E_{T} (p_{T}).

Lepton candidates fulfilling these criteria are called tight leptons. In the analysis described the lepton selection is further restricted to central leptons. Thus only events are considered that contain tight CEM electrons or tight CMX or CMUP muons. Nevertheless, the tight forward lepton categories (PHX and BMU) are still considered in the dilepton veto.

Jet Requirements

Jets are clustered with the JetClu algorithm with a cone size of $R = 0.4$. Energy deposits associated with any reconstructed charged lepton are not considered in the clustering. The reconstructed jets have to lie within the tracker acceptance $|\eta| < 2.0$, since only in this range b tagging is possible. The transverse jet energy corrected up to Level 5 (absolute energy correction) has to be larger than 20 GeV. Due to the four quarks in the final state of a lepton+jets $t\bar{t}$ event at least four jets passing these selection criteria have to be present in the event. Given the possibility of additional jets from initial- or final-state radiation the maximal number of jets in the event is not restricted to exactly four jets. Furthermore, since one expects two b quarks from the two top-quark decays, at least one of the selected jets has to be tagged as b jet by the SecVtx algorithm.

Neutrino / Missing Transverse Energy Requirements

The missing transverse energy in the event is corrected for muons and for all Level 5 corrected jets with $p_{\mathrm{T}} > 12\,\mathrm{GeV}/c$ and $|\eta| < 2.4$. The corrected value has to exceed 20 GeV, otherwise the event is rejected.

Beyond these identification criteria, applied to the physics objects candidates, additional requirements on the whole event are imposed in order to improve the purity of the selected dataset and to suppress background contributions.

$\int Ldt = 1.9\,\mathrm{fb}^{-1}$	Charged lepton type			All
Sample	CEM	CMUP	CMX	lepton types
$N_{b-\mathrm{tag}} = 1$	206	111	49	366
$N_{b-\mathrm{tag}} > 1$	71	28	19	118
$N_{b-\mathrm{tag}} \geq 1$	277	139	68	**484**

Table 4.2: $t\bar{t}$ candidate events passing the described lepton+jets event selection. The numbers are given separately for the three different tight lepton types and the number of b tags in the event.

Conversion Veto

Electron events are rejected if the electron forms a common vertex with an additional nearby high-p_{T} track of opposite curvature, since this electron is likely to stem from a conversion of a photon into an e^+e^- pair.

Cosmic Muon Veto

Events in which the reconstructed tight muon is a cosmic muon are rejected by exploiting the characteristic track timing and topology of these muons. Further reduction of cosmic muon events is achieved through the requirement of a small impact parameter of the muon track.

Dilepton Veto

Exactly one tight charged lepton is required and events with additional non-isolated or loose leptons are rejected. Loose leptons are lepton candidates that either pass not all selection criteria or that are detected in a subsystem that is not linked to a tight lepton type. For example muons detected in the CMU or CMP solely fall in this category.

Cut on the Distance of the Lepton from the Primary Vertex

In order to ensure that the high-energy charged lepton comes from the primary vertex, the distance between the intersection of the lepton trajectory with the beam axis z_0 and the z position of the primary vertex has to be smaller than 5 cm. Furthermore, the z position of the primary vertex is required to be less than 60 cm away from the nominal interaction point at $z = 0$.

Z-Boson Veto

All events in which the tight lepton and a second more loosely defined object can be paired to form an invariant mass M within a window around the Z-boson mass, are rejected to reduce the contribution from Z-boson events. The mass window is defined as $76\,\mathrm{GeV}/c^2 \leq M \leq 106\,\mathrm{GeV}/c^2$.

Table 4.2 summarizes the number of events passing the lepton+jets event selection. The numbers are given separately for the different types of tight leptons and the number of b tagged jets in the event. In total, 484 $t\bar{t}$ candidate events are selected in the dataset corresponding to an integrated luminosity of $1.9\,\mathrm{fb}^{-1}$.

4.1.3 Signal Modelling

Samples of simulated collision events are indispensable ingredients for each high-energy particle-physics analysis. Since in this analysis a property of top quarks is measured, especially the proper simulation of signal events is crucial. A large $t\bar{t}$ signal MC sample containing 4.8 million events generated with Pythia is used for this purpose. The W-boson helicity-fractions in this sample are consistent with the SM predictions of 70% longitudinally polarized W bosons and 30% left-handed W bosons.

In order to test the sensitivity of the measurement method on helicity fractions deviating from the SM prediction it is also crucial to generate samples which exhibit non-SM values for F_0, F_-, and F_+. Two different generators have been used for this purpose.
A set of samples has been generated with Ggwig, a modified version of Herwig, in which the fraction of events with left-handed, right-handed, or longitudinally polarized W bosons can be specified. During the decay of the top quark the angles between the top quark and its decay products are determined according to the implemented probability distribution. This is also done for the angle θ^*, which obeys the distribution given by

$$F(\cos\theta^*) = F_0 \cdot \frac{3}{4}(1-\cos^2\theta^*) + F_- \cdot \frac{3}{8}(1-\cos\theta^*)^2 + F_+ \cdot \frac{3}{8}(1+\cos\theta^*)^2 \ . \quad (4.1)$$

Equation 4.1 is a composition of the three distributions each corresponding to one of the possible W-boson helicity-states. Arbitrary proportions of the W-boson helicity-fractions can be generated directly by changing the parameters F_0, F_-, and F_+ to the desired values. Averaging over the whole sample the obtained $\cos\theta^*$ distribution reflects then exactly the adjusted input distribution used in the top-quark decay.
Another set of samples has been generated using MadGraph/MadEvent, where one can alter the structure of the top-quark decay from first principle by changing explicitly the form factors f_1^L and f_1^R in the Wtb vertex. By this, only the physics of the top-quark decay are affected, the subsequent decay of the W boson follows the rules of the $V-A$ structure of the SM weak interaction. In contrast to the event generation with Ggwig, in which the $\cos\theta^*$ distribution is altered by manipulating the distribution itself, in the MadGraph/MadEvent samples the $\cos\theta^*$ distribution is changed as an implication of the altered Wtb vertex structure. The parameters f_1^L and f_1^R have only influence on the transverse fractions F_+ and F_-, the fraction of longitudinally polarized W bosons F_0 remains constant. Consequently, only the relative proportion between F_+ and F_- can be modified and the relation $\frac{F_+}{F_-} = \left(\frac{f_1^R}{f_1^L}\right)^2$ can be used for the proper adjustment of f_1^R and f_1^L to yield

the desired proportions. This relation can be derived from equations 1.41 and 1.42 and by assuming that f_2^L and f_2^R vanish.

For the generation of the SM signal MC sample as well as for the generation of the dedicated helicity samples a top-quark mass of $175\,\mathrm{GeV}/c^2$ has been used. A detailed list of all used signal MC samples can be found in appendix A.1.

4.1.4 Background Modelling

The dataset obtained by applying the described selection criteria is still contaminated with background events that mimic the experimental signature of $t\bar{t}$ events. These non-$t\bar{t}$ processes can be divided into four main groups. The largest fraction are events with W-boson production in association with the production of additional jets (W+jets). Depending on the jet flavor, this contribution is further subdivided into two categories: W+jets events, in which the jets originate from b or c quarks (W+heavy flavor) and W+jets events with a falsely reconstructed secondary vertex (Mistags or W+light flavor). Another substantial background source are QCD multijet processes that contain no real W boson (non-W). Non-W events mimic the experimental signature of $t\bar{t}$ events either through a real high-energy lepton originating from a B hadron decay or through a jet faking a charged isolated electron in interplay with the appearance of artificial missing transverse energy. Although the probability for these events to survive the stringent event selection is very low, they still constitute a substantial background due to their huge cross section. Additional sources of background arise from electroweak processes like diboson production (WW, WZ, ZZ) and the production of single Z bosons or single top quarks. In order to model the shapes of differential distributions for background events, MC samples are used for all but the non-W background. The W+jets background processes have been simulated using Alpgen interfaced with Pythia. The diboson background samples as well as the single Z-boson production have been simulated using Pythia. For the generation of single top-quark events MadGraph/MadEvent interfaced with Pythia has been used. In order to model the background coming from non-W events, generic jet trigger data from the same periods of data taking as the analyzed electron and muon trigger data are used. In the jetele method the complete event selection but the lepton requirements is applied to these events. If an event contains a jet with $E_\mathrm{T} > 20\,\mathrm{GeV}$ and with an electromagnetic fraction between 0.8 and 0.95, this jet gets redefined as lepton and is taken out of the list of jets. The electromagnetic fraction of a jet is calculated by dividing the jet energy that is deposited in the electromagnetic calorimeter by the total jet energy. The charge is then randomly assigned to this jet-lepton. Since the b tag requirement would strongly reduce the number of events in the jetele sample, it is not applied and the b tag information is rather randomly assigned to one of the remaining taggable jets in the event. The proportions of single tagged and double tagged events are considered as well as the fractions of light quark jets and c- or b-quark jets. A list of all used background samples can be found in appendix A.2.

4.1.5 Background Estimation

The expected numbers of events for the different processes in the SecVtx tagged lepton+jets sample are determined using CDF II's so-called Method II. This method is based on the assumption that the only processes contributing to the selected dataset are $t\bar{t}$ signal, W+heavy flavor, W+light flavor, electroweak processes, and non-W processes. Sequentially the normalizations for the different contributions are determined. With this method the background contributions in both the pretag and the tagged dataset can be estimated. The pretag sample is the selected dataset before applying the b tag requirement in the event selection. For practical reasons it is useful to estimate first the background amount in the pretag sample and based on this the background contribution in the tagged sample.
In a first step the contributions of processes that are theoretically well understood are estimated in a MC based way. The number of expected events is calculated from the theoretical cross section of the process, the integrated luminosity, and efficiencies derived from MC studies. The production of top quarks and all electroweak processes fall into this category.
In the second step the contribution of QCD multijet events is estimated. These events contain no real W bosons and will therefore rarely have a high-p_{T} neutrino. As a result they exhibit a well discriminating $\not\!\!E_{\mathrm{T}}$ distribution peaking in the region of small values, which can be exploited for the estimation of the non-W contribution in the selected dataset. The $\not\!\!E_{\mathrm{T}}$ distribution, obtained by omitting the $\not\!\!E_{\mathrm{T}}$ cut in the event selection, is fitted using a MC template for $t\bar{t}$ signal, fixed to the assumed contribution, a MC template for W-boson production, and a non-W template derived from data. From the fit performed in the full range from 0 GeV to 120 GeV the fraction of non-W events in the signal region above 20 GeV is estimated.
The remaining contributions from W+jets events, either W+heavy flavor or W+light flavor, are determined in the pretag sample and subsequently in the tagged sample. First the numbers of predicted non-W, electroweak, and $t\bar{t}$ signal events in the pretag sample are subtracted from the total number of pretag events. The remaining number of events is multiplied with a MC derived heavy-flavor fraction factor $F_{\mathrm{h.f.}}$ and corrected with a correction factor K obtained from data. The resulting number is an estimate of the W+heavy flavor content in the pretag sample. To this estimate a tagging efficiency ϵ_{tag} is applied leading to the predicted contribution of W+heavy flavor events in the tagged lepton+jets sample

$$N^{\mathrm{tag}}_{W+\mathrm{h.f.}} = (N^{\mathrm{pretag}} - N^{\mathrm{pretag}}_{\mathrm{ewk}} - N^{\mathrm{pretag}}_{t\bar{t}} - N^{\mathrm{pretag}}_{\mathrm{non-W}}) \cdot F_{\mathrm{h.f.}} \cdot K \cdot \epsilon_{\mathrm{tag}} \ . \tag{4.2}$$

The amount of W+light flavor events in the pretag sample is obtained by subtracting all estimated contributions including the one for W+heavy flavor from the total number of pretag events. In the next step it is estimated how many of these W+light flavor events in the pretag sample get mistagged and thus survive the full lepton+jets event selection. For this purpose the pretag estimate for W+light flavor is multiplied with the predicted mistag rate in the pretag sample $N^{\mathrm{mistag}}/N^{\mathrm{pretag}}$

$$N^{\mathrm{tag}}_{W+\mathrm{l.f.}} = (N^{\mathrm{pretag}} - N^{\mathrm{pretag}}_{\mathrm{ewk}} - N^{\mathrm{pretag}}_{t\bar{t}} - N^{\mathrm{pretag}}_{\mathrm{non-W}} - N^{\mathrm{pretag}}_{W+\mathrm{h.f}}) \cdot \frac{N^{\mathrm{mistag}}}{N^{\mathrm{pretag}}} \ . \tag{4.3}$$

Background	$N_{b-\text{tag}} = 1$	$N_{b-\text{tag}} > 1$	total
W + heavy flavor	31.3 ± 12.8	4.2 ± 1.7	35.5 ± 14.5
Mistags	19.5 ± 4.6	0.4 ± 0.1	19.9 ± 4.7
non-W	18.4 ± 16.0	0.6 ± 3.0	19.0 ± 19.0
Electroweak	10.4 ± 1.0	1.7 ± 0.2	12.1 ± 1.2
Total background	79.6 ± 21.0	6.9 ± 3.5	86.5 ± 24.5
Observed events	366	118	484

Table 4.3: Expected number of background events and the number of observed events in the $1.9\,\text{fb}^{-1}$ data sample selected applying the selection criteria described in section 4.1.2.

The latter is derived from data using events with jets that have negative decay lengths [141]. This treatment is motivated by the fact that mistagged jets do not really originate from a B hadron. The reconstructed secondary vertex is only due to falsely reconstructed tracks that seem to cross each other in a displaced vertex. The distribution of the decay length of jets originating from light quarks with quasi-zero lifetime is found to be approximately symmetric around zero. Thus the fraction of jets with a non-physical negative decay length is at leading order a good estimate for the fraction of mistagged jets with a positive decay length. The probability for jets to have a negative decay length can be parametrized in a so-called mistag matrix which consists of several jet variables. The mistag matrix is obtained from a large jet-trigger sample and then applied to the selected lepton+jets pretag sample to obtain the estimate of mistagged W+light flavor events. The resulting estimate has to be corrected for the mistag contribution due to decays of long-living particles and due to nuclear interactions with the detector material.
Table 4.3 summarizes the background estimation for the four background categories in the selected sample in descending order. The numbers are given for events with one b tag, more than one b tag, and the total sample. Among the 484 observed events, 87 events are estimated to stem from background processes. Concerning $t\bar{t}$ events thus the purity of the selected data sample is about 82%.

4.1.6 Comparison between Data and Simulation

In order to validate the signal and background modelling, kinematic distributions of the physics objects selected in the lepton+jets event selection are compared to the corresponding distributions obtained from data. Figure 4.1 shows the E_{T} distributions of the four leading jets in descending order in E_{T}, the p_{T} distribution of the charged lepton, and the $\not\!\!E_{\text{T}}$ distribution. Figure 4.2 provides the η distributions of the four leading jets and the charged lepton. The background templates and the signal template are normalized according to their estimated contributions such that the combined template is normalized to the total number of observed events in the selected dataset. Within statistical fluctuations the distributions obtained from data and from the signal and background model show good agreement.

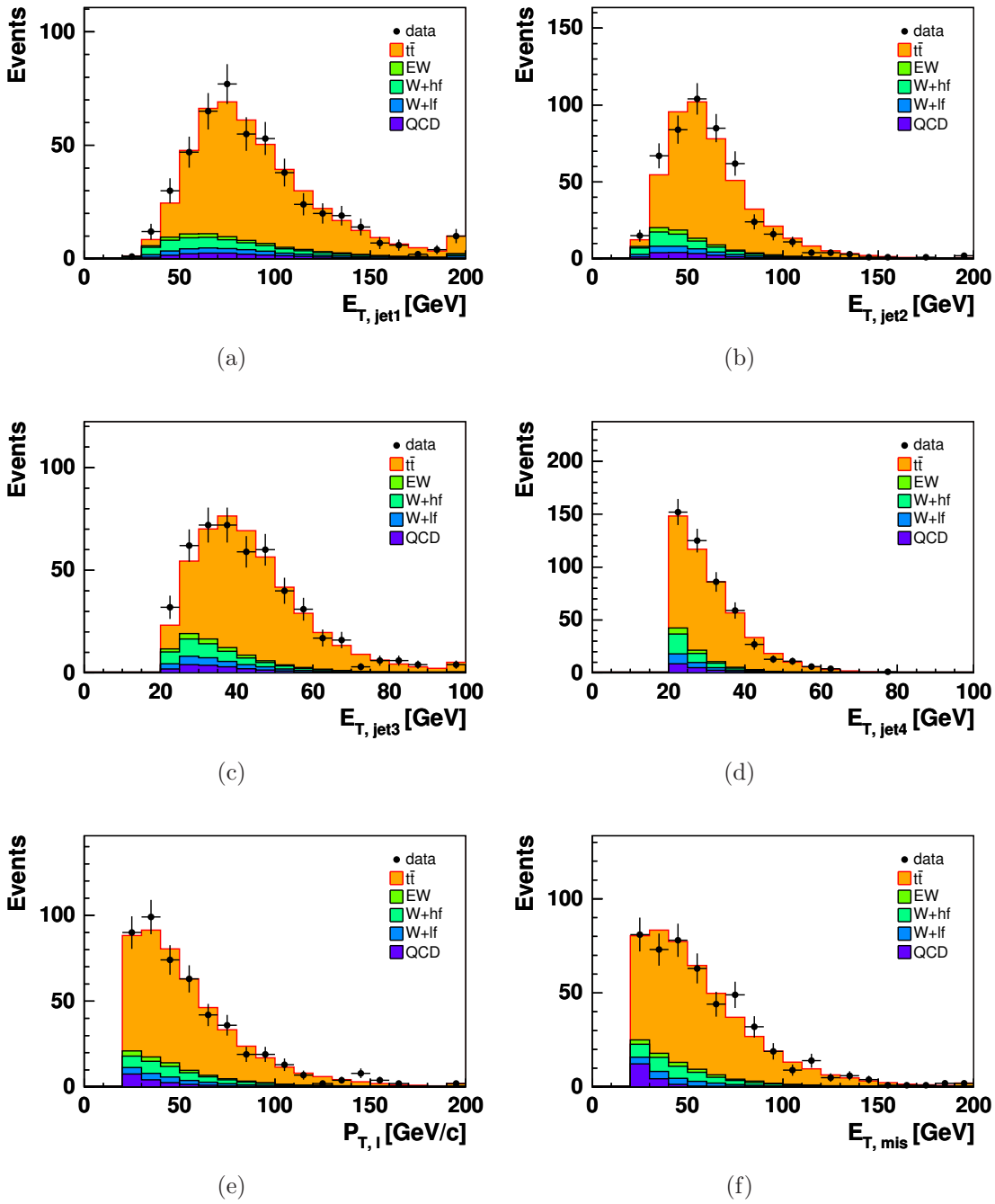

(a) (b) (c) (d) (e) (f)

Figure 4.1: Comparison of kinematic distributions obtained from data and from signal and background modelling: (a)–(d) the transverse energy of the four leading jets, (e) the transverse momentum of the charged lepton, and (f) the missing transverse energy.

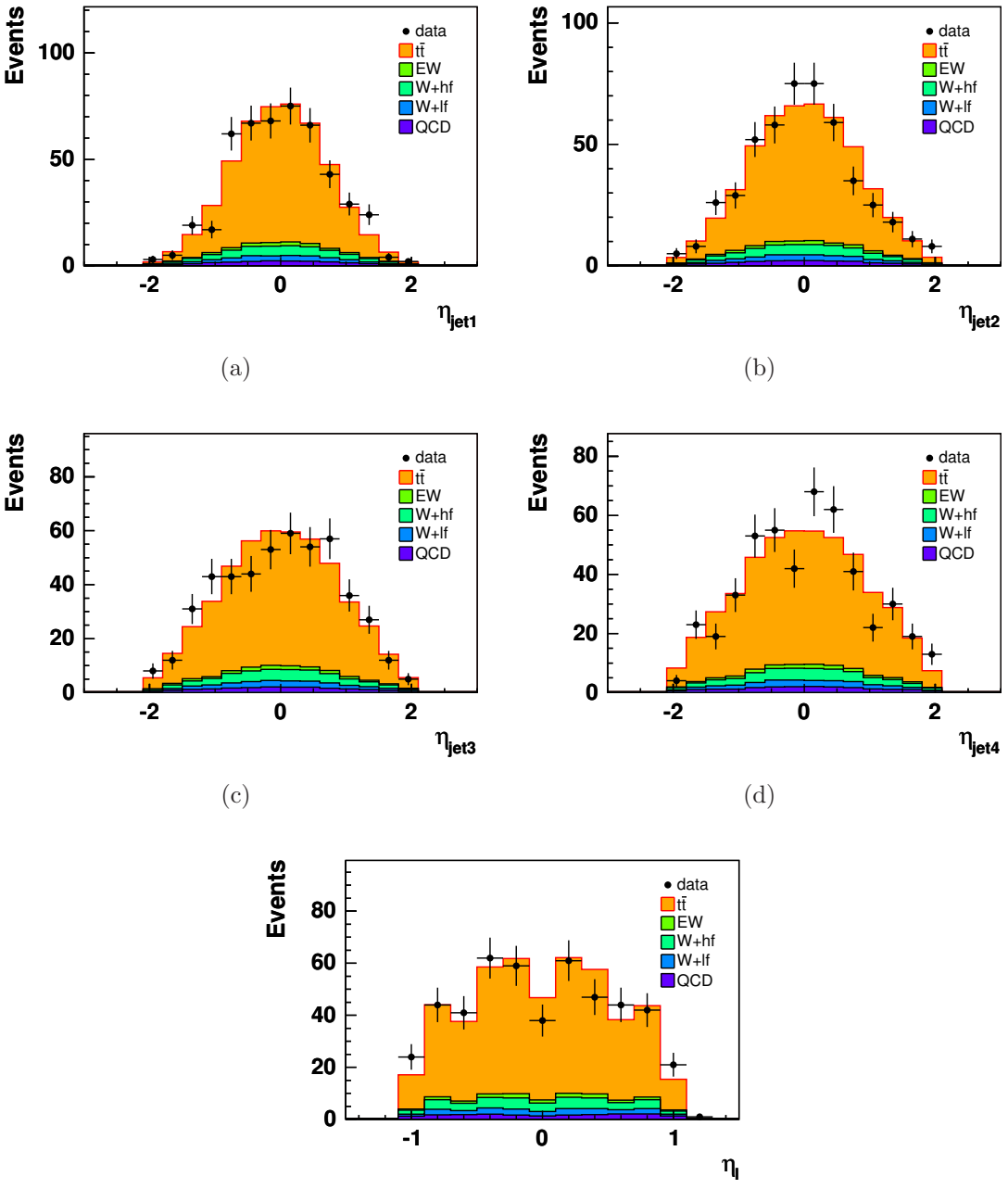

(a) (b) (c) (d) (e)

Figure 4.2: Comparison of the η distributions of (a)–(d) the four leading jets and (e) of the charged lepton from data and simulation.

4.2 Full Reconstruction of $t\bar{t}$ Candidate Events

As discussed in section 1.2.4 the basis of the whole analysis is the $\cos\theta^*$ distribution from $t\bar{t}$ events. In order to obtain this distribution the four-vectors of the involved particles are needed. Unlike the charged lepton, top quarks and W bosons cannot be observed directly and have therefore to be reconstructed from their observable decay products. But the assignment of the observed charged lepton, $\vec{\not{E}}_{\mathrm{T}}$, and jets to the decay products of W bosons and top quarks is not unambiguous. The different possibilities for each event to combine the measured objects to the desired W bosons and top quarks are called event hypotheses. Event by event a decision has to be made which event hypothesis to take in order to reconstruct as good as possible the underlying kinematics of the $t\bar{t}$ event. For this purpose a dedicated selection criterion is applied to all hypotheses of an event.
In the lepton+jets channel one top quark decays semileptonically, while the other top quark decays hadronically. Although the reconstruction of the leptonic leg of the $t\bar{t}$ decay would be sufficient for the purpose of this analysis, the reconstruction method is developed as full reconstruction of the complete $t\bar{t}$ kinematics. This offers a broad applicability of the method and it can therefore be used for any analysis in the lepton+jets channel that relies on four-vectors of top quarks and W bosons. The method described has for example already been adopted in an analysis measuring the forward-backward charge asymmetry in $t\bar{t}$ events [144].
The reconstruction and hypothesis selection algorithms are developed based on samples of simulated $t\bar{t}$ events and tuned to provide an optimal reconstruction of the kinematics of $t\bar{t}$ events. However, the selected dataset consists of $t\bar{t}$ candidate events with an estimated background contamination of about 18%. Nevertheless, all selected events are reconstructed under the assumption of a $t\bar{t}$ event. Thus, it has to made sure that the signal and background modelling describe well the kinematic distributions of reconstructed objects in the selected dataset. The method to reconstruct event hypotheses and to select one hypothesis for each event as well as the performance of this method are described in the following sections.

4.2.1 Reconstruction of Event Hypotheses

The observed objects serving as input for the reconstruction of the W bosons and top quarks are the charged lepton, the measured $\vec{\not{E}}_{\mathrm{T}}$, and the selected jets. Since the goal is an as accurate as possible determination of the four-vectors of quarks and bosons, the jets are further corrected to the parton level (Level 7 corrections). $\vec{\not{E}}_{\mathrm{T}}$ is corrected only up to Level 6 to avoid a double counting of the out-of-cone energy, for which the jets are already corrected. The four-vectors of these objects are successively recombined to W-boson and top-quark candidates considering all possible combinations.

Leptonically decaying W Boson: $W_{\mathrm{lep}} \to \ell\nu_\ell$

The reconstruction of the top-quark pair starts with the reconstruction of the W boson that decays into a charged lepton and a neutrino (W_{lep}). While the charged lepton is reconstructed almost perfectly, the neutrino can only be inferred from the reconstructed $\vec{\not{E}}_{\mathrm{T}}$. This treatment only defines the x and y component of the neutrino momentum and nothing is known about the z component. Considering the W boson to be on-shell, its pole mass $M_W = 80.4\,\mathrm{GeV}^2$ can be used as constraint to obtain an equation for the missing z component of the neutrino momentum (for a detailed derivation of this equation see appendix A.4):

$$p_{z,\nu}^2 - 2 \cdot \frac{\mu p_{z,\ell}}{E_\ell^2 - p_{z,\ell}^2} \cdot p_{z,\nu} + \frac{E_\ell^2 p_{\mathrm{T},\nu}^2 - \mu^2}{E_\ell^2 - p_{z,\ell}^2} = 0 \ , \tag{4.4}$$

$$\text{with } \mu = \frac{M_W^2}{2} + p_{\mathrm{T},\ell} p_{\mathrm{T},\nu} \cos\Delta\phi \ . \tag{4.5}$$

E_ℓ and $p_{z,\ell}$ denote the energy and the z component of the momentum of the charged lepton, respectively. The azimuthal angle difference between the charged lepton and $\vec{\not{E}}_{\mathrm{T}}$ is given by $\Delta\phi$. This equation is solved by

$$p_{z,\nu}^{\pm} = \frac{\mu p_{z,\ell}}{p_{\mathrm{T},\ell}} \pm \sqrt{\frac{\mu^2 p_{z,\ell}^2}{p_{\mathrm{T},\ell}^4} - \frac{E_\ell^2 p_{\mathrm{T},\nu}^2 - \mu^2}{p_{\mathrm{T},\ell}^2}} \ , \tag{4.6}$$

which yields two real solutions for most events, the so-called type I events. However, in about 30% of all events the radicand in equation 4.6 becomes negative and consequently the $p_{z,\nu}^{\pm}$ solutions become complex. Events with complex $p_{z,\nu}$ solutions are called type II events.
A closer look to the radicand in equation 4.6 reveals the reason for negative values:

$$\begin{aligned} & \frac{\mu^2 p_{z,\ell}^2}{p_{\mathrm{T},\ell}^4} - \frac{E_\ell^2 p_{\mathrm{T},\nu}^2 - \mu^2}{p_{\mathrm{T},\ell}^2} < 0 \\ \Leftrightarrow \quad & \mu^2 (p_{z,\ell}^2 + p_{\mathrm{T},\ell}^2) - E_\ell^2 p_{\mathrm{T},\ell}^2 p_{\mathrm{T},\nu}^2 < 0 \ . \end{aligned} \tag{4.7}$$

Equation 4.7 is obtained from the preceding by multiplying both sides with $p_{\mathrm{T},\ell}^4$. One can identify $p_{z,\ell}^2 + p_{\mathrm{T},\ell}^2$ in equation 4.7 with E_ℓ^2, which reduces the term to

$$\mu^2 < p_{\mathrm{T},\ell}^2 p_{\mathrm{T},\nu}^2 \ . \tag{4.8}$$

Taking the square root of this expression and replacing μ with equation 4.5 the conditions which lead to complex $p_{z,\nu}$ solutions become apparent:

$$\begin{aligned} M_W^2 &< 2 p_{\mathrm{T},\ell} p_{\mathrm{T},\nu} (1 - \cos\Delta\phi) \\ \Leftrightarrow \quad M_W &< \sqrt{2 p_{\mathrm{T},\ell} p_{\mathrm{T},\nu} (1 - \cos\Delta\phi)} \ . \end{aligned} \tag{4.9}$$

[2] For these calculations natural units with $c = 1$ are used for simplicity reasons.

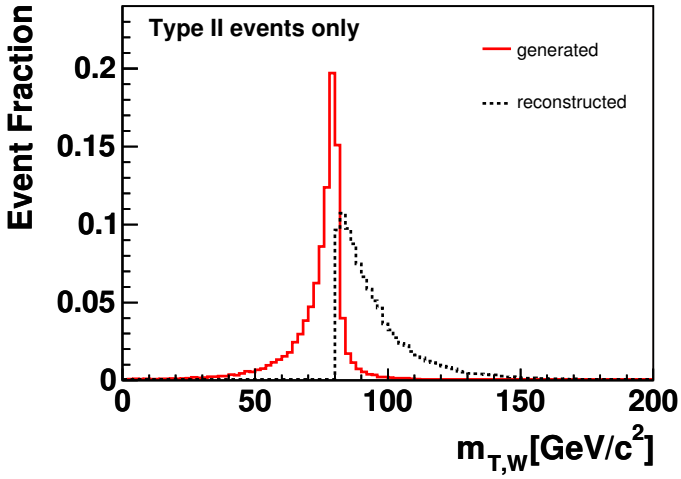

Figure 4.3: Generated and reconstructed transverse mass of the W boson for events of type II.

The right-hand side of equation 4.9 is the transverse mass of the W boson, which is defined as

$$\begin{aligned} m_{\mathrm{T},W} &= \sqrt{(p_{\mathrm{T},\ell} + p_{\mathrm{T}\nu})^2 - (p_{x,\ell} + p_{x,\nu})^2 - (p_{y,\ell} + p_{y,\nu})^2} \\ &= \sqrt{2(p_{\mathrm{T},\ell} p_{\mathrm{T}\nu} - p_{x,\ell} p_{x,\nu} - p_{y,\ell} p_{y,\nu})} \\ &= \sqrt{2 p_{\mathrm{T},\ell} p_{\mathrm{T},\nu} (1 - \cos\Delta\phi)} \ . \end{aligned} \tag{4.10}$$

The measured $m_{\mathrm{T},W}$ is obtained by inserting the measured momentum of the charged lepton and the measured $\vec{\not{E}}_{\mathrm{T}}$ and its x and y components into this equation.
In conclusion, the solutions for the neutrino-momentum z-component become complex, if the reconstructed transverse mass of the W boson exceeds the pole mass M_W. Equation 4.4 has been derived constraining the W-boson mass exactly to the pole mass and neglecting the finite width of the W-boson mass. As can be seen in figure 4.3, for all type II events the reconstructed $m_{\mathrm{T},W}$ is larger than $80.4\,\mathrm{GeV}/c^2$ while the generated $m_{\mathrm{T},W}$ distribution reaches its maximum at the pole mass and exceeds this value only in few events. Thus the finite width of the W boson cannot explain the reconstructed $m_{\mathrm{T},W}$ distribution of these events. The main reason for large reconstructed $m_{\mathrm{T},W}$ values is the imperfect resolution of the $\not{E}_{\mathrm{T}}$ measurement.

One way to handle complex solutions would be to take only the real part of the complex $p_{z,\nu}$ and neglect the imaginary part. But this solution then does no longer fulfill the initial assumption in equation 4.4 and therefore leads to reconstructed W-boson four-vectors that differ significantly from the generated ones.

In the approach developed in this analysis, events of type II are treated in a dedicated way. Under the assumption that the momentum of the charged lepton is measured precisely and that the deviations arise from mismeasured $\vec{\not{E}}_{\mathrm{T}}$ only, the idea of this method is to not directly link $\vec{\not{E}}_{\mathrm{T}}$ to $\vec{p}_{\mathrm{T},\nu}$. Instead its x and y component are modified

as minimal as possible such, that the resulting solution for the z component becomes real. The smallest modification that guaranties a real z solution is obtained for an exactly vanishing imaginary part and is achieved if $m_{\mathrm{T},W}$ equals $M_W = 80.4\,\mathrm{GeV}$. Requiring $m_{\mathrm{T},W} = M_W$ in equation 4.10 leads to a quadratic relation between the two transverse components $p_{x,\nu}$ and $p_{y,\nu}$. The solutions of the obtained quadratic equation are

$$p^{\pm}_{y,\nu}(p_{x,\nu}) = \frac{M_W^2 p_{y,\ell} + 2p_{x,\ell}p_{y,\ell}p_{x,\nu}}{2p_{x,\ell}^2} \pm \frac{M_W p_{T,\ell}}{2p_{x,\ell}^2}\sqrt{M_W^2 + 4p_{x,\ell}p_{x,\nu}}\ . \tag{4.11}$$

Nevertheless, it is assumed that the measured $\vec{\not{E}}_{\mathrm{T}}$ is at least roughly correct. In an iterative way the two components $p_{x,\nu}$ and $p_{y,\nu}$ are searched for, which are as close as possible to the measured values $\not{E}_{\mathrm{T},x}$ and $\not{E}_{\mathrm{T},y}$. For this purpose the distance δ between the current values of $p_{x,\nu}$ and $p_{y,\nu}$ and the measured $\not{E}_{\mathrm{T},x}$ and $\not{E}_{\mathrm{T},y}$ is defined:

$$\delta^{\pm}(p_{x,\nu}) = \sqrt{(p_{x,\nu} - \not{E}_{\mathrm{T},x})^2 + (p^{\pm}_{y,\nu}(p_{x,\nu}) - \not{E}_{\mathrm{T},y})^2}\ . \tag{4.12}$$

Since $p_{y,\nu}$ can be expressed as a function of $p_{x,\nu}$ the distance δ depends only on the free minimization parameter $p_{x,\nu}$. The latter is constrained to a range that avoids complex solutions for $p_{y,\nu}$. Due to the two possible values for $p^{\pm}_{y,\nu}(p_{x,\nu})$, two distance functions $\delta^{\pm}(p_{x,\nu})$ exist which are both minimized. After the minimization step the resulting $p_{x,\nu}$ and the $p^{\pm}_{y,\nu}$ yielding the $\delta^{\pm}(p_{x,\nu})$ with the smaller absolute value are used in order to keep the modified transverse momentum of the neutrino as close as possible to the measured $\vec{\not{E}}_{\mathrm{T}}$.
The final values for $p_{x,\nu}$ and $p_{y,\nu}$ satisfy the underlying assumption of the W-boson decay of equation 4.4 and the corresponding z component can be calculated. By construction the radicand vanishes, thus in events of type II only one single real solution for the z component of the neutrino momentum is found.

Figure 4.4 shows the distribution of the single components of the reconstructed neutrino momentum for events of type II for the two different methods of dealing with complex z solutions. The distributions are compared to the distributions obtained from the generated neutrino momenta. It can clearly be seen that the modified values describe the generated distributions much better than using the x and y component directly from $\vec{\not{E}}_{\mathrm{T}}$ and taking the real part of the complex z component. In addition, for each component also the distribution of the event-by-event difference between the generated and the reconstructed value is depicted. The modified x and y component are obviously closer to the true values than the pure $\vec{\not{E}}_{\mathrm{T}}$ components, while the event-by-event difference between the p_z of the generated and the reconstructed neutrino is nearly the same for the two methods described. Overall, the method of modifying x and y components yields a momentum vector with consistent components that satisfies the assumption of a neutrino stemming from a W-boson decay.
Figure 4.5 shows the relative difference between the measured $\not{E}_{\mathrm{T}}$ and the reconstructed $p_{\mathrm{T},\nu}$ using the modified values $p^{\mathrm{mod}}_{x,\nu}$ and $p^{\mathrm{mod}}_{y,\nu}$. The modified value is by construction always smaller than the measured value, thus in this treatment only a

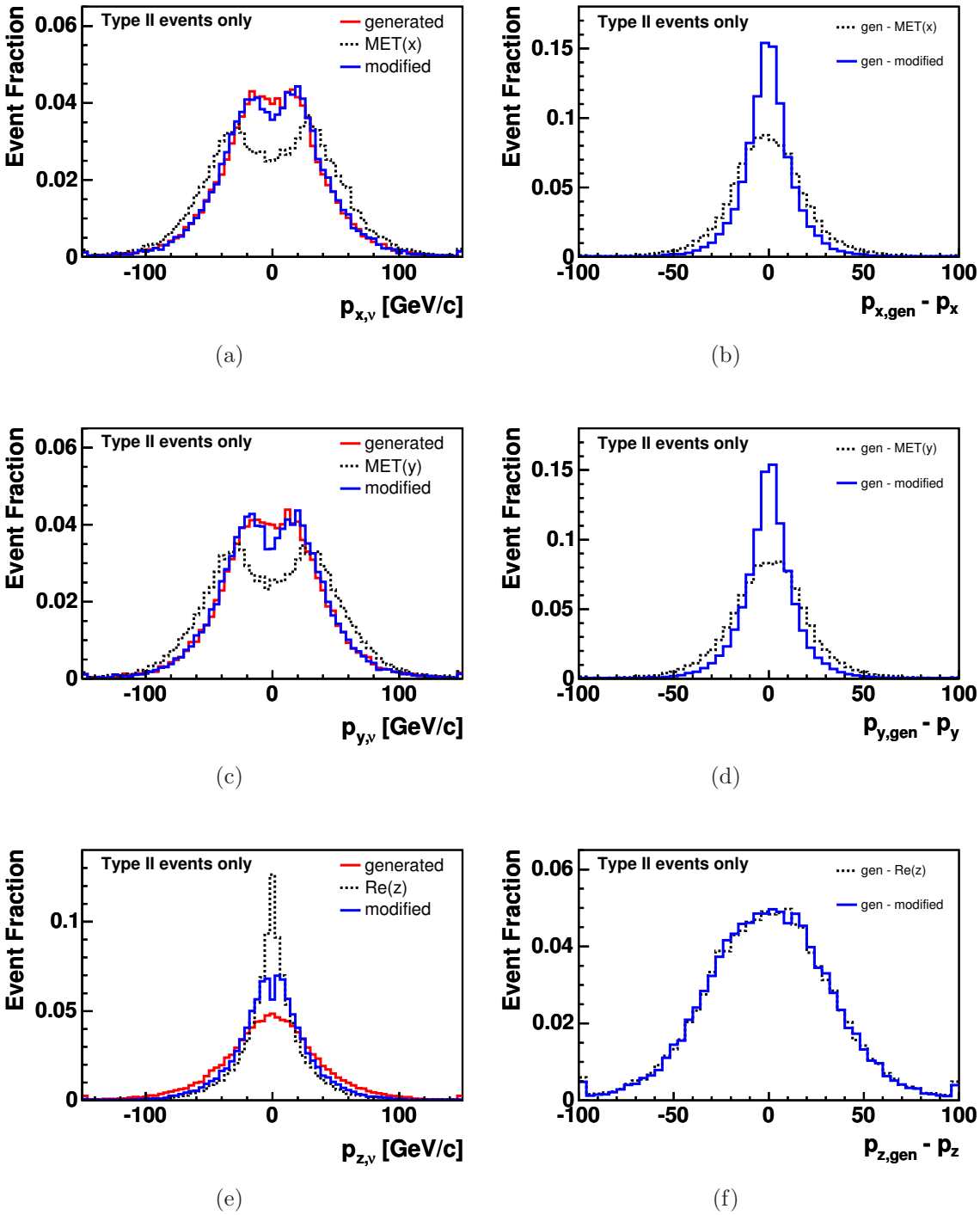

Figure 4.4: (a), (c), (e) Comparison between the components of the generated and reconstructed p_ν for type II events. In the latter case, both methods to reconstruct p_ν by either assigning $\vec{\not{E}}_{\mathrm{T},x}$ and $\vec{\not{E}}_{\mathrm{T},y}$ to $p_{x,\nu}$ and $p_{y,\nu}$ and taking the real part of the complex z solution $Re(z)$ or by modifying the measured $\vec{\not{E}}_{\mathrm{T}}$ to obtain a real $p_{z,\nu}$ solution are considered. The figures (b), (d), and (f) provide the distributions of the event-by-event difference between generated and reconstructed momentum component for the two reconstruction approaches.

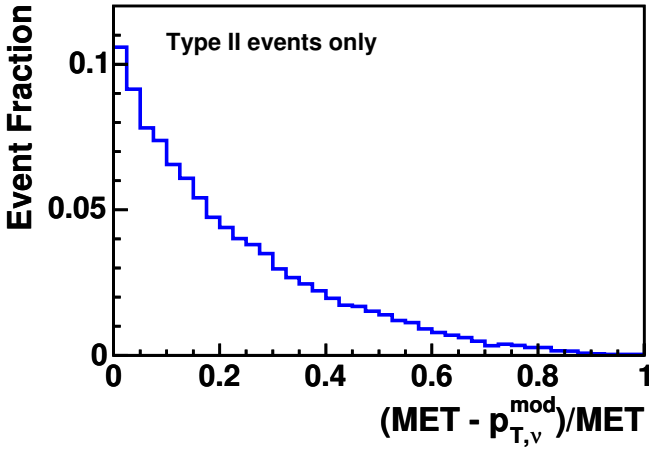

Figure 4.5: Relative difference between the measured missing transverse energy (MET) and the transverse component of the modified neutrino momentum p_ν^{mod}.

part of the measured transverse energy is accounted to the neutrino.
Having calculated the missing $p_{z,\nu}$ component, the four-vector of the leptonically decaying W boson is obtained by combining the reconstructed p_ν with the four-vector of the charged lepton. Depending on the number of $p_{z,\nu}$ solutions this results in either one or two possible W_{lep} four-vectors.

After the combination of the charged lepton and the neutrino to a W_{lep} candidate, all remaining objects to be considered are jets. These jets now have to be assigned to the two b quarks and two light quarks from the $t\bar{t}$ decay to yield candidates for the two top quarks and the hadronically decaying W boson.

Semileptonically decaying Top Quark: $t_{\mathrm{lep}} \rightarrow b\ell\nu_\ell$

The next step is the reconstruction of the semileptonically decaying top quark (t_{lep}) by combining the reconstructed W_{lep} with one of the selected jets in the event. At this stage no b-tag information is used and all jets are considered to be possible candidates for the b_{lep} quark from this semileptonic top-quark decay. The total number of possible combinations resulting in a t_{lep} candidate is given by the number of selected jets in the event and the number of solutions for the z component of the neutrino momentum: $N_{t_{\mathrm{lep}}}^{\mathrm{hyp}} = N_{z,\nu} \cdot N_{\mathrm{jets}}$.

Hadronically decaying W Boson: $W_{\mathrm{had}} \rightarrow jj$

For each semileptonically decaying top-quark hypothesis several possible combinations for the four-momentum of the hadronically decaying W boson (W_{had}) exist. They are obtained by combining the four-momenta of two of the remaining jets, which are not assigned to the b_{lep} quark. The permutation of the two cho-

sen jets leads to the same resulting four-vector and therefore only one of the possible combinations is considered for each pair of jets, which reduces the number of hypotheses for this object by a factor of two. The number of combinations for the reconstruction of the W_{had} boson for each t_{lep} hypothesis is thus given by: $N^{\mathrm{hyp}}_{W_{\mathrm{had}}} = \frac{1}{2} \cdot (N_{\mathrm{jets}} - 1) \cdot (N_{\mathrm{jets}} - 2)$.

Hadronically decaying Top Quark: $t_{\mathrm{had}} \rightarrow bjj$

The last step is the assignment of one of the remaining selected jets to the b_{had} quark from the hadronic top-quark decay. Regardless of their b-tag information, again all jets in the event are considered, which are not assigned so far to the b_{lep} quark or to the two light quarks from the W_{had}-boson decay. The four-momentum of the chosen jet is combined with the four-momentum of the reconstructed W_{had} boson to yield the four-vector of the hadronically decaying top quark. For each set of W_{lep}, t_{lep}, and W_{had} four-vectors this leads to $N^{\mathrm{hyp}}_{t_{\mathrm{had}}} = (N_{\mathrm{jets}} - 3)$ combinations for the reconstruction of the t_{had} candidate.

Total Number of Hypotheses: N^{hyp}

The total number of possibilities to arrange and combine the measured objects charged lepton, missing transverse energy, and jets to the four-vectors of the two W bosons and two top quarks, is then given by

$$N^{\mathrm{hyp}} = N_{z,\nu} \cdot N_{\mathrm{jets}} \cdot \frac{1}{2} \cdot (N_{\mathrm{jets}} - 1) \cdot (N_{\mathrm{jets}} - 2) \cdot (N_{\mathrm{jets}} - 3) \; . \tag{4.13}$$

For a typical $t\bar{t}$ event with four selected jets and two real solutions for the z component of the neutrino momentum there exist 24 hypotheses for the complete reconstruction of the $t\bar{t}$ kinematics. Although the number of possibilities grows significantly with the number of jets in the events, it is reasonable to consider all jets of one event rather than restricting the jet assignment to the four leading jets. MC studies show that only in about 37% of all events with more than four jets the correct assignment is given by the four jets with the largest E_{T}.

4.2.2 Best Possible Hypothesis in each Event

All these possible combinations are considered as hypotheses for the reconstruction of the kinematics of a $t\bar{t}$ event. Using simulated events it is possible to determine the combination of physics objects among all hypotheses which is closest to the generated true event topology. Due to the hadronization there is no information in the jet objects available from which generated quark they originate. Therefore it cannot be determined directly which hypothesis is the correct one. Rather a metric has to be defined that measures how close the reconstructed event topology is to the generated one. Thus not the correct combination, but only the best possible one can be defined.
The goal of the full reconstruction is the optimal reconstruction of the four-vectors

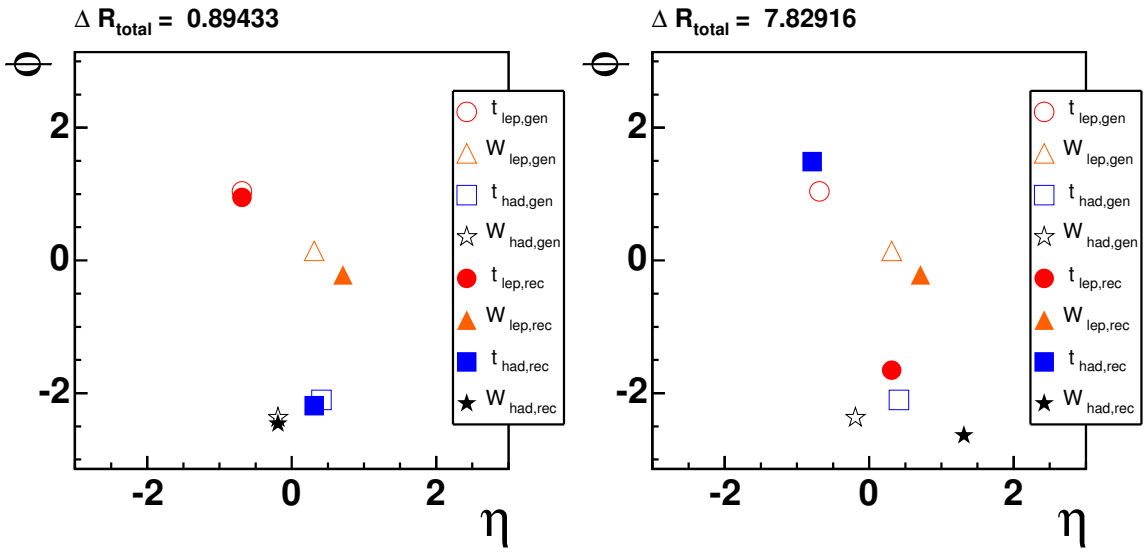

(a) (b)

Figure 4.6: Illustration of the definition of the best possible event hypothesis. The positions in the $\eta - \phi$ plane of the generated top quarks and W bosons are indicated by the open symbols, while the positions of the corresponding reconstructed objects are indicated by the filled symbols. (a) The best possible combination and (b) an arbitrary other hypothesis for the same event are depicted. One can see that in (b) the wrong jet-quark assignment leads to large deviations of the positions of the reconstructed objects.

of the two top quarks and of the two W bosons. Thus one way to define the best possible hypothesis is to look for the hypothesis with the minimal distance of these objects from the generated ones in the $\eta - \phi$ plane. For this purpose the total distance ΔR_{total} of the four reconstructed objects from the corresponding generated objects is defined as

$$\Delta R_{\text{total}} = \Delta R_{W_{\text{lep}}} + \Delta R_{t_{\text{lep}}} + \Delta R_{W_{\text{had}}} + \Delta R_{t_{\text{had}}} \ . \tag{4.14}$$

The distance ΔR_i between the generated and the reconstructed four-vector of object i is given by $\Delta R_i = \sqrt{(\phi_{i,\text{gen}} - \phi_{i,\text{rec}})^2 + (\eta_{i,\text{gen}} - \eta_{i,\text{rec}})^2}$.
The advantage of this definition of the best possible hypothesis is that it exists for each event, regardless of whether one jet from a quark from the $t\bar{t}$ decay is missing or if an object is misreconstructed. For each event exists one way to arrange the given physics objects that leads to the event interpretation closest to the generated truth. This definition of the best possible hypothesis is illustrated for an arbitrary simulated $t\bar{t}$ event in figure 4.6.

4.2.3 Selection of one Hypothesis per Event

In order to analyze the selected dataset, one single hypothesis has to be chosen for each event. For this purpose a criterion based on the properties of the reconstructed

four-vectors of the top quarks and W bosons has to be found that gives a quantitative estimate of how well the hypothesis matches the $t\bar{t}$ event assumption.
The criterion for the hypothesis selection developed in this analysis is based on information on the masses of the reconstructed four-vectors, on the transverse energy of the $t\bar{t}$ system, and on the flavor of the jets assigned to the b quarks. The exploited information are collected in the quantity

$$\psi = Z_\nu \cdot \chi^2 \cdot L_{b-\text{light}} \ , \tag{4.15}$$

which is calculated for each hypothesis of an event. The hypothesis yielding the smallest value of ψ is selected in each event. In the following the single components that enter the computation of ψ are described.

Neutrino-Momentum z-Component Solution: Z_ν

In events of type II only one $p_{z,\nu}$ solution exists and no ambiguities for the reconstruction of the W_{lep} four-vector arise. Events of type I on the other hand feature due to the two $p_{z,\nu}$ solutions two hypotheses for the reconstruction of the W_{lep} four-vector. From studies on simulated $t\bar{t}$ events one knows that in 71% of all type I events the $p_{z,\nu}$ solution with the smaller absolute value leads to the W_{lep} four-vector that is closer to the generated one.
This feature is accounted for in ψ by the weighting factor Z_ν, which is defined to be 0.29 for hypotheses using the neutrino momentum with the smaller absolute value of $p_{z,\nu}$ and 0.71 for the other hypotheses. Since the criterion for the hypothesis selection is the minimal ψ value, the weighting factor Z_ν ensures that hypotheses based on the smaller absolute $p_{z,\nu}$ value are preferred.

Mass and Energy Constraints: χ^2

In a correct combination of observed objects the mass of the reconstructed W_{had} is expected to be close to the known W-boson mass. The difference between the masses of the two reconstructed top quarks is expected to be small. Small non-vanishing values for the difference between the two top-quark masses arise from the different detector performance in the energy resolution between jets and leptons. While the reconstructed t_{had} quark is composed of three jets, only one jet is used for the reconstruction of the t_{lep} quark. It is further expected that for a typical $t\bar{t}$ event the scalar sum of the transverse energies of the two reconstructed top quarks is approximately equal to the scalar sum of the transverse energies of all observed physics objects like jets, charged leptons, and $\not\!\!E_{\text{T}}$.
All these expectations for the mass $m_{W_{\text{had}}}$ of the hadronically decaying W boson, the difference Δm_t between the masses of t_{lep} and t_{had}, and the E_{T} fraction of the $t\bar{t}$ pair are formulated in

$$\chi^2 = \frac{(m_{W_{\text{had}}} - \overline{m}_{W_{\text{had}}})^2}{\sigma^2_{m_{W_{\text{had}}}}} + \frac{(\Delta m_t - \overline{\Delta m_t})^2}{\sigma^2_{\Delta m_t}} + \frac{(f_{\text{E}} - \overline{f}_{\text{E}})^2}{\sigma^2_{f_{\text{E}}}} \ . \tag{4.16}$$

The E_{T} fraction f_{E} is defined as the transverse energy of the reconstructed $t\bar{t}$ system

divided by the total transverse energy of the event,

$$f_{\mathrm{E}} = \frac{\sqrt{p_{\mathrm{T},t_{\mathrm{lep}}}^2 + m_{t_{\mathrm{lep}}}^2} + \sqrt{p_{\mathrm{T},t_{\mathrm{had}}}^2 + m_{t_{\mathrm{had}}}^2}}{\sum_{i}^{N_{\mathrm{jets}}} p_{\mathrm{T},i} + \not{E}_{\mathrm{T}} + E_{\mathrm{T},\ell}} \; . \tag{4.17}$$

Here $p_{\mathrm{T},t_{\mathrm{lep}}}$ and $m_{t_{\mathrm{lep}}}$ represent the transverse momentum and the mass of the semileptonically decaying top quark. The corresponding quantities of the hadronically decaying top quark are indicated by $p_{\mathrm{T},t_{\mathrm{had}}}$ and $m_{t_{\mathrm{had}}}$. The transverse momentum of jet i is denoted by $p_{\mathrm{T},i}$ and $E_{\mathrm{T},\ell}$ is the transverse energy of the charged lepton.
Since the hypothesis closest to the generated true event topology is in each event by definition the best possible hypothesis, the reconstructed values of $m_{W_{\mathrm{had}}}$, Δm_t, and f_{E} are compared with the mean values obtained from the best possible event interpretations in simulated $t\bar{t}$ events. The mean values $\overline{m}_{W_{\mathrm{had}}}$, $\overline{\Delta m_t}$, and $\overline{f}_{\mathrm{E}}$ are derived by fitting the sum of two Gaussian functions (a so-called double Gaussian) to the corresponding distribution as shown in figure 4.7. For each distribution the estimated mean value and width of the Gaussian with the smaller width are taken as parameters of the χ^2 function. Table 4.4 summarizes these values.

Parameter	Value
$\overline{m}_{W_{\mathrm{had}}}$ [GeV/c^2]	79.8
$\sigma_{m_{W_{\mathrm{had}}}}$ [GeV/c^2]	10.5
$\overline{\Delta m_{\mathrm{t}}}$ [GeV/c^2]	-1.5
$\sigma_{\Delta m_t}$ [GeV/c^2]	26.5
$\overline{f_{\mathrm{E}}}$	1.1
$\sigma_{f_{\mathrm{E}}}$	0.07

Table 4.4: Parameters of χ^2 as obtained from fits to the distributions for the best possible event hypotheses.

Light-Quark Likeliness of the Jets assigned to b_{lep} and b_{had}: $L_{b-\mathrm{light}}$

All selected jets of an event are considered as possible candidates for the b quarks from the top-quark decays, regardless of their b tag information. In the calculation of ψ the flavor information is taken into account by the factor $L_{b-\mathrm{light}}$. The quantity $L_{b-\mathrm{light}}$ is a measure for the light-quark likeliness of the jets assigned to the b_{lep} and b_{had} quarks and is defined as

$$L_{b-\mathrm{light}} = (\mathcal{P}_{b_{\mathrm{lep}}} + (1 - R'_{b_{\mathrm{lep}}})) \cdot (\mathcal{P}_{b_{\mathrm{had}}} + (1 - R'_{b_{\mathrm{had}}})) \; . \tag{4.18}$$

Each of the two jets contributes with the sum of the two probabilities $\mathcal{P}_b$ and $(1 - R'_b)$. $\mathcal{P}_b$ is the probability of the chosen jet to belong to the primary vertex and therefore to originate from a light quark. This probability is calculated

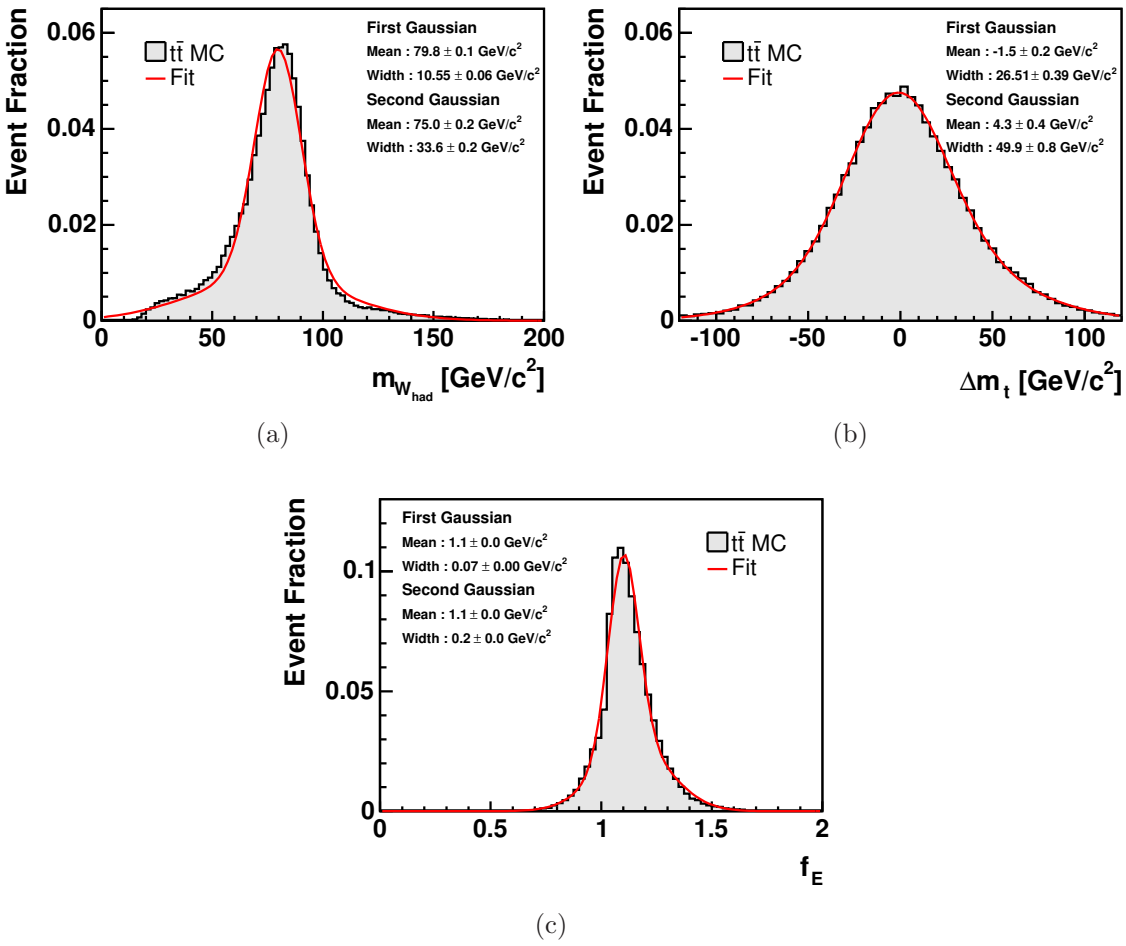

Figure 4.7: Determination of the mean values and widths used in the calculation of χ^2: (a) the distributions of the mass of the reconstructed W_{had}, (b) the mass difference between the two reconstructed top quarks, and (c) the E_{T} fraction of the reconstructed $t\bar{t}$ system. Each distribution is obtained from the best possible event hypothesis and fitted with a double Gaussian. The Gaussian with the smaller width is called *first* Gaussian and its mean value and width are taken as parameters of the χ^2 function.

with the JetProb algorithm [145] which is based on the positive impact parameter of the tracks assigned to the jet in the $r-\phi$ plane.
The information whether a jet has been tagged by the SecVtx algorithm is considered in R_b. Rather than just considering if the jet is tagged or not, also the quality of the SecVtx tag is taken into account. The quality of a b tag can be estimated using the KIT flavor separator [142,146] developed for the search for the electroweak production of single top-quarks. This tool is based on neural networks and delivers for each tagged jet a continuous output value between -1 and 1 that corresponds to the quality of the b tag. The probability R_b for a tagged jet to really originate from a b quark can be computed by linearly shifting the output-value range of the KIT flavor-separator to the interval between zero and one. However, this is only true if the estimated signal to background ratio in the dataset to which the tool

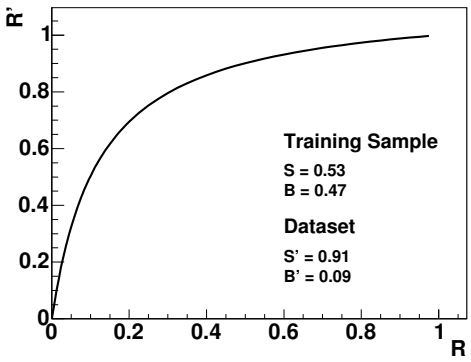

Figure 4.8: Translation of the probability R derived from the KIT flavor-separator output to the probability R' in the dataset taking the estimated signal and background fractions into account.

is applied is the same as in the training sample the neural nets were trained on. Since the flavor separator operates on jets tagged by the SecVtx algorithm, all processes in which real b jets are produced are considered as signal. The neural net has been trained on a tagged jet collection with a fraction of 53% real b jets and 47% mistagged jets. The fraction of real b jets among all tagged jets in the selected dataset used for this analysis is estimated by adding the estimated numbers for the contribution of $t\bar{t}$ events, $W + b\bar{b}$, and single top-quark production. Half of the estimated QCD contribution is also counted as signal. Events with two tagged jets are counted twice. This yields an estimate of 91% for the fraction of real b jets in the selected dataset. To account for the different signal to background ratio in the selected dataset and the training sample, R_b has to be modified. Requiring that the ratio of the measured probabilities to be background $(1 - R_b)$ or signal (R_b) times the ratio of the a priori probabilities for signal (S) and background (B) has to be the same for different a priori probabilities,

$$\frac{1 - R'_b}{R'_b} \cdot \frac{S'}{B'} = \frac{1 - R_b}{R_b} \cdot \frac{S}{B} \ , \tag{4.19}$$

a relation between R_b and R'_b can be obtained:

$$R'_b = \frac{1}{1 + (\frac{1}{R_b} - 1) \cdot \frac{B' \cdot S}{S' \cdot B}} \ . \tag{4.20}$$

This relation is also illustrated in figure 4.8. The probability for a tagged jet to originate from a light quark is then given by $(1 - R'_b)$. For jets without b tag this probability is set to 1.

$L_{b-\mathrm{light}}$ is constructed such that the correct assignment of jets to the b_{lep} and b_{had} quarks lead to small values for this quantity. Event hypotheses in which the two chosen jets have a low probability of being light flavor jets and one or both jets have a SecVtx tag of good quality are therefore preferred.

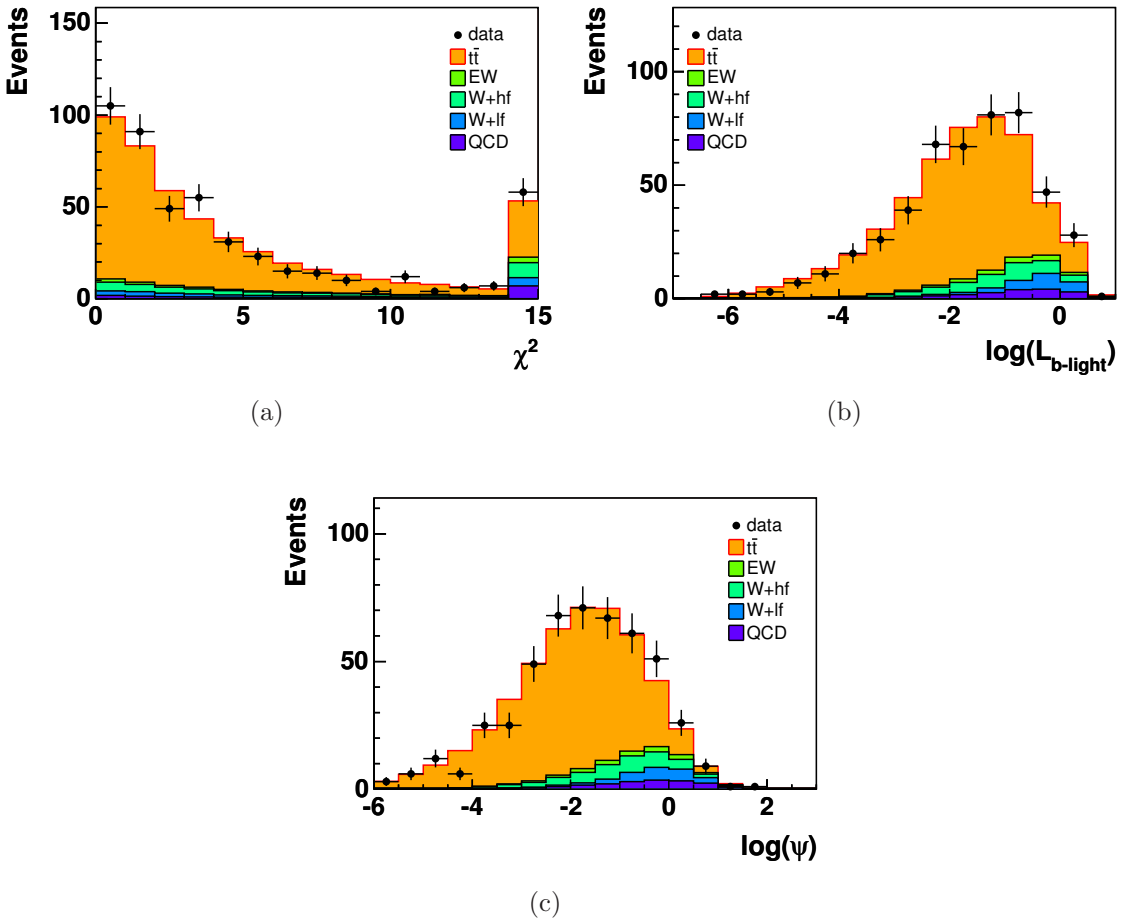

Figure 4.9: (c) Distributions of the hypothesis selection qualifier ψ and its main ingredients (a) χ^2 and (b) $L_{b-\text{light}}$. For each quantity a comparison of the distribution obtained in data with the distribution obtained from the signal and background modelling is shown. For each event only the hypothesis yielding the smallest ψ value is used. Since the ranges of the values of $L_{b-\text{light}}$ and ψ include several orders of magnitude, the logarithm of these quantities is shown rather than their absolute values.

As defined in equation 4.15 the quantity ψ is calculated by multiplying the three presented components Z_ν, χ^2, and $L_{b-\text{light}}$. Figure 4.9 shows the distributions of ψ and its two main ingredients χ^2 and $L_{b-\text{light}}$. The distributions obtained from the selected dataset are well described by the signal MC and background modelling.

4.2.4 Performance of the Hypothesis Selection Procedure

In each event the hypothesis with the smallest value of ψ is chosen. In order to evaluate the quality of this selection criterion the hypotheses selected in this way are compared with the best possible event hypotheses of each event.
Applying the full reconstruction and hypothesis selection method to a sample of

	Selected $t\bar{t}$ hypothesis [%]
Best possible	33.0
$\Delta R_{\text{total}} < 2.0$	44.4
$\Delta R_{\text{total}} < 4.0$	68.4
$\Delta R_{\text{total}} < 6.0$	82.8

Table 4.5: Quality of the hypothesis selection procedure based on the minimal ψ value. Given is the fraction of events in which the selected hypothesis is the best possible. In addition, the fractions of events are given in which the selected hypothesis are within a certain distance ΔR_{tot} with respect to the generated event topology. The numbers are obtained using simulated $t\bar{t}$ lepton+jets events, where the generated lepton is an electron or muon.

simulated $t\bar{t}$ lepton+jets events the fraction of events in which the selected hypothesis is the best possible one is estimated to be about 33%. In table 4.5 also the fractions of events in which the selected hypothesis lies within a certain distance ΔR_{total} with respect to the generated true $t\bar{t}$ kinematics are given.
In figure 4.10 the ΔR_{total} distribution of the hypotheses selected by the minimal ψ value is compared with the corresponding distribution of the best possible hypotheses. In this figure one can also see that even the best possible combination of observed physics objects can be away from the generated objects. Besides effects due to possible mismeasurement of physics object quantities also missing jets from one top-quark decay or additional initial- or final-state radiation can lead to this imperfect reconstruction of the top-quark and W-boson four-vectors. Furthermore, due to the hadronization of quarks into jets one can never achieve a precise one-to-one correspondence of primary partons and observed jets.

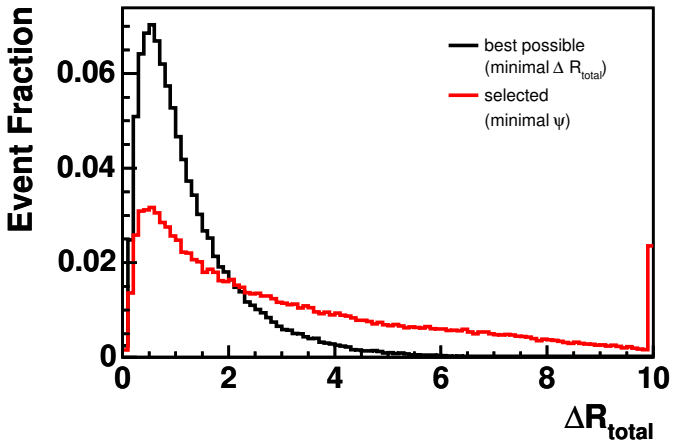

Figure 4.10: ΔR_{total} distributions for the hypotheses selected by the minimal ψ and for the best possible hypotheses.

Comparison of Kinematic Distributions for Different Hypotheses

Studying simulated $t\bar{t}$ events the kinematic distributions for the reconstructed objects obtained from different hypotheses can be compared. The distributions obtained from the hypotheses selected by the minimal ψ criterion are compared with the distributions obtained from the best possible hypotheses and with those of all other hypotheses. For the latter in each event all hypotheses but the best possible are considered and weighted by $1/(N^{\text{hyp}} - 1)$ to ensure that each event contributes with the same weight. In addition, the reconstructed distributions are compared with the distributions obtained from the generated objects. In figure 4.11 this comparison is shown for the p_{T} and η distributions of the reconstructed neutrino. In figure 4.12 and figure 4.13 the same distributions are shown for the two reconstructed W bosons and top quarks. The kinematic distributions obtained from the selected hypotheses approximate reasonably well the best possible distributions, while the distributions of all other hypotheses differ considerably. Furthermore also the mass distributions of the reconstructed W_{had}, t_{lep}, and t_{had} are presented. While the mass distributions of the generated objects are very narrow the reconstructed distributions are broader due to the finite resolution of the detector.
The comparison of the kinematic distributions supports the conclusion that the hypothesis selection procedure based on the selection criterion ψ performs reasonable well in reconstructing the kinematic distributions of $t\bar{t}$ events.

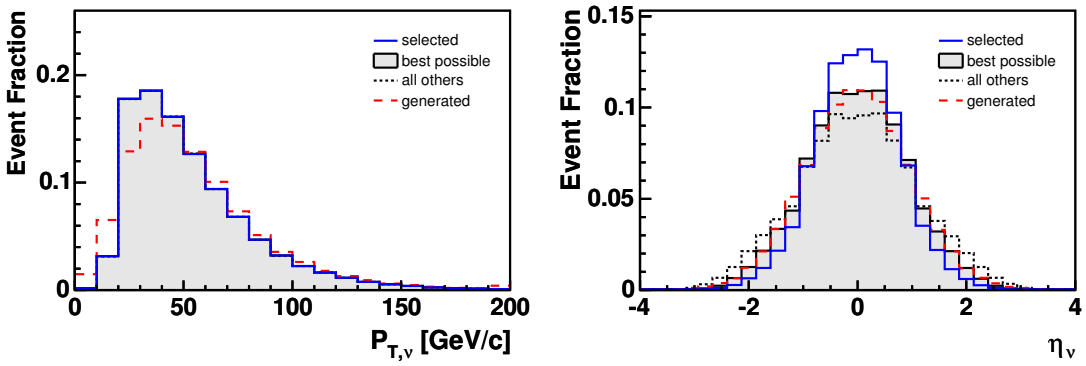

(a) (b)

Figure 4.11: Comparison of (a) the p_{T} and (b) the η distributions for the reconstructed and the generated neutrino.

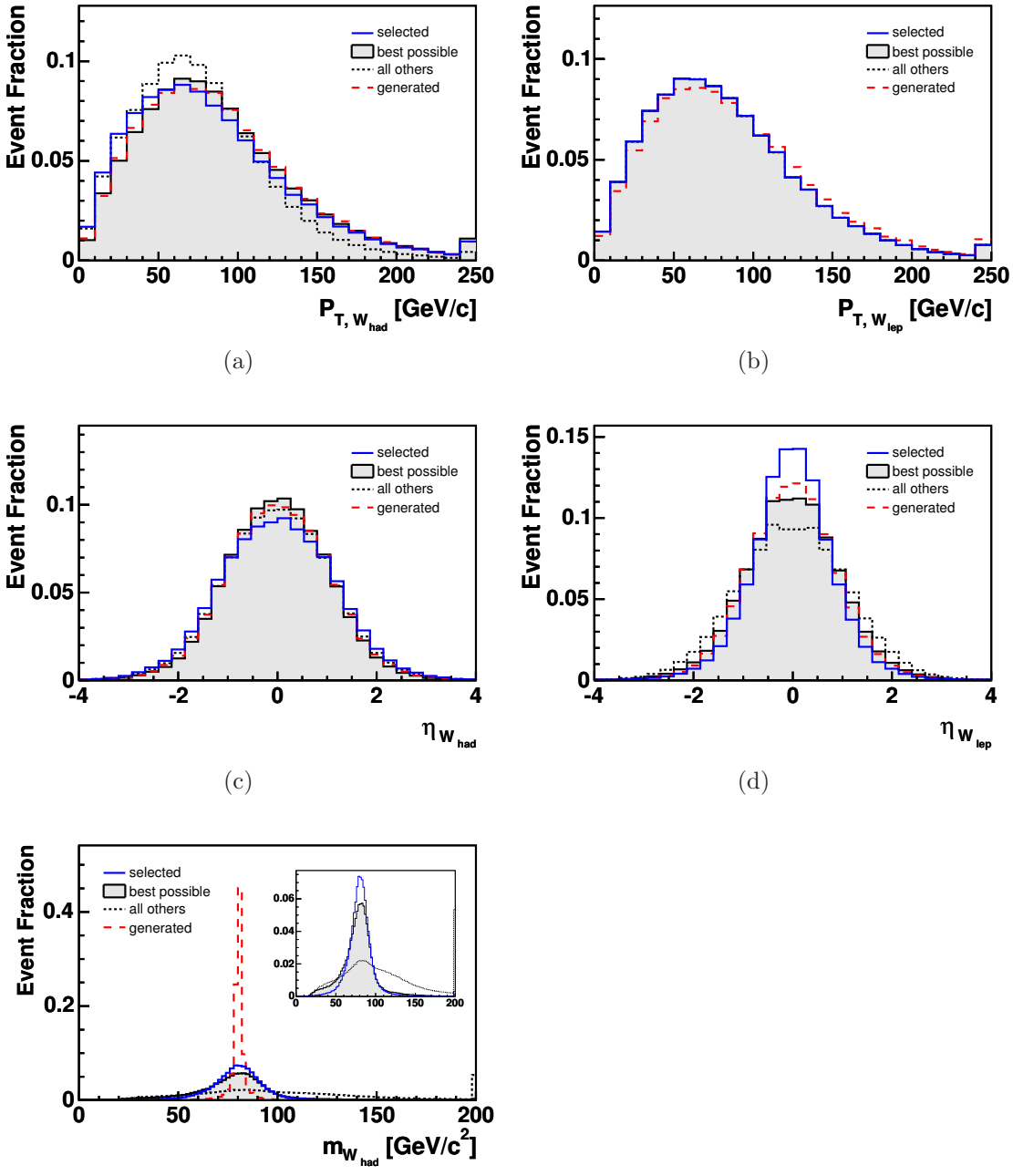

Figure 4.12: Comparison of the p_{T} and η distributions for the reconstructed and generated W_{had} in (a) and (c) and the reconstructed and generated W_{lep} in (b) and (d). The mass of the reconstructed W_{lep} is by construction equal to the pole mass, therefore only the mass distribution of the reconstructed W_{had} is presented in (e). Since the generated distribution for the latter is very narrow and to be able to compare the mass distributions for selected, best possible, and all other hypotheses, the generated distribution is omitted in the embedded figure.

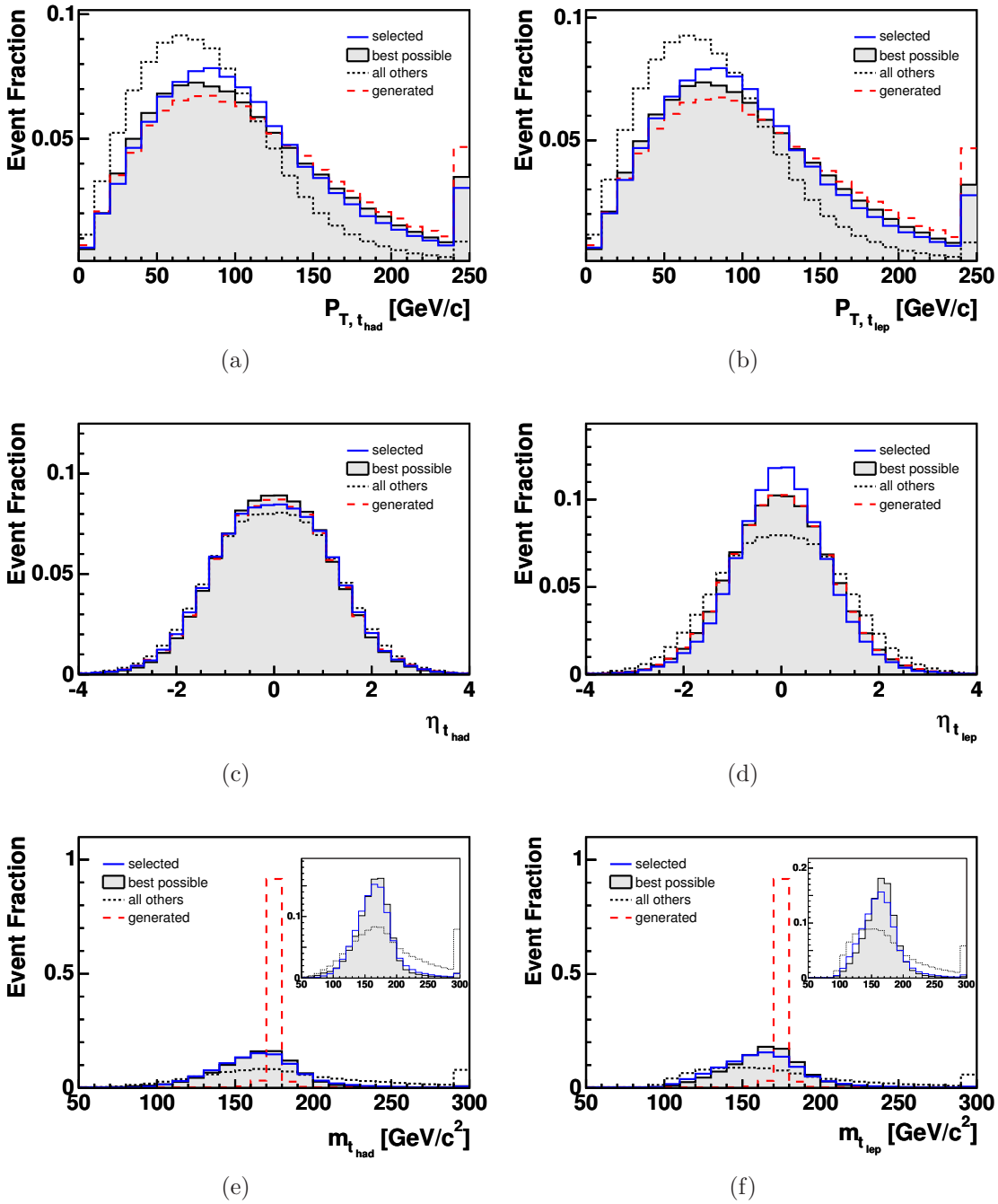

Figure 4.13: Comparison of the p_{T}, η, and mass distributions for the reconstructed and generated t_{had} in (a), (c), and (e) and the reconstructed and generated t_{lep} in (b), (d), and (f). Since the generated mass distributions are very narrow and to allow to compare the mass distributions for selected, best possible, and all other hypotheses, the generated distributions are omitted in the embedded figures.

Comparison between Data and Simulation

The procedure to select the hypothesis that reflects best the assumed $t\bar{t}$ kinematics is developed using MC generated events. In order to apply this method to observed data events one has to make sure that the signal and background modelling describe reasonably well the obtained distributions. For this purpose the samples described in sections 4.1.3 and 4.1.4 are used and the resulting distributions are compared to the distributions from data. Each background template is normalized to its estimated contribution as given in table 4.3. The $t\bar{t}$ signal MC is normalized such that the total number of simulated events is equal to the number of observed events in the selected lepton+jets dataset. In figure 4.14 the p_{T} and η distributions of the charged lepton and the reconstructed neutrino are depicted. Figure 4.15 shows the same distributions for the two reconstructed W bosons. In addition also the mass of the reconstructed W_{had} is presented. The p_{T}, η, and mass distributions of the two reconstructed top quarks can be found in figure 4.16.

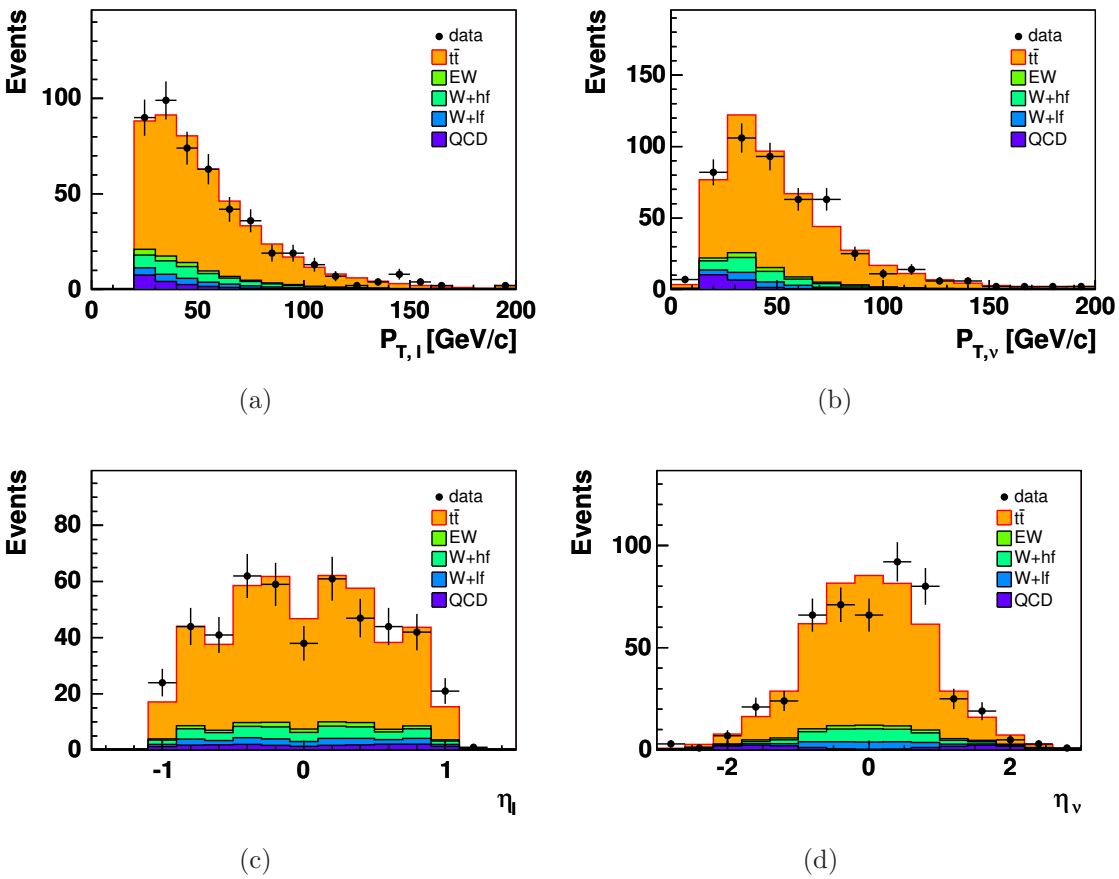

Figure 4.14: Comparison of distributions obtained from data and from signal and background modelling: the p_{T} and η distributions of the charged lepton in (a) and (c) and of the reconstructed neutrino in (b) and (d).

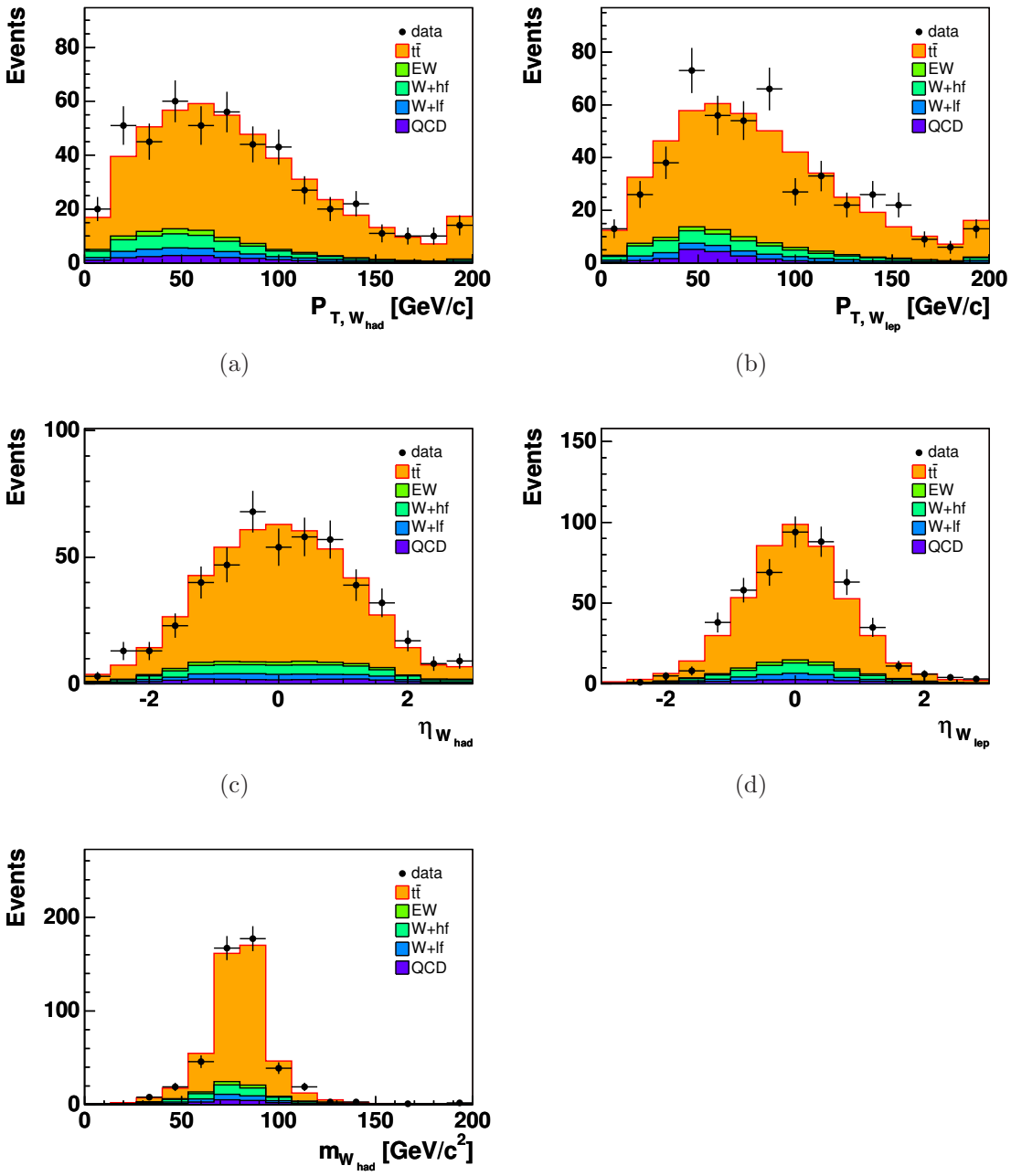

Figure 4.15: Comparison of kinematic distributions obtained from data and from signal and background modelling: p_{T} and η distributions of the reconstructed W_{had} in (a) and (c) and of the reconstructed W_{lep} in (b) and (d). The mass of the reconstructed W_{lep} is by construction equal to the pole mass, therefore only the mass distribution of the reconstructed W_{had} is depicted in (e).

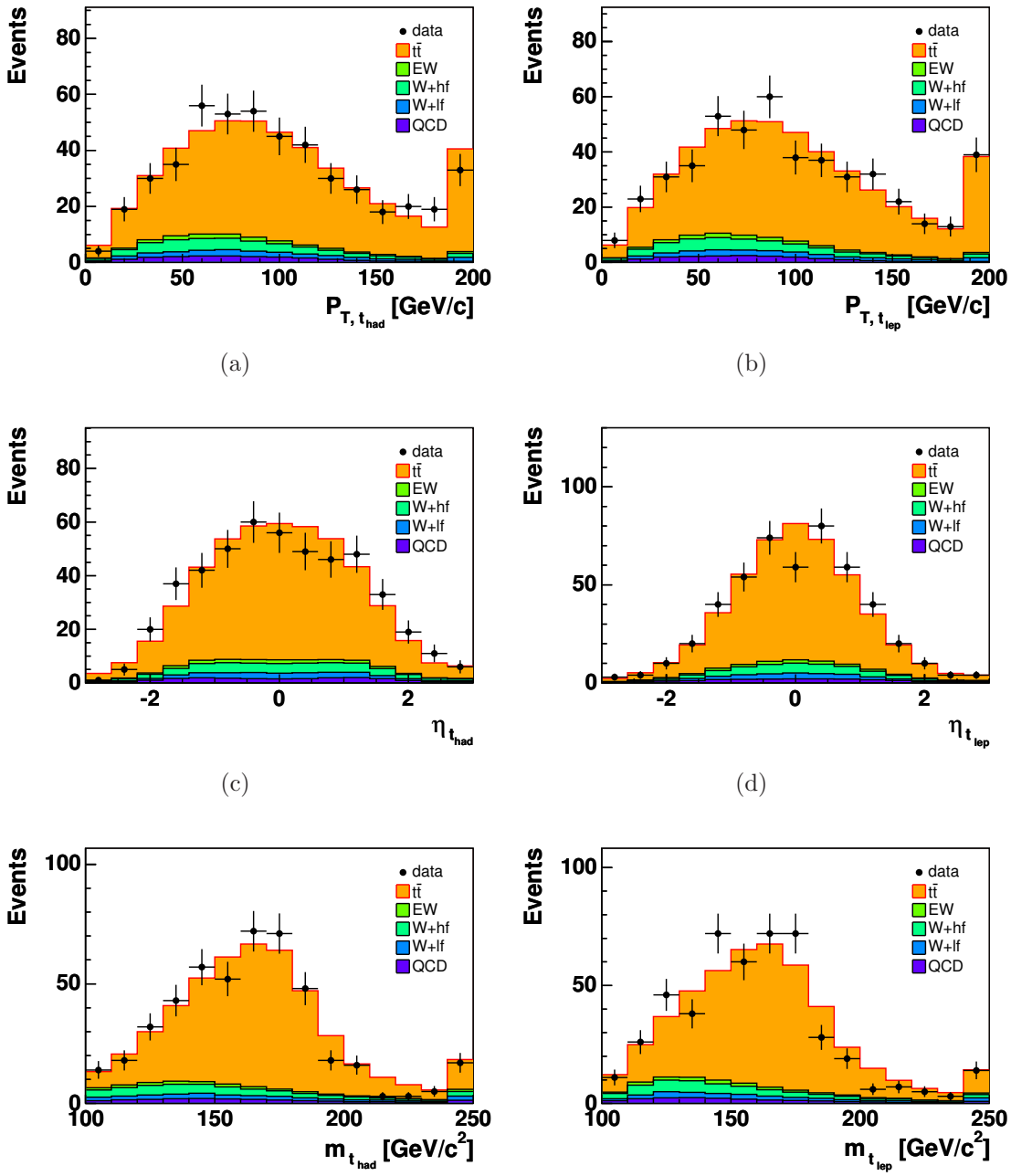

Figure 4.16: Comparison of kinematic distributions obtained from data and from signal and background modelling. The left-hand side shows the p_{T}, η, and mass distributions of the reconstructed t_{had} in (a), (c), and (e), while the right-hand side shows the same distributions for the reconstructed t_{lep} in (b), (d), and (f).

Within statistical fluctuations the simulated distributions describe well the kinematic distributions obtained by applying the full reconstruction to the selected dataset. Therefore, the conclusions on the performance of this method derived from MC studies and stated in the previous paragraph can be assumed to be valid in real data.

4.2.5 Final Correction of the Top-Quark Four-Vectors

After performing the full reconstruction and event hypothesis selection, for each event exactly one pair of reconstructed top quarks is used for the further analysis. Under the assumption that these reconstructed objects correspond to real top quarks their four-vectors are corrected. The momentum components remain unchanged, while the energy is recalculated to force the top-quark mass to the value $m_t = 175\,\mathrm{GeV}/c^2$.

4.3 Extraction of the W-Boson Helicity-Fractions

The fractions of the different W boson helicities are measured using the $\cos\theta^*$ distribution, which is sensitive to the structure of the Wtb vertex. For each event $\cos\theta^*$ is calculated from the four-vectors of the charged lepton, the W_{lep}, and the t_{lep} of the chosen hypothesis. Taking into account influences on the $\cos\theta^*$ distribution due to event selection and reconstruction the observed data are subjected to binned likelihood fits in three different scenarios:

- Measure F_0 under the assumption $F_+ = 0$. This corresponds to a model in which the form factors f_1^R and f_2^L are zero, implying there are no right-handed bottom-quark couplings present.
- Measure F_+ under the assumption that F_0 takes its SM value of 0.7. This measurement is sensitive to models with vanishing form factors f_2^L and f_2^R but with the presence of an additional $V + A$ current in top-quark decays.
- Measure F_0 and F_+ simultaneously in a model independent two-parameter fit.

Several effects lead to distortions of the true $\cos\theta^*$ distribution. The nature of these distortions, their sources, and how they are considered in the convolution method is described in the following sections. In addition, tests of the method for varied input values and the estimation of the systematic uncertainties are discussed.

4.3.1 Distortions of the $\cos\theta^*$ Distribution

The observed $\cos\theta^*$ distribution obtained from the reconstructed four-vectors for all events passing the lepton+jets event selection deviates from the distribution calculated on parton level. The reasons for this effect can be factorized into two groups linked to the two analysis steps event selection and full kinematic reconstruction. The impact of the two kinds of effects is illustrated in figure 4.17, where the shapes of the $\cos\theta^*$ distributions at the different stages of the analysis are compared with each other.

Impact of the Event Selection

Comparing the $\cos\theta^*$ distributions calculated on parton level from the generated objects before and after applying the event selection the most apparent difference is the strong suppression of events with $\cos\theta^*$ values between -1 and -0.7. This strong suppression can be linked to two event-selection requirements on the charged lepton candidates, the isolation requirement and the cut on p_{T} of the lepton. From figure 4.18(a) one can see that large negative values of $\cos\theta^*$ correspond to event topologies in which the charged lepton is emitted backwards to the direction of motion of the W boson and thus parallel to the b quark momentum. Consequently, the nearby b-quark jet enhances the energy around the charged lepton track and these

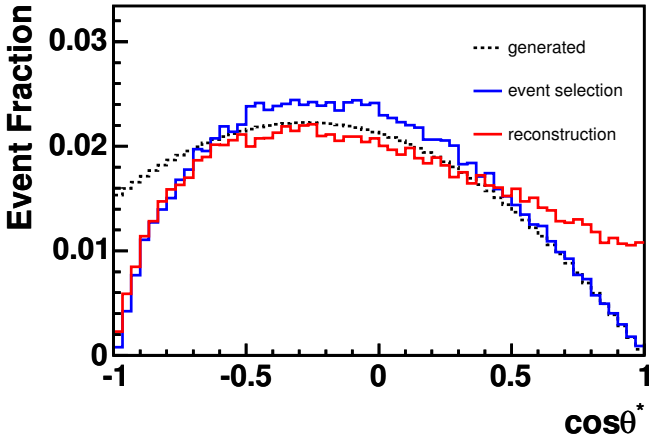

Figure 4.17: Shape comparison of the $\cos\theta^*$ distributions obtained from simulated $t\bar{t}$ events at the different stages of the analysis: the distributions calculated from the generated objects before and after the event selection and the distribution obtained from the reconstructed objects for all selected events.

events have therefore a higher probability to be rejected by the isolation requirement. This requirement rejects leptons for which the non-lepton E_{T} in a cone in the $\eta-\phi$ plane with radius 0.4 around the lepton track is more than 10% of the lepton's E_{T} or p_{T}, respectively.
Moreover, these leptons exhibit a softer p_{T} spectrum compared to leptons which are not emitted backwards to the W boson's momentum and are therefore more likely to fail the lepton-p_{T} cut in the event selection.
Events in which the charged lepton is emitted perpendicular or parallel to the W boson's momentum have a harder lepton-p_{T} spectrum and a smaller fraction of deposited energy around the lepton's track and therefore a higher probability to pass the two discussed event-selection requirements. However, for events with large $\cos\theta^*$ values the situation is reversed with the neutrino being emitted backward with respect to the direction of motion of the W boson, see figure 4.18(b). Therefore the momentum of the neutrino and thus also $\not\!\!E_{\mathrm{T}}$ decreases with increasing $\cos\theta^*$ and these events are more likely to fail the $\not\!\!E_{\mathrm{T}}$ cut in the event selection. The enhancement due to increasing lepton p_{T} is compensated by the suppression due to decreasing $\not\!\!E_{\mathrm{T}}$ and the resulting $\cos\theta^*$ distributions in the region $0.7 < \cos\theta^* < 1.0$ before and after applying the event selection are approximately the same.
Due to the discussed effects the event-selection efficiency is not flat as a function of $\cos\theta^*$. Since the $\cos\theta^*$ distribution is highly sensitive to F_0 and F_+ this leads to different total event-selection efficiencies for different values of the W-boson helicity-fractions. But in contrast to the absolute scale, the shape of the event-selection efficiency as a function of $\cos\theta^*$ does not depend on the actual proportions of the W-boson helicity-fractions. This is illustrated in figures 4.19(a) and (b), where the normalized event-selection efficiencies as a function of $\cos\theta^*$ are compared for different samples of simulated $t\bar{t}$ events with different W-boson helicity-fractions. The

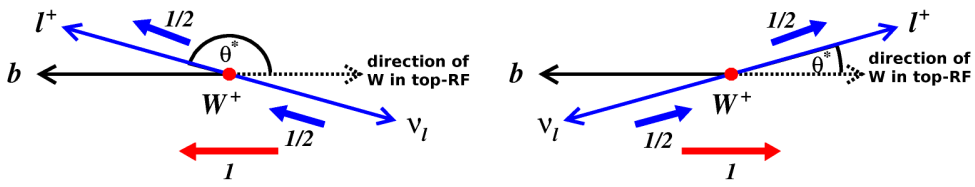

(a) (b)

Figure 4.18: The decay of a (a) left-handed and a (b) right-handed W boson in its rest frame. In (a) the charged lepton is emitted backwards compared to the direction of the W-boson momentum in the top-quark rest-frame (top-RF), while in (b) the charged lepton is emitted parallel to this direction.

normalized event-selection efficiency in each bin of the $\cos\theta^*$ distribution is defined as $\epsilon_i^{\text{norm}} = \frac{\epsilon_i}{\sum_i \epsilon_i}$, with the event-selection efficiency $\epsilon_i = \frac{N_i^{\text{sel}}}{N_i}$, where N_i^{sel} is the number of selected events in bin i.

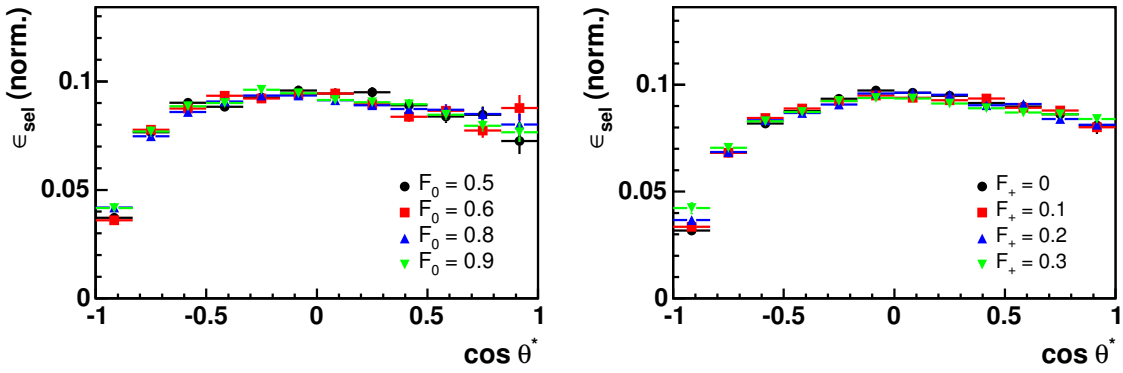

(a) (b)

Figure 4.19: Normalized event-selection efficiencies as a function of $\cos\theta^*$ for different $t\bar{t}$ MC samples with different W-boson helicity-fractions. The comparison of normalized event-selection efficiencies for different values of F_0 in (a) and for different values of F_+ in (b) validate that the shape of the event-selection efficiency as a function of $\cos\theta^*$ is independent of F_0 and F_+.

Impact of the Event Reconstruction

The event selection affects the shape of the true $\cos\theta^*$ distribution by a $\cos\theta^*$ dependent event-selection efficiency. At the second stage of the analysis the kinematic reconstruction transfers the generated true $\cos\theta^*$ values into the corresponding reconstructed values. Since the latter can differ from the true values, the whole $\cos\theta^*$ distribution obtained from the reconstructed four-vectors deviates from the distribu-

tion obtained from the corresponding four-vectors of the generated objects. Several effects contribute to this deviation.
In section 4.2.4 the probability that the best possible among all event hypotheses for a given event is chosen by selecting the hypothesis yielding the smallest value of ψ is estimated to be 33%. Thus in 2/3 of all events not the best possible hypothesis is chosen and the $\cos\theta^*$ value calculated based on the selected hypothesis will deviate from the true value.
But even if one would select for each event the best possible hypothesis, the reconstruction would still not be perfect. Imperfect measurement of physics objects quantities, especially jet energies and consequently $\not\!\!E_{\mathrm{T}}$, as well as not reconstructed jets originating from a final-state parton of the $t\bar{t}$ decay lead to this finite resolution of the reconstruction. These experimental issues are joined by a more fundamental reason. The measured energy and direction of observed jets are correlated to the corresponding quantities of the initially outgoing parton and jets can therefore be linked to partons. But due to hadronization effects one can never achieve a perfectly matching assignment.
Finally, about 7% of the signal contribution in the selected dataset are estimated to come from τ+jets events. In these events the W_{lep} decays into a τ and the corresponding neutrino. Taus are unstable and can decay further via $\tau \to \ell + \nu_\tau + \bar{\nu}_\ell$ into an electron or muon and the events are therefore accepted by the event selection. Since these detected electrons or muons stem not directly from the top-quark decay, the $\cos\theta^*$ value calculated from the reconstructed four-vectors of the observed charged lepton, the W_{lep}, and the t_{lep} can therefore differ significantly from the value obtained from the four-vectors of the generated τ, W boson, and top quark.
All these effects lead to a migration of events with a given true $\cos\theta^*$ value into bins of the reconstructed distribution corresponding to different $\cos\theta^*$ value. The migration can be described by a migration matrix that translates generated $\cos\theta^*$ values into the corresponding reconstructed values. The migration is universal and depends only on the topology of the event with respect to $\cos\theta^*$, but does not depend on the values of F_0, F_+, and F_-. This is illustrated in figures 4.20 and 4.21, where the migration matrices for different samples of simulated $t\bar{t}$ events with different values for F_0 and F_+ are compared. In both figures the twelve rows of 12×12 migration matrices are depicted as a function of the reconstructed $\cos\theta^*$. Each row corresponds to one of the twelve bins of generated $\cos\theta^*$. Within statistical fluctuations the distributions for the different settings of F_0 and F_+ show good agreement.

Figure 4.22(a) shows the event-by-event differences between the generated and the reconstructed $\cos\theta^*$ values as a function of the generated true value. For each $\cos\theta^*$ bin the corresponding $\cos\theta^*_{\mathrm{gen}} - \cos\theta^*_{\mathrm{rec}}$ distribution is fitted with a Gaussian. The widths of these Gaussians depicted in figure 4.22(b) determine the $\cos\theta^*$ resolution of the kinematic reconstruction as a function of $\cos\theta^*$. From the resolution of the kinematic reconstruction a recommendation for the number of bins to use in the analysis can be derived. A reasonable approach is to require that the bin width corresponds to the average resolution. The mean resolution obtained by averaging over all $\cos\theta^*$ bins is roughly 0.35 and thus six bins are chosen for the $\cos\theta^*$ distribution in the analysis.

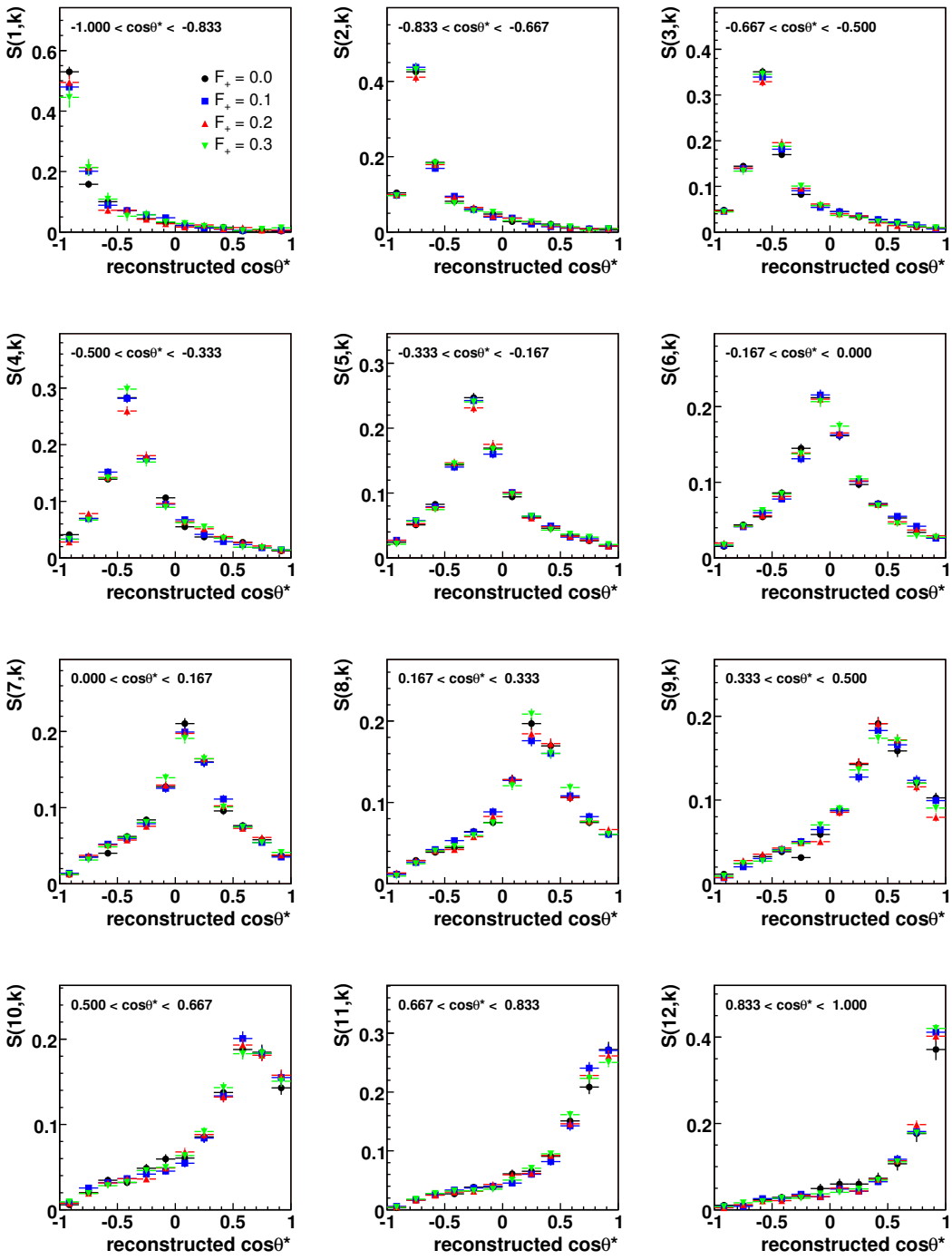

Figure 4.20: The twelve rows of a 12×12 migration matrix S as a function of reconstructed $\cos\theta^*$ values for different $t\bar{t}$ MC samples with different values of F_+. F_0 is 0.7 in all samples and F_- is given by $0.3 - F_+$. Each row corresponds to a certain interval of generated $\cos\theta^*$ values. Within statistical fluctuations the distributions for the different $t\bar{t}$ MC samples with different values of F_+ show good agreement and demonstrate that the migration does not depend on F_+.

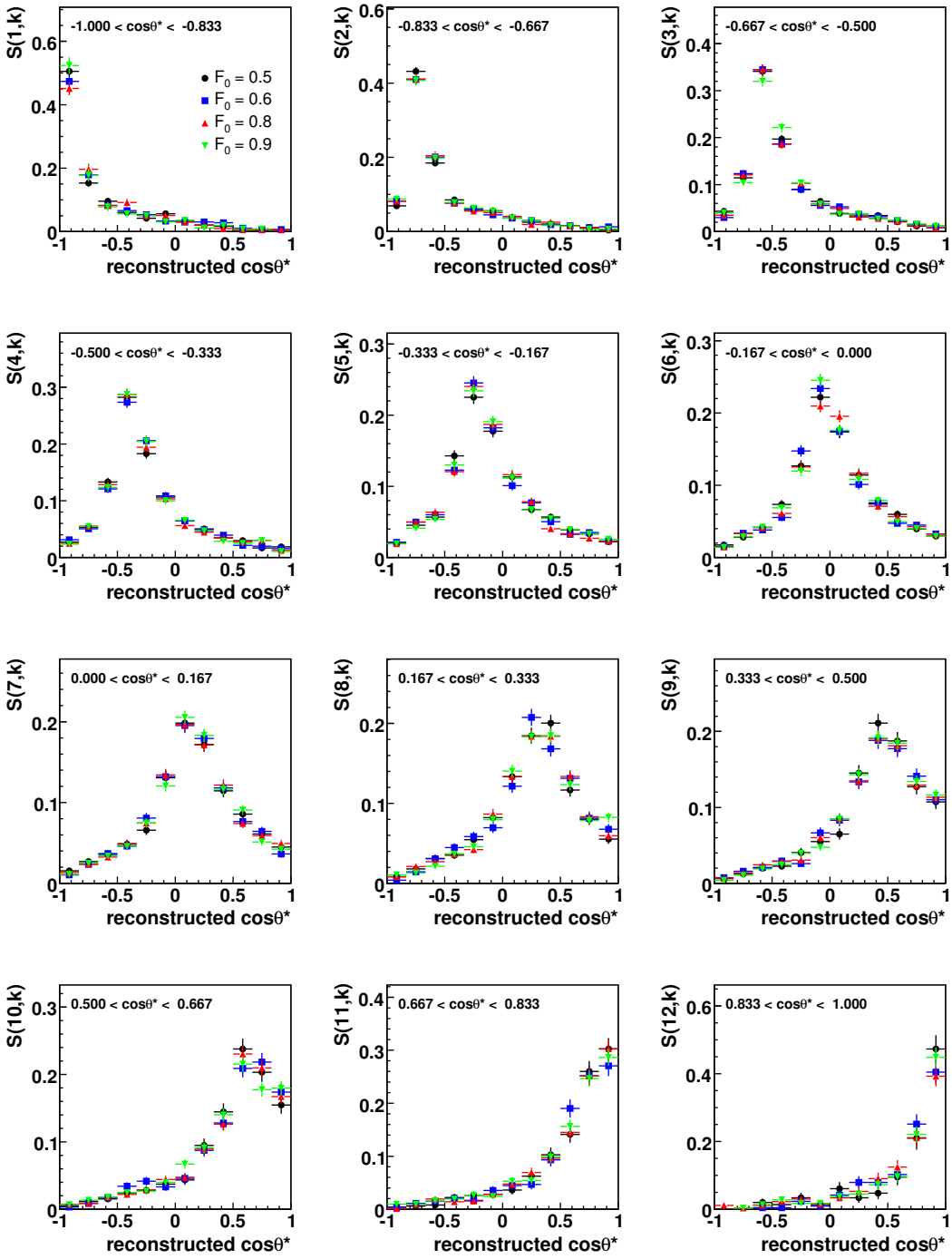

Figure 4.21: The twelve rows of a 12×12 migration matrix S as a function of reconstructed $\cos\theta^*$ values for different $t\bar{t}$ MC samples with different values of F_0. F_+ is 0.0 in all samples and F_- is given by $1.0 - F_0$. Each row corresponds to a certain interval of generated $\cos\theta^*$ values. Within statistical fluctuations the distributions for the different $t\bar{t}$ MC samples with different values of F_0 show good agreement and demonstrate that the migration does not depend on F_0.

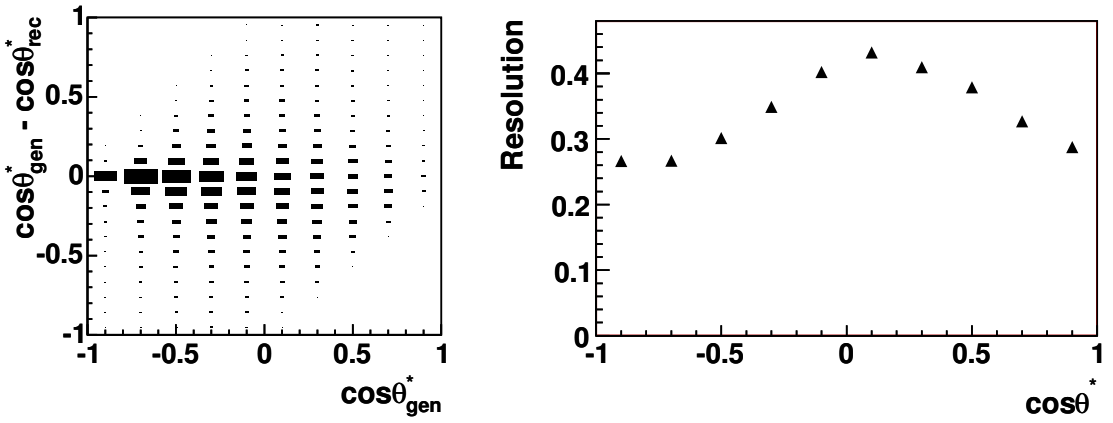

(a) (b)

Figure 4.22: (a) Difference between generated and reconstructed $\cos\theta^*$ values as a function of the generated true value. (b) The widths of the Gaussians fitted to the $\cos\theta^*_{\text{gen}} - \cos\theta^*_{\text{rec}}$ distribution in each bin of $\cos\theta^*_{\text{gen}}$ define the resolution for $\cos\theta^*$ as a function of $\cos\theta^*$.

4.3.2 Convolution Method

In the binned likelihood fit described in section 4.3.3 the number of observed events is compared to the number of expected events for each bin of the $\cos\theta^*$ distribution. The number of expected events in each bin is calculated in the convolution method from first principle using the theoretical predictions and convoluting the effects of $\cos\theta^*$ dependent efficiencies and migration with this prediction.
The starting point is the calculation of the theoretically predicted number of signal events in each of the six $\cos\theta^*$ bins as a function of the helicity fractions F_0, F_-, and F_+. Exploiting the relation $F_0 + F_- + F_+ = 1$ the dependency can be reduced to two free parameters, F_0 and F_+. The predicted fraction of signal events in bin i of the $\cos\theta^*$ distribution is given by

$$\hat{\mu}_i^{\text{sig,theo}}(F_0, F_+) = F_0 f_i^0 + (1 - F_0 - F_+) f_i^- + F_+ f_i^+ \ , \tag{4.21}$$

with

$$f_i^0 = \int_{a_i}^{b_i} \frac{3}{4}(1 - \cos^2\theta^*) d\cos\theta^* \ , \tag{4.22}$$

$$f_i^- = \int_{a_i}^{b_i} \frac{3}{8}(1 - \cos\theta^*)^2 d\cos\theta^* \ , \tag{4.23}$$

$$f_i^+ = \int_{a_i}^{b_i} \frac{3}{8}(1 + \cos\theta^*)^2 d\cos\theta^* \ . \tag{4.24}$$

The factors f_i^0, f_i^-, and f_i^+ are the normalized $\cos\theta^*$ distributions corresponding to the three different helicity states, integrated from the lower boundary a_i to the

upper boundary b_i of bin i. By construction $\hat{\mu}_i^{\text{sig,theo}}$ is normalized and

$$\sum_i \hat{\mu}_i^{\text{sig,theo}}(F_0, F_+) = 1 \tag{4.25}$$

holds for all values of F_0 and F_+.

Accounting for the $\cos\theta^*$ Dependence of the Event-Selection Efficiency

As discussed in section 4.3.1 the event-selection efficiency depends on $\cos\theta^*$. This is accounted for in the convolution method by multiplying $\hat{\mu}_i^{\text{sig,theo}}$ with the corresponding relative event-selection efficiency ϵ_i^{rel}, which reflects how likely events with a given $\cos\theta^*$ value are selected compared to the total efficiency. Consequently the relative event-selection efficiency is defined as the efficiency $\epsilon_i = \frac{N_i^{\text{sel}}}{N_i}$ for bin i divided by the total efficiency $\epsilon^{\text{tot}} = \frac{N^{\text{sel}}}{N}$ of the event selection:

$$\epsilon_i^{\text{rel}} = \frac{\epsilon_i}{\epsilon^{\text{tot}}} = \frac{N_i^{\text{sel}} \cdot N}{N^{\text{sel}} \cdot N_i} \ . \tag{4.26}$$

The total number of events is given by N, while N^{sel} denotes the number of selected events. The corresponding numbers for each bin are given by N_i and N_i^{sel}. As mentioned before, the efficiency ϵ_i as well as the total overall efficiency ϵ^{tot} depend on F_0 and F_+. Thus also the relative event-selection efficiency depends on the proportions of the W-boson helicity fractions. Only the normalized event-selection efficiency

$$\epsilon_i^{\text{norm}} = \frac{\epsilon_i}{\sum_i \epsilon_i} \tag{4.27}$$

is independent of F_0 and F_+, see figure 4.19. Combining equation 4.26 and equation 4.27, the relative event-selection efficiency can be expressed in terms of the normalized event-selection efficiency

$$\epsilon_i^{\text{rel}} = \epsilon_i^{\text{norm}} \cdot \sum_i \epsilon_i^{\text{rel}}. \tag{4.28}$$

Fortunately, relative and normalized event-selection efficiency differ only by a multiplicative factor $D(F_0, F_+) = \sum_i \epsilon_i^{\text{rel}}$, that contains the whole dependence on the helicity fractions. Consequently the fraction of selected signal events in bin i can be defined as

$$\hat{\mu}_i^{\text{sig,sel}}(F_0, F_+) = \frac{\hat{\mu}_i^{\text{sig,theo}}(F_0, F_+) \cdot \epsilon_i^{\text{rel}}}{\sum_i \hat{\mu}_i^{\text{sig,theo}}(F_0, F_+) \cdot \epsilon_i^{\text{rel}}} \ , \tag{4.29}$$

and the dependency on F_0 and F_+, introduced by the relative efficiency, cancels out in the normalization. Therefore, any $t\bar{t}$ MC sample regardless of its proportions of the W-boson helicity-fractions can be used to determine ϵ_i^{rel}. For the sake of precision the default SM Pythia sample is used, which exhibits the largest statistics. The resulting efficiency is shown in figure 4.23.

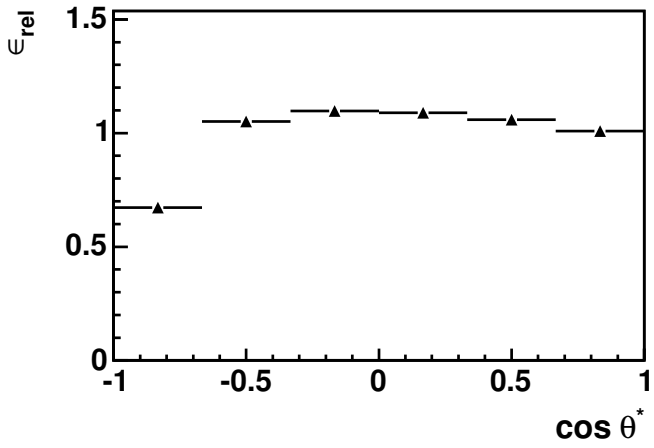

Figure 4.23: Relative event-selection efficiency ϵ^{rel} as a function of $\cos\theta^*$ as derived from the default PYTHIA $t\bar{t}$ MC sample.

Accounting for the Impact of the Event Reconstruction

So far the impact on the true $\cos\theta^*$ distribution by the event selection has been addressed. In the second step the translation from the true to the reconstructed $\cos\theta^*$ distribution is carried out and the migration of events between different bins is accounted for. For this purpose the migration matrix S is defined. Each matrix element $S(i,k)$ gives the probability for an event with a true $\cos\theta^*$ value corresponding to bin i of the distribution to be reconstructed with a $\cos\theta^*$ value corresponding to bin k. By construction the relation

$$\sum_k S(i,k) = 1 \tag{4.30}$$

holds for all bins i, which implies that all events with a certain true $\cos\theta^*$ value have to occur in one of the bins of the reconstructed $\cos\theta^*$ distribution and the total number of reconstructed events is equal to the number of selected events.
Since the migration is independent of F_0 and F_+ and for the sake of precision the migration matrix is obtained from the large $t\bar{t}$ PYTHIA MC sample. The obtained 6×6 migration matrix S is illustrated in figure 4.24.
Taking the migration effect into account by applying the migration matrix S and summing over all bins of $\cos\theta^*_{\text{true}}$, the predicted fraction of reconstructed signal events in bin k is then given by

$$\hat{\mu}_k^{\text{sig,rec}} = \sum_i \hat{\mu}_i^{\text{sig,sel}} \cdot S(i,k) = \frac{\sum_i \hat{\mu}_i^{\text{sig,theo}} \cdot \epsilon_i^{\text{rel}} \cdot S(i,k)}{\sum_i \hat{\mu}_i^{\text{sig,theo}} \cdot \epsilon_i^{\text{rel}}} \ . \tag{4.31}$$

Again, $\hat{\mu}_i^{\text{sig,rec}}$ is by construction normalized to 1:

$$\sum_k \hat{\mu}_k^{\text{sig,rec}} = \sum_k \sum_i \hat{\mu}_i^{\text{sig,sel}} \cdot S(i,k) = \sum_i \hat{\mu}_i^{\text{sig,sel}} \cdot \sum_k S(i,k) = 1 \ . \tag{4.32}$$

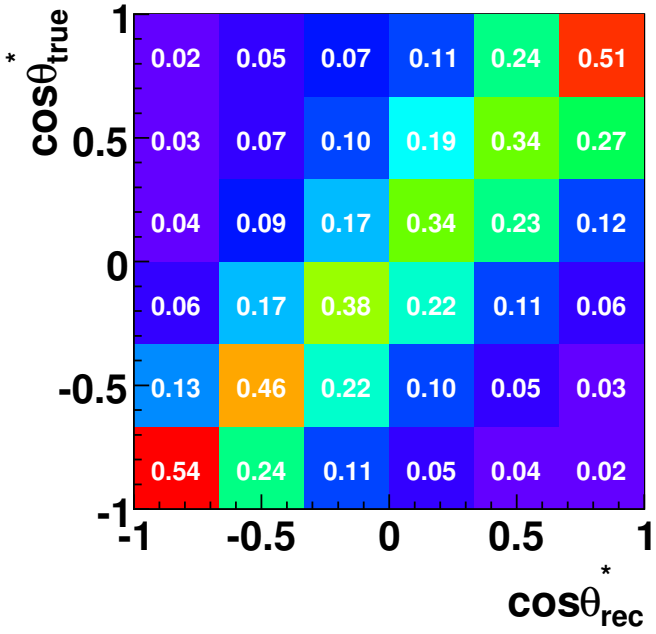

Figure 4.24: The elements of the 6×6 migration matrix S give the probability for events with a given $\cos\theta^*_{\text{true}}$ value to be reconstructed with a value corresponding to one of the six bins of the $\cos\theta^*_{\text{rec}}$ distribution. The matrix is constructed such that the sum of the probabilities in each row is 1.

4.3.3 Binned Likelihood Fit

In order to extract the values of F_0 and F_+ from the observed $\cos\theta^*$ distribution the number of observed events n_i in each bin i is compared to the predicted number of reconstructed events μ_i^{rec} in bin i. The latter is calculated from the expected fraction of reconstructed signal events $\hat{\mu}_i^{\text{sig,rec}}(F_0, F_+)$ and the fraction of background events $\hat{\mu}_i^{\text{BG}}$,

$$\mu_i^{\text{rec}}(F_0, F_+, \beta) = (N^{\text{data}} - N^{\text{BG}} \cdot \beta) \cdot \hat{\mu}_i^{\text{sig,rec}}(F_0, F_+) + N^{\text{BG}} \cdot \beta \cdot \hat{\mu}_i^{\text{BG}} \ , \qquad (4.33)$$

where N^{data} is the total number of observed events and N^{BG} is the estimated total number of background events in the selected dataset. A possible variation of the total number of background events is taken into account via the parameter β. The number of signal events is then altered accordingly. The normalized fraction of background events $\hat{\mu}_i^{\text{BG}}$ is obtained from the combined background template.
Predicted and observed numbers of events enter the likelihood function, defined as

$$L(F_0, F_+, \beta) = \left(\prod_{i=1}^{N_{\text{bins}}} \frac{(\mu_i^{\text{rec}}(F_0, F_+, \beta))^{n_i} \cdot e^{-\mu_i^{\text{rec}}(F_0, F_+, \beta)}}{n_i!} \right) \cdot e^{-\frac{(1-\beta)^2}{2\Delta_{\text{BG}}^2}} \ . \qquad (4.34)$$

The β parameter is constrained to a window around 1 with the width of Δ_{BG} corresponding to the uncertainty in the background estimation of 28% as given in

table 4.3 via a multiplicative Gaussian term. The negative logarithm of the likelihood function $-\ln L(F_0, F_+, \beta)$ is minimized by varying the fit parameters. This determines the set of values for the parameters F_0, F_-, and F_+ yielding expected event numbers for each bin that describe best the observed distribution.
Depending on the fit scenario either F_0 is fixed to its SM expectation of 0.7 and F_+ is the free fit-parameter or F_+ is fixed to 0.0 and F_0 is considered as the free parameter. In the model-independent two-parameter fit, both parameters are unconstrained.

4.3.4 Pseudo Experiments

In order to test the validity of the analysis method and in order to estimate the expected statistical uncertainties as well as the expected systematic uncertainties for the three different measurements, ensembles of pseudo experiments are performed. In each pseudo experiment the measurement is repeated on a simulated data sample using the same statistics as in the real dataset. This procedure offers the opportunity to obtain a whole series of simulated measurements and to determine how the obtained results compare to the average and how the mean fit results are affected by systematic uncertainties.
For each pseudo experiment the number of signal and different background events is thrown according to a Poisson distribution with the mean values corresponding to the background estimation given in table 4.3. Only combinations of numbers of signal and background events which sum up to the total number of 484 observed events are considered.
Depending on the purpose of the pseudo experiments the number of signal events is then drawn from one of the signal MC samples, either from the default sample, from a sample with altered helicity fractions, or from samples dedicated to the study of systematic uncertainties. The background events are drawn from the corresponding background templates described in section 4.1.4. The resulting $\cos\theta^*$ distribution for each pseudo experiment is then subjected to the three fit scenarios and the results and uncertainties are averaged over the whole ensemble of pseudo experiments. Unless stated otherwise the likelihood function for each pseudo experiment is calculated using the relative efficiency and the migration matrix which are used for the actual measurement.

4.3.5 Consistency Check and Estimation of Expected Statistical Uncertainties

In order to test the consistency of the whole method 5,000 pseudo experiments are performed. The signal fraction of the pseudo data is drawn from the same sample of simulated $t\bar{t}$ events, that is used to derive ϵ^{rel} and S.
The distributions of the fit results for the one-parameter fits and the two-parameter fit are depicted in figures 4.25 and 4.26, subfigures (a) and (b), respectively. In both cases the mean values estimated by fitting a Gaussian to the distribution are

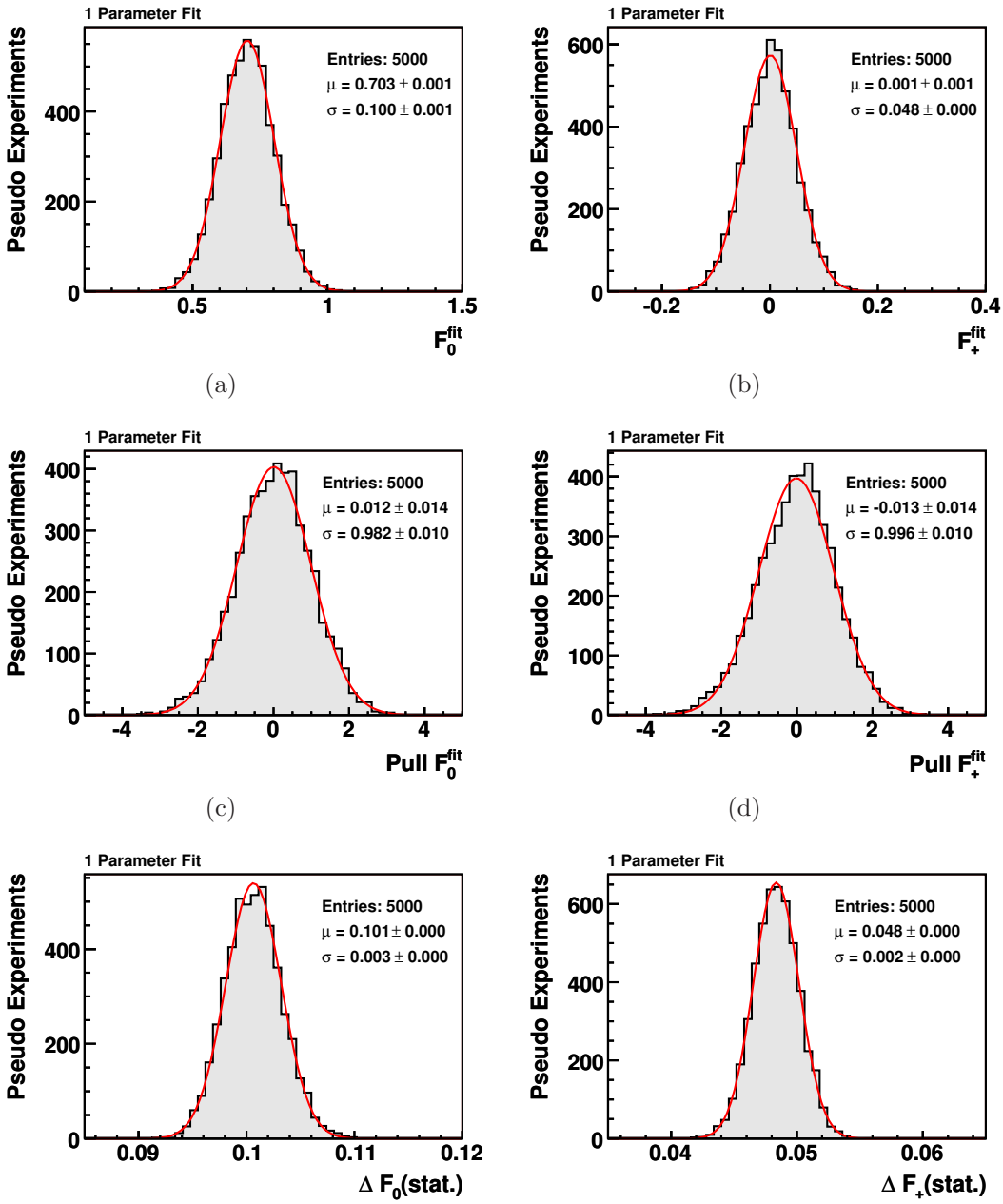

Figure 4.25: Distribution of the fit values F_0 in (a) and F_+ in (b) and the corresponding pull distributions in (c) and (d) for the one-parameter fit. The pull is defined as $(F^{\text{fit}} - F^{\text{true}})/\sigma_{F^{\text{fit}}}$. (e) and (f) Distributions of the statistical uncertainties of each pseudo experiment.

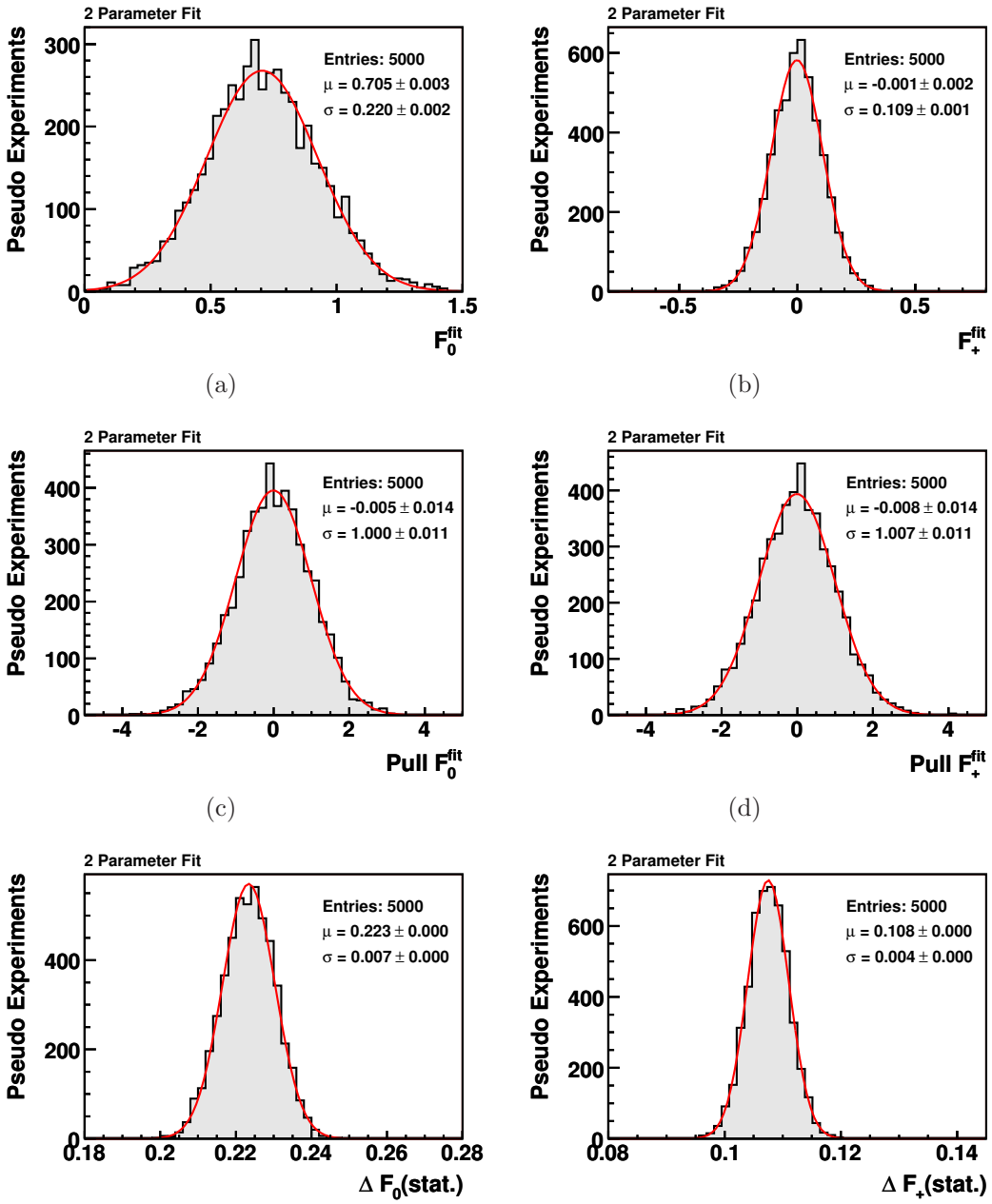

Figure 4.26: Distribution of the fit values F_0 in (a) and F_+ in (b) and the corresponding pull distributions in (c) and (d) for the two-parameter fit. The pull is defined as $(F^{\text{fit}} - F^{\text{true}})/\sigma_{F^{\text{fit}}}$. (e) and (f) Distributions of the statistical uncertainties of each pseudo experiment.

in perfect agreement with the expected values of $F_0 = 0.7$ and $F_+ = 0.0$. Another quality criterion for a method is the so-called pull distribution which is defined as the difference between the fit value and the true value divided by the statistical uncertainty of the fit:

$$\text{pull} = \frac{F_{0/+}^{\text{fit}} - F_{0/+}^{\text{true}}}{\sigma_{F_{0/+}^{\text{fit}}}} \; . \tag{4.35}$$

For a consistent method the mean of the pull distribution is expected to be zero. The width of the pull distribution is a measure of the correctness of the estimated statistical uncertainty. A width of 1.0 corresponds to a correct error estimation of the single fit results. The pull distributions of the one-parameter fits and the two-parameter fit displayed in figures 4.25 and 4.26 (c) and (d) are as expected and thus proof the consistency of the method.
In addition the average statistical uncertainties of the single measurements are estimated. The distributions of the statistical uncertainties of the single measurements obtained from pseudo experiments are presented in figures 4.25 and 4.26 (e) and (f). The average statistical uncertainties of the two one-parameter fits are $\Delta F_0(\text{stat.}) = \pm 0.10$ and $\Delta F_+(\text{stat.}) = \pm 0.05$. The corresponding uncertainties of the two-parameter fit are $\Delta F_0(\text{stat.}) = \pm 0.22$ and $\Delta F_+(\text{stat.}) = \pm 0.11$.

4.3.6 Linearity Check

In order to test that W-boson helicity-fractions deviating from the SM predictions are measured correctly, linearity checks with samples of simulated $t\bar{t}$ events with different values for F_0 and F_+ are performed. For varied right-handed fractions MadGraph/MadEvent samples are used, while the outcome for different longitudinal fractions is studied using Ggwig samples. A list of all used samples can be found in appendix A.1.
Since simulated $t\bar{t}$ events generated with MadGraph/MadEvent or Ggwig are used as pseudo data while events generated with Pythia are used to obtain ϵ_i^{rel} and S, the results of these pseudo experiments have to be corrected for the bias introduced by comparing different event generators. The bias is estimated in pseudo experiments using the MadGraph/MadEvent or Ggwig samples with SM settings as pseudo signal and comparing the results to the mean values of the consistency check.
For each input value of F_0 and F_+ 5,000 pseudo experiments are performed. The distribution of the obtained fit results is then fitted with a Gaussian and the mean fit result is calculated. Performing a large number of pseudo experiments, the uncertainty on this mean value reflects only the statistical uncertainty due to the number of pseudo experiments, but not the uncertainty due to the limited statistics of the used MC samples. In order to account also for the latter, for each fit scenario and each used sample of simulated $t\bar{t}$ events one pseudo experiment is performed using the full statistics of the given signal sample and accordingly scaled background contributions. The statistical uncertainties on the results obtained in these single pseudo experiments with maximal MC statistics are proper estimates for the uncer-

True values		One-parameter fits		Two-parameter fit	
F_0	F_+	F_0	F_+	F_0	F_+
0.70	0.00	–	0.00 ± 0.01	0.70 ± 0.02	0.00 ± 0.01
0.70	0.05	–	0.06 ± 0.01	0.68 ± 0.03	0.07 ± 0.02
0.70	0.10	–	0.10 ± 0.01	0.65 ± 0.03	0.13 ± 0.02
0.70	0.15	–	0.16 ± 0.01	0.70 ± 0.03	0.16 ± 0.02
0.70	0.20	–	0.20 ± 0.01	0.69 ± 0.03	0.21 ± 0.02
0.70	0.25	–	0.26 ± 0.01	0.71 ± 0.03	0.25 ± 0.02
0.70	0.30	–	0.29 ± 0.01	0.71 ± 0.03	0.28 ± 0.02
0.50	0.00	0.49 ± 0.02	–	0.49 ± 0.04	-0.01 ± 0.02
0.60	0.00	0.60 ± 0.02	–	0.62 ± 0.04	-0.01 ± 0.02
0.80	0.00	0.80 ± 0.02	–	0.78 ± 0.04	0.01 ± 0.02
0.90	0.00	0.91 ± 0.02	–	0.92 ± 0.03	0.00 ± 0.02

Table 4.6: Linearity check of the fit method using MC samples with different helicity fractions. The mean values obtained by performing 5,000 pseudo experiments are presented for the one-parameter and the two-parameter fit. The uncertainty on the mean fit results are estimated performing single pseudo experiments using the full statistics of the corresponding MC sample and determining the statistical uncertainty of these pseudo experiments.

tainties on the mean fit values that can be obtained with the limited statistics of the given MC samples.
The one-parameter fits are based on the assumed SM value for F_0 or F_+. Thus, performing the measurement on a MC sample in which this assumption is not valid, will yield meaningless results. Consequently, in the one-parameter fits only the respective altered fraction is fitted, either F_0 in the Ggwig samples or F_+ in the MadGraph/MadEvent samples. Within the estimated uncertainties the results for the different input values of F_0 and F_+, summarized in table 4.6, show good agreement with the true values and the method proofs to be bias free.

4.3.7 Systematic Uncertainties

The systematic uncertainties of the fit results caused by uncertainties in the theoretical model and the experimental setup are studied performing 5,000 pseudo experiments for each source of systematic uncertainties. Depending on the systematic uncertainty under study the events are drawn from the corresponding dedicated sample of simulated $t\bar{t}$ events. A compilation of the special systematic MC samples can be found in appendix A.3.
The individual systematic uncertainty is given by the difference between the mean fit result obtained from the pseudo experiments using the systematic sample and the mean fit result obtained from pseudo experiments in which the signal events are drawn from the default MC sample. If available, positive and negative variations obtained are conservatively symmetrized by choosing the larger deviation for the

uncertainty in both directions. In the following the uncertainties considered are described.

MC Generator

In order to estimate the uncertainty on the measurement due to the modelling of $t\bar{t}$ signal events, two different MC generators are compared with each other. The pseudo signal events are either drawn from the default sample generated with Pythia or from a sample generated with Herwig.

Initial- and Final-State Radiation

The influence of variations in the initial- and final-state radiation (ISR, FSR) is estimated by utilizing samples of simulated events for which the simulation was altered to produce either less or more gluon radiation compared to the standard settings. Specifically, two parameters controlling the parton shower in the Pythia program are varied: Λ_{QCD} and the scale factor K to the transverse momentum scale of the showering. The different settings are derived from studies of ISR in Drell-Yan events. All differences between the default sample and the samples with less or more radiation are determined and the largest deviation is taken as systematic uncertainty.

Parton Distribution Function

The contribution to the total systematic uncertainty arising from the uncertainties on the PDF used for the generation of the simulated events is estimated by comparing the default PDF Cteq5l [147] with Mrst72 [148]. In addition the difference between Mrst72 and Mrst75 is investigated. The Cteq6m [149] PDF is parametrized in 20 eigenvectors each corresponding to one potential source of systematic uncertainty. In order to cover all sources of uncertainties the negative and positive variations of these eigenvectors are studied. All these different settings are considered by reweighting the $\cos\theta^*$ distributions according to the varied parameters and using the reweighted distribution as input for the pseudo experiments. The uncertainties of the individual contributions are added in quadrature.

Variations in the Jet Energy Scale

The uncertainty of the measurement due to the uncertainty in the jet energy scale is quantified by varying the jet energy corrections within one standard deviation as defined in [98] in both the negative and the positive direction. As a result, the event yield as well as the reconstructed kinematics change and thus the resulting $\cos\theta^*$ distribution is altered.

Background Shape

Variations in the background normalization are already accounted for in the likelihood function by the background normalization parameter β and the Gauss con-

	One-parameter fits		Two-parameter fit	
Uncertainty	ΔF_0	ΔF_+	ΔF_0	ΔF_+
Jet energy scale	0.045	0.025	0.016	0.032
ISR	0.010	0.003	0.036	0.014
FSR	0.025	0.011	0.045	0.016
MC generator	0.012	0.005	0.015	0.002
Bkg modelling	0.032	0.019	0.028	0.032
PDF	0.005	0.002	0.014	0.006
Total	0.063	0.034	0.069	0.050

Table 4.7: Systematic uncertainties of the one-parameter fits and the two-parameter fit. The total systematic uncertainties are defined as the square root of the quadratic sum of the individual contributions.

straint.
In order to address the uncertainties arising from possible mismodelling of the different background shapes of the $\cos\theta^*$ distribution, pseudo experiments with different relative fractions of background contributions are performed.
For this purpose the contribution of one of the four background categories is modelled by one of the remaining three templates. All combinations are considered and the largest deviation with respect to the default modelling is taken as systematic uncertainty.

The analysis is carried out using samples of simulated $t\bar{t}$ events in order to derive the event-selection efficiency and the resolution of the reconstruction. These events have been generated with a top-quark mass of $175\,\mathrm{GeV}/c^2$. Since the fraction of longitudinally polarized W bosons, F_0, explicitly depends on the value of the top-quark mass, the dependency of the measured result on m_t is not treated as systematic uncertainty. The measured value of F_+ is only negligibly affected by variations in the assumed top-quark mass.
Table 4.7 summarizes the individual contributions to the total systematic uncertainties for the three fit scenarios. In total the systematic uncertainties for the one parameter fits are $\Delta F_0 = \pm 0.06$ and $\Delta F_+ = \pm 0.03$, respectively. For the two parameter fit the total systematic uncertainties are estimated to be $\Delta F_0 = \pm 0.07$ and $\Delta F_+ = \pm 0.05$.

4.4 Results

The observed $\cos\theta^*$ distribution obtained from the selected dataset by applying the full kinematic reconstruction to each event is shown in figure 4.27. This distribution is subjected to the two one-parameter fits, in which either F_0 or F_+ are measured and the respective other fraction is fixed to its value predicted by the standard model, and to the model independent two-parameter fit. In the following the results for these three fit scenarios are presented.

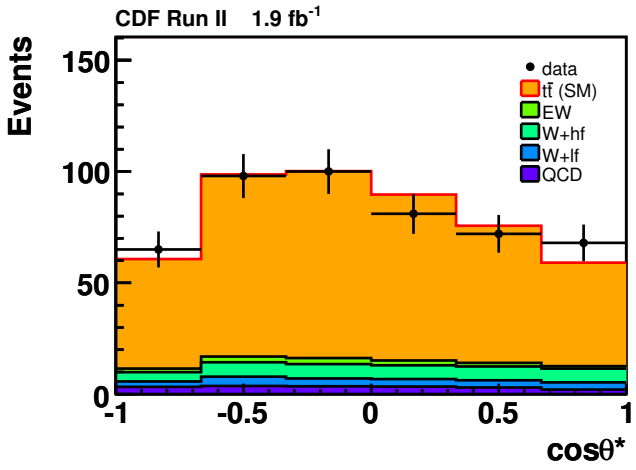

Figure 4.27: Observed $\cos\theta^*$ distribution in the selected dataset. The $t\bar{t}$ signal modelling is obtained from the default standard model MC sample.

4.4.1 One-Parameter Fit Results

The fraction of longitudinally polarized W bosons F_0 is measured assuming that there are no right-handed W bosons. The fraction of right-handed W bosons F_+ is measured under the assumption of the SM value $F_0 = 0.7$. The negative logarithms of the likelihood functions for these two fit scenarios are presented in figure 4.28 (a) and (c). The results of these two measurements are:

$$\begin{aligned} F_0(F_+ = 0.0) &= 0.66 \pm 0.10\ (\text{stat.})\ \pm 0.06\ (\text{syst.}) \\ F_+(F_0 = 0.7) &= 0.01 \pm 0.05\ (\text{stat.})\ \pm 0.03\ (\text{syst.}) \end{aligned}$$

In both cases the fitted value of the background normalization parameter β is obtained to $\beta = 1.02 \pm 0.20$. The statistical uncertainty of the two results is consistent with the expected value derived from pseudo experiments. Both results are within the uncertainties in good agreement with the SM predictions of $F_0 = 0.7$ and $F_+ = 0.0$. In order to estimate the probability to obtain such results given the SM fractions, the fraction of pseudo experiments yielding larger deviations from the SM

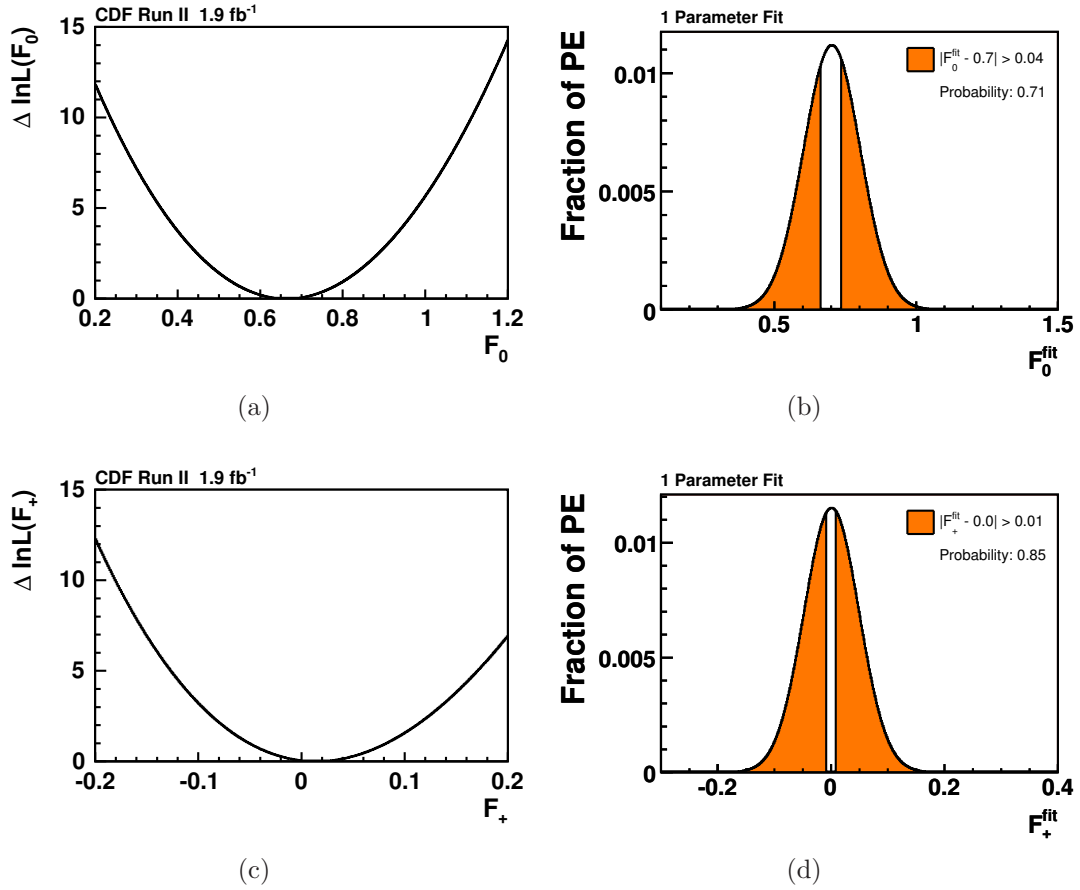

Figure 4.28: $\Delta \ln L$ as (a) a function of F_0 with fixed right-handed fraction and (c) as a function of F_+ with fixed longitudinal fraction. The Gaussians fitted to the distributions of the fit results for the consistency check of the two one-parameter fits are shown in (b) and (d). The areas yielding results with larger deviations than the actual measurements are indicated in orange.

predictions than the observed results is calculated. The probability to measure F_0 with a larger deviation from 0.7 than the measured value of $F_0 = 0.66$ is estimated to be 71% and the probability to measure F_+ with a deviation of 0.01 or more from zero is estimated to be 85%.

Since the measured F_+ is compatible with the SM prediction of zero within statistical and systematic uncertainties, no evidence for a nonzero fraction of right-handed W bosons from top-quark decays is observed. Consequently, an upper limit on F_+ can be calculated. In order to account for the systematic uncertainties the likelihood function $L(F_+)$ is convoluted with a Gaussian centered around zero and with a width corresponding to the estimated overall systematic uncertainty. The probability density $P(F_+)$ is calculated by dividing this smeared likelihood function $L(F_+)$ by the integrated likelihood function. In a Bayesian approach the integration is carried out only in the physical allowed region $0 \leq F_+ \leq 0.3$ by applying a flat prior which is

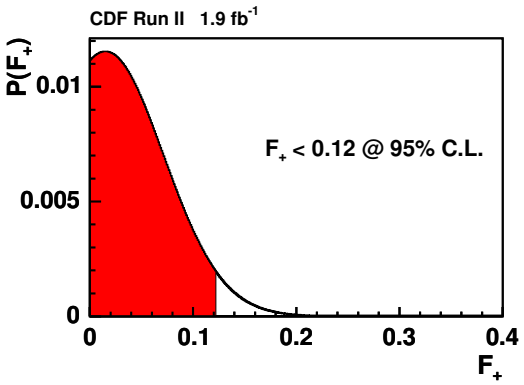

Figure 4.29: Posterior probability density of the one-parameter fit of F_+ assuming $F_0 = 0.7$. The 95% coverage region is indicated in red.

one in the interval $[0, 0.3]$ and zero elsewhere:

$$P(F_+) = \frac{L(F_+)}{\int_{0.0}^{0.3} L(F_+)dF_+} \; . \tag{4.36}$$

The posterior probability density is integrated from zero to the maximal value $F_+^{\max}$ that yields a coverage of 95% of the total area of $P(F_+)$. Figure 4.29 shows the posterior probability density with the region corresponding to a confidence level (C.L) of 95% indicated in red. The upper limit on F_+ is estimated to be

$$F_+ < 0.12 \; @ \; 95\% \text{ C.L.} \; .$$

Given the observed results it is possible to obtain an unfolded $\cos\theta^*$ distribution corrected for acceptance and resolution. After subtracting the background estimate and correcting the reconstructed distribution by applying a bin-by-bin correction factor the resulting unfolded distribution can be compared to theory predictions. The correction factor

$$C_i(F_0, F_+) = \frac{\hat{\mu}_i^{\text{sig,theo}}}{\hat{\mu}_i^{\text{sig,rec}}} \tag{4.37}$$

translates the observed distribution into the undistorted parton level distribution corresponding to the measured values of F_0 and F_+. The correction factors C_i explicitly depend on the values of F_0 and F_+ and for each of the two one-parameter measurements the observed distribution has to be corrected independently. Figure 4.30 shows the unfolded distribution for the result of the F_0 measurement and for the result of the F_+ measurement. The distributions are normalized to the theoretically predicted $t\bar{t}$ cross section and are compared to theoretical curves corresponding to different proportions of helicity fractions. Both differential cross section distributions demonstrate the compatibility of the measured results with the SM prediction.

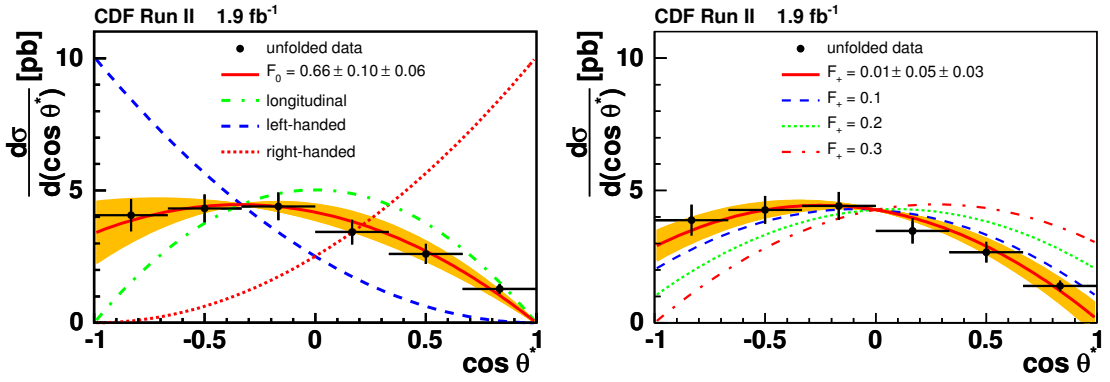

(a) (b)

Figure 4.30: $\cos\theta^*$ distributions corrected for acceptance and resolution using the obtained fit results. The yellow band around the fit curve indicates the total uncertainty on the measurement. In (a) the three curves corresponding to purely left-handed, purely right-handed and purely longitudinally polarized W bosons are shown for comparison. In (b) the corrected distribution is compared to three curves corresponding to F_+ values of 0.1, 0.2, and 0.3, respectively.

4.4.2 Two-Parameter Fit Results

In the third fit scenario neither F_0 nor F_+ are fixed, but both fractions are simultaneously fitted. The obtained results are:

$$\begin{aligned} F_0 &= 0.38 \pm 0.21\ (\text{stat.}) \pm 0.07\ (\text{syst.}) \\ F_+ &= 0.15 \pm 0.10\ (\text{stat.}) \pm 0.05\ (\text{syst.}) \end{aligned}$$

The statistical uncertainty of the measurement is slightly reduced compared to the expected value of 0.22 for F_0 and 0.11 for F_+, obtained from pseudo experiments. The fitted value of the β parameter in this measurement is $\beta = 1.0 \pm 0.2$. The correlation between F_0 and F_+ in the two-parameter fit is determined to be -0.89. Due to this high degree of anticorrelation the low observed F_0 and the large F_+ value condition each other. Figure 4.31(a) shows the two-dimensional $\Delta \ln L$ distribution with the observed minimum indicated. The point corresponding to the SM prediction in the F_0 – F_+ plane is marked by a star and lies within the 68% contour around the observed result.
The probability of observing a larger discrepancy than the observed one, given the SM values of F_0 and F_+, is estimated performing 5,000 pseudo experiments. In each pseudo experiment the difference between the value of the likelihood function for the SM values and the minimal value of the likelihood function, $\ln L(0.7, 0.0) - \ln L(F_0^{\text{fit}}, F_+^{\text{fit}})$, is calculated. Figure 4.31(b) shows the corresponding distribution. The fraction of pseudo experiments yielding a deviation larger than the observed one of 1.1 is estimated to be 34%.

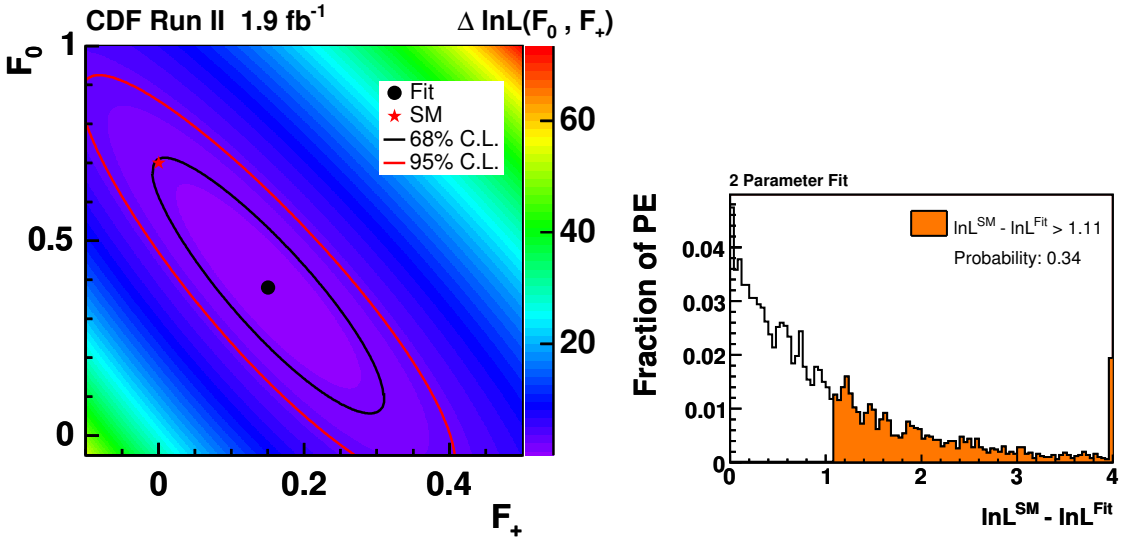

(a) (b)

Figure 4.31: (a)$\Delta \ln L$ of the two-parameter fit. The contours corresponding to the 68% and 95% confidence level (C.L.) are indicated by the black and the red ellipse. The minimum is indicated by the black dot, while the star denotes the SM values. (b) Difference between the values of $\ln L$ for the SM values and for the fitted values of F_0 and F_+ from 5,000 pseudo experiments. The fraction of pseudo experiments (PE) yielding a larger deviation compared to the measured values of F_0 and F_+ is marked in orange.

The presented measurements of the W-boson helicity fractions on a dataset corresponding to an integrated luminosity of $1.9\,\mathrm{pb}^{-1}$ using the distribution of $\cos\theta^*$ yield results that are within statistical and systematic uncertainties consistent with the values predicted by the SM. Although the two-parameter fit suggests a smaller amount of longitudinally polarized W bosons and a relatively large fraction of right-handed W bosons, the probability to observe such a deviation from the SM values or an even larger one is estimated to be 34% and thus the measured deviations are not statistically significant.

Chapter 5

Prospects for an Early $t\bar{t}$ Cross-Section Measurement with CMS

For more than one decade the Tevatron at Fermilab has been the only collider in the world capable of producing top quarks. But now, with the LHC being operational, a new era in top-quark physics will soon be entered. Due to its large center-of-mass energy the LHC will produce top quarks copiously and can be considered a top-quark factory. Figure 5.1 illustrates the theoretically predicted cross sections for several processes in $p\bar{p}$ and pp collisions as a function of the center-of-mass energy. While the NLO $t\bar{t}$ production cross-section increases strongly from $7.61^{+0.60}_{-0.65}$ pb at the Tevatron with a center-of-mass energy of $\sqrt{s} = 1.96\,\text{TeV}$ to $414^{+41}_{-33}\,\text{pb}$ at the LHC at $\sqrt{s} = 10\,\text{TeV}$, the major background processes like W- and Z-boson production or the production of b quarks do not show such a strong increase. From this it can be expected that it will be possible to select large $t\bar{t}$ enriched datasets and to study top quarks with unprecedented statistics and precision. Consequently the precise determination of the properties of the top quark are of particular interest in the LHC physics program, besides the search for the Higgs boson and new physics beyond the SM. A first step towards this new era of precision measurements in the top-quark sector is the rediscovery of $t\bar{t}$ production with early data and the measurement of its cross section.

Furthermore, top-quark physics is not only interesting for its own sake, but plays also a key role in the process of commissioning the two large multipurpose detectors at the LHC. Top quark events in the lepton+jets channel contain almost all relevant experimental signatures which need to be understood in order to claim successful detector commissioning, such as jets, missing transverse energy, and charged leptons. Establishing a $t\bar{t}$ signal and measuring the production cross-section can therefore be considered as a milestone on the way to a fully commissioned, aligned, and understood detector. In addition, $t\bar{t}$ production will constitute a major background to searches for new physics processes and a precise determination of its cross section is therefore crucial for many LHC analyses.

In the study described in this chapter, the potential of CMS to measure the $t\bar{t}$ production cross-section in the lepton+jets channel with early data corresponding

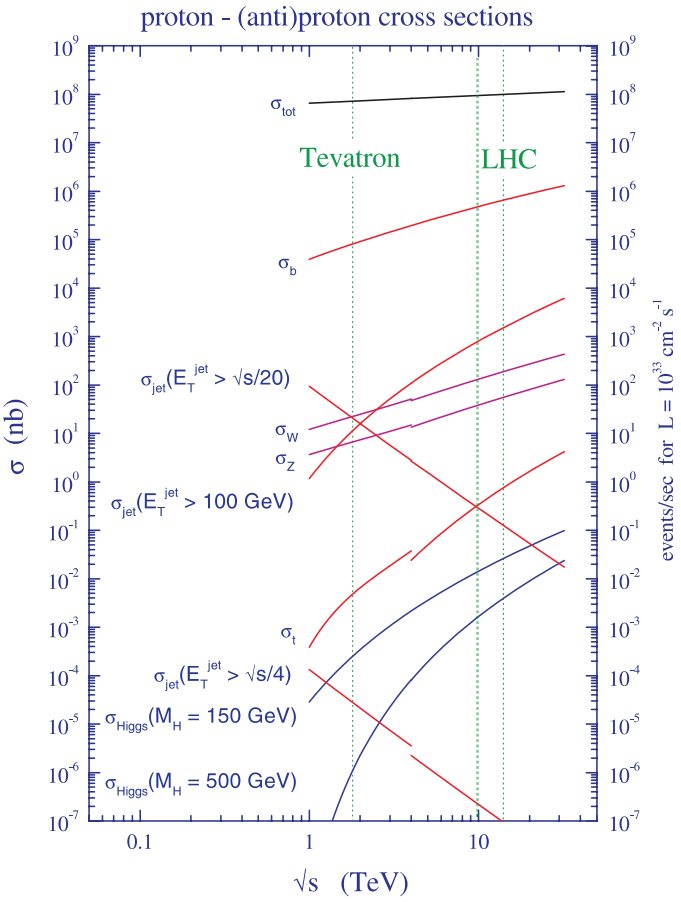

Figure 5.1: Next-to-leading order cross sections for different processes for proton-antiproton (for $\sqrt{s} < 4\,\text{TeV}$) and proton-proton collisions (for $\sqrt{s} > 4\,\text{TeV}$) as a function of $\sqrt{s}$. The center-of-mass energies $\sqrt{s} = 1.96\,\text{TeV}$ of the Tevatron and $\sqrt{s} = 10\,\text{TeV}$ for an early period of data taking and the design value $\sqrt{s} = 14\,\text{TeV}$ of the LHC are indicated by the dotted green lines.

to an integrated luminosity of $20\,\text{pb}^{-1}$ collected at a center-of-mass energy of 10 TeV is investigated. Since the reconstruction of electrons and muons and the expected background contributions are quite different for the two different channels, most CMS studies on final states containing leptons for the early days of data taking restrict themselves either to electrons or to muons. The study described in this chapter covers the electron+jets channel. Parts of it have been published in [9], while a study on the prospects for an early $t\bar{t}$ cross-section measurement in the muon+jets channel can be found in [8]. The developed method consists of three main parts, the selection of $t\bar{t}$ candidate events, the estimation of certain background contributions, and the extraction of the $t\bar{t}$ cross section by exploiting the discrimination power of a suitable observable. The three steps of the analysis method and studies on the statistical and systematic uncertainties of this early measurement are presented in the following sections.

5.1 Event Selection and Signal and Background Modelling

The aim of this study is to evaluate the prospects for a measurement of the $t\bar{t}$ production cross-section in the electron+jets channel with early $20\,\mathrm{pb}^{-1}$ of collision data at a center-of-mass energy of 10 TeV. The study is performed using samples of simulated events for $t\bar{t}$ production and the relevant background processes. In the electron+jets channel, one top quark decays semileptonically into an electron, the corresponding neutrino, and a b quark, see figure 5.2. The other top quark decays hadronically into two non-b quarks and a b quark[1]. The event selection applied on the simulated events in order to select $t\bar{t}$ candidate events exploits the experimental signature of four jets, exactly one electron, and missing transverse energy.
In the following sections the relevant background processes and the modelling of signal and background processes are described and the selection criteria are discussed.

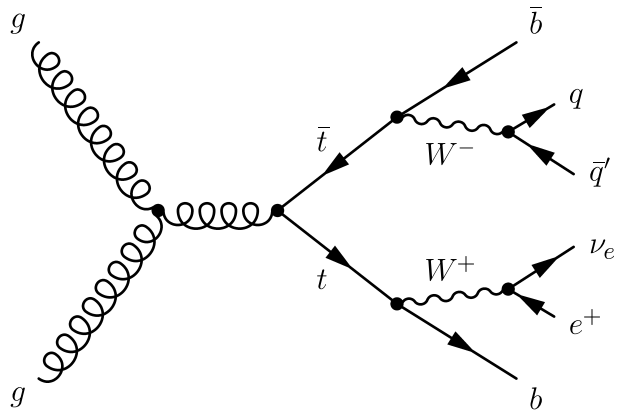

Figure 5.2: LO Feynman diagram of $t\bar{t}$ production via gluon-gluon fusion and the decay of the top quarks in the electron+jets channel: one top quark decays semileptonically into a b quark and an electron and an electron-neutrino and the other top quark decays hadronically into three quarks.

5.1.1 Main Backgrounds in the Electron+Jets Channel

The major backgrounds that mimic the experimental signature of $t\bar{t}$ events in the electron+jets channels can be broadly divided into two categories. They are either background events with real prompt electrons like W-boson, Z-boson, or single top-quark production in association with additional jets, or background events with fake or secondary electrons arising from QCD multijet processes.

[1] Actually either the W^+ from the top quark or the W^- from the anti top-quark decays leptonically and the respective other one hadronically. Thus the decay products from the leptonical decay are either e^+ and ν_e or e^- and $\bar{\nu}_e$. For the sake of simplicity this decay is in the following always described as the decay of a W boson into an electron and electron-neutrino, where the latter are used as umbrella terms for electron/positron and neutrino/antineutrino.

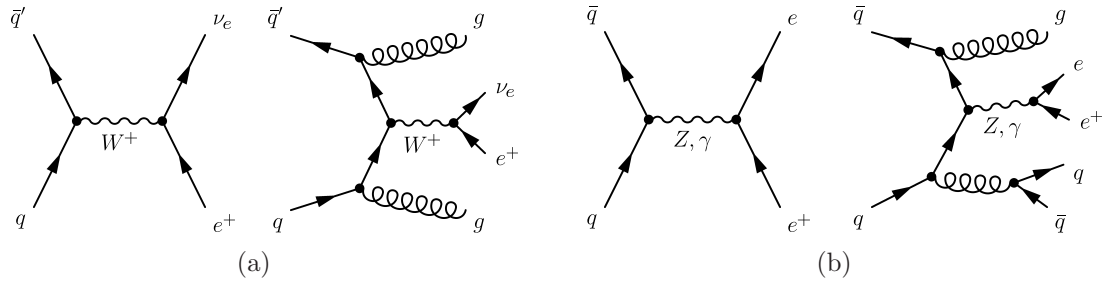

Figure 5.3: Feynman diagrams for the production of (a) W bosons and (b) Z bosons. In addition to the LO processes also examples for higher order processes with additional partons in the final state are depicted. Depending on the number of additional gluons and quarks these processes can exhibit signatures similar to that of $t\bar{t}$ events in the electron+jets channel.

W+Jets and Z+Jets Production

The main background contribution arises from processes in which on-shell W bosons or Z bosons are produced. If accompanied by additional jets due to higher order effects, the produced W and Z bosons can lead to an experimental signature similar to that of $t\bar{t}$ events. Figure 5.3 provides some Feynman diagrams of these processes. Especially the production of W bosons with additional jets mimic the electron+jets topology of $t\bar{t}$ events if the W boson decays leptonically into an electron and an electron-neutrino. In case of Z-boson production one of the produced electrons has to fail the electron requirements of the applied event selection in order to satisfy the requirement of exactly one identified electron candidate.

Single Top-Quark Production

The background process with the most $t\bar{t}$ like event topology is the electroweak production of single top-quarks, which can take place via three different modes. In the s-channel, illustrated in figure 5.4(a), an incoming quark and an incoming antiquark produce a virtual W boson which decays into a top quark and a b quark. In the t-channel, depicted in figure 5.4(b), an incoming light quark and a b quark interact via the exchange of a W boson. By this interaction the b quark changes flavor into a top quark. In the third production mode the single top quark is produced in association with a real W boson and this channel is therefore referred to as the tW-channel, see figure 5.4(c). For the latter two production mechanisms the incoming b quark is a sea quark from the splitting of virtual gluons inside the proton. When accompanied by additional jets, single top-quark production exhibits the same experimental signature as $t\bar{t}$ events. If the W boson in the tW-channel decays hadronically, already the LO final state of this production mode consists of three quarks. Therefore this channel constitutes the main contribution to the background from single top-quark production.

QCD Multijet Backgrounds

All background processes discussed so far contain prompt electrons from the hard

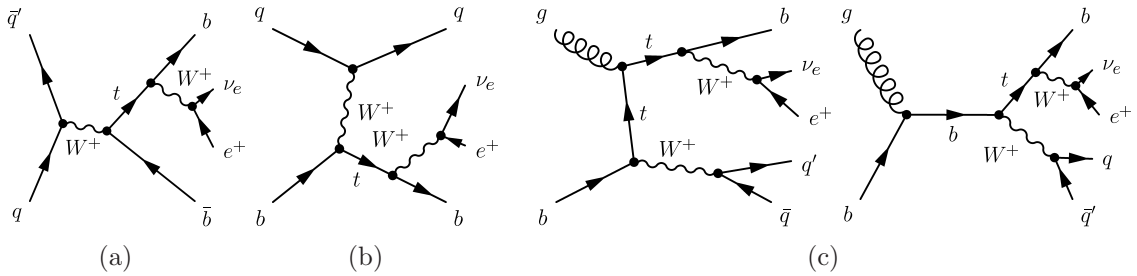

Figure 5.4: LO Feynman diagrams for the electroweak production of single top-quarks via (a) the s-channel, (b) the t-channel, and (c) the associated production (tW-channel). In all cases the top quark decays semileptonically into a b quark and an electron and the corresponding neutrino. The additional W boson in (c) decays hadronically. When accompanied by additional quarks or gluons from higher order radiation the final state of these processes can be similar to the $t\bar{t}$ final state.

process in the final state, either from a decaying W boson or from a decaying Z boson. In addition to these processes, also events with secondary electrons from the decay of hadrons containing b or c quarks during the hadronization process or from the conversion of a photon into an electron-positron pair have to be considered. Furthermore, electron signatures can be faked by jets or charged pions and kaons that are misinterpreted as electron candidates. A background process which can lead to secondary or fake electrons is the production of jets via the strong interaction. The partonic final state of these events contains only gluons and quarks and the electrons or electron-like objects originate from radiation or decay of particles within jets. In figure 5.5 two example Feynman diagrams for multijet production are illustrated. Although the probability for jets or charged pions or kaons to fake an electron and the probability for secondary electrons to pass the stringent quality criteria applied to the electron candidates is very small, these processes can still contribute considerably to the total amount of background events due to their enormous cross section.

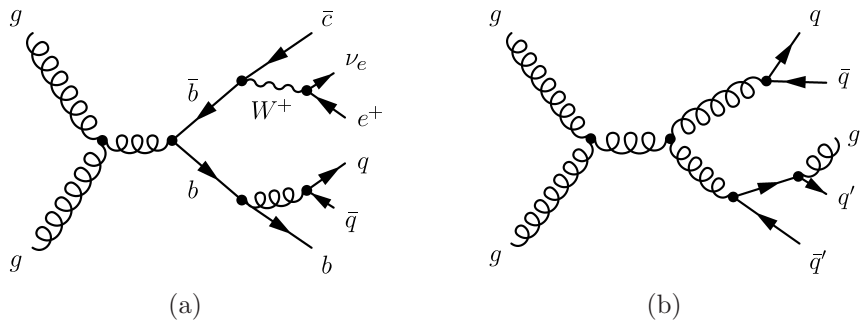

Figure 5.5: Example Feynman diagrams for QCD processes. In (a) the direct production of $b\bar{b}$ is illustrated with additional gluon radiation. One b quark decays in the process of hadronization into a c quark and an electron and neutrino. In (b) the production of four quarks and one gluon is depicted, which then hadronize into five jets. A photon emitted from one of the resulting jets can convert into a secondary e^+e^- pair, or a charged pion or kaon in one of the jets, generated in the hadronization process can fake an electron.

5.1.2 Signal and Background Modelling

In the absence of real high-energy collision data, samples of simulated events are the ingredients of this study. The cross sections of the different processes considered in this study vary over a large range. In order to achieve reliable estimates for the number of selected events for each process and in order to model kinematic distributions with sufficient statistics a large number of simulated events for each process is desirable. For the purpose of a realistic event yield corresponding to a dataset of an integrated luminosity of $20\,\mathrm{pb}^{-1}$ the events of the different samples have to be weighted with the process dependent factor w that accounts for the cross section of the process and the number of generated events in the sample. For a process with cross section σ this factor is defined as

$$w = \frac{L \cdot \sigma \cdot f}{N} \ , \tag{5.1}$$

where L is the integrated luminosity ($20\,\mathrm{pb}^{-1}$ in the case of this study) and N is the number of generated events in the sample. For some processes it is convenient to apply a filter on generator level. This reduces the number of events that have to be generated in order to achieve a sufficient number of events that have a chance to survive the event selection. The product of the cross section σ and the filter efficiency f is also referred to as effective cross section. If available, NLO cross sections are used for the calculation of the event weights of the various processes.
The samples used in this study have been generated within the 2.1 and 2.2 cycles of the CMS software framework (CMSSW) and for the detector simulation the full simulation has been used.

Modelling of $t\bar{t}$ Signal Events and the Single Top-Quark Background

Signal events and single top-quark background events are simulated with MadGraph/MadEvent using a top-quark mass of $170.9\,\mathrm{GeV}/c^2$. The top quarks are accompanied by up to four additional hard jets. These hard parton configurations are matched to the parton shower from Pythia using the MLM matching scheme. The generated final-state partons are handed over to Pythia for the simulation of the hadronization and the decay of unstable particles. The cross sections, numbers of generated events, and the weighting factors to scale the number of events to an integrated luminosity of $20\,\mathrm{pb}^{-1}$ can be found in table 5.1 for the different processes.

Modelling of the W+Jets and Z+Jets Backgrounds

Like $t\bar{t}$ and single top-quark production, also the production of W bosons and Z bosons is simulated using MadGraph/MadEvent interfaced to Pythia for the simulation of the showering and the hadronization. Again the MLM scheme is used for the matching procedure. In order to reduce the number of events that have to be simulated, only leptonically decaying W bosons and Z bosons are generated. For Z-boson production also the matrix elements containing a virtual photon have to be included. On generator level a lower threshold of $50\,\mathrm{GeV}/c^2$ on the invariant mass

Process	$\sigma \cdot f$ [pb]	generated events N	event weight w
$t\bar{t}$, inclusive	414.0	1,028,322	0.00805
s-channel, $t \to b\ell\nu_\ell$	1.6	11,999	0.00280
t-channel, $t \to b\ell\nu_\ell$	42.1	281,756	0.00296
tW-channel, inclusive	29.0	169,048	0.00340

Table 5.1: Processes containing top quarks: $t\bar{t}$ and single top-quark production. All samples are produced using a top-quark mass of $170.9\,\mathrm{GeV}/c^2$. The quoted cross sections are NLO values. The t-channel cross section has been calculated at $\sqrt{s} = 10\,\mathrm{TeV}$ as in [150], while the values for s-channel and tW-channel have been rescaled from the values for $\sqrt{s} = 14\,\mathrm{TeV}$ given in [150] and [151]. For the single top-quark production in the s- and t-channel only events in which the top quark decays semileptonically via $t \to b\ell\nu_\ell$ with $\ell = e, \mu, \tau$ are generated. The branching fraction is included in the effective cross sections. The event weights correspond to an integrated luminosity of $20\,\mathrm{pb}^{-1}$.

Process	$\sigma \cdot f$ [nb]	generated events N	event weight w
W+jets, $W \to \ell\nu_\ell$	45.6	10,334,223	0.0883
Z+jets, $Z \to \ell^+\ell^-$	4.2	1,163,479	0.0725

Table 5.2: W+jets and Z+jets production. The quoted cross sections are $\geq$ 0-jets inclusive LO values scaled with a K factor, derived from [152], to obtain NLO estimates. They also include the branching ratio for the leptonic decay of the vector bosons via $W \to \ell\nu_\ell$ and $Z \to \ell^+\ell^-$ with $\ell = e, \mu, \tau$. The event weights correspond to an integrated luminosity of $20\,\mathrm{pb}^{-1}$.

of the two charged leptons from the decay of the Z boson is applied in order to increase the statistics of events that have a chance to pass an event selection requiring a high-p_T charged lepton. The parameters of these processes and the corresponding MC samples are listed in table 5.2.

Modelling of the QCD Multijet Background

Due to the large cross section of QCD multijet processes a huge number of events has to be generated and filters on generator level have to be applied in order to achieve a reasonable number of simulated events passing the event selection. As can be seen from the event weights in table 5.3 even the large number of generated events is not sufficient to rely on the simulated samples in order to describe kinematic distributions. Nevertheless the samples of simulated events can still be used to get an impression of the order of magnitude of the expected QCD background contribution. The events are simulated using the Pythia event generator. In order to increase the statistics of events that have a chance to pass the electron selection requirements two filters on generator level are applied.
The first filter (BCtoE) searches for events that contain electrons having at least an energy of 10 GeV and that originate from the decays of hadrons containing b or c quarks and fall within the tracker acceptance. Also multi step decays are taken into account.

Process	$\hat{p}_T$ [GeV]	$\sigma \cdot f$ [nb]	generated events	event weight
e from b/c hadrons	$20-30$	192	2,218,990	1.730
e from b/c hadrons	$30-80$	240	2,032,649	2.361
e from b/c hadrons	$80-170$	22	798,039	0.571
em-enriched QCD	$20-30$	3,200	19,662,277	3.257
em-enriched QCD	$30-80$	4,700	36,080,803	2.604
em-enriched QCD	$80-170$	285	5,661,833	1.007

Table 5.3: QCD multijet background samples. The two different samples are subsamples of the inclusive multijet sample. The two orthogonal samples are each further divided into three $\hat{p}_T$ regions. The quoted effective cross sections are LO values. The event weights correspond to an integrated luminosity of $20\,\mathrm{pb}^{-1}$.

The second filter (em-enriched) operates on stable final-state particles and searches for candidate objects that are likely to be reconstructed as electrons. This filter module consists of two components. The first component clusters the energy from photons, electrons, charged pions, and charged kaons with $E_T \geq 1\,\mathrm{GeV}$ which fall into the tracker acceptance. The total transverse energy of the cluster is required to exceed 20 GeV. The second component of this filter searches for single electrons, charged pions, and charged kaons with transverse energies larger than 20 GeV within the tracker acceptance. In order to ensure that the found objects are isolated, in both components a generator-level isolation-energy is calculated and an upper threshold on this energy is applied. The em-enriched filter includes an explicit veto on events passing the BCtoE filter in order to avoid double counting of events if using both samples.
The cross section for QCD multijet events decreases strongly with increasing transverse momentum of the hard process, $\hat{p}_T = \sqrt{\frac{\hat{t}\hat{u}}{\hat{s}}}$, where $\hat{t}$, $\hat{u}$, and $\hat{s}$ are Mandelstam variables. The samples are therefore generated separately for three different ranges in $\hat{p}_T$. The parameters for the six subsamples can be found in table 5.3.

5.1.3 Event Selection

For the purpose of the selection of events with an electron+jets signature a set of requirements is applied to all generated events, starting with the trigger request and the identification of electron candidates. In addition at least four jets satisfying several quality criteria are required. In order to reduce certain amounts of background events, further cuts are applied to all remaining events. The single steps of the event selection are described in the following.

Trigger

The first stage of the selection of events containing electrons is the CMS trigger system. For this study the events are required to be triggered by the high-level trigger

HLT_Ele15_LW_L1R. This single electron trigger searches for electron candidates with $E_{\mathrm{T}} > 15\,\mathrm{GeV}$ and with a supercluster with E_{T} larger than 5 GeV. Furthermore the ratio H/E of the energy of the supercluster deposited in the HCAL and the energy deposited in the ECAL has to be smaller than 0.2.

Electron Requirements

In order to be identified as electrons, candidate objects have to pass the electron identification (electron-ID) requirements. Currently, two kinds of cut based electron-IDs are available in the CMSSW framework, the fixed threshold identification and the category based identification. Each of these electron-IDs comes along in two levels of identification: loose and tight requirements.
The fixed threshold identification is aimed for early data taking and is designed to be as simple, efficient, and robust as possible. This electron-ID relies on a set of four quantities which are independent of the measured fraction of bremsstrahlung and which are insensitive to a possible tracker misalignment.

- $\boldsymbol{H/E}$: The ratio of the energy of the electron candidate deposited in the HCAL and the energy deposited in the ECAL.
- $\boldsymbol{\sigma_{\eta\eta}}$: The extent of the electron supercluster in η,

$$\sigma_{\eta\eta} = \frac{\sum_i^{5\times5} w_i(\eta_i - \bar{\eta}_{5\times5})^2}{\sum_i^{5\times5} w_i} \ , \tag{5.2}$$

  where i runs over all crystals in the 5×5 block of crystals centered on the seed crystal, η_i denotes the position in η of the i^{th} crystal, and $\bar{\eta}_{5\times5}$ is the energy weighted mean value of η of the 5×5 unit of crystals. The weight w_i of the i^{th} crystal is defined as

$$w_i = 4.2 + \ln(E_i/E_{5\times5}) \ , \tag{5.3}$$

  with E_i and $E_{5\times5}$ being the energies of crystal i and of the 5×5 block of crystals respectively.
- $\boldsymbol{\Delta\eta_{\mathrm{in}}}$: The difference in η between the supercluster of the electron candidate and the associated track at the ECAL face. The latter is calculated from the track extrapolated using the track parameters at the vertex and neglecting bremsstrahlung effects.
- $\boldsymbol{\Delta\phi_{\mathrm{in}}}$: The difference in ϕ between the supercluster of the electron candidate and the associated track at the ECAL face. The latter is calculated from the track extrapolated using the track parameters at the vertex and neglecting bremsstrahlung effects.

In the category based electron identification an additional fifth quantity is used:

	Barrel	Endcap
H/E	0.0150	0.0180
$\sigma_{\eta\eta}$	0.0092	0.0250
$\lvert\Delta\eta_{\text{in}}\rvert$	0.0025	0.0040
$\lvert\Delta\phi_{\text{in}}\rvert$	0.0200	0.0200

Table 5.4: Upper thresholds for the four variables used in the tight fixed threshold electron identification. Two different sets of cuts are used for the barrel and endcap region.

- $\boldsymbol{E_{\text{seed}}/p_{\text{in}}}$: The ratio between the energy of the supercluster seed and the momentum of the electron track at the vertex.

Furthermore in this identification scheme the electrons are categorized utilizing the fractions E/p_{in} and $f_{\text{Brem}} = \frac{p_{\text{in}}-p_{\text{out}}}{p_{\text{in}}}$, where E is the energy deposited in the ECAL and p_{in} and p_{out} are the track momenta of the electron candidate at the vertex and at the ECAL, respectively. The fraction f_{Brem} is the fraction of energy of the initial electron that is lost through bremsstrahlung on its way to the ECAL. Based on these two properties the electron candidates are categorized into three groups. Candidates with $0.8 < E/p_{\text{in}} < 1.2$ are divided into electrons with a high fraction of bremsstrahlung ($f_{\text{Brem}} > 0.06$ in the barrel region and $f_{\text{Brem}} > 0.1$ in the endcap region) and electrons with low fractions of bremsstrahlung. All electron candidates with $E/p_{\text{in}} < 0.8$ or $E/p_{\text{in}} > 1.2$ form the third category. The use of electron categories allows to account for the large differences in the ratio of real to fake electrons in the different regions in the $E/p_{\text{in}} - f_{\text{Brem}}$ plane and to tune the thresholds for the cut values of the discussed variables for each region separately.

For early analyses the recommended electron-ID to use is the fixed threshold identification, since it is more robust and less sensitive to possible tracker misalignment compared to the category based identification. The thresholds for the four used quantities are different for the barrel and the endcap region and there are two different levels of identification, one loose cut scenario and one tight cut scenario. In order to select electrons coming from W-boson decays, the tight version of the fixed threshold electron-ID has to be used. The thresholds for this electron-ID are listed in table 5.4. They have been optimized based on studies within the 1.6 cycle of the CMS software.

Electron candidates passing this tight electron identification are further required to have $E_{\text{T}} > 20\,\text{GeV}$ and to fall within the trigger acceptance of $|\eta| < 2.5$. Candidates falling into the transition region between the barrel and the endcap regions ($1.422 < |\eta| < 1.560$) are excluded, since these particles deposit considerable fractions of their energy into the uninstrumented ECAL support structures. In addition an transverse impact parameter with respect to the primary vertex less than 200 µm is required in order to select prompt electrons from the hard interaction and to reject secondary electrons.
For a further improvement of the quality of the selected electrons the candidates

have to be isolated. In contrast to the CDF lepton+jets event selection, where the excess E_{T} in the calorimeter around the lepton direction is used, an isolation variable including tracker information is used for this purpose at CMS. The relative combined isolation variable I_{rel} is calculated as the sum of the contributions from the tracker, the ECAL, and the HCAL divided by the transverse energy of the electron candidate:

$$I_{\mathrm{rel}} = \frac{I_{\mathrm{Trk}} + I_{\mathrm{ECAL}} + I_{\mathrm{HCAL}}}{E_{\mathrm{T}}} \ . \tag{5.4}$$

The tracker isolation energy I_{Trk} is defined as the sum of the transverse momenta of tracks with a p_{T} of at least $1\,\mathrm{GeV}/c$ within a cone of radius $R = 0.3$. In order to remove the footprint of the electron, the track of the electron candidate is excluded and an inner veto cone of radius $R = 0.015$ is applied. The ECAL isolation energy I_{ECAL} is calculated by summing the deposited transverse energies in the ECAL crystals in a cone of radius $R = 0.4$ centered on the supercluster. The footprint removal region consists of a strip of a specified η width of 0.04 and an additional circular region with a radius of $R = 0.045$ in the barrel and $R = 0.070$ in the endcap region. This footprint removal is intended to account for the energy deposited in a wide spread in ϕ due to the bremsstrahlung of electrons. The energies of HCAL towers are summed in a cone of radius $R = 0.4$ centered on the ECAL supercluster position associated to the electron candidate to calculate the HCAL isolation energy I_{HCAL}. To be considered as isolated the total isolation energy is required to be less than 10% of the electron's E_{T}.
Only events with exactly one reconstructed electron satisfying all described criteria are selected for further consideration.

Muon Veto

In order to be statistically independent from similar analyses in the muon+jets channel [8], events which contain muon candidates are rejected. Only global muons with $p_{\mathrm{T}} > 20\,\mathrm{GeV}/c$, $|\eta| < 2.5$, and $I_{\mathrm{rel}} < 0.2$ are considered for this veto.

Jet Requirements

Jets are clustered with the SisCone algorithm with a cone size of $R = 0.5$ and have to lie within $|\eta| < 2.4$. Relative and absolute energy corrections (Level 2 and Level 3, for details see chapter 3.3.4) are applied to the reconstructed jets. The transverse momenta of the corrected jets have to be above $30\,\mathrm{GeV}/c$.
As jets are reconstructed from energy deposits in the calorimeters, care has to be taken not to reconstruct isolated electrons as jets and the jet collection has to be cleaned from electrons. Therefore, jets which fall within $\Delta R < 0.3$ of an identified electron are considered as electrons and removed from the jet collection. The remaining number of selected jets has to be equal to four or larger to account for additional jets from higher order gluon radiation.
In contrast to the CDF event selection, in this study explicitly no b tag information is used for the selection of events in the lepton+jets channel.

In order to reduce certain background contributions, further requirements are imposed on the events.

Loose Electron Veto for the Reduction of Z+Jets Events

The background contribution coming from Z-boson production in association with additional jets is reduced by rejecting events with additional, more loosely defined electrons. For this veto all electron candidates with $E_{\mathrm{T}} > 20\,\mathrm{GeV}$, $|\eta| < 2.5$, and $I_{\mathrm{rel}} < 0.3$ are considered. No electron-ID or impact parameter cut is applied. The cut aims at reducing Z+jets events with leptonically decaying Z bosons via $Z \to e^+e^-$, where one of the two electrons satisfies the tight selection criteria but the second electron fails these criteria.
The efficiency of this cut in terms of Z-boson event rejection and the associated signal loss are estimated using simulated events and comparing the event yields obtained from the full event selection and from the event selection where the loose electron veto has been omitted. While the number of Z+jets events can be reduced by a factor of two, only 4% of the signal (mostly $t\bar{t}$ dilepton events) are lost.

Additional Cuts for the Rejection of the QCD Multijet Background

In the event yields obtained by applying the event selection described so far, the contribution from QCD multijet events is still large as can be seen in the third from last row of table 5.5. In order to suppress these processes two additional requirements are imposed on the selected events.

The first cut is motivated by the fact that the contribution from QCD processes increases with increasing $|\eta|$ values, while top quarks are mostly produced centrally in the detector. This behavior can be seen in figure 5.6, where the η distribution for all processes is shown. The main reason for the large QCD contribution in the

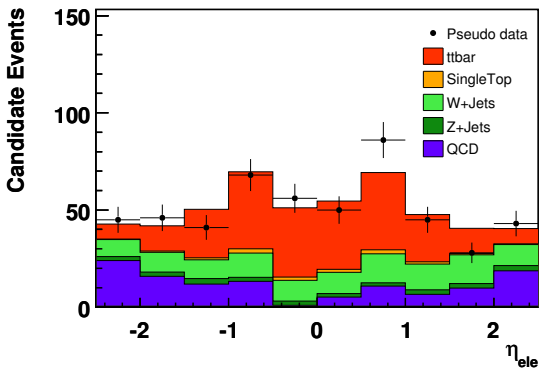

Figure 5.6: Distribution of the electron-η after the loose electron veto and before applying the additional cut on η of the selected electron. The different processes are normalized according to their event yields for $20\,\mathrm{pb}^{-1}$. The points depict pseudo data, which are randomly drawn from the overall distribution obtained by adding the five single distributions, and reflect the expected statistical fluctuations.

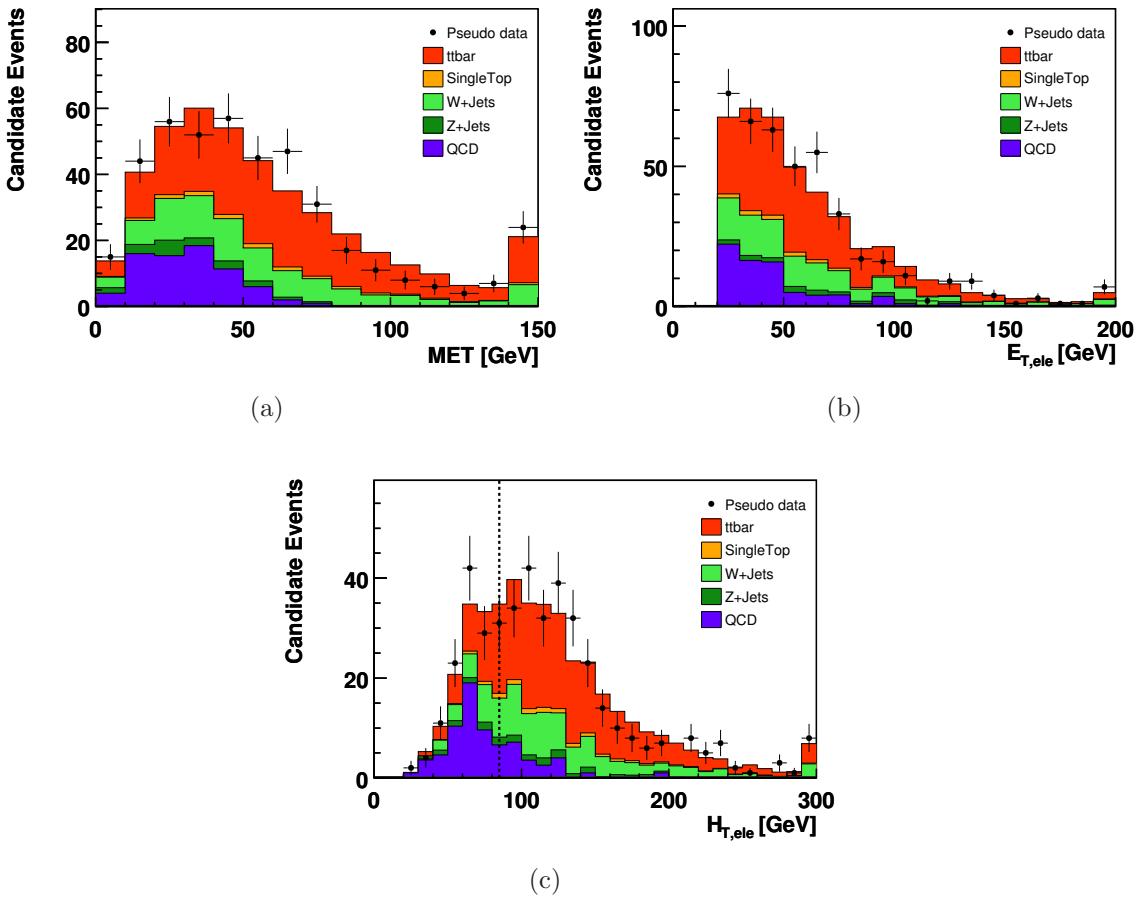

Figure 5.7: Distribution of (a) the missing transverse energy (MET), (b) the transverse energy of the electron, and (c) of $H_{\mathrm{T,ele}}$ for all events after the additional cut on the pseudorapidity of the selected electron and before the cut on $H_{\mathrm{T,ele}}$. The cut value of $H_{\mathrm{T,ele}} = 85\,\mathrm{GeV}$ is indicated in (c) by the dotted line. The different processes are normalized according to the event yields for $20\,\mathrm{pb}^{-1}$. The points depict pseudo data, which are randomly drawn from the overall distribution obtained by adding the five single distributions, and reflect the expected statistical fluctuations.

forward direction is the increasing amount of tracker material. This leads to an increasing probability for conversions of photons into e^+e^-. Requiring the selected electron further to fall within the region $|\eta| < 2$ leads to a significant reduction of the QCD contribution, while the effect on the $t\bar{t}$ signal is bearable. The number of QCD events is reduced by this cut by 37%, while only 16 events or 7% of the signal are lost. As a side effect, also the amount of W+jets background events is reduced by 17% and therefore stronger than the signal contribution, which is due to the broader η distribution compared to that of $t\bar{t}$ events.

The second requirement exploits the E_{T} spectrum of the electron and the $\not\!\!E_{\mathrm{T}}$ distribution. Both variables have some power to separate QCD events from the other processes, which can be seen in figure 5.7 (a) and (b). In events containing semileptonically decaying top quarks or leptonically decaying on-shell W bosons substantial missing transverse energy is expected as a result of the produced neutrino. In con-

trast to this, the $\not\!\!E_{\mathrm{T}}$ in QCD events is due to the finite jet energy resolution only and these events should contain therefore no or only small amounts of $\not\!\!E_{\mathrm{T}}$. Prompt electrons from the hard interaction are expected to exhibit a harder E_{T} spectrum than secondary or fake electrons. The variable $H_{\mathrm{T,ele}}$ combines the separation power of these variables, see figure 5.7(c). It is defined as the sum of the transverse energy of the electron and $\not\!\!E_{\mathrm{T}}$ in the event. The latter is corrected for the momenta of all reconstructed muons and for all Level 2 and Level 3 corrected jets with $p_{\mathrm{T}} > 20\,\mathrm{GeV}/c$ and an electromagnetic fraction smaller than 0.9.
Requiring $H_{\mathrm{T,ele}}$ to be greater than 85 GeV leads to a significant reduction of QCD events. This cut is crucial for the entire analysis for two reasons. It does not only reduce the QCD contribution considerably but also facilitates the estimation of the amount of QCD events in the signal region by measuring the amount of QCD events in the sideband region $H_{\mathrm{T,ele}} < 85\,\mathrm{GeV}$ and extrapolating into the region with $H_{\mathrm{T,ele}} > 85\,\mathrm{GeV}$. This method to estimate the background contribution from QCD events will be discussed in the next section.

Expected Event Yields for an Integrated Luminosity of $20\,\mathrm{pb}^{-1}$

The expected event yields for the different processes in a dataset corresponding to an integrated luminosity of $20\,\mathrm{pb}^{-1}$ are estimated based on the samples of simulated events described in section 5.1.2. In the cut-flow table 5.5 these event yields are listed after each step of the event selection. The quoted uncertainties reflect the statistics available in the MC samples.

Cut	$t\bar{t}$	single top	W+Jets	Z+Jets	QCD
Trigger	$4,726 \pm 6$	670 ± 1	$196,449 \pm 132$	$26,599 \pm 44$	$33,760,624 \pm 9434$
1 electron	735 ± 2	178 ± 1	$89,502 \pm 89$	$10,927 \pm 28$	$23,659 \pm 254$
Muon veto	665 ± 2	172 ± 1	$89,488 \pm 89$	$10,897 \pm 28$	$23,651 \pm 254$
> 1 Jet	660 ± 2	158 ± 1	$13,933 \pm 35$	$7,106 \pm 23$	$11,320 \pm 169$
> 2 Jets	619 ± 2	96 ± 1	$2,539 \pm 15$	$1,296 \pm 10$	$3,023 \pm 81$
> 3 Jets	476 ± 2	39 ± 0	533 ± 7	250 ± 4	631 ± 34
≥ 4 Jets	250 ± 1	12 ± 0	117 ± 3	53 ± 2	117 ± 15
2^{nd} ele veto	241 ± 1	12 ± 0	117 ± 3	22 ± 1	117 ± 15
$\lvert\eta_{\mathrm{ele}}\rvert < 2.0$	225 ± 1	11 ± 0	97 ± 3	17 ± 1	74 ± 12
$H_{\mathrm{T,ele}}$ cut	184 ± 1	9 ± 0	75 ± 3	12 ± 1	21 ± 7

Table 5.5: Cut-flow table of the electron+jets event selection. The event yields are normalized to an integrated luminosity of $20\,\mathrm{pb}^{-1}$. The numbers are obtained from the described MC samples. Thus W+Jets and Z+jets refer to leptonically decaying W and Z bosons only. The quoted uncertainties reflect the statistics available in the MC samples.

In a dataset selected in the described way one expects in total about 301 events, of which 184 events are expected to be $t\bar{t}$ events and 117 events are expected to stem from background processes. This corresponds to a signal to background ratio of $S/B = 1.57$ and a pseudo significance for the $t\bar{t}$ signal of $S/\sqrt{B} = 17.01$.
The 184 expected signal events are composed of 159 $t\bar{t}$ events from the electron+jets channel, 8 events from the τ+jets channel, no events from the μ+jets and the all hadronic channels, and 17 events from dilepton channels. In the latter case one top quark decays into an electron and the other top quark decays in about 11 events into a tau, in 4 events into an electron and in 2 events into a muon. The largest contribution to the 117 background events stems from W+jets processes with 75 ± 3 events followed by the QCD contribution with 21 ± 7 events. Due to its large uncertainty especially the expected number of QCD events can only be considered as rough estimate. Therefore it is desirable to develop a data based method for the estimation of the QCD contribution.
In figures 5.8(a) and (b) the expected number of signal and background events as a function of the jet multiplicity is depicted, while figures 5.8(c)–(f) show the transverse momenta of the four leading jets. Figure 5.9 provides the E_{T} and η distributions of the electron as well as the $\not\!\!E_{\mathrm{T}}$ distribution for signal and background events. For all distributions the normalization of the different processes is according to the event yields given in table 5.5. In order to demonstrate how this distributions would look like in real data corresponding to an integrated luminosity of $20\,\mathrm{pb}^{-1}$, pseudo data points are added. The pseudo data are randomly drawn from the respective overall distribution obtained by adding up the distributions of all processes considered and reflect the statistical fluctuations expected in the selected dataset.

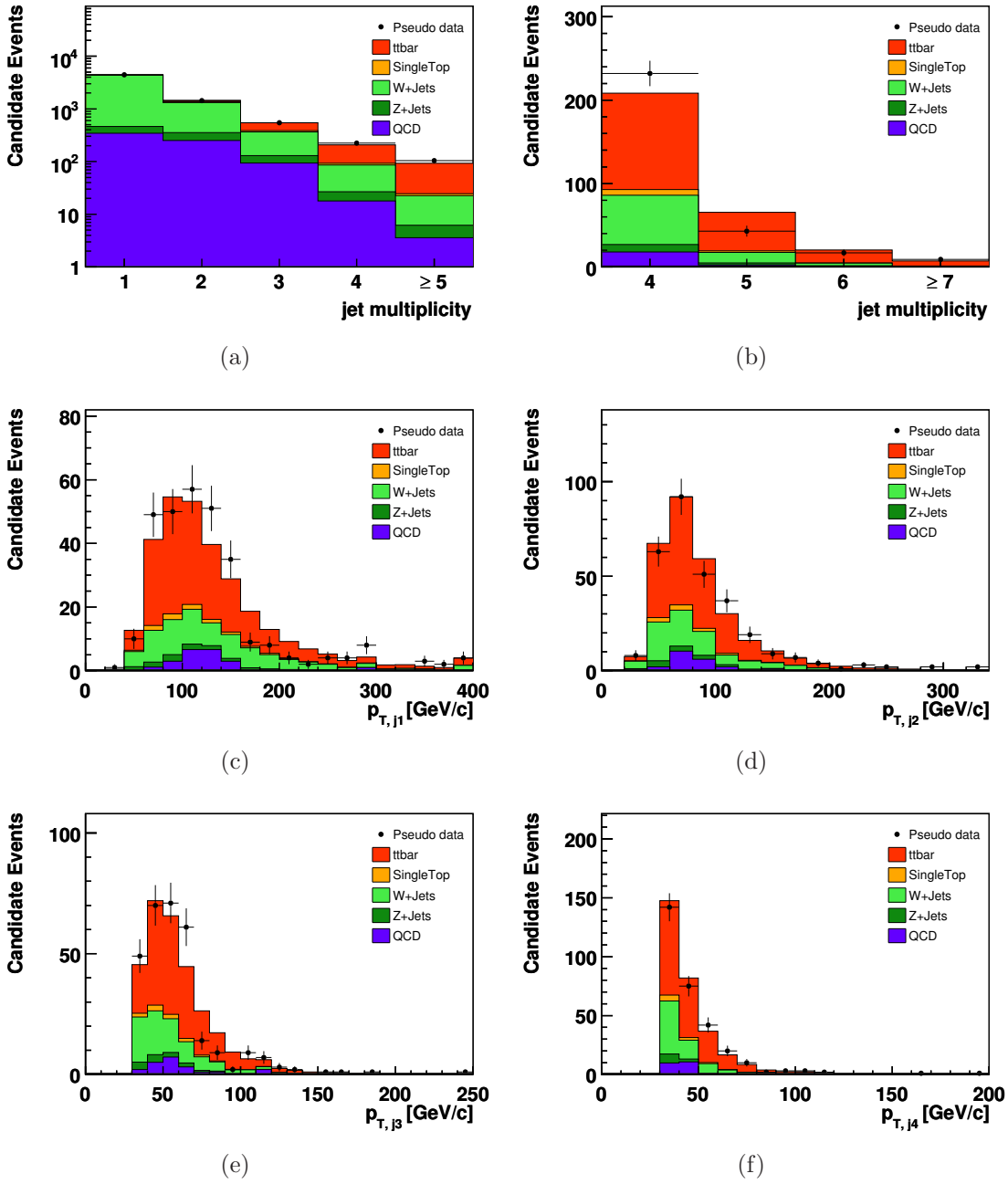

Figure 5.8: (a) and (b) The numbers of expected events for the different processes as a function of the jet multiplicity, and (c)–(f) the p_{T} distributions of the four jets with the highest p_{T} in descending order. In (a) the requirement of at least four jets has been omitted, while in (b) the full set of selection requirements has been applied. The points depict pseudo data, which are randomly drawn from the overall distribution obtained by adding the five single distributions, and reflect the expected statistical fluctuations.

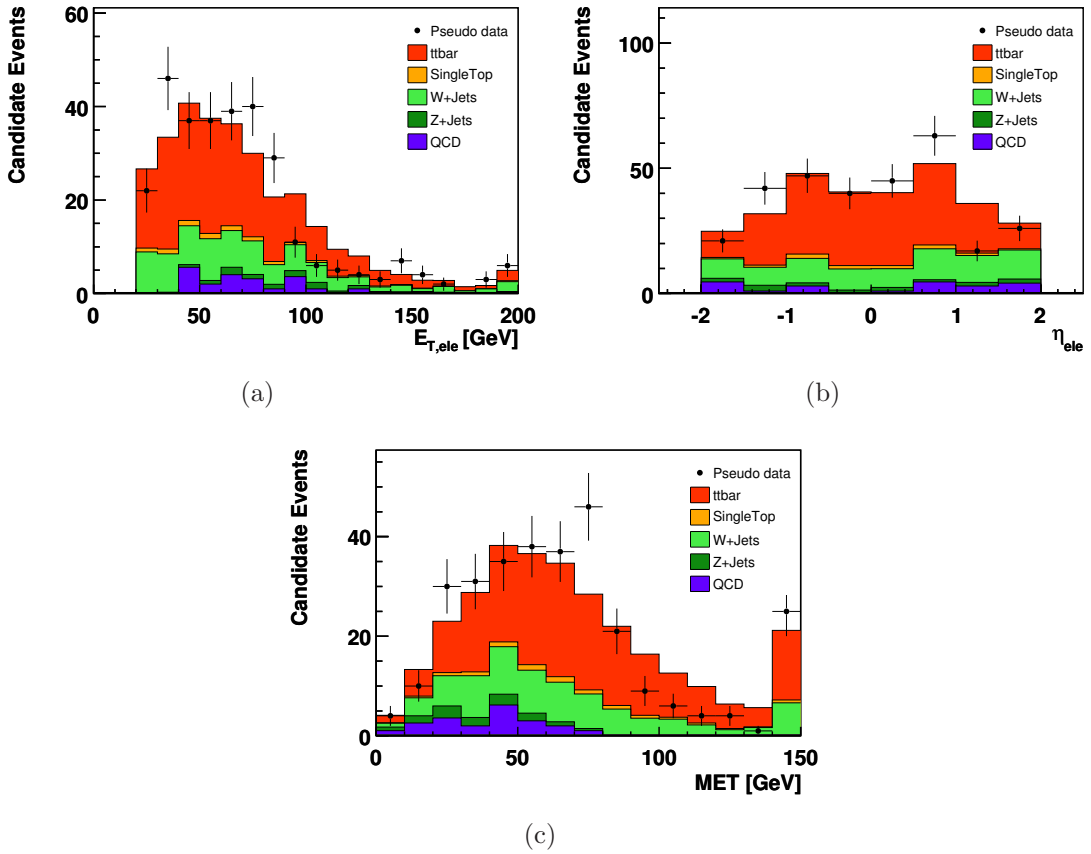

(a) (b)

(c)

Figure 5.9: (a) E_{T} and (b) η distributions of the electron and (c) the distribution of the missing transverse energy (MET) for all events selected by the full event selection. The different processes are normalized according to the event yield for $20\,\mathrm{pb}^{-1}$. The points depict pseudo data, which are randomly drawn from the overall distribution obtained by adding the five single distributions, and reflect the expected statistical fluctuations.

5.2 Estimation of the QCD Background Contribution from Data

The large number of simulated QCD events available is not sufficient for a reliable estimation of the QCD contribution in the selected dataset. Compared to the other processes, the event weights for the simulated QCD events are large and lie between 0.57 and 2.36, as can be seen in table 5.3. This implies that the number of generated events is similar to or even smaller than the expected number of events in $20\,\mathrm{pb}^{-1}$ of data. Thus the kinematic distributions for QCD events suffer from large statistical fluctuations. In addition, it is not clear to what extent one can trust the MC simulation of QCD processes, especially in terms of the description of the tails of kinematic distributions. For these reasons it is crucial to develop a method to estimate this background contribution in the selected dataset directly from data without relying on MC simulations of these processes.

5.2.1 Discriminating Variable and Strategy

In section 5.1.3 the variable $H_{\mathrm{T,ele}}$, defined as the sum of the E_{T} of the electron and the $\not{E}_{\mathrm{T}}$ in the event, has been introduced as a powerful variable for the reduction of QCD events. Moreover this variable can be used to determine the QCD contribution in the selected dataset. The idea behind this method is to divide the events selected by the default event selection without the cut on $H_{\mathrm{T,ele}}$ into two separate datasets, the sideband region with $H_{\mathrm{T,ele}} < 85\,\mathrm{GeV}$ and the signal region with $H_{\mathrm{T,ele}} > 85\,\mathrm{GeV}$. In the following these two regions will also be referred to as region SH (small $H_{\mathrm{T,ele}}$ values) and region LH (large $H_{\mathrm{T,ele}}$ values), respectively. The signal region LH corresponds to the final dataset selected by applying the full event selection including the $H_{\mathrm{T,ele}}$ cut. By fitting the $H_{\mathrm{T,ele}}$ distribution in the sideband region SH, where the amount of QCD events is comparable to the amount of events due to the non-QCD processes[2], the normalization of the QCD contribution can be obtained. From this the number of QCD events in the signal region can be extrapolated. Since the aim of this method is to estimate the QCD contribution without relying on MC simulations for these processes the crucial point is to construct a $H_{\mathrm{T,ele}}$ template for QCD events directly from data.

$H_{\mathrm{T,ele}}$ Template for QCD

A suitable template for the $H_{\mathrm{T,ele}}$ distribution from QCD events can be obtained by modifying the default electron+jets event selection such that events from phase space regions which are highly occupied by QCD events are selected. For this purpose two different approaches are pursued.

[2] Although top-antitop quark pairs are also produced via the strong interaction, the term QCD processes refers throughout this thesis only to QCD multijet processes and consequently non-QCD processes refers to all other processes, including production of $t\bar{t}$.

Sample	$t\bar{t}$	W+jets	Z+jets	single top	QCD	All events
Antiele	3.1%	0.7%	0.2%	0.1%	95.9%	1,7363
Jetele	1.3%	0.1%	0.0%	0.0%	98.6%	118,051

Table 5.6: Composition of the two QCD enriched samples obtained by two different modifications of the event selection. The last column gives the total number of expected events for an integrated luminosity of $20\,\mathrm{pb}^{-1}$.

The first approach aims at selecting QCD events by explicitly requiring that the selected electron satisfies the η and E_T requirement as well as the impact parameter cut but fails the tight electron identification. In order to further enhance the statistics of the selected sample in QCD events, the cut on the relative isolation variable I_rel is inverted. Since I_rel is correlated with E_T, which is one ingredient of $H_\mathrm{T,ele}$, the cut is not completely inverted and I_rel is required to lie within $0.1 < I_\mathrm{rel} < 0.3$. The upper limit guarantees that there is no significant bias in the E_T distribution of the selected events due to the inverted I_rel requirement. The motivation for these modifications is that secondary or fake electrons originating from multijet processes are mostly not well isolated and are likely to fail the stringent criteria of the tight electron identification. Apart from the described modifications the default event selection including the muon veto, the jet requirements, the loose electron veto, and the additional η cut on the selected electron, is applied. Since the electron candidates are explicitly required to fail the tight electron-ID, the sample selected in this way is referred to as the Antiele sample.

In the second approach a QCD enriched sample of events is obtained by selecting events in a phase space region where none of the electron candidates satisfies the default electron requirements. Instead, the jet with the highest electromagnetic fraction f_em, defined as the energy deposited in the ECAL divided by the energy deposited in the HCAL, that falls within the η and E_T range required for electron candidates, is considered as electron if f_em is larger than 0.7. Consequently this jet is removed from the collection of selected jets. By vetoing events containing identified electrons, the sample is highly enriched in QCD events and by requiring one of the jets to have a large electromagnetic fraction, only QCD events are selected which contain a physics object, which is a candidate for faking an electron.

In the absence of real data, the two approaches to model the $H_\mathrm{T,ele}$ distribution for QCD events from data are applied to the complete set of simulated events of all processes considered in this analysis. Table 5.6 shows the expected composition of the two samples obtained by the two modified event selections and the total statistics available in each sample. Both samples are highly enriched in QCD events with negligible contribution from non-QCD processes. From now on, the $H_\mathrm{T,ele}$ distributions obtained from these two samples are referred to as the QCD templates or abbreviated $\mathcal{T}^J_\mathrm{QCD}$ and $\mathcal{T}^A_\mathrm{QCD}$, respectively. The index J or A indicates whether the Jetele or the Antiele template is described. The $H_\mathrm{T,ele}$ distribution obtained from the simulated QCD events passing the default event selection without the cut on

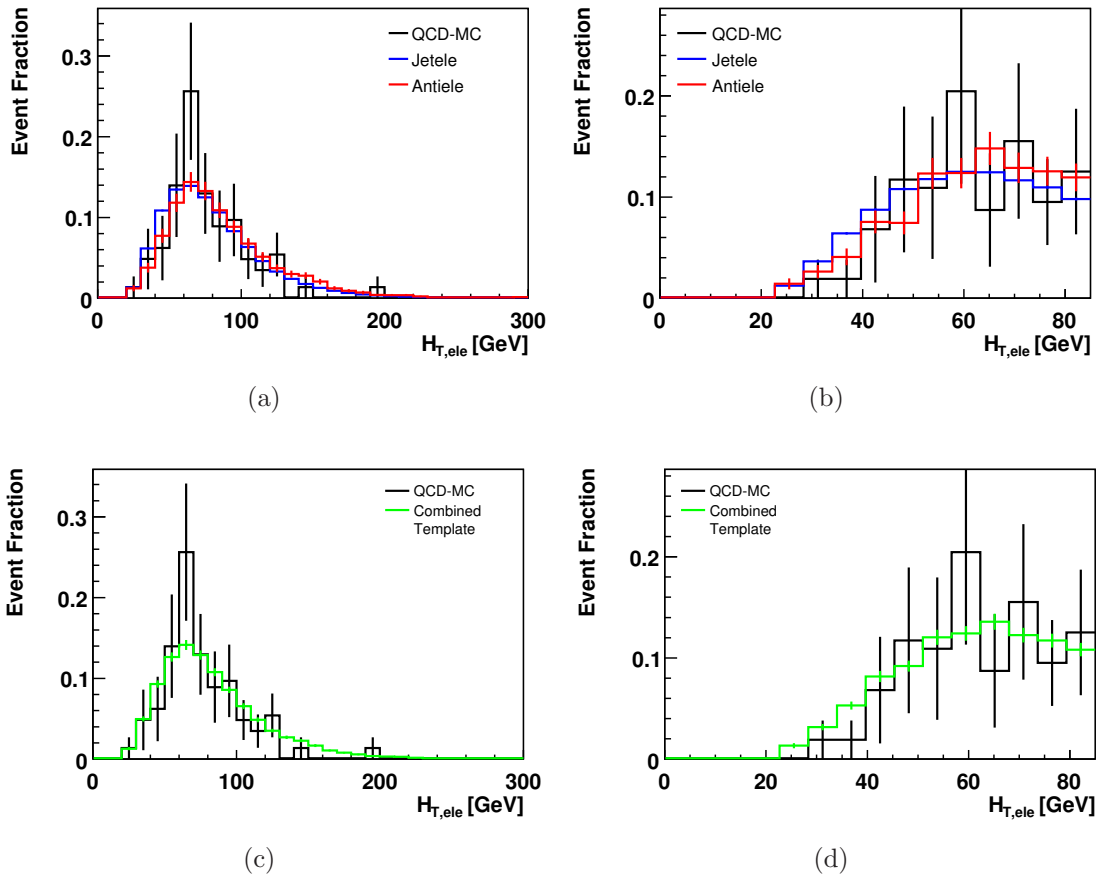

Figure 5.10: Shape comparison of the two $H_{\mathrm{T,ele}}$ templates $\mathcal{T}^{J}_{\mathrm{QCD}}$ and $\mathcal{T}^{A}_{\mathrm{QCD}}$ with the QCD-MC distribution of $H_{\mathrm{T,ele}}$ for (a) the whole region SH+LH and for (b) the sideband region SH. The same shape comparisons for the combined QCD template and the QCD-MC distribution of $H_{\mathrm{T,ele}}$ are depicted in (c) and (d).

$H_{\mathrm{T,ele}}$ is in the following referred to as the QCD-MC distribution of $H_{\mathrm{T,ele}}$.
The method is based on the assumption that the QCD templates, obtained in the specified way, describe the $H_{\mathrm{T,ele}}$ distribution of QCD events passing the default event selection. Although the statistics available in simulated QCD events passing the default event selection is limited, this assumption can be validated by comparing the shapes of the different QCD models with the QCD-MC distribution, which is done in figure 5.10. Within its large statistical uncertainties the QCD-MC distribution is described reasonably well by the two QCD templates and both could in principle be used as QCD model. But as there are small differences between the shapes of $\mathcal{T}^{J}_{\mathrm{QCD}}$ and $\mathcal{T}^{A}_{\mathrm{QCD}}$, the combined template is used to model QCD events and the single templates are used later for the determination of the influence of deviating shapes on the result. The combined template $\mathcal{T}^{c}_{\mathrm{QCD}}$ is constructed by adding the two normalized templates, $\mathcal{T}^{c}_{\mathrm{QCD}} = \hat{\mathcal{T}}^{J}_{\mathrm{QCD}} + \hat{\mathcal{T}}^{A}_{\mathrm{QCD}}$.
In order to test the QCD model with higher statistics, the same comparison is carried out on selected datasets, where the number of jets in each event is required to

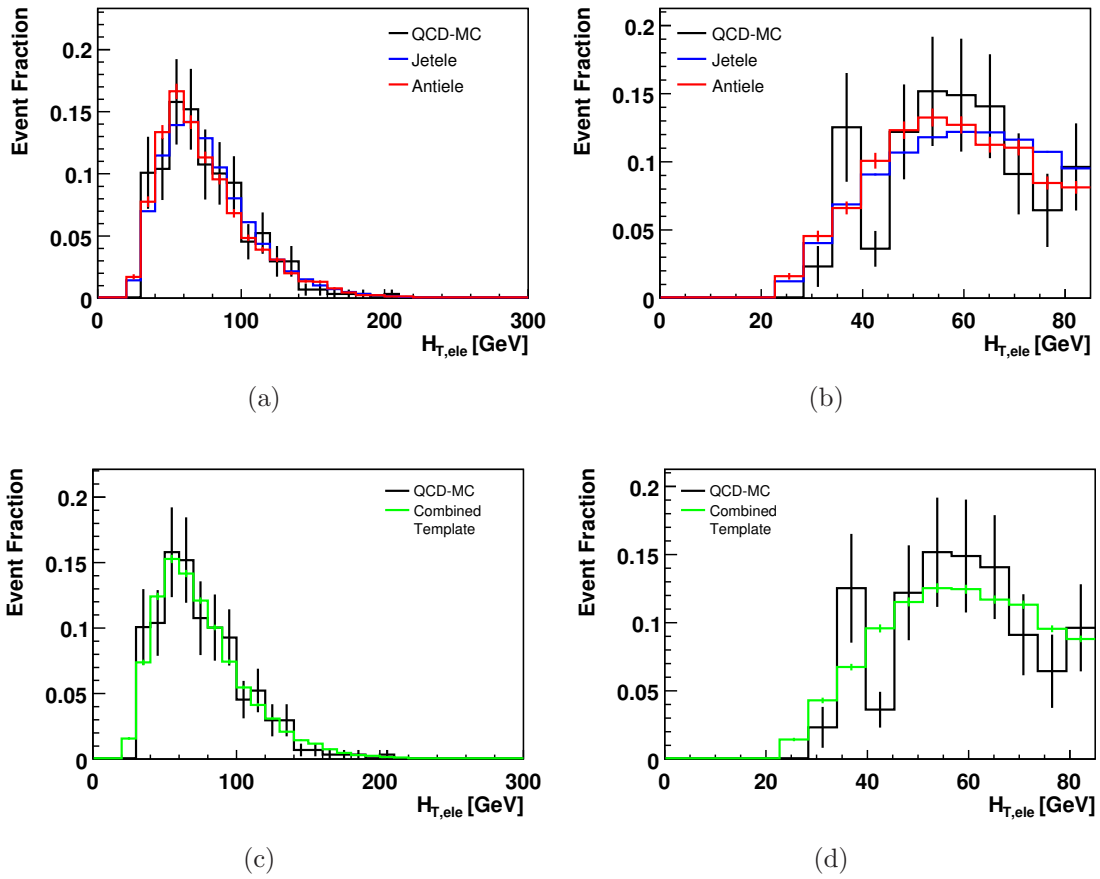

Figure 5.11: Shape comparison for events with exactly three jets of the two $H_{\mathrm{T,ele}}$ templates $\mathcal{T}^{J}_{\mathrm{QCD}}$ and $\mathcal{T}^{A}_{\mathrm{QCD}}$ with the QCD-MC distribution of $H_{\mathrm{T,ele}}$ (a) for the whole region SH+LH and (b) for the sideband region SH. The same shape comparisons of the combined QCD template and the QCD-MC distribution of $H_{\mathrm{T,ele}}$ are depicted in (c) and (d). In order to increase the statistics in the QCD-MC distribution, the event selection has been modified and requires exactly three jets.

be equal to three, and therefore the number of events in the QCD-MC distribution is significantly larger. The shape comparisons presented in figure 5.11 show good agreement between the QCD-MC distribution and the QCD templates and thus confirm the conclusions drawn from the selected datasets with $N_{\mathrm{jets}} \geq 4$.

Comparison of the $H_{\mathrm{T,ele}}$ Distributions of QCD and Non-QCD Processes

The $H_{\mathrm{T,ele}}$ distributions for $t\bar{t}$ and single top-quark events are obtained from the corresponding samples of simulated events described in section 5.1.2. As the number of W+jets and Z+jets events in the MC samples simulated with the full simulation that pass the event selection is insufficient, the corresponding MC samples simulated with the fast simulation are used. The $H_{\mathrm{T,ele}}$ distributions obtained using the fast simulated samples feature ten times larger statistics. The details on these samples can be found in appendix B.1.

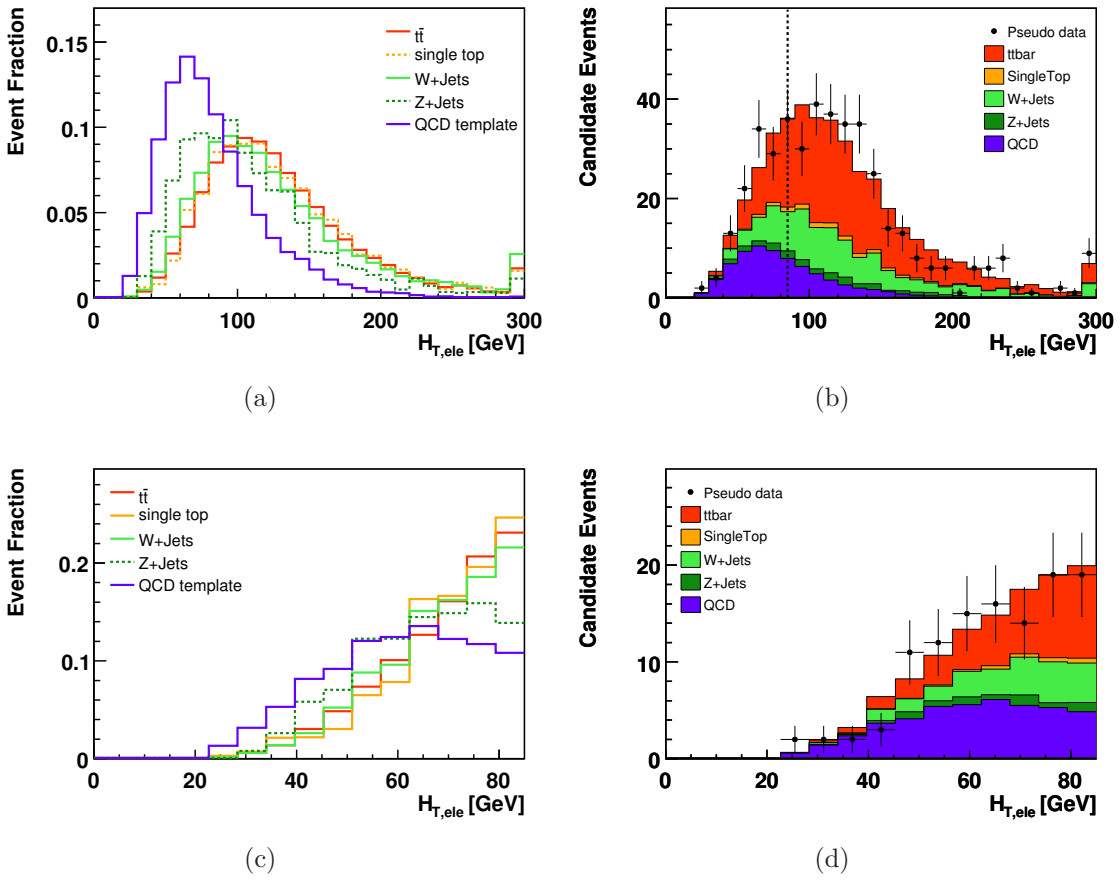

Figure 5.12: (a) Shape comparison for the $H_{\mathrm{T,ele}}$ distributions for the different processes and (b) the $H_{\mathrm{T,ele}}$ distribution as expected in a dataset corresponding to an integrated luminosity of $20\,\mathrm{pb}^{-1}$. For the latter the different processes are normalized to the event yields given in table 5.7. The QCD contribution is modelled using the combined QCD template. The sideband region SH and signal region LH are divided by the dotted line. The points depict pseudo data, which are randomly drawn from the overall distribution obtained by adding the five single distributions, and reflect the expected statistical fluctuations. The same distributions are shown in (c) and (d) for region SH only. The binning is the one used in the fit.

Figure 5.12(a) shows a comparison of the normalized $H_{\mathrm{T,ele}}$ distributions for the different processes from which the discrimination power of this variable can clearly be seen. While the $H_{\mathrm{T,ele}}$ distribution for QCD events peaks at a value around 60 GeV, the distributions for non-QCD processes reach their maxima at around 100 GeV. Table 5.7 compares the composition of the two regions SH and LH. The numbers for all processes but the QCD contribution are taken from the cut-flow table 5.5. Since the statistics in the QCD-MC sample, especially in the region with large $H_{\mathrm{T,ele}}$ values, is very small, only the absolute normalization of QCD events before the $H_{\mathrm{T,ele}}$ cut is obtained from the QCD-MC sample. The value is given in the next to last row of table 5.5. The relative fractions of QCD events in the signal and sideband region are then obtained from the combined QCD template described in the previous section. Figure 5.12(b) provides the corresponding distribution of the

Process	N_k^{SH}	N_k^{LH}
$t\bar{t}$	41	184
single top	2	9
W+jets	22	76
Z+jets	5	12
QCD	45	29

Table 5.7: Expected event yields for the different processes N_k in the sideband region SH with $H_{\mathrm{T,ele}} < 85\,\mathrm{GeV}$ and in the signal region LH with $H_{\mathrm{T,ele}} > 85\,\mathrm{GeV}$. For all but the QCD process the numbers are taken from table 5.5. For QCD events the total number is obtained using the QCD-MC sample while the fractions of events in the sideband and in the signal regions are calculated based on the combined QCD template τ^{c}_{QCD}.

expected numbers of events for the different processes as a function of $H_{\mathrm{T,ele}}$. The sideband region SH and the signal region LH are separated by the dotted vertical line.

5.2.2 Template Fit

In order to estimate the QCD contribution in a data driven way, the $H_{\mathrm{T,ele}}$ distribution obtained in data will be subjected to a binned likelihood fit in the region $0 < H_{\mathrm{T,ele}} < 85\,\mathrm{GeV}$. The likelihood function is defined as

$$L(N_k^{\mathrm{SH}}) = \prod_{i=1}^{N_{\mathrm{bins}}} \frac{\mu_i^{n_i} \cdot e^{-\mu_i}}{n_i!} \ , \tag{5.5}$$

where i is the bin index, μ_i is the number of predicted events in bin i, and n_i is the number of observed events in the same bin. The total number of bins, N_{bins}, is 15. The number of predicted events in each bin is a linear combination of the different contributions and given by

$$\mu_i = N_{t\bar{t}/t}^{\mathrm{SH}} \cdot \alpha_i^{t\bar{t}/t} + N_W^{\mathrm{SH}} \cdot \alpha_i^W + N_Z^{\mathrm{SH}} \cdot \alpha_i^Z + N_{\mathrm{QCD}}^{\mathrm{SH}} \cdot \alpha_i^{\mathrm{QCD}} \ , \tag{5.6}$$

where N_k^{SH} are the parameters of the likelihood function and refer to the number of events of process k in the sideband region SH. The fractions of events of process k in bin i, α_i^k, are obtained from the four fit templates described in the previous section. Since the expected number of single top-quark events in the sideband region is very small (only 2 out of 115 events) and since the shape of the $H_{\mathrm{T,ele}}$ distribution for single top-quark events is very similar to the shape for $t\bar{t}$ events, both processes are fitted together using the common parameter $N_{t\bar{t}/t}^{\mathrm{SH}}$ and the $H_{\mathrm{T,ele}}$ template obtained from simulated $t\bar{t}$ events. The $H_{\mathrm{T,ele}}$ distribution most similar to the one from QCD events is the shape for Z+jets events. Since the expected contribution from this processes to the total amount of events in the sideband region is only 5 out of 115 total events, N_Z^{SH} is constrained in the likelihood function to the expected

value $\mu_Z^{\mathrm{SH}} = 5$ in order to not adulterate the result. This constraint is implemented by a multiplicative Gaussian term with a relatively large relative uncertainty of $\Delta_Z = 300\%$ of the mean value in order to not constrain the fraction of Z+jets events too strongly. The likelihood function is then finally given by

$$L(N_k^{\mathrm{SH}}) = \left(\prod_{i=1}^{N_{\mathrm{bins}}} \frac{\mu_i^{n_i} \cdot e^{-\mu_i}}{n_i!} \right) \cdot e^{-\frac{\left(\frac{N_Z^{\mathrm{SH}}}{\mu_Z^{\mathrm{SH}}} - 1\right)^2}{2\Delta_Z^2}} \quad . \tag{5.7}$$

The fitted number of QCD events in the sideband region which yields the maximum value of the likelihood function, $\tilde{N}_{\mathrm{QCD}}^{\mathrm{SH}}$, gives the absolute normalization of the $H_{\mathrm{T,ele}}$ QCD template. From this the number of QCD events in the signal region, $\tilde{N}_{\mathrm{QCD}}^{\mathrm{LH}}$, can then be extrapolated via

$$\tilde{N}_{\mathrm{QCD}}^{\mathrm{LH}} = \tilde{N}_{\mathrm{QCD}}^{\mathrm{SH}} \cdot R \ . \tag{5.8}$$

The extrapolation factor R is given by

$$R = \frac{\int_{85}^{\infty} \mathcal{T}_{\mathrm{QCD}}^{\mathrm{c}} dH_{\mathrm{T,ele}}}{\int_{0}^{85} \mathcal{T}_{\mathrm{QCD}}^{\mathrm{c}} dH_{\mathrm{T,ele}}} \ , \tag{5.9}$$

where $\mathcal{T}_{\mathrm{QCD}}^{\mathrm{c}}$ is the combined QCD template for $H_{\mathrm{T,ele}}$ and R is calculated to be 0.64.

5.2.3 Consistency Check and Estimation of the Expected Uncertainty

For the purpose of testing the developed method, 5,000 pseudo experiments are performed. For each pseudo experiment the number of events in the sideband region SH for the five different processes is thrown according to Poisson distributions each centered at the mean values N^{SH} given in table 5.7. The resulting numbers of events are then randomly drawn from the corresponding templates. The resulting $H_{\mathrm{T,ele}}$ distribution is then fitted with the four fit templates as described in the previous sections. In order to compare the extrapolated number of QCD events to the mean value $\mu_{\mathrm{QCD}}^{\mathrm{LH}} = 29$ given in table 5.7 the parameter $\beta_{\mathrm{QCD}} = \frac{\tilde{N}_{\mathrm{QCD}}^{\mathrm{LH}}}{\mu_{\mathrm{QCD}}^{\mathrm{LH}}}$ is defined. Figure 5.13 shows the distribution of β_{QCD}, which is well centered around one, as expected for a consistent method, and the corresponding pull distribution, which is defined as

$$\mathrm{pull}_{\mathrm{QCD}} = \frac{1 - \beta_{\mathrm{QCD}}}{\sigma_{\beta_{\mathrm{QCD}}}} \ , \tag{5.10}$$

where $\sigma_{\beta_{\mathrm{QCD}}}$ is the statistical uncertainty of the single fit result. The expected statistical uncertainty of the extrapolated number of QCD events in the region LH is given by the width of the β_{QCD} distribution. From the distribution in figure 5.13(a) the expected relative statistical uncertainty is obtained to be 45%.
The whole method is based on the assumption that the $H_{\mathrm{T,ele}}$ distribution of QCD events selected by the default event selection is modelled by the combined QCD

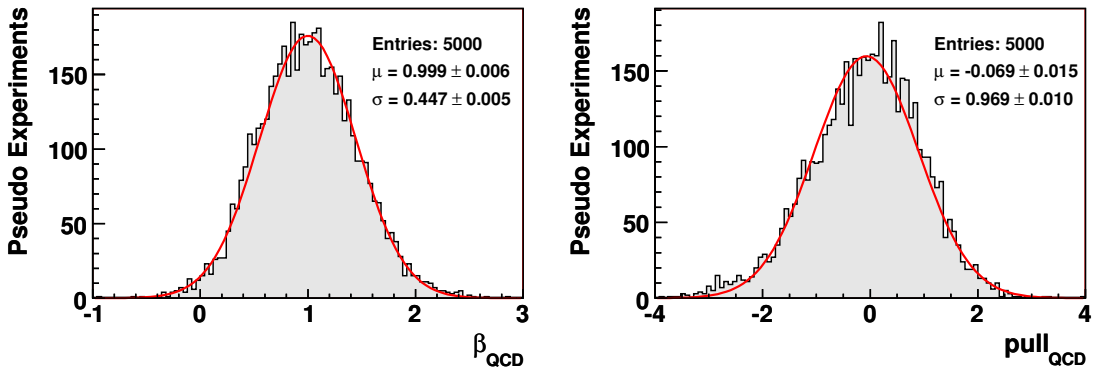

(a) (b)

Figure 5.13: Distribution of (a) β_{QCD} and (b) the corresponding pull distribution.

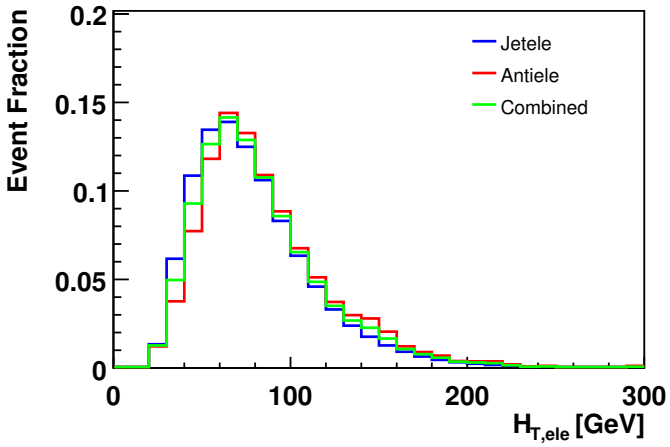

Figure 5.14: Shape comparison between the $H_{\mathrm{T,ele}}$ distributions obtained from the Jetele sample, the Antiele sample, and the combined QCD template.

template obtained from the two modified event selections. This template is not only used as fit template in the sideband region SH but is also used to determine the ratio R used for the extrapolation of the number of QCD events in the signal region. To evaluate the impact of possible differences between the $H_{\mathrm{T,ele}}$ distributions from QCD events in the signal region and the QCD templates derived from the phase space regions defined by the modified event selections, two ensembles of pseudo experiments are performed. The QCD pseudo data are either drawn from the Jetele or from the Antiele template, while as fit template in both cases the default combined QCD template is used. The three different distributions are compared in figure 5.14.

The difference in the shape implies also a difference in the ratio of QCD events in the signal region and in the sideband region as can be seen in table 5.8, where the numbers for both regions are listed for the two templates and the combined template. For this comparison the total number of expected QCD events before

	Input values		Extrapolation	Deviation
QCD pseudo data	$N_{\mathrm{QCD}}^{\mathrm{SH}}$	$N_{\mathrm{QCD}}^{\mathrm{LH}}$	$\overline{\tilde{N}_{\mathrm{QCD}}^{\mathrm{LH}}}$	$\left(N_{\mathrm{QCD}}^{\mathrm{LH}} - \overline{\tilde{N}_{\mathrm{QCD}}^{\mathrm{LH}}}\right) / \overline{\tilde{N}_{\mathrm{QCD}}^{\mathrm{LH}}}$
Jetele	47	27	35	0.23
Antiele	43	31	23	0.35
Combined	45	29	29	–

Table 5.8: Number of expected QCD events in the sideband region SH and in the signal region LH obtained from the three different templates. The absolute number of QCD events in the full region SH+LH is for all three cases fixed to the estimation based on the QCD-MC distribution (74 events). The third column lists the mean values of the extrapolated number of QCD events in region LH obtained by fitting the corresponding distribution of extrapolated $\tilde{N}_{\mathrm{QCD}}^{LH}$ values from 5,000 pseudo experiments with a Gaussian.

the $H_{\mathrm{T,ele}}$ cut is set to 74 events according to table 5.5. Consequently in the set of pseudo experiments in which the QCD pseudo data are modelled with the Jetele template, the number of QCD events is thrown according to a Poisson distribution with the mean value of 47 events. In the set of pseudo experiments using the Antiele template for the modelling of QCD events, the corresponding mean value of 43 events is used. Since the fit and the extrapolation are based on the combined QCD template this introduces a bias. The mean values of the extrapolated number of QCD events, $\overline{\tilde{N}_{\mathrm{QCD}}^{\mathrm{LH}}}$, obtained from 5,000 pseudo experiments are listed in the last column of table 5.8. These values are defined as the mean values of the Gaussians fitted to the distributions of the extrapolated values $\tilde{N}_{\mathrm{QCD}}^{\mathrm{LH}}$. Comparing the three values one obtains a deviation of 23% in the case, where the pseudo data are drawn from the Jetele template and a deviation of 35% in the case where the QCD events are modelled by the Antiele template. In a conservative approach the larger value is taken as uncertainty in both the negative and the positive direction. Adding this uncertainty and the statistical uncertainty in quadrature, the total relative uncertainty of the QCD estimation is

$$\Delta\tilde{N}_{\mathrm{QCD}}^{\mathrm{LH}} / \tilde{N}_{\mathrm{QCD}}^{\mathrm{LH}} = 0.57 \; . \tag{5.11}$$

In the absence of data the proof of principle for the method developed to estimate the QCD background contribution by means of a fit to an appropriate kinematic variable in a data driven way has been presented. The relative uncertainty of 57% on the estimated QCD contribution is comparable to that of other methods used in similar studies [8].

5.3 A Method for the Measurement of the $t\bar{t}$ Cross Section

In the previous section it has been demonstrated how the amount of QCD events in the selected dataset can be estimated directly from data. The remaining background contributions stem from the production of single top quarks and from W+jets and Z+jets processes. The idea behind the method for the determination of the number of $t\bar{t}$ events in the selected dataset, $N_{t\bar{t}}$, is to exploit an appropriate kinematic variable which is able to discriminate between the signal and background. Given this number the cross section of $t\bar{t}$ production can be obtained via

$$\sigma_{t\bar{t}} = \frac{N_{t\bar{t}}}{A \cdot \epsilon_{t\bar{t}} \cdot L} \ , \tag{5.12}$$

where $A \cdot \epsilon_{t\bar{t}}$ is the acceptance times the efficiency of the event selection for $t\bar{t}$ events and L is the integrated luminosity. The efficiency of the event selection can be factorized into several efficiencies each corresponding to a certain cut in the event selection. Given real data some of these efficiencies, like the trigger efficiency, will be determined directly from data using the tag-and-probe method [153], while the acceptance has to be obtained from MC studies. For the study presented in this thesis the acceptance and overall efficiency are determined from MC studies.
In the following sections the discriminating variable, the template fit to extract the number of $t\bar{t}$ events, and the estimation of statistical and systematic uncertainties are introduced and described.

5.3.1 Discriminating Variable

A promising approach in order to find an appropriate variable capable of discriminating $t\bar{t}$ events from other processes is to look at a distribution which is sensitive to the top-quark mass. A simple way to identify the three jets which originate from the hadronic top-quark decay is to calculate the vectorially summed transverse momentum of any combination of three jets. The jets of the combination with the highest summed p_{T} are deemed to originate from the hadronic top-quark decay, and their invariant mass is denoted M3. Compared to the full reconstruction of $t\bar{t}$ events developed in the CDF analysis, this method of reconstructing top quarks is very simple and coarse. Although it is clear that applying this simple method one cannot expect to reconstruct the hadronically decaying top-quark correctly for all $t\bar{t}$ events, the resulting M3 distribution provides sufficient discrimination power. Figure 5.15 shows the distribution of M3 for the different processes considered in this study. The peak of the $t\bar{t}$ M3 distribution around the nominal top-quark mass is clearly visible. The shift to higher values is due to the fact that the jet energies are corrected using correction factors derived from QCD dijet events, which contain mostly gluon jets. When applied to jets in $t\bar{t}$ events, which are mostly quark jets, these jets are overcorrected [154].
Since single top-quark events contain also a top quark, the M3 distribution for these

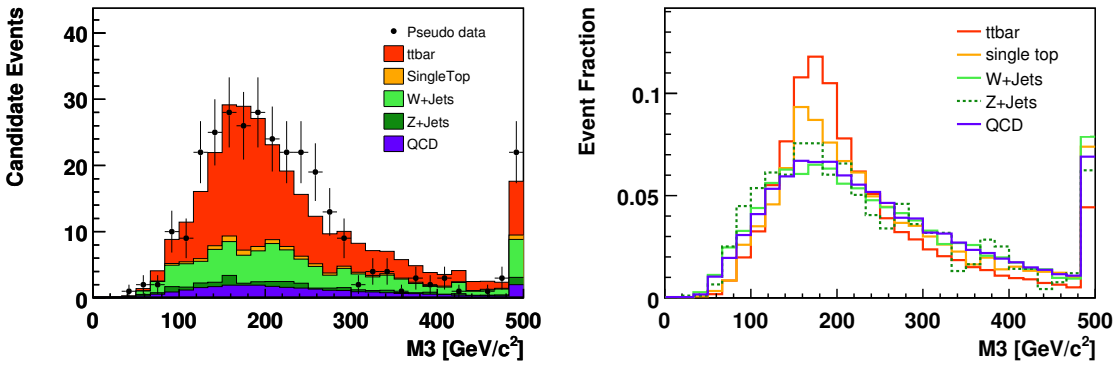

(a) (b)

Figure 5.15: (a) M3 distribution for all processes normalized to their event yields given in table 5.5. The QCD distribution is modelled using the Jetele template and is normalized to the expected value given in table 5.7. The points depict pseudo data, which are randomly drawn from the overall distribution obtained by adding the five single distributions, and reflect the expected statistical fluctuations. In (b) the shapes for the different processes considered in the analysis are compared. The distributions for W+Jets and Z+Jets processes are obtained using samples simulated with the fast simulation.

events is very signal-like and thus hardly distinguishable from the distribution for $t\bar{t}$ events. However, from table 5.5 one can see that the expected number of single top-quark events is relatively small. Since this background process is theoretically well understood, the number of single top-quark events in the selected dataset can be estimated based on the theoretically predicted cross section and acceptance and efficiency of the event selection determined using samples of simulated events. Therefore the prediction for single top-quark events can be taken from table 5.5. All other backgrounds exhibit a broader M3 distribution with maxima around the top-quark mass but without a prominent peak.

M3 Templates

For the sake of sufficient numbers of simulated events which allow to obtain M3 distributions with only small statistical fluctuations, as for the $H_{\mathrm{T,ele}}$ fit described in the previous section, the MC samples simulated with the fast simulation are used for modelling W+jets and Z+jets processes. Since the shape of the M3 distributions from W+jets and Z+jets is very similar, the distributions of both processes are fitted with one single template. Due to the ten times larger number of available simulated events, the W+jets MC sample is used for this purpose.
It seems that also the shape of the M3 distribution for QCD events is very similar to that for W+jets events and one could in principle use one single template for the three background processes. But this can be different in real data and therefore a separate M3 template for the QCD contribution is used. M3 distributions for QCD events can be obtained from the Jetele and Antiele samples. As both templates are very similar, which can be seen in figure 5.16, the Jetele template is due to

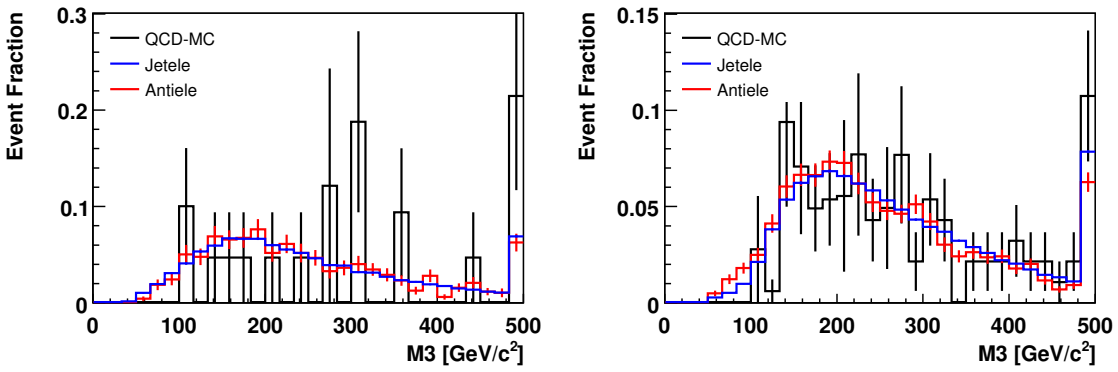

(a) (b)

Figure 5.16: Shape comparison for the M3 distributions from the QCD-MC and the two QCD templates (a) for events with $N_{\text{jets}} \geq 4$ and (b) for events with exactly three jets. The two QCD templates are very similar and describe the QCD-MC distribution within its large statistical fluctuations reasonably well.

its larger statistics used as QCD model in the following. In order to validate the use of this template, figure 5.16 additionally compares the QCD template to the M3 distribution obtained from the QCD-MC sample of events passing the full event selection. However, the number of events in the latter is by far too small to allow for a conclusive statement. Therefore the same comparison is carried out on a selected dataset where the number of jets in an event is required to be equal to three, which leads to a larger number of available events passing the event selection. Within the still large statistical uncertainties the shape is modelled well by the QCD template and it is therefore assumed that this also holds for the dataset selected with the requirement $N_{\text{jets}} \geq 4$.

5.3.2 Template Fit

The fraction of $t\bar{t}$ events in the selected dataset will be estimated by means of a binned likelihood fit to the M3 distribution, similar to the method described in section 5.2.2. The likelihood function is defined as

$$L(N_k) = \prod_{i=1}^{N_{\text{bins}}} \frac{\mu_i^{n_i} \cdot e^{-\mu_i}}{n_i!} \ , \tag{5.13}$$

where i is the bin index, μ_i is the number of predicted events in bin i, and n_i is the number of observed events in the same bin. The total number of used bins is $N_{\text{bins}} = 30$. The number of predicted events in each bin is a linear combination of the different contributions:

$$\mu_i = N_{t\bar{t}} \cdot \alpha_i^{t\bar{t}} + N_{W/Z} \cdot \alpha_i^{W/Z} + N_t \cdot \alpha_i^t + N_{\text{QCD}} \cdot \alpha_i^{\text{QCD}} \ . \tag{5.14}$$

Here, N_k are the parameters of the likelihood function and the index k refers to the process. The fraction of events of process k in bin i is given by α_i^k and is

obtained from the corresponding fit template $\mathcal{T}_k$. As already mentioned, the fraction of W+jets and Z+jets events are fitted with a common fit template due to their similar M3 distributions. In order to facilitate the comparison between the results of the likelihood fit and the expected number of events N_k^{pred} corresponding to the assumed cross section values, it is convenient to define the parameter β_k for each process k:

$$\beta_k = \frac{N_k}{N_k^{\text{pred}}} \ . \tag{5.15}$$

The parameter β_k can also be interpreted as the ratio of the measured and the predicted cross section, $\beta_k = \frac{\sigma_k}{\sigma_k^{\text{pred}}}$. In terms of the β parameters, μ_i can be rewritten as

$$\mu_i = \sum_k \beta_k N_k^{\text{pred}} \cdot \alpha_i^k \ . \tag{5.16}$$

The shape of the M3 distribution of single top-quark events is very similar to the distribution of $t\bar{t}$ events. Due to this similarity and because of the very small number of expected single top-quark events, an unconstrained fit of the single top-quark contribution is not possible. But as this process is theoretically well understood and described, the amount of single top-quark events can be estimated based on MC simulations. The amount of QCD events is estimated using the data driven method described in the previous section. Both contributions are constrained in the likelihood function to their predicted values. This is done by two multiplicative Gaussian terms of the form

$$\frac{1}{\sqrt{2\pi\Delta_k^2}} e^{-\frac{(\beta_k-1)^2}{2\Delta_k^2}} \ , \tag{5.17}$$

where the widths Δ_k of the Gaussian terms are chosen to account for the respective uncertainties on the estimations. In case of single top-quark production the standard deviation of the Gaussian is set to $\Delta_t = \sqrt{N_t^{\text{pred}} + (0.3N_t^{\text{pred}})^2}/N_t^{\text{pred}}$, motivated by the statistical uncertainty $\sqrt{N_t}$ and the 30% theoretical uncertainty. In case of the QCD contribution the 57% uncertainty of this estimation derived in section 5.2.3 is used as standard deviation Δ_{QCD}. Including these two Gauss constraints the likelihood function is given by

$$L(\beta_k) = \left(\prod_{i=1}^{N_{\text{bins}}} \frac{\mu_i^{n_i} \cdot e^{-\mu_i}}{n_i!} \right) \cdot \frac{1}{\sqrt{2\pi\Delta_t^2}} e^{-\frac{(\beta_t-1)^2}{2\Delta_t^2}} \cdot \frac{1}{\sqrt{2\pi\Delta_{\text{QCD}}^2}} e^{-\frac{(\beta_{\text{QCD}}-1)^2}{2\Delta_{\text{QCD}}^2}} \ . \tag{5.18}$$

5.3.3 Consistency Check and Estimation of the Expected Statistical Uncertainty

In order to test the developed method for the measurement of the $t\bar{t}$ cross section for consistency, an ensemble of 5,000 pseudo experiments is generated. For each pseudo experiment the number N_k^{PE} of events for process k is thrown according to a Poisson distribution centered on the predicted values N_k^{pred} given in table 5.9. For

Process	Events N_k^{pred}
$t\bar{t}$	184 ± 1
W+jets	75 ± 3
Z+jets	12 ± 1
single top	9 ± 0
QCD	29 ± 7

Table 5.9: Numbers of events for each process k after the full event selection scaled to an integrated luminosity of $20\,\text{pb}^{-1}$. The quoted uncertainties reflect the statistics available in the MC samples. These numbers are used as mean values of the Poisson distributions from which the numbers of pseudo data events for each process are drawn.

each process the respective Poisson distributed number of events N_k^{PE} is drawn from the corresponding templates. In the consistency check the pseudo data are drawn only from the templates that are used as fit templates. Therefore the total number of $N_W + N_Z$ events is drawn from the W+jets template. In each pseudo experiment the resulting pseudo data M3 distribution is subjected to a binned likelihood fit as described in section 5.3.2 and the set of β_k parameters yielding the maximum value of the likelihood function as well as the corresponding statistical uncertainties σ_{β_k} are extracted.
The two unconstrained parameters of the fit are $\beta_{t\bar{t}}$ and $\beta_{W/Z}$, whereas in case of the consistency check the latter is indeed β_W and for its calculation the combined number of predicted events $N_{W/Z}^{\text{pred}} = N_W^{\text{pred}} + N_Z^{\text{pred}}$ is used. For a consistent method, both β_k distributions should be centered around 1.0 and the corresponding pull distributions, defined as

$$\text{pull}_k = \frac{1 - \beta_k}{\sigma_{\beta_k}} \,, \tag{5.19}$$

should be centered around zero with a width of 1.0. Figure 5.17 shows the β_k distributions and the corresponding pull distributions for $t\bar{t}$ events and W+jets events. As can be seen from these distributions, both β_k distributions are centered around 1.0 and the pull distributions show no significant deviation from a normal distribution and thus the fitting procedure shows no systematic bias.

In addition to this consistency check, also the expected statistical uncertainty of the single measurement can be determined by means of pseudo experiments. For this purpose the numbers N_k^{PE} for each process are again thrown from Poisson distributions with the mean values given in table 5.9, but this time, each process is modelled with its own template. In explanation, N_Z and N_W events are drawn separately from the M3 templates for Z+jets and W+jets events, while for the fit only the W+jets template is used, as will be done in the actual measurement on real data. The distribution of the statistical uncertainties, obtained from the fit results of the 5,000 pseudo experiment, is presented in figure 5.18. The mean value of this distribution is considered as the expected statistical uncertainty of the single measurement. Thus a relative statistical uncertainty of 22% is expected.

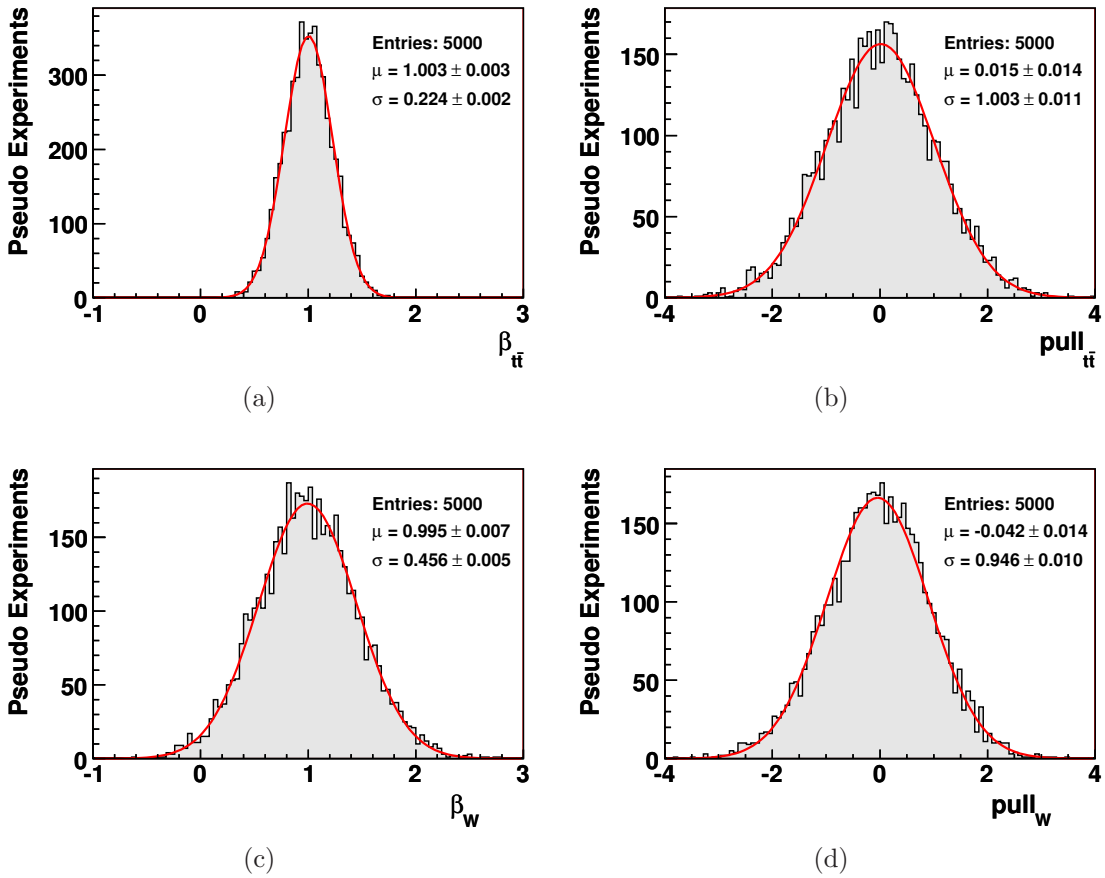

Figure 5.17: The distributions of β_k for the fitted fraction of (a) $t\bar{t}$ and (c) W+jet events in the consistency check and the corresponding pull distributions in (b) and (d). Each distribution is fitted with a Gaussian and the mean value μ and the width σ of the Gaussians are quoted for each distribution.

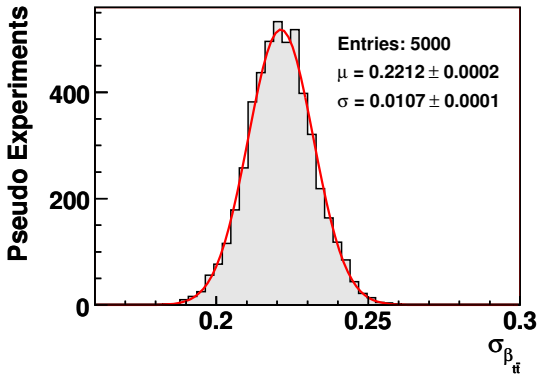

Figure 5.18: Distribution of the relative statistical uncertainties of the measured $\beta_{t\bar{t}}$ values. The mean value of this distribution is considered as the expected statistical uncertainty for the single measurement. This mean value is consistent with the width of the $\beta_{t\bar{t}}$ distribution in figure 5.17 (a), as expected for a consistent method.

5.3.4 Systematic Uncertainties

The systematic uncertainties on the extracted number of $t\bar{t}$ events caused by uncertainties in the theoretical modelling and the experimental setup are studied performing 5,000 pseudo experiments for each possible source of systematic uncertainties. The source of a systematic uncertainty can affect the number of selected events of a certain process k by altering the selection efficiency, as well as the shape of the M3 distribution itself. Therefore the combined effect due to altered rate and altered shape, abbreviated rate+shape uncertainty, has to be studied. For each set of pseudo experiments the number of events of a certain process is thrown according to a Poisson distribution around the altered mean value N_k^{sys}, accounting for the rate uncertainty. The N_k^{sys} events are then drawn from the corresponding template $\mathcal{T}_k^{\text{sys}}$, which is affected by the source of systematic uncertainty under study. These templates are obtained from dedicated samples of events simulated with varied parameters with respect to the default samples. For a list of these samples see appendix B.1. Uncertainties on the modelling of the $t\bar{t}$ signal as well as uncertainties on the modelling of the main background process, W+jets production, are estimated. In addition the influence of variations in the jet energy scale is estimated. All pseudo experiments are performed using the default fit templates, but drawing the pseudo data from the different dedicated templates $\mathcal{T}_k^{\text{sys}}$. The systematic uncertainty due to a certain effect is then given by the difference $\Delta\beta_{t\bar{t}} = \overline{\beta_{t\bar{t}}} - \overline{\beta_{t\bar{t}}^{\text{sys}}}$, where $\overline{\beta_{t\bar{t}}}$ is the mean value of the $\beta_{t\bar{t}}$ distribution obtained by performing 5,000 pseudo experiments with default settings and $\overline{\beta_{t\bar{t}}^{\text{sys}}}$ the corresponding mean value obtained from the pseudo experiments using the altered numbers N_k^{sys} of events of process k and the altered M3 templates $\mathcal{T}_k^{\text{sys}}$. In case of two available variations of one source of systematic uncertainty the respective larger deviation is defined as systematic uncertainty for both the negative and the positive direction.

Modelling of $t\bar{t}$: MC Generator

The impact of different modelling of the $t\bar{t}$ signal on the measured cross section is studied using a signal sample generated with Pythia, while for the generation of the events used to obtain the default fit template MadGraph/MadEvent is used. While the effect on the rate of $t\bar{t}$ events is only small, which can bee seen in table 5.10, the sample of events generated with Pythia exhibits a considerably different shape compared to the default distribution. This difference, illustrated in figure 5.19(a), results in a relatively large systematic uncertainty of 13%.

Modelling of $t\bar{t}$: Initial- and Final-State Radiation

For further investigation of the influence of uncertainties due to the modelling of signal events, parameters of the parton shower have been varied in order to either increase or decrease the initial- and final-state radiation (ISR/FSR). From table 5.10 one can see that the number of selected $t\bar{t}$ events is for both cases smaller compared to the default setting, and the larger deviation is observed for less gluon radiation. This effect is compensated by the altered shape leading to a relatively small system-

Setting	$t\bar{t}$ Events $N_{t\bar{t}}^{\mathrm{sys}}$
Default	184
Pythia	183
less ISR/FSR	169
more ISR/FSR	180

Table 5.10: Effect on the rate of the selected $t\bar{t}$ events due to different modelling compared to the default setting. The numbers are normalized to an integrated luminosity of $20\,\mathrm{pb}^{-1}$.

atic uncertainty of 2%. The M3 shape comparison for the variations in the initial- and final-state radiation is shown in figure 5.19(c).

Modelling of $t\bar{t}$: Parton Distribution Function

The contribution to the total systematic uncertainty arising from the uncertainty on the PDF used for the generation of the simulated signal events is evaluated with the CTEQ6.6 [155] PDF set and the LHAPDF package [156] using a reweighting procedure. For each positive and negative variation of the 22 eigenvectors the selected events are reweighted and an altered rate and the corresponding altered M3 distribution are obtained. The mean fit results for each of the 2×22 eigenvector variations are determined performing 5,000 pseudo experiments each and compared to the default. For each eigenvector the variation yielding the larger deviation from the default is considered and the total uncertainty is given as the square root of the quadratically summed single contributions. This procedure yields a systematic uncertainty on the measured $\sigma_{t\bar{t}}$ of 5% due to the uncertainty on the PDF.

Modelling of W+Jets: Variations in the Factorization Scale

In order to estimate the impact of the factorization scale in the generation of W+jets events on the extraction of the $t\bar{t}$ cross section, the Q^2 scale is varied by a factor of 0.5 and 2.0 with respect to its default value. The effect on the rate is relatively large as can be seen in table 5.11, but partially compensated by the effect on the shape and the resulting systematic uncertainty is found to be 3%. The M3 shape comparison for variations in the factorization scale can be found in figure 5.19(b).

Modelling of W+Jets: Variations of the Matching Threshold

In addition to the factorization scale uncertainty, the uncertainty on the matching threshold for the matching between matrix element and parton shower in the generation of W+jets events is investigated. The matching threshold has been varied to $5\,\mathrm{GeV}/c$ and to $20\,\mathrm{GeV}/c$ compared to the default matching threshold of $10\,\mathrm{GeV}/c$. Compared to the variations in the factorization scale, the rate of selected $t\bar{t}$ events is not that strongly affected, as can be seen from table 5.11, and thus cannot compensate the impact due to the altered shape, depicted in figure 5.19(d). The systematic

Setting	W+Jets Events N_W^{sys}
Default	75
Factorization scale $\times 2.0$	46
Factorization scale $\times 0.5$	126
Matching threshold $\times 2.0$	94
Matching threshold $\times 0.5$	67

Table 5.11: Effect on the rate of selected W+jets events due to different modelling compared to the default setting. The numbers are normalized to an integrated luminosity of $20\,\text{pb}^{-1}$.

Setting	$N_{t\bar{t}}^{\text{sys}}$	N_t^{sys}	N_W^{sys}	N_Z^{sys}
Default	184	9	75	12
JES +10%	218	11	105	16
JES −10%	147	6	51	8

Table 5.12: Effect of 10% variations in the jet energy scale on the rate of the various processes. The numbers are normalized to an integrated luminosity of $20\,\text{pb}^{-1}$. Since the amount of QCD events will be estimated directly from data and the M3 template for QCD events is obtained from data, this process is not considered here.

uncertainty on the measured $t\bar{t}$ cross section due to variations in the W+jets matching threshold is estimated to be 5%.

Variations in the Jet Energy Scale

In the absence of a jet-p_{T} and jet-η dependent model of the jet energy scale (JES) uncertainty a general uncertainty of 10% on the four-vector of each jet is assumed. Hence the four-vector of each jet is multiplied with 1.1 or 0.9, respectively, before the event enters the event selection. Table 5.12 summarizes the variations in the event yields for the different processes. The amount of QCD events and the M3 templates for QCD will be estimated in a data driven way. Therefore, there is no additional systematic uncertainty due to JES variations for this process and only the remaining processes have to be considered. While the rate uncertainty and the shape uncertainty for the upwards variation in the jet energy scale compensate each other, the −10% variation leads to a large effect of 19% on the extracted number of $t\bar{t}$ events.

Variations in the Number of Single Top-Quark and QCD Events

Possible uncertainties arising from deviations of the number of single top-quark and QCD events from the predicted values used as constraints in the likelihood function are already partially accounted for by the width of the Gaussian terms, which correspond to the uncertainties on these predictions. However, the robustness of the fit

Source of uncertainty	Relative uncertainty on $\sigma_{t\bar{t}}$
$t\bar{t}$ MC Generator	13%
$t\bar{t}$ ISR/FSR	2%
W+jets MC Factorization Scale	3%
W+jets MC Matching Threshold	5%
Jet Energy Scale	19%
PDF uncertainty	5%
Total	24%

Table 5.13: Summary of the relative systematic uncertainties on the estimation of the $t\bar{t}$ production cross section. Following a conservative approach the single contributions are symmetrized by quoting the respective larger deviation. The total uncertainty is calculated as the square root of the quadratic sum of the single uncertainties.

with respect to the Gaussian constraints is investigated by varying the mean values of the number of single top-quark events and QCD events by ±50%. The effect on $\beta_{t\bar{t}}$ is negligible and no additional contribution to the systematic uncertainty has to be assigned.

A summary of all systematic uncertainties can be found in table 5.13. The single contributions are assumed to be uncorrelated and the total systematic uncertainty is therefore calculated as the square root of the quadratic sum of the single contributions. The total systematic uncertainty estimated in the described way is 24% of the measured cross section, where the largest contribution is due to possible variations in the jet energy scale. In addition, a 10% uncertainty on the integrated luminosity value is assumed, which yields another additional 10% relative uncertainty on the measured cross section.

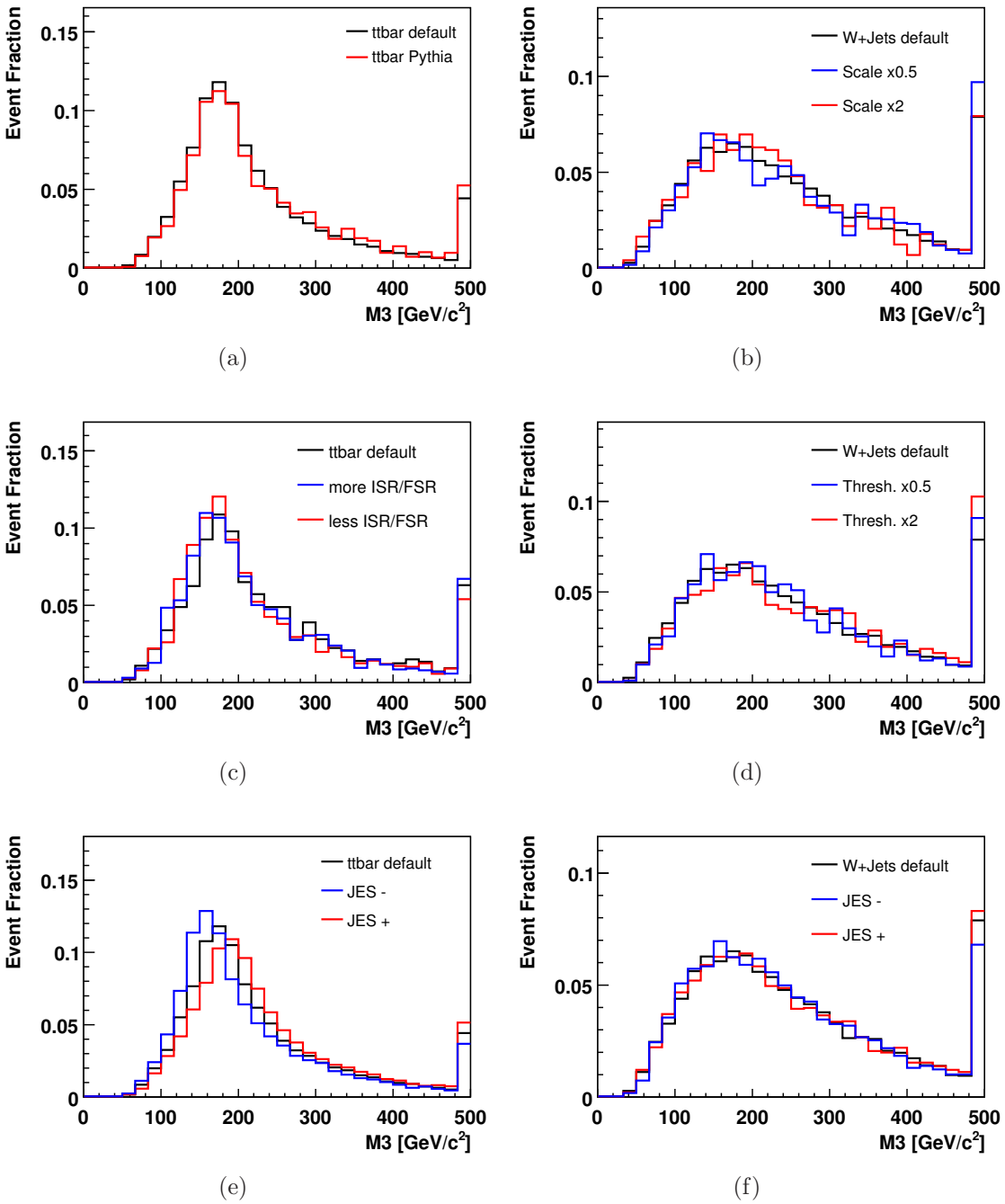

Figure 5.19: Shape comparisons of the default M3 distribution and the distributions affected by various sources of systematic uncertainties for $t\bar{t}$ (left-hand side) and W+jets (right-hand side) events: (a) comparison between two different MC generators for $t\bar{t}$ events, (b) variations in the factorization scale for W+jets events, (c) variations in ISR/FSR for $t\bar{t}$ events, (d) variations in the matching threshold for W+jets events, and (e) and (f) variations in the JES for both processes. In the latter case JES− refers to a variation of −10% and JES+ to a variation of +10% in the jet energy scale.

5.4 Results

Based on an assumed dataset corresponding to an integrated luminosity of $20\,\mathrm{pb}^{-1}$ the prospects for an early measurement of the $t\bar{t}$ production cross-section at a center-of-mass energy of 10 TeV in the electron+jets channel with the CMS detector have been studied using samples of simulated events. One crucial point, especially in the early phase of data taking, is the estimation of the background contribution stemming from QCD multijet processes. For this purpose a data-driven method has been developed, which is able to estimate the QCD fraction directly from data with an uncertainty of 57%. The $t\bar{t}$ cross section will then be measured by means of a binned likelihood fit to the M3 distribution, which is able to discriminate between $t\bar{t}$ processes and the main background processes. With this method it will be possible to measure the $t\bar{t}$ production cross-section at the following precision:

$$\sigma_{t\bar{t}} = \sigma_{t\bar{t}}^{\mathrm{fit}} \ \pm 22\%(\mathrm{stat.}) \ \pm 24\%(\mathrm{syst.}) \ \pm 10\%(\mathrm{lumi.})$$

It has been demonstrated that the measurement of the $t\bar{t}$ cross section will already be possible with an early dataset at a center-of-mass energy of 10 TeV. Figure 5.20 shows the expected decrease of the statistical uncertainty with increasing integrated luminosity available. Given $100\,\mathrm{pb}^{-1}$ of collision-data at $\sqrt{s} = 10\,\mathrm{TeV}$, which are likely to be accumulated within one year of operation, the relative statistical uncertainty will drop below 10%. Already with with $20\,\mathrm{pb}^{-1}$ of data this measurement is limited by the systematic uncertainties, dominated by the uncertainty due to variations in the jet energy scale. But with increasing understanding of the detector it can be assumed that also many of the systematic uncertainties can be decreased in order to improve the precision of the measurement.

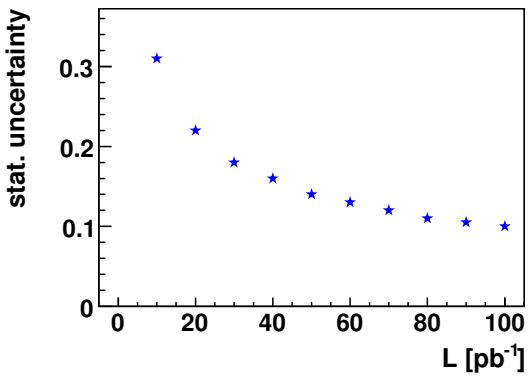

Figure 5.20: Expected statistical uncertainty of the $t\bar{t}$ cross section measurement with this method as a function of the integrated luminosity.

Summary and Discussion

The top quark was discovered in 1995 by the CDF and DØ collaborations at Fermilab's Tevatron [3, 4] as the last of the six quarks predicted by the standard model (SM). Since then a large effort has been made in order to investigate the nature of the heaviest quark. While especially its mass has been determined to very high accuracy, many other top-quark properties have not yet been measured with comparable precision. In this thesis two analyses have been described, each dedicated to an aspect of top-quark physics, top-quark production via the strong force and the decay of top quarks via the weak interaction. In the first analysis described, a property of top-quark decay related to the nature of the weak interaction has been measured. In the second part of the thesis the prospects for a measurement of the top-quark pair production at the LHC have been evaluated.

Top quarks decay via the weak interaction almost exclusively into a b quark and a W boson. The mediators of the charged weak interaction, the W bosons, couple only to left-handed particles and right-handed antiparticles due to the $V - A$ structure of the charged weak interaction in the standard model. As a consequence the W bosons from top-quark decays can thus only be either longitudinally polarized or left-handed. The predictions by the standard model are that 70% of the W bosons from top-quark decays are longitudinally polarized, while the remaining 30% are left-handed. The fraction of right-handed W bosons is strongly suppressed. Deviating values for these fractions would be clear indications for physics beyond the SM and would imply that the nature of charged current weak interactions at high momentum transfers differs from its nature at low energy scales.

The first part of this thesis described a measurement of the W-boson helicity-fractions on a dataset corresponding to an integrated luminosity of $1.9\,\mathrm{fb}^{-1}$ collected with the CDF II experiment. The collected data have been subjected to a lepton+jets event selection resulting in 484 $t\bar{t}$ candidate events of which 87 events have been estimated to stem from background processes.
The sensitive observable used for the extraction of the W-boson helicity-fractions is the cosine of the decay angle θ^*. In order to obtain a $\cos\theta^*$ value for each event, a method to reconstruct the kinematics of $t\bar{t}$ events has been developed. Therein several ambiguities in the reconstruction of the four-vector of the neutrino and in the assignment of the jets to the quarks from the two top-quark decays have to be resolved. The method described exploits different quantities of the reconstructed four-vectors of the W bosons and top quarks to select one out of the several possible

hypotheses for reconstructing the kinematics of each $t\bar{t}$ event.
The resulting $\cos\theta^*$ distribution has been subjected to three different fit scenarios. In two separate measurements the fractions of longitudinally polarized (F_0) and right-handed (F_+) W bosons have been extracted, while the respective other fraction has been set to its SM value. In a third measurement, both fractions have been measured simultaneously in a model-independent way.
A maximum likelihood method has been used to extract F_0 and F_+. In this method for each bin of the $\cos\theta^*$ distribution the number of observed events is compared to the predicted number of events depending on the values for the helicity fractions. At this juncture, distortion effects on the $\cos\theta^*$ distribution arising from $\cos\theta^*$ dependent event-selection efficiencies and from the migration of events due to the finite resolution of the full reconstruction have been taken into account by convolving these effects with the theoretical predictions. The obtained results from the one-parameter fits are:

$$\begin{aligned} F_0(F_+ = 0.0) &= 0.66 \pm 0.10\ (\text{stat.})\ \pm 0.06\ (\text{syst.}) \\ F_+(F_0 = 0.7) &= 0.01 \pm 0.05\ (\text{stat.})\ \pm 0.03\ (\text{syst.}) \end{aligned}$$

Since within the quoted uncertainties no evidence for a non-zero fraction of right-handed W bosons has been found, in addition an upper limit on F_+ has been calculated:

$$F_+ < 0.12\ @\ 95\%\ \text{C.L.}$$

The model independent two-parameter fit yields W-boson helicity-fractions of:

$$\begin{aligned} F_0 &= 0.38\ \pm 0.21\ (\text{stat.})\ \pm 0.07\ (\text{syst.}) \\ F_+ &= 0.15\ \pm 0.10\ (\text{stat.})\ \pm 0.05\ (\text{syst.}) \end{aligned}$$

Within the quoted uncertainties all results are consistent with the SM predictions. Although the two-parameter fit results suggest a lower fraction of longitudinally polarized W bosons and a higher value for the fraction of right-handed W bosons, the probability to observe such a deviation or a larger one from the SM values has been estimated to be 34% and the deviations are thus not significant.
The results have been combined [6] with the results of another CDF analysis which used the same dataset and a template fit method. DØ measured the W boson helicity fractions in a dataset corresponding to an integrated luminosity of $1.0\,\text{fb}^{-1}$ in the combined dilepton and lepton+jets channel [7]. The results of the individual analyses are compared in figure 5.21. Given these values one can conclude that the results of the analysis presented in this thesis are consistent with the SM predictions and with results from other measurements. The CDF combination yields up to now the most precise published determinations of these quantities.

These results help to unveil the nature of this last discovered and least well studied quark. As no significant deviations from the SM predictions have been found, they support the picture the SM draws of its heaviest quark. Like the presented results many other measurements of top-quark properties at the Tevatron are still statistically limited. Further precise measurements of top-quark properties will be

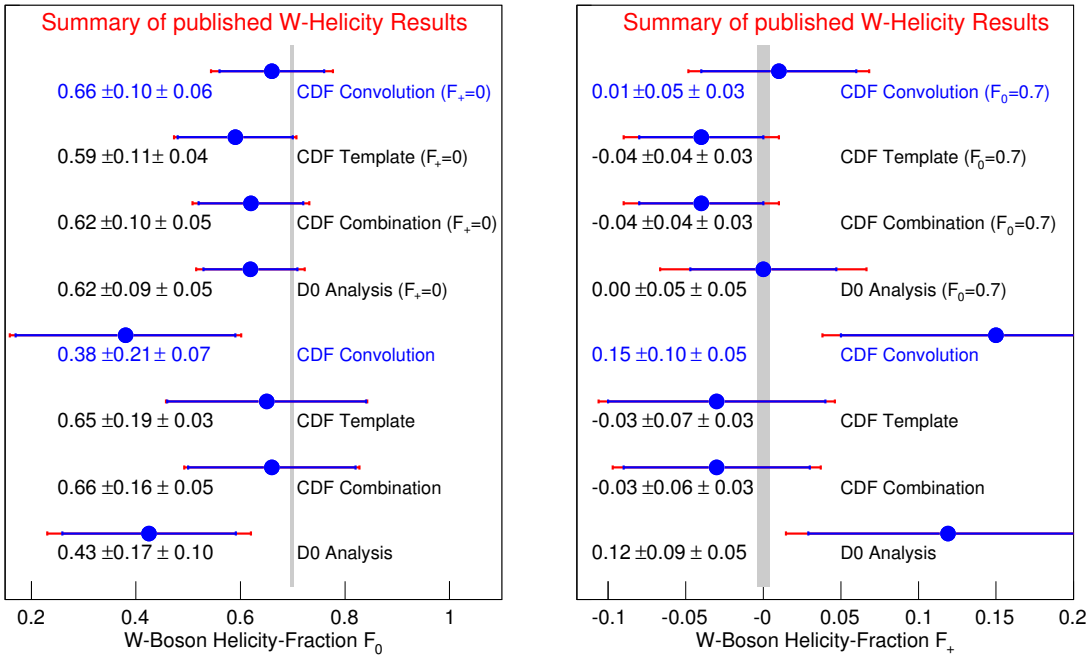

(a) (b)

Figure 5.21: Comparison of published results for the measurement of the fractions of (a) longitudinally polarized and (b) right-handed W bosons from top-quark decays. *CDF Convolution*, highlighted in blue, refers to the analysis presented in this thesis, while the second CDF analysis [6] is denoted *CDF Template*. Both analyses use a lepton+jets selected dataset corresponding to an integrated luminosity of $1.9\,\mathrm{fb}^{-1}$. The combination of both results is denoted *CDF Combination* [6]. The DØ analysis [7] uses a dataset in the combined lepton+jets and dilepton channel corresponding to an integrated luminosity of $1.0\,\mathrm{fb}^{-1}$. The upper four results are the values obtained in the one-parameter fits, while the lower four values are the model independent results. The blue error bars indicate the statistical error of the measurements, while the red error bars indicate the total error calculated as the square root of the quadratically summed statistical and systematic uncertainties. The grey lines indicate the LO predictions by the SM, $F_0 = 0.70$ and $F_+ = 0.00$.

soon possible with the expected large amount of LHC collision data collected by the ATLAS and CMS experiments.
Due to the larger center-of-mass energy the $t\bar{t}$ production cross-section at the LHC will be significantly enhanced compared to the Tevatron value. The pairwise production of top quarks will therefore be one of the first signals that will be established already with early LHC data. It will serve as standard candle in order to understand the detectors and their responses and will also constitute a major background to many searches for new physics.

In the second part of this thesis a study has been described which evaluated the prospects for an early $t\bar{t}$ cross-section measurement at a center-of-mass energy of 10 TeV with data corresponding to an integrated luminosity of $20\,\mathrm{pb}^{-1}$ collected with the CMS detector. In the absence of high-energy collision data, the study has been carried out on samples of simulated events. The focus in this study was on the electron+jets channel and a dedicated event selection has been developed

exploiting this signature. Applying this event selection on a dataset corresponding to an integrated luminosity of $20\,\mathrm{pb}^{-1}$ one expects to select about 300 events of which about 184 events are deemed to be $t\bar{t}$ events.
The background contribution from QCD multijet processes is particularly hard to simulate. Producing a sufficient number of simulated events for a proper estimation based on Monte Carlo simulations is nearly impossible due to the large cross section and small selection efficiency of these processes. In addition it is not clear to what extent one can trust the simulation of the detector response, which leads to this instrumental background. Therefore a data-driven technique for the estimation and modelling of the QCD multijet background has been developed. The QCD multijet contribution can be estimated exploiting an appropriate variable and extrapolating the fitted amount of QCD multijet events in a sideband region into the signal region. In the absence of collision data this method has been developed and tested using samples of simulated events.
The $t\bar{t}$ signal can be extracted exploiting the M3 variable, which is sensitive to the top-quark mass. M3 is defined as the invariant mass of the combination of three jets in each event that yields the highest vectorially summed p_{T}. In a maximum likelihood method the amount of $t\bar{t}$ events can be extracted from the M3 distribution and the corresponding cross section can be calculated. The precision that is expected to be achieved with this method has been estimated to:

$$\sigma_{t\bar{t}} = \sigma_{t\bar{t}}^{\mathrm{fit}} \ \pm 22\%(\mathrm{stat.}) \ \pm 24\%(\mathrm{syst.}) \ \pm 10\%(\mathrm{lumi.})$$

The quoted uncertainties are comparable with the ones estimated for similar analyses in the electron+jets and in the muon+jets channels aiming at a $t\bar{t}$ cross-section measurement assuming the same integrated luminosity [8, 9]. From this result one can conclude that it will be possible to establish a $t\bar{t}$ signal and to measure the $t\bar{t}$ production cross-section in the lepton+jets channel already with early data.
Meanwhile the most recent schedules for LHC operation envisage a first period of data taking at a center-of-mass energy of 7 TeV. Therefore, it is perfectly possible that already at this lower center-of-mass energy first $t\bar{t}$ events at the LHC will be detected. But since the $t\bar{t}$ cross section at a center-of-mass energy of 7 TeV is about two times smaller compared to the value at $\sqrt{s} = 10\,\mathrm{TeV}$, a two times larger dataset has to be used in order to achieve a comparable precision.

Better understanding and improved calibration and alignment of the detector will soon reduce the relatively large systematic uncertainties. With this better understanding of the detector and with reliable b tagging available it will also soon be possible to select datasets highly enriched in $t\bar{t}$ events. It can be expected that a top-quark purity will be achieved which is comparable to the one of the Tevatron experiments but with a significantly increased number of events. Therefore measurements of top-quark properties like the W-boson helicity-fractions will be possible with statistical uncertainties comparable to the ones of the CDF-analysis described in this thesis with datasets corresponding to an integrated luminosity of around $50\,\mathrm{pb}^{-1}$ at $\sqrt{s} = 10\,\mathrm{TeV}$. With increasing size of the collected and selected datasets the statistical uncertainties will decrease substantially [157]. This will open the window to studies of the top quark and its properties with unprecedented pre-

cision and will deepen our knowledge of the heaviest of the six quarks and of the interactions described in the standard model of elementary particle physics.

Appendix A

Additional Information on the CDF II Analysis

A.1 Used Signal MC Samples

Sample	Comment	Generator	Events [10^6]
ttop75	SM	Pythia	4.8
utop7j	$F_0 = 0.5, F_- = 0.5, F_+ = 0.0$	Herwig (Ggwig)	0.25
utop8j	$F_0 = 0.6, F_- = 0.4, F_+ = 0.0$	Herwig (Ggwig)	0.25
utop9j	$F_0 = 0.8, F_- = 0.2, F_+ = 0.0$	Herwig (Ggwig)	0.25
utopaj	$F_0 = 0.9, F_- = 0.1, F_+ = 0.0$	Herwig (Ggwig)	0.25
mtopgt	SM	MadGraph/MadEvent	1.0
mtopgu	$F_0 = 0.7, F_- = 0.25, F_+ = 0.05$	MadGraph/MadEvent	1.0
mtopgv	$F_0 = 0.7, F_- = 0.20, F_+ = 0.10$	MadGraph/MadEvent	1.0
mtopgw	$F_0 = 0.7, F_- = 0.15, F_+ = 0.15$	MadGraph/MadEvent	1.0
mtopgx	$F_0 = 0.7, F_- = 0.10, F_+ = 0.20$	MadGraph/MadEvent	1.0
mtopgy	$F_0 = 0.7, F_- = 0.05, F_+ = 0.25$	MadGraph/MadEvent	1.0
mtopgz	$F_0 = 0.7, F_- = 0.00, F_+ = 0.30$	MadGraph/MadEvent	1.0

Table A.1: $t\bar{t}$ signal MC samples used in the analyis. For the generation of the events a top-quark mass of $175\,\mathrm{GeV}/c^2$ has been used. The hadronization and showering for the MadGraph/MadEvent samples has been done using Pythia. In case of the samples with modified helicity fractions the quoted numbers refer always to the helicity of the W^+; the W^- have opposite helicity, but lead to the same angular distribution of the decay particles. In the Ggwig samples only the leptonically decaying W bosons exhibit the quoted helicity fractions, the hadronically decaying W bosons decay according to the SM expectation. The last column quotes the number of generated events.

A.2 Used Background MC Samples

Process	Sample	σ[pb]	Events [10^6]
$W(e,\nu)+2p$	ptop2w	35.5	1.0
$W(e,\nu)+3p$	ptop3w	5.59	1.0
$W(e,\nu)+4p$	ptop4w	1.03	1.0
$W(\mu,\nu)+3p$	ptop8w	5.59	1.0
$W(\mu,\nu)+4p$	ptop9w	1.03	1.0
$W(\tau,\nu)+3p$	utop3w	5.60	1.0
$W(\tau,\nu)+4p$	utop4w	1.03	1.0
$W(e,\nu)+b\bar{b}$	btop0w	2.98	1.5
$W(e,\nu)+b\bar{b}+1p$	btop1w	0.888	1.5
$W(e,\nu)+b\bar{b}+2p$	btop2w	0.287	1.5
$W(\mu,\nu)+b\bar{b}$	btop5w	2.98	1.5
$W(\mu,\nu)+b\bar{b}+1p$	btop6w	0.889	1.5
$W(\mu,\nu)+b\bar{b}+2p$	btop7w	0.286	1.5
$W(\tau,\nu)+b\bar{b}$	dtop0w	2.98	1.5
$W(\tau,\nu)+b\bar{b}+1p$	dtop1w	0.888	1.5
$W(\tau,\nu)+b\bar{b}+2p$	dtop2w	0.286	1.5
$W(e,\nu)+c\bar{c}$	ctop0w	5.0	2.0
$W(e,\nu)+c\bar{c}+1p$	ctop1w	1.79	2.0
$W(e,\nu)+c\bar{c}+2p$	ctop2w	0.628	2.0
$W(\mu,\nu)+c\bar{c}$	ctop5w	5.0	2.0
$W(\mu,\nu)+c\bar{c}+1p$	ctop6w	1.79	2.0
$W(\mu,\nu)+c\bar{c}+2p$	ctop7w	0.628	2.0
$W(\tau,\nu)+c\bar{c}+1p$	etopw1	1.80	2.0
$W(\tau,\nu)+c\bar{c}+2p$	etopw2	0.628	2.0
$W(e,\nu)+c+1p$	stopw1	3.39	2.0
$W(e,\nu)+c+2p$	stopw2	0.507	2.0
$W(e,\nu)+c+3p$	stopw3	0.083	2.0
$W(\mu,\nu)+c+1p$	stopw6	3.39	2.0
$W(\mu,\nu)+c+2p$	stopw7	0.507	2.0
$W(\mu,\nu)+c+3p$	stopw8	0.083	2.0
$W(\tau,\nu)+c+2p$	stopwc	0.507	1.5
$W(\tau,\nu)+c+3p$	stopwd	0.083	1.5

Table A.2: MC background samples for W+light flavor and W+heavy flavor backgrounds. The events have been generated with ALPGEN interfaced to PYTHIA. The W bosons are forced to decay leptonically into the quoted lepton type. All processes are produced separately for different numbers of additional partons and merged weighted according to their cross sections. Only samples of which at least one event survives the event selection are listed. The last column gives the number of generated events.

Process	Sample	Generator	Events [10^6]
single top (s-channel)	stop00	MadGraph/MadEvent	1.0
single top (t-channel)	stopm0	MadGraph/MadEvent	1.0
Diboson (WW)	itopww	Pythia	2.4
Diboson (WZ)	itopwz	Pythia	2.4
Diboson (ZZ)	itopzz	Pythia	2.4
$Z(\tau,\tau)+ \geq 2p$	ztopt2	Pythia	2.4

Table A.3: MC background samples for the electroweak backgrounds used in the analysis. The hadronization and showering for the MadGraph/MadEvent samples has been done using Pythia. The Z boson backgrounds are solely modelled by the $Z \to \tau\tau$ sample, since the samples for the other two processes were not available. However, the contribution of Z boson events to the total background is estimated to be only small, about two events, with the largest contribution of about one event from the $Z \to \tau\tau$ mode.

A.3 Used Systematic MC Samples

Sample	Systematic	Generator	Events [10^6]
itoprk	more ISR	Pythia	1.0
itoprl	less ISR	Pythia	1.0
ftoprj	more FSR	Pythia	1.0
ftoprl	less ISR	Pythia	1.0
htop75	MC Generator	Herwig	1.0

Table A.4: MC signal samples with varied parameters used for the estimation of systematic uncertainties.

A.4 Calculation of the z-Component of the Neutrino Momentum

The neutrino originates from the leptonical decay of a W boson, thus the sum of the four-vectors p_ℓ and p_ν of the charged lepton and the neutrino respectively has to be equal to the four-vector p_W of the W boson[1]

$$p_W = p_\ell + p_\nu \ . \tag{A.1}$$

Squaring this equation

$$p_W^2 = (p_\ell + p_\nu)^2 = p_\ell^2 + p_\nu^2 + 2p_\ell p_\nu \ , \tag{A.2}$$

[1]For simplicity for this calculation natural units with $c = 1$ are used.

and neglecting the invariant masses $p_\ell^2 = M_\ell^2$ and $p_\nu^2 = M_\nu^2$, it can be rewritten as:

$$\begin{aligned} M_W^2 &= 2p_\ell p_\nu = 2 \cdot (E_\ell E_\nu - \vec{p}_\ell \cdot \vec{p}_\nu) \\ &= 2 \cdot (E_\ell E_\nu - \vec{p}_{\mathrm{T},\ell} \cdot \vec{p}_{\mathrm{T},\nu}) \\ &= 2 \cdot (E_\ell E_\nu - p_{\mathrm{T},\ell} p_{\mathrm{T},\nu} \cos\Delta\phi - p_{z,\ell} p_{z,\nu}) \ . \end{aligned} \tag{A.3}$$

By introducing the abbreviation $\mu = \frac{M_W^2}{2} + p_{\mathrm{T},\ell} p_{\mathrm{T},\nu} \cos\Delta\phi$, this can be further simplified to

$$E_\ell E_\nu = \mu + p_{z,\ell} p_{z,\nu} \ . \tag{A.4}$$

The energy E_ν of the massless neutrino can be expressed in terms of its momentum components

$$E_\ell \sqrt{p_{\mathrm{T},\nu}^2 + p_{z,\nu}^2} = \mu + p_{z,\ell} p_{z,\nu} \ . \tag{A.5}$$

After squaring the equation and rearranging its terms, a quadratic equation in $p_{z,\nu}$ is obtained

$$p_{z,\nu}^2 - 2 \cdot \frac{\mu p_{z,\ell}}{E_\ell^2 - p_{z,\ell}^2} \cdot p_{z,\nu} + \frac{E_\ell^2 p_{\mathrm{T},\nu}^2 - \mu^2}{E_\ell^2 - p_{z,\ell}^2} = 0 \ . \tag{A.6}$$

The two solutions of this equation are

$$p_{z,\nu}^{\pm} = \frac{\mu p_{z,\ell}}{p_{\mathrm{T},\ell}^2} \pm \sqrt{\frac{\mu^2 p_{z,\ell}^2}{p_{\mathrm{T},\ell}^4} - \frac{E_\ell^2 p_{\mathrm{T},\nu}^2 - \mu^2}{p_{\mathrm{T},\ell}^2}} \ , \tag{A.7}$$

where $p_{\mathrm{T},\ell}^2 = E_\ell^2 - p_{z,\ell}^2$ has been used.

Appendix B

Additional Information on the CMS Study

B.1 Used Systematic MC Samples

Process	Comment	$\sigma \cdot f$ [pb]	events N	event weight w
$t\bar{t}$, inclusive	FullSim	414	106,540	0.0777
$t\bar{t}$, inclusive	FastSim, ISR/FSR default	414	100,000	0.0828
$t\bar{t}$, inclusive	FastSim, less ISR/FSR	414	100,000	0.0828
$t\bar{t}$, inclusive	FastSim, more ISR/FSR	414	100,000	0.0828

Table B.1: Samples of simulated $t\bar{t}$ events used for the estimation of the systematic uncertainties of the $t\bar{t}$ cross-section measurement due to variations in the signal modelling. All samples are generated with PYTHIA using a top-quark mass of 170.9 GeV/c^2. The events of the first sample are simulated with the full simulation, while for the other three samples the fast simulation is used.

Process	Comment	$\sigma \cdot f$ [nb]	events N	event weight w
Z+jets	default	4.2	9,964,055	0.0085
W+jets	default	45.6	101,467,739	0.0090
W+jets	Factorization Scale $\times 0.5$	45.6	15,537,883	0.0567
W+jets	Factorization Scale $\times 2.0$	45.6	18,690,697	0.0488
W+jets	Matching Threshold $\times 0.5$	45.6	15,480,461	0.0589
W+jets	Matching Threshold $\times 2.0$	45.6	21,865,945	0.0417

Table B.2: Samples of simulated Z+jets and W+jets events. All listed samples are generated with MADGRAPH/MADEVENT and simulated using the fast simulation. Only events with leptonically decaying bosons, via $Z \to \ell^+\ell^-$ and $W \to \ell\nu_\ell$, are generated. While the first two samples, labeled as default samples, are used to obtain the fit templates for the $H_{\mathrm{T,ele}}$ and M3 fits, the remaining samples are used to estimate the systematic uncertainties of the $t\bar{t}$ cross-section measurement due to variations in the modelling of the W+jets background.

List of Figures

List of Tables

Bibliography

[1] E. Rutherford, "The Scattering of α and β Particles by Matter and the Structure of the Atom", Phil. Mag. 21, 669–688 (1911).

[2] M. Gell-Mann, "A Schematic Model of Baryons and Mesons", Phys. Lett. 8, 214–215 (1964).

[3] F. Abe et al., "Observation of Top Quark Production in anti-p p Collisions", Phys. Rev. Lett. 74, 2626–2631 (1995).

[4] S. Abachi et al., "Observation of the Top Quark", Phys. Rev. Lett. 74, 2632–2637 (1995).

[5] Tevatron Electroweak Working Group, "Combination of CDF and D0 Results on the Mass of the Top Quark", FERMILAB-TM-2427-e (2009).

[6] T. Aaltonen et al., "Measurement of W-Boson Helicity Fractions in Top-Quark Decays Using $\cos\theta^*$", Phys. Lett. B674, 160–167 (2009).

[7] V. M. Abazov et al., "Model-Independent Measurement of the W Boson Helicity in Top Quark Decays at D0", Phys. Rev. Lett. 100, 062004 (2008).

[8] "Prospects for the First Measurement of the $t\bar{t}$ Cross Section in the Muon-plus-Jets Channel at $\sqrt{s} = 10\,\text{TeV}$ with the CMS Detector", CMS Physics Analysis Summary TOP-09-003 (2009).

[9] "Plans for an Early Measurement of the $t\bar{t}$ Cross Section in the Electron+Jets Channel at $\sqrt{s} = 10\,\text{TeV}$", CMS Physics Analysis Summary TOP-09-004 (2009).

[10] S. Weinberg, "A Model of Leptons", Phys. Rev. Lett. 19, 1264–1266 (1967).

[11] A. Salam and J. C. Ward, "Electromagnetic and Weak Interactions", Phys. Lett. 13, 168–171 (1964).

[12] S. L. Glashow, "Partial Symmetries of Weak Interactions", Nucl. Phys. 22, 579–588 (1961).

[13] S. L. Glashow, J. Iliopoulos, and L. Maiani, "Weak Interactions with Lepton-Hadron Symmetry", Phys. Rev. D2, 1285–1292 (1970).

[14] H. Georgi and S. L. Glashow, "Unified Weak and Electromagnetic Interactions without Neutral Currents", Phys. Rev. Lett. 28, 1494–1497 (1972).

[15] G. 't Hooft and M. J. G. Veltman, "Regularization and Renormalization of Gauge Fields", Nucl. Phys. B44, 189–213 (1972).

[16] D. J. Gross and F. Wilczek, "Asymptotically Free Gauge Theories. I", Phys. Rev. D8, 3633–3652 (1973).

[17] D. J. Gross and F. Wilczek, "Ultraviolet Behavior of Non-Abelian Gauge Theories", Phys. Rev. Lett. 30, 1343–1346 (1973).

[18] H. D. Politzer, "Reliable Perturbative Results for Strong Interactions?", Phys. Rev. Lett. 30, 1346–1349 (1973).

[19] Y. Fukuda et al., "Evidence for Oscillation of Atmospheric Neutrinos", Phys. Rev. Lett. 81, 1562–1567 (1998).

[20] Q. R. Ahmad et al., "Measurement of the Charged Current Interactions Produced by B-8 Solar Neutrinos at the Sudbury Neutrino Observatory", Phys. Rev. Lett. 87, 071301 (2001).

[21] S. Fukuda et al., "Solar ^{8}B and hep Neutrino Measurements from 1258 Days of Super-Kamiokande Data", Phys. Rev. Lett. 86, 5651–5655 (2001).

[22] Q. R. Ahmad et al., "Direct Evidence for Neutrino Flavor Transformation from Neutral-Current Interactions in the Sudbury Neutrino Observatory", Phys. Rev. Lett. 89, 011301 (2002).

[23] S. Khalil and E. Torrente-Lujan, "Neutrino Mass and Oscillation as Probes of Physics Beyond the Standard Model", J. Egyptian Math. Soc. 9, 91–141 (2001).

[24] P. Ramond, "Neutrinos: A Glimpse Beyond the Standard Model", Nucl. Phys. Proc. Suppl. 77, 3–9 (1999).

[25] O. W. Greenberg, "Spin and Unitary Spin Independence in a Paraquark Model of Baryons and Mesons", Phys. Rev. Lett. 13, 598–602 (1964).

[26] M. Y. Han and Y. Nambu, "Three-Triplet Model with Double SU(3) Symmetry", Phys. Rev. 139, B1006–B1010 (1965).

[27] H. Fritzsch, M. Gell-Mann, and H. Leutwyler, "Advantages of the Color Octet Gluon Picture", Phys. Lett. B47, 365–368 (1973).

[28] C. Amsler et al., "Review of Particle Physics", Phys. Lett. B667, 1 (2008).

[29] A. Einstein, "Grundlage der Allgemeinen Relativitätstheorie", Annalen Phys. 49, 769–822 (1916).

[30] A. Einstein, "Prinzipielles zur Allgemeinen Relativitätstheorie", Annalen Phys. 55, 241 (1918).

[31] R. P. Feynman, "The Theory of Positrons", Phys. Rev. 76, 749–759 (1949).

[32] R. P. Feynman, "Space-Time Approach to Quantum Electrodynamics", Phys. Rev. 76, 769–789 (1949).

[33] R. P. Feynman, "Mathematical Formulation of the Quantum Theory of Electromagnetic Interaction", Phys. Rev. 80, 440–457 (1950).

[34] J. S. Schwinger, "Quantum Electrodynamics. I: A Covariant Formulation", Phys. Rev. 74, 1439 (1948).

[35] J. S. Schwinger, "Quantum Electrodynamics. II: Vacuum Polarization and Selfenergy", Phys. Rev. 75, 651 (1948).

[36] J. S. Schwinger, "Quantum Electrodynamics. III: The Electromagnetic Properties of the Electron: Radiative Corrections to Scattering", Phys. Rev. 76, 790–817 (1949).

[37] S. Tomonaga, "On a Relativistically Invariant Formulation of the Quantum Theory of Wave Fields", Prog. Theor. Phys. 1, 27–42 (1946).

[38] N. Cabibbo, "Unitary Symmetry and Leptonic Decays", Phys. Rev. Lett. 10, 531–532 (1963).

[39] M. Kobayashi and T. Maskawa, "CP Violation in the Renormalizable Theory of Weak Interaction", Prog. Theor. Phys. 49, 652–657 (1973).

[40] P. W. Higgs, "Broken Symmetries, Massless Particles and Gauge Fields", Phys. Lett. 12, 132–133 (1964).

[41] P. W. Higgs, "Broken Symmetries and the Masses of Gauge Bosons", Phys. Rev. Lett. 13, 508–509 (1964).

[42] P. W. Higgs, "Spontaneous Symmetry Breakdown without Massless Bosons", Phys. Rev. 145, 1156–1163 (1966).

[43] Y. Nambu and G. Jona-Lasinio, "Dynamical Model of Elementary Particles Based on an Analogy with Superconductivity. I", Phys. Rev. 122, 345–358 (1961).

[44] Y. Nambu and G. Jona-Lasinio, "Dynamical Model of Elementary Particles Based on an Analogy with Superconductivity. II", Phys. Rev. 124, 246–254 (1961).

[45] J. Goldstone, "Field Theories with Superconductor Solutions", Nuovo Cim. 19, 154–164 (1961).

[46] J. Goldstone, A. Salam, and S. Weinberg, "Broken Symmetries", Phys. Rev. 127, 965–970 (1962).

[47] R. D. Peccei and X. Zhang, "Dynamical Symmetry Breaking and Universality Breakdown", Nucl. Phys. B337, 269–283 (1990).

[48] R. D. Peccei, S. Peris, and X. Zhang, "Nonstandard Couplings of the Top Quark and Precision Measurements of the Electroweak Theory", Nucl. Phys. B349, 305–322 (1991).

[49] Y. Grossman and I. Nachshon, "Hadronization, Spin, and Lifetimes", JHEP 07, 016 (2008).

[50] J. R. Incandela, A. Quadt, W. Wagner, and D. Wicke, "Status and Prospects of Top-Quark Physics", Prog. Part. Nucl. Phys. 63, 239–292 (2009).

[51] T. Aaltonen et al., "Observation of Electroweak Single Top Quark Production", Phys. Rev. Lett. 103, 092002 (2009).

[52] V. M. Abazov et al., "Observation of Single Top-Quark Production", Phys. Rev. Lett. 103, 092001 (2009).

[53] V. D. Barger and R. J. N. Phillips, "Collider Physics (Frontiers in Physics)", Addison Wesley Publishing Company (1987).

[54] W. K. Tung, H. L. Lai, A. Belyaev, J. Pumplin, D. Stump, and C. P. Yuan, "Heavy Quark Mass Effects in Deep Inelastic Scattering and Global QCD Analysis", JHEP0702 053 (2007).

[55] S. Moch and P. Uwer, "Theoretical Status and Prospects for Top-Quark Pair Production at Hadron Colliders", Phys. Rev. D78, 034003 (2008).

[56] M. Cacciari, S. Frixione, M. L. Mangano, P. Nason, and G. Ridolfi, "Updated Predictions for the Total Production Cross Sections of Top and of Heavier Quark Pairs at the Tevatron and at the LHC", JHEP 09, 127 (2008).

[57] C. T. Hill, "Topcolor Assisted Technicolor", Phys. Lett. B345, 483–489 (1995).

[58] G. L. Kane, G. A. Ladinsky, and C. P. Yuan, "Using the Top Quark for Testing Standard Model Polarization and CP Predictions", Phys. Rev. D45, 124–141 (1992).

[59] A. Denner and T. Sack, "The Top Width", Nucl. Phys. B358, 46–58 (1991).

[60] M. Jezabek and J. H. Kuhn, "QCD Corrections to Semileptonic Decays of Heavy Quarks", Nucl. Phys. B314, 1 (1989).

[61] G. Eilam, R. R. Mendel, R. Migneron, and A. Soni, "Radiative Corrections to Top-Quark Decay", Phys. Rev. Lett. 66, 3105–3108 (1991).

[62] M. Fischer, S. Groote, J. G. Korner, M. C. Mauser, and B. Lampe, "Polarized Top Decay into Polarized W: t(polarized) → W(polarized) + b at $O(\alpha_s)$", Phys. Lett. B451, 406–413 (1999).

[63] M. Jezabek and J. H. Kuhn, "The Top Width: Theoretical Update", Phys. Rev. D48, 1910–1913 (1993).

[64] M. Fischer, S. Groote, J. G. Korner, and M. C. Mauser, "Longitudinal, Transverse-Plus and Transverse-Minus W-Bosons in Unpolarized Top-Quark Decays at $O(\alpha_s)$", Phys. Rev. D63, 031501 (2001).

[65] H. S. Do, S. Groote, J. G. Korner, and M. C. Mauser, "Electroweak and Finite Width Corrections to Top-Quark Decays into Transverse and Longitudinal W Bosons", Phys. Rev. D67, 091501 (2003).

[66] J. A. Aguilar-Saavedra, "Effects of Mixing with Quark Singlets", Phys. Rev. D67, 035003 (2003).

[67] J.-j. Cao, R. J. Oakes, F. Wang, and J. M. Yang, "Supersymmetric Effects in Top-Quark Decay into Polarized W Boson", Phys. Rev. D68, 054019 (2003).

[68] C.-R. Chen, F. Larios, and C. P. Yuan, "General Analysis of Single Top Production and W Helicity in Top Decay", Phys. Lett. B631, 126–132, and references therein (2005).

[69] J. A. Aguilar-Saavedra, J. Carvalho, N. F. Castro, F. Veloso, and A. Onofre, "Probing Anomalous W t b Couplings in Top Pair Decays", Eur. Phys. J. C50, 519–533 (2007).

[70] X.-l. Wang, Q.-l. Zhang, and Q.-p. Qiao, "Studying Top-Quark Decay into the Polarized W^- Boson in the TC2 Model", Phys. Rev. D71, 014035 (2005).

[71] L. Evans and P. Bryant (editors), "LHC Machine", JINST 3, S08001 (2008).

[72] R. F. Welton, "Overview of High-Brightness H^- Ion Sources", Proceedings of LINAC 2002, Korea (2002).

[73] "Fermilab Linac Upgrade Conceptual Design Revision 4A", FERMILAB-LU-CONCEPTUAL-DESIGN (1989).

[74] S. D. Holmes, R. E. Gerig, and D. E. Johnson, "The Fermilab Main Injector", Part. Accel. 26, 193–198 (1990).

[75] D. Mohl, G. Petrucci, L. Thorndahl, and S. Van Der Meer, "Physics and Technique of Stochastic Cooling", Phys. Rept. 58, 73–119 (1980).

[76] G. Jackson, "The Fermilab Recycler Ring Technical Design Report. Rev. 1.2", FERMILAB-TM-1991 (1996).

[77] G. I. Budker, "An Effective Method of Damping Particle Oscillations in Proton and Antiproton Storage Rings", Sov. Atom. Energ. 22, 438–440 (1967).

[78] S. Nagaitsev et al., "Experimental Demonstration of Relativistic Electron Cooling", Phys. Rev. Lett. 96, 044801 (2006).

[79] P. H. Garbincius, "Tevatron Collider Operations and Plans", `arXiv:hep-ex/0406013` (2004).

[80] L. Arnaudon et al., "Linac4 Technical Design Report", CERN-AB-2006-084 (2006).

[81] K. Schindl, "The PS Booster as Pre-Injector for LHC", Part. Accel. 58, 63–78 (1997).

[82] R. Cappi, "The PS in the LHC Injector Chain", Part. Accel. 58, 79–89 (1997).

[83] T. Linnecar, "Preparing the SPS for LHC", Part. Accel. 58, 91–101 (1997).

[84] G. Arnison et al., "Experimental Observation of Isolated Large Transverse Energy Electrons with Associated Missing Energy at $\sqrt{s} = 540\,\mathrm{GeV}$", Phys. Lett. B122, 103–116 (1983).

[85] M. Banner et al., "Observation of Single Isolated Electrons of High Transverse Momentum in Events with Missing Transverse Energy at the CERN anti-p p Collider", Phys. Lett. B122, 476–485 (1983).

[86] G. Arnison et al., "Experimental Observation of Lepton Pairs of Invariant Mass around $95\,\mathrm{GeV}/c^2$ at the CERN SPS Collider", Phys. Lett. B126, 398–410 (1983).

[87] P. Bagnaia et al., "Evidence for $Z^0 \to e^+e^-$ at the CERN anti-p p Collider", Phys. Lett. B129, 130–140 (1983).

[88] R. Blair et al., "The CDF-II Detector: Technical Design Report", FERMILAB-PUB-96-390-E (1996).

[89] C. S. Hill, "Initial Experience with the CDF Layer 00 Silicon Detector", Nucl. Instrum. Meth. A511, 118–120 (2003).

[90] A. Sill, "CDF Run II Silicon Tracking Projects", Nucl. Instrum. Meth. A447, 1–8 (2000).

[91] A. Affolder et al., "Intermediate Silicon Layers Detector for the CDF Experiment", Nucl. Instrum. Meth. A453, 84–88 (2000).

[92] A. A. Affolder et al., "CDF Central Outer Tracker", Nucl. Instrum. Meth. A526, 249–299 (2004).

[93] H. Minemura et al., "Construction and Testing of a 3-m Diameter × 5-M Superconducting Solenoid for the Fermilab Collider Detector Facility (CDF)", Nucl. Instrum. Meth. A238, 18–34 (1985).

[94] L. Balka et al., "The CDF Central Electromagnetic Calorimeter", Nucl. Instrum. Meth. A267, 272 (1988).

[95] R. Oishi, "New CDF End-Plug Calorimeter", Nucl. Instrum. Meth. A453, 227–229 (2000).

[96] M. G. Albrow et al., "The CDF Plug Upgrade Electromagnetic Calorimeter: Test Beam Results", Nucl. Instrum. Meth. A480, 524–546 (2002).

[97] S. Bertolucci et al., "The CDF Central and Endwall Hadron Calorimeter", Nucl. Instrum. Meth. A267, 301 (1988).

[98] A. Bhatti et al., "Determination of the Jet Energy Scale at the Collider Detector at Fermilab", Nucl. Instrum. Meth. A566, 375–412 (2006).

[99] C. M. Ginsburg, "CDF Run 2 Muon System", Eur. Phys. J. C33, s1002–s1004 (2004).

[100] G. Ascoli et al., "CDF Central Muon Detector", Nucl. Instrum. Meth. A268, 33 (1988).

[101] T. Dorigo, "The Muon System Upgrade for the CDF II Experiment", Nucl. Instrum. Meth. A461, 560–562 (2001).

[102] G. L. Bayatian et al., "CMS Physics: Technical Design Report", CERN-LHCC-2006-001.

[103] R. Adolphi et al., "The CMS Experiment at the CERN LHC", JINST 0803, S08004 (2008).

[104] "Commissioning of the CMS Experiment and the Cosmic Run at Four Tesla", CMS CFT-09-008, to be submitted to JINST (2009).

[105] Karimäki, V., "The CMS Tracker System Project: Technical Design Report", CERN-LHCC-98-006 (1997).

[106] "Addendum to the CMS Tracker TDR", CERN-LHCC-2000-016 (2000).

[107] "The CMS Electromagnetic Calorimeter Project: Technical Design Report", CERN-LHCC-97-033 (1997).

[108] P. Adzic et al., "Energy Resolution of the Barrel of the CMS Electromagnetic Calorimeter", JINST 2, P04004 (2007).

[109] "The CMS Hadron Calorimeter Project: Technical Design Report", CERN-LHCC-97-031 (1997).

[110] S. Abdullin et al., "The CMS Barrel Calorimeter Response to Particle Beams from 2 GeV/c to 350 GeV/c", Eur. Phys. J. C60, 359–373 (2009).

[111] G. Bayatian et al., "Design, Performance and Calibration of the CMS Forward Calorimeter Wedges", Eur. Phys. J. C53, 139–166 (2008).

[112] "CMS, the Compact Muon Solenoid. Muon Technical Design Report", CERN-LHCC-97-32 (1997).

[113] B. Andersson, G. Gustafson, and B. Soderberg, "A General Model for Jet Fragmentation", Z. Phys. C20, 317 (1983).

[114] B. Andersson, G. Gustafson, G. Ingelman, and T. Sjostrand, "Parton Fragmentation and String Dynamics", Phys. Rept. 97, 31 (1983).

[115] B. R. Webber, "A QCD Model for Jet Fragmentation Including Soft Gluon Interference", Nucl. Phys. B238, 492 (1984).

[116] D. Amati and G. Veneziano, "Preconfinement as a Property of Perturbative QCD", Phys. Lett. B83, 87 (1979).

[117] M. L. Mangano et al., "ALPGEN, a Generator for Hard Multiparton Processes in Hadronic Collisions", J. High Energy Phys. 07, 001 (2003).

[118] F. Maltoni and T. Stelzer, "MadEvent: Automatic Event Generation with MadGraph", J. High Energy Phys. 02, 027 (2003).

[119] T. Sjostrand et al., "High-Energy-Physics Event Generation with PYTHIA 6.1", Comput. Phys. Commun. 135, 238–259 (2001).

[120] G. Corcella et al., "HERWIG 6: An Event Generator for Hadron Emission Reactions with Interfering Gluons (Including Supersymmetric Processes)", J. High Energy Phys. 01, 010 (2001).

[121] S. Catani, F. Krauss, R. Kuhn, and B. R. Webber, "QCD Matrix Elements + Parton Showers", J. High Energy Phys. 11, 063 (2001).

[122] S. Hoche et al., "Matching Parton Showers and Matrix Elements", `arXiv:hep-ph/0602031` (2006).

[123] R. Brun and C. Carminati, "GEANT Detector Description and Simulation Tool", CERN Program Library Writeup W5013 (1993).

[124] R. Veenhof, "GARFIELD, recent Developments", Nucl. Instrum. Meth. A419, 726–730 (1998).

[125] G. Grindhammer, M. Rudowicz, and S. Peters, "The Fast Simulation of Electromagnetic and Hadronic Showers", Nucl. Instrum. Meth. A290, 469 (1990).

[126] F. D. Snider, "Tracking at CDF: Algorithms and Experience from Run I and Run II", Nucl. Instrum. Meth. A566, 133–141 (2006).

[127] C. Hays et al., "Inside-Out Tracking at CDF", Nucl. Instrum. Meth. A538, 249–254 (2005).

[128] T. Speer et al., "Track Reconstruction in the CMS Tracker", Nucl. Instrum. Meth. A559, 143–147 (2006).

[129] R. Kalman, "A New Approach to Linear Filtering and Prediction Problems", Transactions of the ASME. Series D: Journal of Basic Engineering 82, 35–45 (1960).

[130] S. Baffioni et al., "Electron Reconstruction in CMS", Eur. Phys. J. C49, 1099–1116 (2007).

[131] W. Adam, R. Fruhwirth, A. Strandlie, and T. Todorov, "Reconstruction of Electrons with the Gaussian-Sum Filter in the CMS Tracker at LHC", ECONF C0303241, TULT009 (2003).

[132] R. Fruhwirth, "Track Fitting with Non-Gaussian Noise", Comput. Phys. Commun. 100, 1–16 (1997).

[133] S. Catani, Y. L. Dokshitzer, M. H. Seymour, and B. R. Webber, "Longitudinally Invariant K_t Clustering Algorithms for Hadron Hadron Collisions", Nucl. Phys. B406, 187–224 (1993).

[134] M. Cacciari, G. P. Salam, and G. Soyez, "The Anti-K_t Jet Clustering Algorithm", JHEP 04, 063 (2008).

[135] Y. L. Dokshitzer, G. D. Leder, S. Moretti, and B. R. Webber, "Better Jet Clustering Algorithms", JHEP 08, 001 (1997).

[136] M. Wobisch and T. Wengler, "Hadronization Corrections to Jet Cross Sections in Deep-Inelastic Scattering", `arXiv:hep-ph/9907280` (1998).

[137] F. Abe et al., "The Topology of Three Jet Events in $\bar{p}p$ Collisions at $\sqrt{s} = 1.8\,\text{TeV}$", Phys. Rev. D45, 1448–1458 (1992).

[138] "Performance of Jet Algorithms in CMS", CMS Physics Analysis Summary JME-07-003 (2008).

[139] G. P. Salam and G. Soyez, "A Practical Seedless Infrared-Safe Cone Jet Algorithm", JHEP 05, 086 (2007).

[140] "Plans for Jet Energy Corrections at CMS", CMS Physics Analysis Summary JME-07-002 (2007).

[141] D. Acosta et al., "Measurement of the $t\bar{t}$ Production Cross Section in $p\bar{p}$ Collisions at $\sqrt{s} = 1.96$ TeV using Lepton + Jets Events with Secondary Vertex $b-$Tagging", Phys. Rev. D71, 052003 (2005).

[142] S. Richter, "Search for Electroweak Single Top-Quark Production with the CDF II Experiment", FERMILAB-THESIS-2007-35 (2007).

[143] "GOOD RUN LIST V18." http://www-cdf.fnal.gov/internal/dqm/goodrun/v18/goodv18.html.

[144] T. Aaltonen et al., "Forward-Backward Asymmetry in Top Quark Production in $p\bar{p}$ Collisions at $\sqrt{s} = 1.96$ TeV", Phys. Rev. Lett. 101, 202001 (2008).

[145] A. Abulencia et al., "Measurement of the $t\bar{t}$ Production Cross Section in $p\bar{p}$ Collisions at $\sqrt{s} = 1.96$-TeV using Lepton + Jets Events with Jet Probability b-Tagging", Phys. Rev. D74, 072006 (2006).

[146] M. Renz, "B-Jet and C-Jet Identification with Neural Networks as well as Combination of Multivariate Analyses for the Search for Single Top-Quark Production", FERMILAB-MASTERS-2008-06 (2008).

[147] H. L. Lai et al., "Global QCD Analysis of Parton Structure of the Nucleon: CTEQ5 Parton Distributions", Eur. Phys. J. C 12, 375–392 (2000).

[148] A. D. Martin, R. G. Roberts, W. J. Stirling, and R. S. Thorne, "Parton Distributions: A New Global Analysis", Eur. Phys. J. C4, 463–496 (1998).

[149] J. Pumplin et al., "New Generation of Parton Distributions with Uncertainties from Global QCD Analysis", JHEP 07, 012 (2002).

[150] J. M. Campbell, R. K. Ellis, and F. Tramontano, "Single Top Production and Decay at Next-to-Leading Order", Phys. Rev. D70, 094012 (2004).

[151] J. Campbell and F. Tramontano, "Next-to-Leading Order Corrections to Wt Production and Decay", Nucl. Phys. B726, 109–130 (2005).

[152] S. Frixione and M. L. Mangano, "How Accurately can We Measure the W Cross Section?", JHEP 05, 056 (2004).

[153] "Measuring Electron Efficiencies at CMS with Early Data", CMS Physics Analysis Summary EGM-07-001 (2008).

[154] "Jet Corrections to Parent Parton Energy", CMS Physics Analysis Summary JME-08-002 (2009).

[155] P. M. Nadolsky et al., "Implications of CTEQ Global Analysis for Collider Observables", Phys. Rev. D78, 013004 (2008).

[156] M. R. Whalley, D. Bourilkov, and R. C. Group, "The Les Houches Accord PDFs (LHAPDF) and Lhaglue".

[157] G. Sartisohn, "Studies for the Measurement of the W Boson Helicity in Top Quark Decays with the CMS Experiment", IEKP-KA/2008-1 (2007).

Dankesworte

Solch eine Arbeit wäre ohne die Unterstützung und Mithilfe vieler Menschen nicht zu bewerkstelligen. Daher möchte ich an dieser Stelle all denjenigen meinen Dank aussprechen, die mich auf meinem Weg begleitet und in irgendeiner Weise zum Gelingen dieser Arbeit beigetragen haben.

Als erstes möchte ich mich bei meinen beiden Doktorvätern, Herrn Prof. Dr. Wolfgang Wagner und Herrn Prof. Dr. Thomas Müller bedanken. Wolfgang Wagner war während der Arbeit an der CDF-Analyse immer für mich da und hatte stets ein offenes Ohr und eine gute Idee. Auch nach seinem Weggang nach Wuppertal blieben wir in engem Kontakt und haben gemeinsam an der Veröffentlichung der Ergebnisse gearbeitet. Für seinen unermüdlichen Einsatz und seine unzähligen Hilfestellungen auch aus der Ferne sowie das freundschaftliche Verhältnis möchte ich ihm nochmals herzlich danken. Thomas Müller danke ich für die Aufnahme in seine Top-Gruppe und die Ermöglichung mehrerer Forschungsaufenthalte am Fermilab und am CERN, sowie das Vertrauen, das er mir und meiner Arbeit entgegengebracht hat.

Ein großes Dankeschön gebührt auch den Postdocs der Top-Gruppe, die mich bei meiner Arbeit unterstützten. Besonders dankbar bin ich Dr. Dominic Hirschbühl, der mir bei der CDF-Analyse stets mit Rat und Tat zur Seite stand und auch nach seinem Weggang nach Wuppertal nie um einen Tipp verlegen war. Bei Dr. Jeannine Wagner-Kuhr und Dr. Frank-Peter Schilling möchte ich mich für die Betreuung während meiner Arbeit und die vielen hilfreichen Ratschläge bedanken. Jeannine sei auch noch einmal sehr herzlich für die gute Vorbereitung auf die Prüfung gedankt.

Des weiteren gilt mein Dank allen Mitgliedern der Karlsruher Top-Gruppe für das stets gute und inspirierende Arbeitsklima und die Hilfsbereitschaft untereinander - es hat sehr viel Spaß gemacht, in diesem Team zu arbeiten. Besonders hervorheben möchte ich meine langjährige Zimmerkollegin, die zunächst als Julia Weinelt später als Julia Bauer sowohl in Karlsruhe als auch am CERN in Genf gemäß dem Motto “geteiltes Leid ist halbes Leid” viele Stationen der Promotion mit mir gemeinsam durchlebte. Was wäre eine Dissertation ohne ein strenges Lektorenteam? An dieser Stelle möchte ich meinen engagierten Korrekturlesern Jasmin Gruschke, Manuel Renz und Jochen Ott danken - ihnen hat die Arbeit nicht nur das ein oder andere “the” zu verdanken, sondern sie haben durch ihr sorgfältiges Lesen und ihre konstruktiven Korrekturvorschläge maßgeblich dazu beigetragen, die Qualität der Arbeit zu verbessern. Bei Jochen möchte ich mich noch voller Bewunderung dafür bedanken, dass er für fast alle Fragen eine Antwort kannte, was sowohl beim Schrei-

ben der Arbeit als auch bei der Vorbereitung auf die Prüfung von unschätzbarem Wert war. Jasmin und Manuel sei auch besonders für die hervorragende Zusammenarbeit bei der CMS-Analyse und Jasmin im Speziellen fürs Drucken meiner Arbeit und meines Posters gedankt. Dr. Jan Lück hat mit seiner Erfahrung der eigenen Doktroprüfung und mit vielen Tipps und Tricks ebenfalls einen sehr großen Anteil an dieser Arbeit.

Den Dank möchte ich gerne ausweiten auf das gesamte EKP und alle seine Mitglieder in Karlsruhe und am CERN. Ich habe hier eine unglaublich hilfsbereite Arbeitsatmosphäre erlebt, egal ob es um die Wohnungssuche am CERN, Computing-Probleme, Fragen zur theoretischen oder experimentellen Aspekten der Analyse oder um die Vorbereitung der Prüfung ging.

Auch dem Admin-Team unter Leitung von Dr. Thomas Kuhr und Dr. Michal Kreps möchte ich gerne danken für den unermüdlichen Einsatz im ständigen Kampf gegen Netzwerk-Probleme, Hardwareausfälle, neue Betriebssystem-Versionen und dergleichen mehr. Die unzähligen Stunden, die hier geopfert werden, um eine funktionierende Computing-Infrastruktur zu gewährleisten, können nicht hoch genug angerechnet werden.

Auch die Zusammenarbeit mit dem Sekretariat des EKP, mit Frau Weissmann und später mit Frau Bräunling war stets unkompliziert. Kleinigkeiten wie die Weihnachtsfeier oder die Geburtstags-Glückwunschzettel an der Bürotür tragen wesentlich zur guten Atmosphäre im Institut bei und haben mit dazu geführt dass ich mich am EKP stets wohlfühlte.

Nach all den Dankesworten an meine Kollegen und das Institut möchte ich zum Abschluss meiner Familie und meinen Freunden danken. Meinen Eltern danke ich für ihre vielfältige Unterstützung und dafür dass sie mir die nötige Rückendeckung gegeben und Verständnis für mich und meine Arbeit aufgebracht haben. Des weiteren danke ich meinen Geschwistern mit Partnern und meinen Großeltern, die mich immer unterstützt und sich mit mir über meine erfolgreiche Promotion gefreut haben. Als letztes - aber dafür umsomehr - möchte ich meiner Freundin Maren danken, die sich nicht nur tapfer meine Probevorträge angehört hat, sondern mich die ganze Zeit über immer wieder auf andere Gedanken gebracht, wenn nötig wieder aufgebaut und immer unterstützt hat.

Euch allen und allen, die hier nicht namentlich aufgeführt sind, nochmals ein herzliches Dankeschön!